SOLUTION-PROCESSED METAL-OXIDE THIN FILMS: TOWARD ENHANCED UNDERSTANDING OF FILM FORMATION CHEMISTRY

by

ELIZABETH A. COCHRAN

A DISSERTATION

Presented to the Department of Chemistry and Biochemistry
and the Graduate School of the University of Oregon
in partial fulfillment of the requirements
for the degree of
Doctor of Philosophy

December 2019

DISSERTATION APPROVAL PAGE

Student: Elizabeth A. Cochran

Title: Solution-Processed Metal-Oxide Thin Films: Toward Enhanced Understanding Film Formation Chemistry

This dissertation has been accepted and approved in partial fulfillment of the requirements for the Doctor of Philosophy degree in the Department of Chemistry and Biochemistry by:

Catherine J. Page	Chairperson
Shannon W. Boettcher	Advisor
Darren W. Johnson	Advisor
James E. Hutchison	Core Member
Emilie Hooft	Institutional Representative

and

Kate Mondloch	Interim Vice Provost and Dean of the Graduate School

Original approval signatures are on file with the University of Oregon Graduate School.

Degree awarded December 2019

© 2019 Elizabeth A. Cochran

DISSERTATION ABSTRACT

Elizabeth A. Cochran

Doctor of Philosophy

Department of Chemistry and Biochemistry

December 2019

Title: Solution-Processed Metal-Oxide Thin Films: Toward Enhanced Understanding Film Formation Chemistry

Metal-oxide thin films serve many functions in electronic and energy devices. As technology progresses, demands for faster performance and improved connectivity within the internet of things (IoT) continually increase. The ability to deposit high-quality materials is required in order to meet such needs. Microelectronics industries have driven the development of methods to deposit dense, smooth, and defect-free metal-oxide thin films in order keep pace with transistor scaling predicted by Moore's law. As a result, the chemical reactions involved in metal-oxide film formation from vapor-phase deposition methods, such as atomic layer deposition (ALD), are well characterized and controlled. However, the energy and infrastructure expense associated with vapor deposition is cost prohibitive for many applications.

Solution processing offers a potentially low-cost, scalable method for metal-oxide thin film deposition to complement vapor-phase methods and expand the application base of these materials. Solution processing is amenable to many large-area deposition methods that use cheap infrastructure, making it a seemingly ideal candidate for roll-to-roll processing on plastic substrates. Achieving high-quality, high-performance metal-oxide thin films from solution precursors has been historically challenging; however, significant progress has been made to narrow the performance gap between vapor- and

solution-deposited materials. This has been made possible by improved understanding and characterization of the thin-film chemical reaction pathway from solution precursor to metal-oxide thin film.

This dissertation details important chemical considerations for preparing high-quality materials via solution deposition, with specific focus on metal-nitrate ($M(NO_3)_x$) precursors. Chapter I introduces the importance of understanding thin-film formation chemistry for the advancement of solution-deposition technologies. Chapters II and III review precursor chemistry and thin-film treatment methods that utilize unique decomposition chemistries of $M(NO_3)_x$ to produce high-quality metal-oxide thin films. Chapters IV and V detail investigations of low-temperature film formation chemistry induced by combustion processing and water-vapor (or "steam") annealing. Chapter VI frames the work of all previous chapters from the perspective of the role chemistry can play in process development of solution-processed metal-oxide thin films for the macroelectronics industry.

This dissertation includes previously published and unpublished coauthored material.

CURRICULUM VITAE

NAME OF AUTHOR: Elizabeth A. Cochran

GRADUATE AND UNDERGRADUATE SCHOOLS ATTENDED:

University of Oregon, Eugene, OR
University of San Francisco, San Francisco, CA

DEGREES AWARDED:

Doctor of Philosophy, Chemistry, 2019, University of Oregon
Master of Science, Chemistry, 2015, University of Oregon
Bachelor of Science, Chemistry, 2013, University of San Francisco

AREAS OF SPECIAL INTEREST:

Materials Chemistry

PROFESSIONAL EXPERIENCE:

Research Assistant, Boettcher Research Group, University of Oregon, 2015-2019

Research Assistant, D.W. Johnson Research Group, University of Oregon, 2015-2019

Process Development Engineer Intern, Micron Technology, Boise, ID, July 2018 to Sept 2018

Research Assistant, Meloni Research Group, University of San Francisco, 2013-2014

GRANTS, AWARDS, AND HONORS:

Science Communication Fellowship, Oregon Museum of Science and Industry, 2016

ACS Inorganic Chemistry Award, University of San Francisco, 2014

Loyola Guild Scholarship, University of San Francisco, 2001-2012

University Scholar, University of San Francisco, 2011-2013

PUBLICATIONS:

Stoerzinger, K.A.; Enman, L.J.; Cochran, E.A.; Diulus, J.T.; Frederick, R.T.; Artyushkova, K.; Crumlin, E.J.; Herman, G.S.; Boettcher, S.W. Understanding Surface Reactivity of Amorphous Transition-Metal-Incorporated Aluminum Oxide Thin Films. *J. Phys. Chem. C*, **2019**, **DOI:** 10.1021/acs.jpcc.9b08227.

Cochran, E.A.; Woods, K.N.; Johnson, D.W.; Page, C.J.; Boettcher, S.W. Solution-Processed Metal-Oxide Thin Films for Electronic and Energy Applications: Unique Chemistries of Metal Nitrate Precursors. *J. Mater. Chem. A*. **2019**, *7*, 24124-24149.

Enman, L.J.; Kast, M.G.; Cochran, E.A.; Pledger, E.; Stevens, M.B.; Boettcher, S.W. Transition-Metal-Incorporated Aluminum Oxide Thin Films: Toward Electronic Structure Design in Amorphous Mixed-Metal Oxides. *J. Phys. Chem. C*, **2018**, *122*, 13691-13704.

Cochran, E.A.; Park, D.H.; Kast, M.G.; Enman, L.J.; Perkins, C.K.; Mansergh, R.H.; Keszler, D.A.; Johnson, D.W.; Boettcher, S.W. Role of Combustion Chemistry in Low-Temperature Deposition of Metal Oxide Thin Films from Solution. Chem. Mater. **2017**, *29*, 9480-9488.

Kast, M.G., Cochran, E.A.; Enman, L.J.; Mitchson, G.; Ditto, J.; Siefe, C.; Plassmeyer, P.N.; Greenaway, A.L.; Johnson, D.C.; Page, C.J.; Boettcher, S.W. Amorphous Mixed-Metal Oxide Thin Films from Aqueous Solution Precursors with Near-Atomic Smoothness. *J. Am. Chem. Soc.*, **2016**, *138*, 16800-16808.

Cochran, E.A., Muller, G., Meloni, G. Stability and Bonding of New Superalkali Phosphide Species. *Dalton Trans.*, **2015**, *44*, 14753-14762.

Cochran, E.A., Meloni, G. Hypervalence in Monoxides and Dioxides of Superalkali Clusters. *J. Chem. Phys.*, **2014**, *140*, Article No. 204319.

ACKNOWLEDGMENTS

First and foremost, I wish to thank the Center for Sustainable Materials Chemistry (CSMC) for funding the research presented in this dissertation (CHE-1606982). The CSMC allowed for many fruitful collaborations that made this work possible. I also thank the CAMCOR staff, particularly Dr. Stephen Golledge, for his invaluable assistance with data collection and interpretation.

To my advisor Prof. Shannon Boettcher: thank you for encouraging me to think more critically about my work than I thought I was capable of; I am a better scientist for it. To my co-advisor, Prof. Darren Johnson, thank you for always being invested in my success and encouraging me to pursue opportunities critical to my professional development. Thank you to my committee members, Prof. Catherine Page, Prof. James Hutchison, and Prof. Emilie Hooft, for your support and your time over the last four years. I am particularly grateful to Cathy, who served as an (unofficial) third advisor to me and has lent her much-needed thin-film expertise to my research.

I would be remiss to not thank the chemistry mentors I had prior to graduate school, including Prof. Giovanni Meloni (and all the USF Chemistry Department), Robert Harper, and Sylvia Maffucci. I would not have been able to accomplish all that I have without your guidance and support as a young(er) chemist.

To my fellow Boettcher lab members, past and present, I cannot thank you all enough for your scientific support but, more importantly, your friendship. To Dr. Matthew Kast, it what an honor to work with you and learn from you. Thanks for putting up with me. To Dr. Lisa Enman, thank you for being a sounding board for any and all ideas, providing critical feedback without judgement. Thank you to: Dr. Mike Nellist, Dr. Forrest Laskowski, Dr. Chris Funch, Dr. Adam Smith, Dr. Adam Batchellor, Dr.

Michaela Burke Stevens, Dr. Annie Greenaway, Dr. Jason Boucher, Dr. Christian Dette, Dr. Jingjing Qiu, and Dr. Sebastian Öner. To the "next-generation" of the Boettcher lab, Raina Krivina, Jessica Fehrs, and Grace Lindquist, thank you for maintaining the spirit of helpfulness that makes the Boettcher lab a special place to work.

To the "DWJ" lab, I am grateful for all the diverse chemistry perspectives you each provide that helped challenge me to think outside the materials chemistry "box." Thank you to: Dr. Meredith Sharps, Dr. Susan Cooper, Dr. Brandon Crockett, Dr. Brantly Fulton, Dr. Lisa Eytel, Dr. Jess Lohrman, Dr. Sean Fontenot, Dr. Toby Sherbow, Jeremey Bard, Hazel Fargher, Jordan Levine, Ngoc-Minh Phan, Trevor Shear, Thais de Faria, Hannah Bates, and Grace Kuhl.

Thank you to the Page lab: Dr. Paul Plassmeyer and Dr. Keenan Woods. I am appreciative of all the help you provided me over the years, long after your time at UO.

To all of my "chemistry friends" I do not have the space to name here, know that your friendship and support is also greatly appreciated.

Last, but not least, I thank my family: Fred, Connie, Sam, Natalie, Corky, and Harper. To my parents, I am grateful for your encouragement of all my educational endeavors. To my sister, Natalie, thank you for being my lifetime source of support. Thank you to my extended family: Linda Bava, Brian Bava (and family), and Nan King. To my partner, Justin Dressler: thank you for your love, support, and comic relief. I look forward to what comes next for us on the other side of grad school.

To my family

TABLE OF CONTENTS

Chapter Page

I. INTRODUCTION ... 1

Authorship Statement ... 1

Metal Oxide Thin Films: Applications and Fabrication Methods ... 1

The Case for Metal Nitrates as Solution Precursors for Metal Oxide Thin Films ... 3

Authorship Statement ... 4

Bridge ... 4

II. METAL NITRATE-BASED PRECURSORS FOR METAL OXIDE THIN FILMS: CHEMISTRY, DESIGN AND CHARACTERIZATION ... 6

Authorship Statement ... 6

Bulk Metal Nitrate Chemistry ... 6

Aqueous Solution Behavior of Metal Nitrates ... 14

Metal Ions in Solution ... 14

Nitrates in Solution ... 20

Tuning Metal Nitrate Precursor Chemistry ... 25

Olation Products as Thin-Film Precursors ... 26

Mitigating Metal-Nitrato ($M-NO_3$) Complex Formation in Solution ... 32

Bridge ... 36

III. SOLUTION-PROCESSED METAL-OXIDE THIN FILMS FOR ELECTRONIC AND ENERGY APPLICATIONS: UNIQUE CHEMISTRIES OF METAL NITRATE PRECURSORS ... 37

Authorship Statement ... 37

The Chemical Evolution of Metal Nitrate Gels: the Initial Stages of Metal Oxide Thin-Film Formation ... 37

From Solution to Thin Films: Fundamental Considerations for the Preparation of Metal Oxide Coatings ... 37

Characterization of the Metal Oxide Thin-Film Reaction Pathway ... 40

Alternatives to Conventional Thermal Processing: a Survey of Low-Temperature Processing Methods Utilizing Unique Metal Nitrate Chemistries ... 46

Combustion Processing ... 47

Ultraviolet (UV) Photo-Annealing ... 52

Controlled-Atmosphere Annealing: the Role of Water Vapor in Film Formation 56
Bridge 60
IV. ROLE OF COMBUSTION CHEMISTRY IN LOW-TEMPERATURE DEPOSITION OF METAL OXIDE THIN FILMS FROM SOLUTION 61
Authorship Statement 61
Introduction 61
Experimental Section 65
Precursor Solution Preparation 65
Chemical and Structural Analyses of Bulk Precursors 65
Thin Film Preparation 67
Chemical and Structural Analysis of Thin Films 67
Results and Discussion 69
Comparing Thermal Behavior of Bulk Powders and Thin Films: TG and QCM analyses 69
Chemical Composition and Structure of Bulk Powders and Thin Films 72
The Reaction Pathway of Thin Films: Monitoring Reaction Byproducts 77
Magnesium Nitrate and Glycine: A Low-Volatility Fuel as a Combustion Model System 79
The Role of Fuels in Thin-Film Synthesis 81
Conclusions 83
Bridge 84
V. CHEMISTRY OF COUNTERION REMOVAL, CONDENSATION, AND DENSIFICATION PROCESSES AT LOW TEMPERATURE VIA STEAM-ANNEALING TO FORM METAL-OXIDE THIN FILMS FROM AQUEOUS PRECURSORS 85
Authorship Statement 85
Introduction 85
Experimental Section 89
Precursor Solution Preparation 89
Thin-Film Preparation 89
Thin-Film Characterization 90
Results and Discussion 91

Susceptibility of Single-Metal Precursors to Counterion Removal by Steam Annealing 91
Temperature Dependence of Counterion Removal with Steam Annealing 97
Counterion Distribution in Dry- and Steam-Annealed Films 100
The Effect of Steam Annealing on MCl_x Film Morphology 102
Understanding the Chemical Factors that Influence Void Formation 104
The Role of Different Annealing Treatments in Void Formation 108
Utilizing Steam Annealing to Maximize Metal-Oxide Thin-Film Quality: A Practical Guide 111
Conclusions 113
Bridge 115
VI. CONCLUSION AND OUTLOOK 116
Authorship Statement 116
Outlook: Toward Implementation of Solution-Processed Metal-Oxide Thin Films in Manufacturing 116
Low Cost per Unit Area and Large Area-Deposition (Drivers 1 & 2) 117
Ability to Deposit on Diverse Substrates (Driver 3) 118
High Yield, Low Variability (Driver 5) 119
Long-Term Stability and Durability (Driver 6) 120
Conclusions 121
APPENDICES 121
A. CHAPTER IV SUPPLEMENTARY INFORMATION 122
B. CHAPTER V SUPPLEMENTARY INFORMATION 164
REFERENCES CITED 173

LIST OF FIGURES

Figure Page

2.1. Bulk Metal Nitrate Decomposition 8

2.2. Thermogravimetric Analysis (TGA) of Metal Nitrates Used as Solution Precursors 10

2.3. Metal-Nitrate Decomposition Temperature (T_d) as a Function of Metal-Cation Charge Density (CD) 11

2.4. Aqueous Solution Speciation of Aluminum and Indium 18

2.5. Nitrate Reduction Chemistry 21

2.6. Metal-Nitrato (M-NO_3) Complex Formation 23

2.7. Metal-Hydroxo Nanoclusters as Thin-Film Precursors 28

2.8. Metal–Nitrato (M-NO_3) Complex Formation in Thin-Film Solution Precursors ... 34

3.1. Stages of Thin-Film Formation from Solution Precursors 39

3.2 Characterization Techniques Used to Study the Metal-Oxide Thin-Film Reaction Pathway by Thermal Annealing 43

3.3. Evaluating the Quality of Metal Oxides from Metal-Nitrate Precursors 46

3.4. Reactivity of Combustion Precursors 48

3.5. Comparison of In_2O_3 Films Prepared by Various Low-Temperature Processing Methods 49

3.6. Photo-Annealing of Metal-Nitrate Gel Films 54

3.7 Chemical Analysis of Steam- and Dry-Annealed LZO Films 58

3.8 Improved Densification of Steam-Annealed Films 59

4.1. Thermal Analysis on (a-b) Bulk Powders and (c-d) Thin Films from $In(NO_3)_3$ and $Y(NO_3)_3$ Precursors 71

4.2. Fits of O 1s XP spectra for a (a) Powder and (b) Film Prepared from the $Y(NO_3)_3$-acac Precursor Annealed Above T_{ig} (~ 215 °C) 74

Figure	Page

4.3. XRD Patterns for (a-b) Powders and (c-d) Films Prepared from $In(NO_3)_3$ and $Y(NO_3)_3$ Precursors 76

4.4. A Comparison of the NO^+ fragment (m/z=30) Detected by TPD-MS for Films Prepared from $Y(NO_3)_3$ Precursors 79

4.5. O 1s spectra for Films Prepared from (a) $Mg(NO_3)_2$ and (b) $Mg(NO_3)_2$-glycine Precursors 81

5.1. FT-IR Spectra for $M(NO_3)_x$ Precursors 92

5.2. XPS Quantification of Counterion Content in Films Annealed Under Dry and Steam Conditions at 140 °C 94

5.3. Temperature Dependence of NO_3^- and Cl^- Removal from Films Prepared Using In_2O_3 Precursors 99

5.4. Fitted O 1s Spectra for Dry- and Steam-Annealed Films (250 °C) from $In(NO_3)_3$ and $InCl_3$ Precursors 100

5.5. TOF-SIMS Evaluation of NO_3^- Distribution in $Sc(NO_3)_3$ Films Annealed at 140 °C 101

5.6. Photographs of (a-b) $AlCl_3$, (c-d) $InCl_3$, and (e-f) YCl_3 Films (Dry- and Steam-annealed at 140 °C) After < 5 min Exposure to Ambient 103

5.7. SEM Images of Mixed NO_3^-/Cl^- Films from Single-Metal Precursors 106

5.8. SEM Images of $M_yZr_{1-y}O_x$ Films 108

5.9. SEM Images of LZO (NO_3^-/Cl^-) Films Thermally Treated Using Various Annealing Profiles 109

A.1. TGA Curves for $In(NO_3)_3$ and $Y(NO_3)_3$ Combustible Mixtures and their Corresponding Controls 122

A.2. Transmission FT-IR Analysis of Films Spun from Acac Precursors and their Corresponding Controls Without Fuels 123

A.3. XP Spectra of a $Y(NO_3)_3$-acac Film for (a) C 1s, (b) Y 3d, and (c) N 1s 126

A.4. XP Spectra of the $Y(NO_3)_3$-acac Powder Combustion Product 127

A.5. XP Spectra for a $Y(NO_3)_3$ Film Without Fuel 128

A.6. XP spectra for a $Y(NO_3)_3$ Powder 129

Figure Page

A.7. XP Spectra for a Film Prepared from $In(NO_3)_3$ Without Fuel 130

A.8. XP Spectra for an $In(NO_3)_3$-acac Film 131

A.9. TGA-MS for $Y(NO_3)_3$ Powders/Gels With and Without Acac 132

A.10. TGA-MS for $Y(NO_3)_3$ Powders/Gels With and Without Acac 135

A.11. H_2O^+ and NO^+ Fragments Observed by TPD for Films Spun from the (a) $Y(NO_3)_3$ and (b) $Y(NO_3)_3$-acac Precursors 136

A.12. H_2O^+ and NO^+ fragments Observed by TPD for Films Spun from the (a) $Y(NO_3)_3$ and (b) $Y(NO_3)_3$-acac Precursors 137

A.13. TGA-MS for Bulk Gels/Powders of (a) $Mg(NO_3)_2$, (b) $Mg(NO_3)_2$-glycine, and (c) glycine 138

A.14. Remaining XP spectra for a $Mg(NO_3)_2$ Film Without Fuel 139

A.15. Remaining XP Spectra for a $Mg(NO_3)_2$-glycine Film 140

A.16. FT-IR spectra of (a) $Mg(NO_3)_2$ and (b) $Mg(NO_3)_2$-glycine Films 141

A.17. XRD Patterns for $Mg(NO_3)_2$ Bulk Precursors and Films Annealed at 300 °C..... 142

A.18. TPD-MS for (a-b) $Mg(NO_3)_2$ and (c-d) $Mg(NO_3)_2$-glycine Films 145

A.19. TPD-MS for Films from $MgCl_2$ Precursors 146

A.20. Thermal Analysis of $Al(NO_3)_3$(-acac) by Bulk TGA and Thin-Film QCM......... 148

A.21. XRD Patterns for $Al(NO_3)_3$ and $Al(NO_3)_3$-acac Powders and Films 149

A.22. Thermal Analysis of Urea-containing Gels by Bulk TGA and Thin-Film QCM. 152

A.23. FT-IR Spectra of Films from Urea Precursors 153

A.24. XRD Patterns of Powders and Thin Film from the $Al(NO_3)_3$-urea Precursor...... 155

A.25. TGA-MS for the $Y(NO_3)_3$-urea Bulk Powder 156

A.26. TPD-MS of a $Y(NO_3)_3$-urea Film.. 157

A.27. Morphological Characterization of Films from Precursors With and Without Combustion Additives 160

Figure Page

A.28. XRR Patterns and Model fits for Films from Precursors With and Without Combustion Additives 162

B.1 FT-IR Spectra of Dry- and Steam-Annealed Films from $Sc(NO_3)_3$ and $Ga(NO_3)_3$ Precursors 164

B.2 Thermogravimetryc Analysis Curves for Hydrated $M(NO_3)_x$ and MCl_x Salts 170

B.3 O 1s Spectra Overlays for $In(NO_3)_3$ and $InCl_3$ Films Dry- and Steam-Annealed at 170 °C 171

B.4. XRR Patterns for Mixed NO_3^-/Cl^- Single-Metal Precursor Films 171

B.5. XRR patterns for LZO Films Treated Using Different Annealing Conditions and Temperature Ramp Profiles 172

LIST OF TABLES

Table Page

2.1 Summary of Metal-Ion Parameters Relevant to Calculating Charge Density and Thermal-Decomposition Temperature (T_d) 12

4.1 Complied XPS results for all powders and films prepared from combustion precursors and their corresponding control samples 75

A.1. Summary of XRR Modeling Outputs 163

B.1 XPS Atomic Percentages from Surface Spectra of $M(NO_3)_x$ Films Dry- and Steam-Annealed at 140 °C 166

B.2 XPS Atomic Percentages from Surface Spectra of MCl_x Films Dry- and Steam-Annealed at 140 °C 167

B.3 XPS Atomic Percentages from Surface Spectra for $In(NO_3)_3$ Films Dry- and Steam-Annealed at Various Temperatures 168

B.4 XPS Atomic Percentages from Surface Spectra for $InCl_3$ Films Dry- and Steam-Annealed at Various Temperatures 169

CHAPTER I

INTRODUCTION

Authorship Statement

This chapter contains material previously published in *Journal of Materials Chemistry A* **2019**, *7*, 24124-24149. This work was coauthored by Elizabeth A. Cochran, Keenan N. Woods, Catherine J. Page, Darren W. Johnson, and Shannon W. Boettcher. This manuscript was written by E.A.C. with contributions and editorial assistance from all authors.

Metal Oxide Thin Films: Applications and Fabrication Methods

The versatility of metal-oxide thin films makes them useful for applications in electronic and energy technologies. Metal oxides are utilized as dielectric,[1,2] semiconductor,[1,3] or metal components (i.e. transparent conducting oxides)[4,5] of thin-film transistors (TFTs) and photovoltaic cells.[6,7] In photovoltaics, metal oxides can also serve as carrier-selective contacts to improve solar-cell efficiencies (silicon, perovskite, organic, etc.), including TiO_2[8–10] and ZnO[10–12] for electron-selective contacts and MoO_x[13,14] and NiO[15,16] for hole-selective contacts. Additional applications include smart windows,[17,18] solid-oxide fuel cells,[19–21] protective layers,[22] and catalysis, as both active[23,24] and support[25,26] materials for renewable fuel production.

Conventional vapor-phase deposition methods produce high-quality metal-oxide thin films for many of the above-mentioned applications but face inherent challenges in large-area deposition critical for "macroelectronics." Such devices require the use of substrates much larger than semiconductor fabrication facilities currently accommodate.[27]

For this reason, solution processing offers opportunity for growth in macroelectronic technology sectors (e.g. photovoltaics, displays, and “smart” window coatings). Additional advantages of solution processing relative to vapor-phase deposition include potentially lower cost, ambient processing, simple composition tuning, and the use of environmentally benign solvents/precursors.[27]

Despite these benefits, solution-processed metal oxides often contain more impurities/defects than vapor-deposited films, resulting in degraded properties relative to vapor-deposited films. However, significant progress has been made over the past decade to enable the production of solution-processed metal-oxide thin films of high (opto)electronic quality competitive with vacuum-deposited films.[7,28,29] These advances have been aided by enhanced understanding of how the solution-precursor chemistry affects the structure/morphology (grain size, density, degree of condensation, etc.) of resulting thin-film materials, which directly influences their function. Such relationships are well-established for films prepared from sol-gel precursors.[30,31] However, significant knowledge gaps remain in the understanding of the chemical reaction pathways from metal-salt precursors to metal-oxide films which, in many cases, produce higher-quality films (i.e. denser, fewer impurities, etc.) than sol-gel precursors.[32,33] Here we discuss how the chemical transformations of metal-nitrate solution precursors influence metal-oxide film formation chemistry and resulting film properties, which requires analysis of the solid-state bulk, solution, and thin-film literature.

The Case for Metal Nitrates as Solution Precursors for Metal-Oxide Thin Films

Among salt precursors for metal-oxide films, metal nitrates, $M(NO_3)_x$, have proved superior to other commonly used precursors (e.g. metal chlorides and acetates). Films produced from metal nitrates are generally denser, contain fewer impurities, and require lower processing temperatures due to the high volatility of their decomposition byproducts.[33,34] Consequently, the resulting thin films often display excellent electronic properties for solution-processed films, and have been implemented as semiconductors,[32,35–38] dielectrics,[2,37,39–45] transparent conducting oxides (TCOs),[46,47] magnets,[48] solid electrolytes,[49] and charge-carrier selective contacts.[50,51] Nitrate counterions exhibit unique reactivities that make them susceptible to decomposition pathways involving little to no thermal annealing. Such "low-temperature processing" methods, including combustion synthesis,[52] ultraviolet (UV) photolysis,[53] and water-vapor (or "steam") annealing,[54] have been investigated for thin-film processing in efforts to improve compatibility with low-melting-point polymeric substrates and enable roll-to-roll processing.[2,29,55,56]

While the use of metal-nitrate precursors has become ubiquitous, a fundamental understanding of the nitrate decomposition pathways and the oxide-formation processes is important for the advancement of thin-film solution-deposition technologies. This review examines the important chemical considerations that enable the preparation of high-quality metal-oxide thin films from metal-nitrate precursors. An improved understanding of metal-nitrate chemistry, including the thermal evolution and decomposition of bulk salts, the chemical nature of metal-nitrate solution precursors, and film-formation reactions in thin-film precursor gels, serves to inform process development for metal-oxide thin-film deposition. Such considerations of the entire film

reaction pathway, from precursor to metal oxide, provide insights that may facilitate manufacturing of high-quality metal-oxide thin films from metal-nitrate precursors.

Authorship Statement

This dissertation contains previously published and unpublished coauthored material. Chapters I, II, III, and VI were previously published in *Journal of Materials Chemistry A* with Keenan N. Woods, Catherine J. Page, Darren W. Johnson, and Shannon W. Boettcher. Chapter IV was previously published in *Chemistry of Materials* with Deok-Hie Park, Matthew G. Kast, Lisa J. Enman, Cory K. Perkins, Ryan H. Mansergh, Douglas A. Keszler, Darren W. Johnson, and Shannon W. Boettcher. Chapter V (unpublished) was coauthored with Peter N.P. Huynh, Keenan N. Woods, Catherine J. Page, Darren W. Johnson, and Shannon W. Boettcher.

Bridge

Chapter I provided an overview of applications for metal oxide thin films, as well as the advantages and opportunities for solution-deposition technologies. Metal-nitrate salts stand out as solution precursors that produce metal-oxide thin films of superior quality compared to other commonly-used solution precursors. Thin-film quality is, however, highly dependent on the entire chemical reaction pathway from the precursor starting material to the final metal-oxide thin film. Chapters II and III provide in-depth discussions of chemical factors that influence the thin-film reaction pathway. Chapter II focuses on metal nitrate bulk and solution chemistries, while Chapter III explains how unique chemical reactions involving metal nitrates have been exploited to influence the transformation of a thin-film gel to a metal oxide. Chapters IV and V contain in-depth

investigations and characterization of two “low-temperature” processing methods for thin-film formation: combustion synthesis and water-vapor “steam” annealing. This dissertation concludes by putting the content of the previous chapters into the context of how understanding film-formation chemistry is crucial for future process development and implementation of solution-processed metal oxide thin films in high-volume manufacturing.

CHAPTER II

METAL NITRATE-BASED PRECURSORS FOR METAL OXIDE THIN FILMS: CHEMISTRY, DESIGN AND CHARACTERIZATION

Authorship Statement

This chapter contains material previously published in *Journal of Materials Chemistry A* **2019**, *7*, 24124-24149. This work was coauthored by Elizabeth A. Cochran, Keenan N. Woods, Catherine J. Page, Darren W. Johnson, and Shannon W. Boettcher. This manuscript was written by E.A.C. with contributions and editorial assistance from all authors.

Bulk Metal Nitrate Chemistry

In addition to thin-film precursors, metal-nitrate salts are used for the preparation of bulk metal oxides (and metals) used in numerous materials-science applications. Nitrate salts are preferred to other metal salts due to their relatively low decomposition temperatures and highly-volatile decomposition products, resulting in few residual contaminants in the final products.[1] Knowledge of metal-nitrate decomposition mechanisms has proved important for optimizing synthesis conditions to improve material properties. For example, in catalysis, changes to the annealing atmosphere (inert, O_2, H_2, etc.) of metal nitrates can influence metal-oxide-catalyst-particle dispersion,[2] as well as the mechanical and chemical nature of catalyst-support interactions.[3,4] Here we discuss the chemical factors that influence decomposition behavior of metal nitrates and

what implications this has for selecting thin-film precursors and processing conditions to control film-formation reactions.

The mechanism(s) of metal-nitrate bulk salt decomposition have been studied extensively by thermogravimetric analysis (TGA).[5–11] Figure 2.1a shows representative chemical reactions for metal-nitrate salt decomposition in air. Prior to decomposition, the salt melts and releases loosely bound waters (~ 25-75 °C), forming a concentrated salt solution. Nitrate can be removed from the salt through two pathways. The first pathway (Figure 2.1a, reaction i) involves the removal of some nitrates via nitric acid (HNO_3) formation and the subsequent evaporation of the water-acid azeotrope (68% HNO_3/ 32% H_2O), which boils at 120 °C. At higher annealing temperatures (~ 200-500 °C, depending on the metal-cation identity), remaining nitrate thermally decomposes to NO_x gases (Figure 2.1a, reaction ii).[1,12] The nitrate thermal decomposition pathway is complex, with many possible NO_x decomposition products (NO, NO_2, N_2O, N_2O_2, etc.).[12] The distribution of products varies with the metal identity and temperature. Thermal decomposition at lower temperatures typically involves formation of NO, NO_2 and N_2O; as the temperature increases, NO and O_2 become the primary decomposition products.[12] This general description of the nitrate decomposition pathway also applies to thin films. Following nitrate decomposition, the resulting solid metal-hydroxide product then condenses to form the final metal oxide (Figure 2.1a, reaction iii). These reactions are often concurrent, resulting in overlapping mass loss events in TGA, which makes full characterization of the metal-nitrate decomposition reactions challenging.

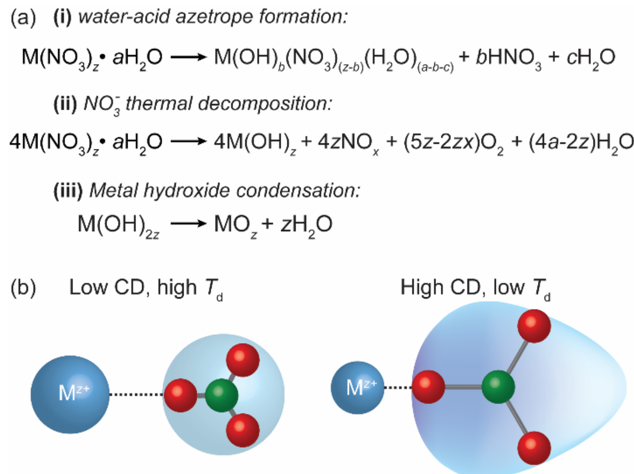

Figure 2.1. Bulk Metal Nitrate Decomposition. (a) Representative chemical reactions for metal-nitrate-hydrate thermal decomposition in air. (b) Schematic depicting the electronic interaction between M^{z+} and nitrate. Low charge-density (CD) metals are unable to polarize the nitrate electron cloud, resulting in high T_d (left), whereas high-CD metals attract the electron density of nitrate (indicated by distortion and shading of the electron cloud), which lowers T_d (right).

Metal-nitrate salts have a wide range of decomposition temperatures due to differing electronic interactions between the metal and nitrate.[1] Positively-charged cations polarize the electron cloud of the negatively-charged nitrates. This lowers the N-O bond order (i.e. lengthens and weakens the bonds), which promotes nitrate dissociation and decomposition. For metals with accessible *d*-orbital vacancies, π-back-donation of nitrate electron density can occur, which further lowers the N-O bond order. The metal-ion charge density (CD) is a measure of its polarizing ability (CD = $\frac{3z}{4\pi r^3}$, where z = atomic charge and r = atomic radius in nm), which dictates the covalent nature of the metal and nitrate interaction. Yuvaraj et al. studied the decomposition behavior of alkali, alkaline-earth, main-group, and transition-metal nitrates,[1] and observed an inverse correlation between metal-cation CD and the nitrate-salt decomposition temperature (T_d).[1] Low-CD cations have little influence on the nitrate electron cloud and T_d tends to

be high (Figure 2.1b, left). High-CD cations effectively polarize nitrates, which facilitates decomposition and lowers T_d (Figure 2.1b, right).

We have studied the decomposition behavior of a broad selection of hydrated metal-nitrate salts that are relevant to solution deposition, including rare-earth lanthanides (Ln), which have recently gained popularity as precursors for LnO_x gate dielectrics.[13–16] TGA curves for these metal-nitrate salts are shown in Figure 2.2. We define T_d as the temperature at which the metal-nitrate salt has lost 75% of its total volatile mass.[17] For the metal-nitrate hydrate salts considered here, the inverse correlation between CD and T_d that Yuvaraj previously established generally holds (Figure 2.3 and Table 2.1). For the lanthanides, which all have similar CDs, we do not observe an obvious trend in T_d. The mechanism behind the experimentally-observed trends in T_d for lanthanides appears to be missing from the literature.

In addition to the metal identity, nitrate decomposition is sensitive to the annealing ambient. Yuvaraj et al. also investigated metal-nitrate decomposition temperatures in reducing atmospheres (T_r) of 10% H_2 in N_2.[1] They observe $T_d < T_r$ for many first-row transition and group 13 metal nitrates, whereas many of the alkali, alkaline-earth, and noble-metal nitrates exhibit $T_d > T_r$. This difference in reactivity is explained by the ability of the lower-CD metals (i.e. alkalis, alkaline earths, and noble metals) to adsorb and dissociate H_2, forming NH_3 (or even N_2) and H_2O as byproducts. The authors propose that the (post-)transition metals, in contrast, do not undergo nitrate reduction by this pathway because the metal cation cannot effectively polarize and dissociate H_2 due to the covalent nature of metal nitrate interactions. Low-CD metals, in contrast, experience mostly ionic metal-nitrate interactions and, therefore, can more effectively dissociate H_2.

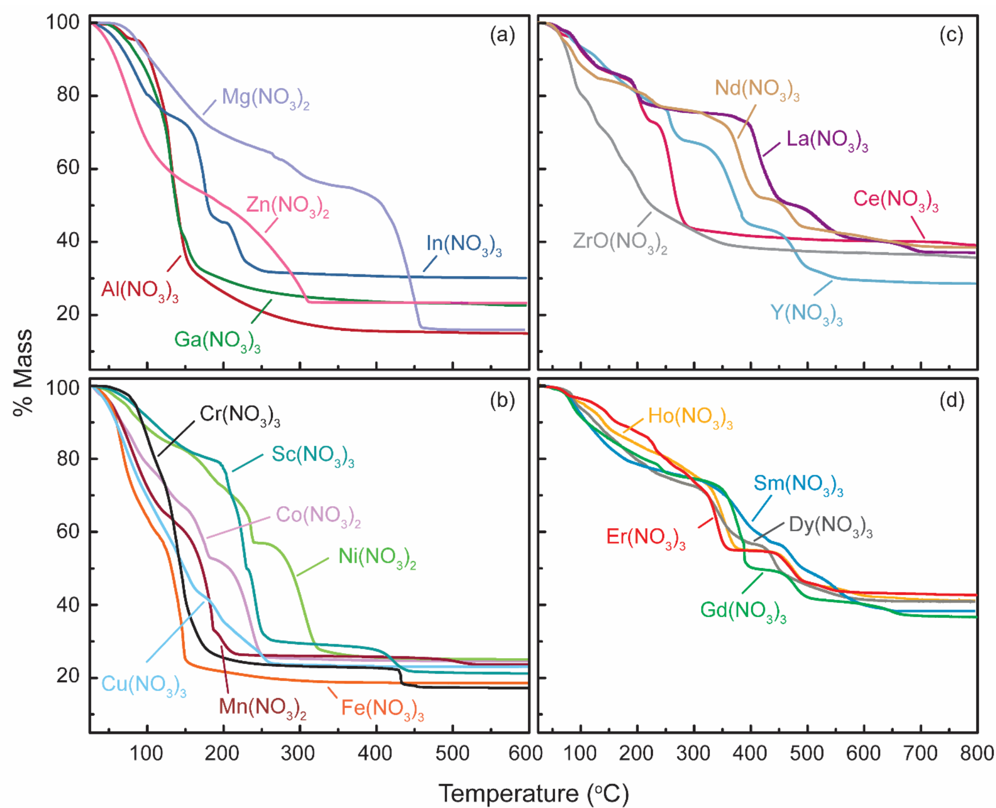

Figure 2.2. Thermogravimetric Analysis (TGA) of Metal Nitrates Used as Solution Precursors. TGA curves are shown for hydrated metal nitrate salts of: (a) main-group metals, (b) first-row transition metals, and (c) and (d) lanthanide(-like) metals. Experimental details can be found in Ref. 18.

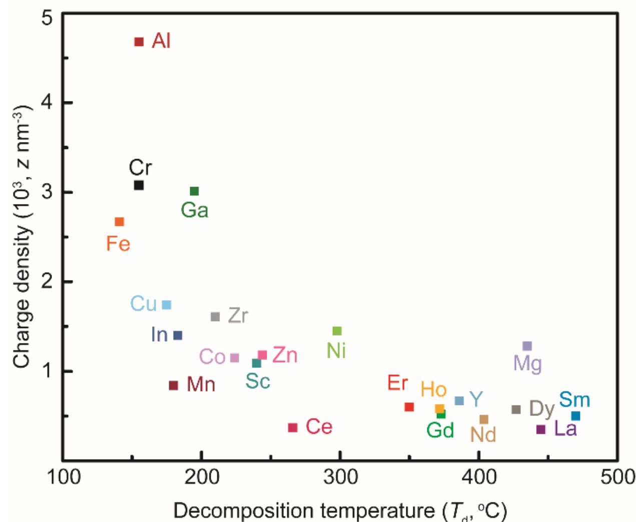

Figure 2.3. Metal-Nitrate Decomposition Temperature (T_d) as a Function of Metal-Cation Charge Density (CD). Metal-nitrate salts exhibit a broad range of decomposition temperatures due to differing electronic interactions between the metal and nitrate. As a general trend, T_d increases with decreasing CD (i.e. the cation polarizing ability decreases). T_d is defined as the temperature at which the salt has lost 75% of its volatile mass.

While additional systematic studies on this effect are lacking, select examples of other annealing atmospheres influencing T_d exist in the literature. Water vapor is observed to lower T_d for some metal-nitrate systems, including $La(NO_3)_3$,[41] $Mn(NO_3)_2$,[11] and a nitrate-ligated scandium dimer species.[42] This effect has been attributed to suppression of metal-carbonate intermediates,[41] which decompose at higher temperatures than nitrates, as well as enhanced nitrate removal via HNO_3-H_2O azeotrope evaporation.[42] When NO is introduced to the annealing atmosphere for $Ni(NO_3)_2$ and $Co(NO_3)_2$, the decomposition rate slows compared to a pure O_2 atmosphere, resulting in improved NiO and Co_3O_4 nanoparticle size dispersity.[43] Support materials can also influence decomposition. Alumina supports have been shown to lower T_d for first-row transition-metal nitrates with *d* occupations other than d^5 and d^{10} (e.g. Ni^{2+}, Co^{2+}, and Cu^{2+}) compared to the bulk; the authors hypothesize that alumina changes the metal-nitrate electronic structure, thereby facilitating decomposition.[44]

Table 2.1. Summary of Metal-Ion Parameters Relevant to Calculating Charge Density and Thermal-Decomposition Temperature (T_d). Coordination numbers (CN) and ionic radii are determined based on the coordination and valence state of the metal in their respective hydrated metal-nitrate salts.

Cation (M^{z+})	T_d (°C)	CN^ref	ionic radius (pm)[19]	CD (10^3 z nm^{-3})
Mg^{2+}	435	6[20]	72	1.28
Al^{3+}	155	6[21]	53.5	4.68
Ga^{3+}	195	6[22]	62	3.01
In^{3+}	183	6[23]	80	1.40
Sc^{3+}	240	8[24]	87	1.09
Cr^{3+}	155	6[25]	61.5	3.08
Mn^{2+}	180	6[26]	83	0.84
Fe^{3+}	141	6[27]	64.5	2.67
Co^{2+}	224	6[28]	74.5	1.15
Ni^{2+}	298	6[29]	69	1.45
Cu^{2+}	175	5[30]	65	1.74
Zn^{2+}	244	6[31]	74	1.18
Y^{3+}	386	8[32]	102	0.67
Zr^{4+}	210	8[33]	84	1.61
La^{3+}	445	10[34]	127	0.35
Ce^{3+}	266	10[35]	125	0.37
Nd^{3+}	404	9[36]	116	0.46
Sm^{3+}	470	10[37]	113	0.50
Gd^{3+}	373	9[38]	111	0.52
Dy^{3+}	427	9[39]	108	0.57
Ho^{3+}	372	9[40]	107	0.58
Er^{3+}	350	9[40]	106	0.60

Metal-nitrate T_d is primarily dictated by the metal-cation identity (i.e. charge density/ electrostatic interaction with nitrate) but is also influenced by ambient conditions (discussed above). For applications where metal-nitrate precursor solutions are employed to deposit metal-oxide films, the metal-nitrate T_d is an important consideration for compatibility with substrates and other device components. In some cases, compatibility may limit the choice of metal-nitrate salts. For example, the high T_d of $Y(NO_3)_3$ and $La(NO_3)_3$ in air (386 and 445 °C, respectively) render them unsuitable as a dielectric layer for flexible TFTs on a polyimide substrate, which softens and deforms above 275 °C.[45] Suitable alternatives would include $Al(NO_3)_3$ or $Ga(NO_3)_3$, as these salts are substantially decomposed by 150 °C (Figure 2.2). In other cases, a particular metal-oxide target may be critical for a desired application. In this instance, strategies to alter the T_d by controlling the ambient annealing atmosphere or thin-film composition may be possible. Our research groups have demonstrated enhanced nitrate removal at low annealing temperatures for Y- and La-based thin films using a water-vapor atmosphere.[46] Additionally, pairing high-T_d salts, like $La(NO_3)_3$, with low-T_d salts (e.g. $Al(NO_3)_3$ or $ZrO(NO_3)_2$) in ternary oxide compositions effectively lowers the overall T_d of the thin-film system.[16,47,48] We hypothesize this effect is a result of high-CD cations polarizing nitrate ions from the low-CD salt, facilitating their decomposition. Indeed, the process parameter space to influence metal-nitrate decomposition chemistry is expansive. Further investigation of factors influencing nitrate T_d could allow for improved control over thermal processing conditions and thus the final film properties/performance.

Aqueous Solution Behavior of Metal Nitrates

Metal nitrate salts are highly soluble in aqueous and (polar) organic solvents. Upon dissolution, complex equilibria and speciation are established, the details of which are generally not well understood. Even in dilute salt solutions ($\geq 10^{-4}$ M M^{z+}), monomeric cations can react to form polynuclear species, which can be present in equal concentrations to monomer, depending on solution conditions.[49] At concentrations relevant to solution processing (≥ 0.1 M M^{z+}), metal-anion complexes can form, further complicating solution speciation.[50–52] Both oligomerization and complex formation depend on pH, concentration, and temperature. Understanding the chemical speciation and interactions taking place in solution can inform precursor design, allowing for control of decomposition pathways and the production of thin films with desired morphology and structure. Examples of speciation-informed precursor design are discussed in this chapter. For simplicity, we focus the solution-speciation discussion here on aqueous metal-nitrate solutions; however, many of the concepts discussed are also relevant to any solvent system that contains water (e.g. alcohol/water mixtures), including traditional sol-gel precursors.[53]

Metal Ions in Solution

When dissolved in water, positively-charged cations (M^{z+}) experience an electrostatic attraction towards the lone electron pairs of oxygen in water to form an ordered hydration shell around M^{z+} – this is referred to as an aquo (or aqua) cation. The electron lone pairs on water molecules in the aquo cation are attracted to the positively-charged M^{z+} and form a strong M-O interaction. Electron density from O-H moves closer

to oxygen in order to compensate for lost electron density that is now shared with M^{z+}. This results in an increased partial positive charge on hydrogen. If the electrostatic attraction between M^{z+} and oxygen is strong enough, the positive charge on hydrogen will increasingly resemble H^+, eventually resulting in hydrolysis and the dissociation of H^+ into solution (Eq. 2.1).

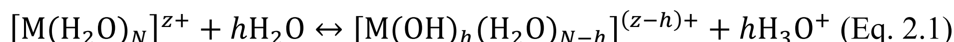

$$[\mathrm{M}(\mathrm{H_2O})_N]^{z+} + h\mathrm{H_2O} \leftrightarrow [\mathrm{M}(\mathrm{OH})_h(\mathrm{H_2O})_{N-h}]^{(z-h)+} + h\mathrm{H_3O^+} \text{ (Eq. 2.1)}$$

Such hydrolysis reactions are the origin of metal-cation acidity. Relative cation acidities can be determined from their pK_a values. Metals with pK_a values ≤ 6 are considered to be acidic, whereas those with pK_a values > 6 are nonacidic.[54]

The presence of hydroxyl ligands makes possible the formation of soluble, polynuclear cationic species through condensation reactions. Two condensation pathways are possible: olation and oxolation. Olation occurs via nucleophilic attack of an M-OH group on another metal aquo cation to form a bridging hydroxyl ligand; water is the leaving group (Eq. 2.2).

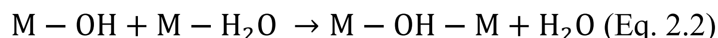

$$\mathrm{M-OH + M-H_2O \rightarrow M-OH-M + H_2O} \text{ (Eq. 2.2)}$$

Oxolation results in metal oxo linkages (M-O-M) when two OH ligands react and form water as a byproduct (Eq. 2.3).

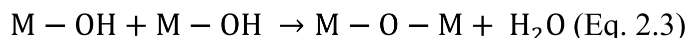

$$\mathrm{M-OH + M-OH \rightarrow M-O-M + H_2O} \text{ (Eq. 2.3)}$$

The kinetics of olation are rapid compared to oxolation.[49] Therefore, oxolation will not occur to an appreciable extent until H_2O ligands have been eliminated by olation.[55] Soluble oxolation products are most common for highly-charged cations ($z \geq 4$), as these cations have high h:M^{z+} ratios (see Eq. 2.1) due to low (or even negative) pKa

values (i.e. few H_2O ligands are present).[54,56] Oxolation reactions of low-valence cations ($z \leq 4$) often results in the precipitation of (oxy)hydroxides. Because most metal-nitrate salts are low-valence (z = 2 and 3), olation products are more commonly observed in metal-nitrate solutions.

Olation products with discrete stoichiometry form due to self-limiting reactivity. Olation kinetics are limited by the lability of H_2O ligands, which is quantified by the water-exchange rate constant ($k_{\mathrm{H_2O}}$, s^{-1}). The $k_{\mathrm{H_2O}}$ is defined as the equilibrium psueodo-first-order rate constant at which water molecules in the inner-most solvation sphere of the metal cation are exchanged with "bulk" water molecules from solution at 25 °C (i.e. $[\mathrm{M(H_2O)_6}]^{z+} + \mathrm{H_2O^*} \overset{k_{\mathrm{H_2O}}}{\longleftrightarrow} [\mathrm{M(H_2O)_5(H_2O^*)}]^{z+} + \mathrm{H_2O}$; rate $= k_{\mathrm{H_2O}}\left(c_{[\mathrm{M(H_2O)_6}]^{z+}}\right)$ where c is the concentration of aquo cations).[57] As a general trend, $k_{\mathrm{H_2O}}$ for metal cations increases with increasing ionic radius (see Figure 2.6c). For d-block metals with partially-occupied d states, the ligand-field stabilization energy (LFSE) also influences the strength and lability of M-H_2O bonds. Cations with higher LFSE experience slower $k_{\mathrm{H_2O}}$ as a result of greater orbital overlap between metal d orbitals and those of H_2O.[57] Additionally, OH ligands must be good nucleophiles in order for olation to occur. The OH ligands on metal olation products become less nucleophilic (i.e. δ(OH) becomes less negative) as they form more bonds and the positive charge on the polynuclear species increases, which slows $k_{\mathrm{H_2O}}$.[49] This leads to the formation of polynuclear species with a defined stoichiometry, rather than indefinite oligomerization. For many metal cations, olation stops at or before hexamer formation,[58] although some cations are capable of forming larger polycations. The OH bridges in small olation products, such as trimers, can remain strong nucleophiles and further react to form large clusters. Such is the case

for Al^{3+}, which forms the tridecameric Keggin ion $[Al_{13}O_4(OH)_{24}(H_2O)_{12}]^{7+}$ under certain pH and concentration conditions.[55]

Solution equilibria and the existence of polynuclear species, which can include multiple hydrolysis products, can be complex and challenging to predict. Pourbaix diagrams are helpful representations that depict predominant species in solution under equilibrium conditions as a function of pH and concentration.[59] We consider here the Pourbaix diagrams of two metal systems commonly used as solution precursors for thin films: aluminum and indium. For an aqueous solution with 0.1 M metal ion concentration, the monomeric trivalent aquo ions Al^{3+} and In^{3+} are the predominant species up to pH ~3.7 and ~2.8, respectively, after which $M(OH)_3$ persists (Figure 2.4a-b). Thin-film precursor solutions should be maintained at a pH below that at which insoluble $M(OH)_3$ forms, as this can result in material loss and/or negatively affect film morphology. Additionally, excess acid should be avoided, as it is typically detrimental to film quality given that additional volatile components must be removed during densification, which can lead to increased porosity. While Pourbaix diagrams are useful for determining the predominant species under equilibrium conditions, they leave out hydrolysis/olation products that may contribute appreciably to soluble species in solution. For a more-complete depiction of solution speciation, we must consider speciation diagrams.

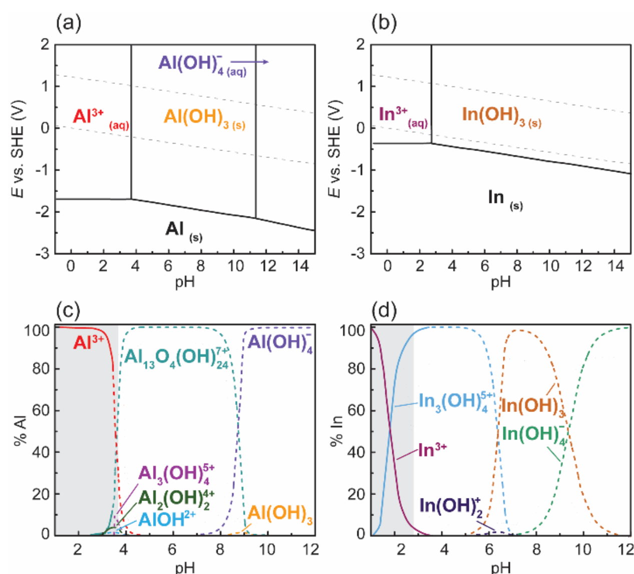

Figure 2.4. Aqueous Solution Speciation of Aluminum and Indium. Pourbaix (a-b) and speciation (c-d) diagrams describing the aqueous chemistry of aluminum and indium. The dashed lines in panels c and d indicate species in solutions super-saturated with respect to α-$Al(OH)_3$ and $In(OH)_3$ (i.e. $[M^{z+}] < 0.1$ M). Grey shading in panels c and d indicates the region to the left of the $M^{3+}|M(OH)_3$ boundary from the Pourbaix diagram (i.e. the pH region where soluble species predominate). The data used to construct the Pourbaix and speciation diagrams are from Ref. 60 and 58, respectively.

Speciation diagrams describe the evolution of solution equilibria as a function of pH. These diagrams are calculated from thermodynamic values and describe the distribution of soluble species in equilibrium with the solid $M(OH)_x$ phase. Baes and Mesmer compiled a library of equilibrium constants for polynuclear hydrolysis products used to formulate such speciation diagrams.[58] For a 0.1 M Al^{3+} solution, monomeric Al^{3+} (i.e. $Al(H_2O)_6^{3+}$) persists as the dominant ionic species up to pH 3.5 (Figure 2.4c). As the pH increases above pH 3, the concentration of $Al_{13}O_4(OH)_{24}^{7+}$ (the "Al_{13}" Keggin ion) increases to ~35% of soluble Al species near the precipitation boundary (pH 3.7). Minor hydrolysis products $Al(OH)^{2+}$, $Al_2(OH)_2^{4+}$, and $Al_3(OH)_4^{5+}$ have narrow stability windows centered around pH 3.5 and, combined, contribute less than 10% of soluble species at pH 3.5 (Figure 2.4c). For a 0.1 M In^{3+} aqueous solution, $In(H_2O)_6^{3+}$ is the

predominant species below pH 2. As the solution pH increases from ~1 to 2, the hydrolysis product $In_3(OH)_4^{5+}$ increasingly contributes to solution speciation up to 50% at pH 2 (Figure 2.4d). Soluble species at pH values above the hydroxide precipitation boundary, indicated by the unshaded region in Figure 2.4b and 2.4c, are not relevant when considering thin-film solution precursors due to low solubilities.

Baes and Mesmer's publication, "The Hydrolysis of Cations," is still considered the most-comprehensive treatment of solution speciation; however, Baes and Mesmer acknowledge their published solution speciation diagrams are far from complete.[58] Identifying and characterizing polynuclear species is a difficult task and is an active area of research. Significant progress toward solution speciation characterization has been made in recent years with the aid of a suite of corroborative techniques, including nuclear-magnetic-resonance (NMR) spectroscopy, dynamic light scattering (DLS), and small-angle x-ray scattering (SAXS).[61] In the field of Al speciation, our research groups have prepared and studied $[Al_{13}(OH)_{24}(H_2O)_{24}]^{15+}$ ("flat"-Al_{13}) and $[Al_8(OH)_{14}(H_2O)_{18}]^{10+}$,[62,63] while others have previously observed $[Al_{30}O_8(OH)_{56}(H_2O)_{24}]^{18+}$ in aqueous solution.[64] Additional indium hydrolysis products ($In_2(OH)_2^{4+}$ and $In_4(OH)_6^{6+}$) have also been experimentally identified.[65] Recent computational work on Al and Ga aqueous speciation predicted some polynuclear species are predominant, thermodynamic products that belong on Pourbaix diagrams.[66] It is important to note that the identity of the counterion can also influence speciation if it is capable of coordination to the metal,[67] which can, in turn, influence the identity and quantity of olation products. Additionally, metastable polynuclear products can become kinetically trapped due to stabilizing effects from counterions.

There are numerous approaches to systematically influence thin-film precursor solution speciation by changing solution pH. Perhaps the most straightforward approach involves controlling the metal salt concentration, which will necessarily change the pH and the olation product distribution. For a constant metal concentration, solution pH can be controlled using acid or base addition. Dissolution of metal oxides/hydroxides using HNO_3 has proven a successful approach for targeting olation products of interest as thin-film precursors.[68,69] However, the addition of excess acid or base to solution should be avoided, as such additives can have a deleterious effect on film morphology, imparting porosity and inhibiting densification. Alternatively, redox reactions that consume protons and nitrate can be used to increase the solution pH and drive olation. This can be accomplished via electrochemical reduction to avoid introducing additives.[70] For mixed-metal precursors, the effect of the component metal cations on the solution pH must also be considered. We have observed the formation of olation products in mixed Al^{3+} and La^{3+} nitrate precursors.[16] Because La^{3+} is less acidic than Al^{3+} (pK_a = 7.6 and 5.0, respectively),[54] La^{3+} increases the solution pH, which drives the formation of Al clusters. An understanding of the solution-speciation chemistry for thin-film precursors is useful for relating solution conditions to thin-film chemistry and morphology, which influences their performance in devices.

Nitrates in Solution

Nitrates do not exhibit the same complex speciation chemistry as metal cations, but can be (electro)chemically reduced to a variety of nitrogen-containing species in aqueous solution. The nitrogen Pourbaix diagram shows the predominant (soluble) reduction products for nitrate as a function of pH and solution potential (E) (Figure 2.5).

For metal-nitrate solutions, which are typically acidic (pH < 7), NH_4^+(aq) is the predominant thermodynamic reduction product in solution at $E < 0.86$ V. From $E \approx 0.1$-1 V, HNO_2 (aq) and NO_2^-(aq) have narrow predominance regions at pH < 3 and from pH = 3-7, respectively. While other nitrate-reduction products are possible, including N_2, NO, N_2O, and N_2O_5, these products are gases with low solubilities.[59,60] Metal-nitrate reduction chemistry is important for the design and control of thin-film precursor solution speciation.

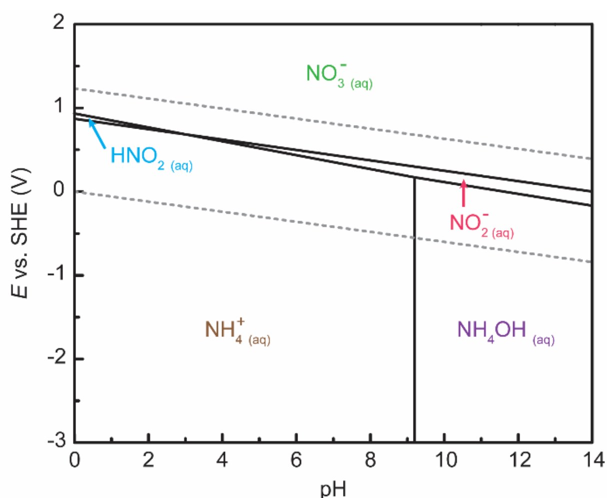

Figure 2.5. Nitrate Reduction Chemistry. The above Pourbaix diagram shows the aqueous solution speciation of nitrogen (0.1 M). The aqueous stability of nitrate is pertinent to understanding its reduction chemistry, which can be utilized to influence metal-nitrate precursor solution speciation. The data used to construct this Pourbaix diagram are from Ref. 60.

In addition to considering metal cation and nitrate solution chemistry independently, it is important to understand how these species interact in solution. Metal-anion complexes form in aqueous solutions under certain concentration conditions.[50–52,71,72] Metal-nitrato complexes (i.e. $[M(NO_3)(H_2O)_{N-1}]^{(z-1)+}$, abbreviated here as "M-NO_3") have been identified and quantified using Raman spectroscopy. For $In(NO_3)_3$, In-NO_3 complex can be identified by a shift in the InO_6 vibrational mode, and the

appearance of additional vibrational modes, as the $In(NO_3)_3$ concentration is increased (Figure 2.6a).[50] Changes to the Raman spectra result from broken symmetry of the aquo cation $[In(H_2O)_6]^{3+}$ when nitrate substitutes for a water molecule to form $In\text{-}NO_3$. The following quantities of $M\text{-}NO_3$ complex (compared to the amount of $[M(H_2O)_N]^{z+}$) for a select few metal cation systems relevant to thin-film solution precursors are as follows: In^{3+}(60%)[50] > Y^{3+}(45%)[51] ≈ La^{3+} (44%)[52] > Ga^{3+}(5%)[72] > Al^{3+}(0%)[71] (~ 2 M $[M^{3+}]$ in aqueous solution). For all metal cations, the quantity of $M\text{-}NO_3$ complex decreases with decreasing $[M^{z+}]$ and $[NO_3^-]$.

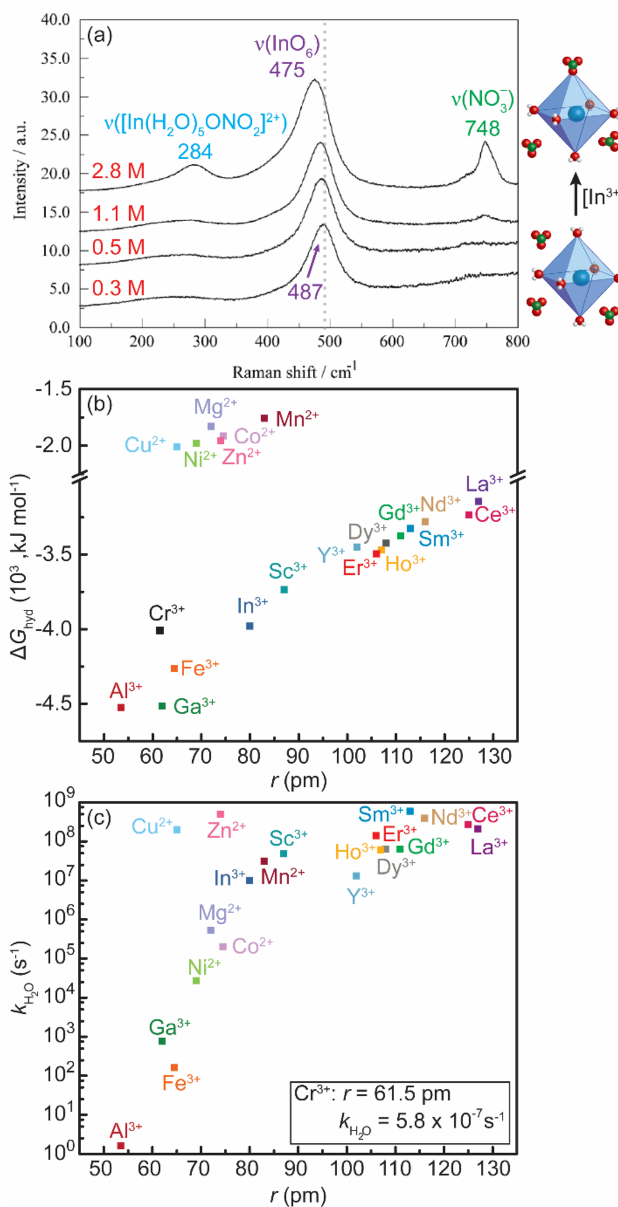

Figure 2.6. Metal-Nitrato (M-NO3) Complex Formation. (a) Raman spectra of $In(NO_3)_3$ solutions. Raman frequencies shift and new vibrational modes appear as $[In^{3+}]$ increases, indicating M-NO3 complex formation. The figure is adapted from Ref. 50 with permission from the PCCP Owner Societies. (b) Relationship between cation radius (r) and ΔG_{hyd} (values from Ref. 73). Cations that are more strongly hydrated (i.e. more negative ΔG_{hyd}) are thermodynamically stable and tend to form fewer M-NO3 complexes. Deviation of $z = +2$ first-row transition metals from this trend is due to weak ligand-field effects, which results in cation radius expansion when e_g orbitals are filled.[57] (c) Relationship between cation radius (r) and k_{H_2O}. Exchange kinetics will dictate how quickly equilibrium concentrations of M-NO3 complex will be established in aqueous solution. Values are compiled from Ref. 50,75,76.

The dependence of M-NO_3 complex formation on metal cation identity can be explained by considering the relative thermodynamic stabilities of the aquo cations and the M-NO_3 complex. The free energy of hydration (ΔG_{hyd} for the reaction: $M^{z+}(g) + nH_2O\ (l) \rightarrow M^{z+}(aq)$) provides a measure of the thermodynamic stability of hydrated metal cations. ΔG_{hyd} for the cations considered here are as follows: -4525 kJ mol^{-1} (Al^{3+}) < -4515 kJ mol^{-1} (Ga^{3+}) < -3980 (In^{3+}) < -3450 (Y^{3+}) < -3145 kJ mol^{-1} (La^{3+}).[73] Al^{3+} and Ga^{3+} form stable aquo cations (i.e. large, negative ΔG_{hyd}), due to their high charge densities, which result in strong M-H_2O bonds; this may explain why little to no M-NO_3 complex is observed for Al^{3+} and Ga^{3+}. In contrast, $In(NO_3)_3$ forms the largest quantity of M-NO_3 complex. The stability constant (log K_1) for In-NO_3 (0.18) is larger than that of La-NO_3 (0.1), despite the trend in ΔG_{hyd}. The reaction described by K_1 is given in Eq. 2.4. The fact that In-NO_3 is more stable than La-NO_3 is likely related to an optimal binding interaction between indium and nitrate due to cation size, charge density, and/or possibly differences in nitrate binding mode (e.g. monodentate vs. bidentate). Significant gaps in published K_1 values for M-NO_3 prevent us from making thorough comparisons of M-NO_3 stabilities.

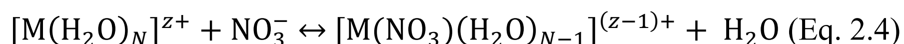

$$[M(H_2O)_N]^{z+} + NO_3^- \leftrightarrow [M(NO_3)(H_2O)_{N-1}]^{(z-1)+} + H_2O \quad \text{(Eq. 2.4)}$$

Consideration of thermodynamic and kinetic parameters of aquo cations can be useful for predicting if M-NO_3 may form, if stability constants are not available. The ΔG_{hyd} exhibits a linear relationship with cation size (r) (Figure 2.6b). Deviations from this trend arise for some first-row transition metal cations; weak ligand-field effects make filling of the anti-bonding e_g orbitals favorable, resulting in an expansion of the cation

radius that weakens M-H_2O bonds (i.e. ΔG_{hyd} values are lower than predictions based on r).[57] To first approximation, strongly-hydrated cations (i.e. large, negative ΔG_{hyd}) are expected to be thermodynamically stable and will likely form lower equilibrium concentrations of M-NO_3. It is also important to know the timescale required to establish equilibrium concentrations of the M-NO_3 complex (Eq. 2.4). This can be determined by considering the water exchange rate (k_{H_2O}). k_{H_2O} values tend to increase with increasing r but level off for $r > 80$ pm as a result of weakening first hydration sphere M-H_2O bond strengths (Figure 2.6c). The k_{H_2O} for the cations reported here suggest equilibrium for most aqueous metal nitrate solution is established in a matter of seconds.[57] The exception, Cr^{3+}, requires several days to reach equilibrium, as the water exchange reaction requires the formation of a high-energy transition state.[74] We discuss below ways in which M-NO_3 complexes in thin-film precursor solutions influence the thin-film reaction pathway and the final metal-oxide thin-film properties.

Tuning Metal Nitrate Precursor Chemistry

While metal-salt solution speciation is complex, some control can be achieved by altering solution pH, concentration, and/or temperature. Changing these parameters influences olation and metal-anion-complex equilibria. Here we discuss strategies to control metal-nitrate solution speciation for thin-film precursor design. We highlight examples that demonstrate how solution speciation influences thin-film morphology, chemical composition, and function.

Olation Products as Thin-Film Precursors

Our research groups (among others) have developed scalable synthetic methods for olation products, specifically nitrate-stabilized metal-hydroxo nanoclusters, for use as thin-film precursors. Such nanoclusters were targeted to solve common challenges associated with traditional sol-gel precursors for film deposition. In sol-gel syntheses, pre-condensation reactions are initiated in solution to control film morphology and ensure atomic-level mixing of multi-metal systems.[77] Organic solvents and additives are critical for controlling hydrolysis and condensation reactions in sol-gel chemistry. Solution equilibria can be shifted in order to influence the sol-gel precursor structure to alter reactivity and selectivity toward hydrolysis and condensation. This can be accomplished by controlling metal-ligand binding strengths, changing metal/ligand ratios, and/or the addition of acid or base catalysts. Danks et al. includes a detailed review of the chemical reactions/interactions relevant to sol-gel formation.[77] Removal of these organic species during thermal processing can negatively influence film morphology through cracking and/or the incorporation of pores.[53,78–80] In contrast, nanoclusters are pre-condensed with networks of hydroxyl linkages. Nanoclusters can be thought of as an “all-inorganic” analog to sol-gel thin-film precursors, as they typically contain inorganic anions for charge balance instead of organic ligands. The presence of a pre-condensed metal-hydroxo network and the lack of organic solvents or ligands allows nanoclusters to densify more readily, resulting in films with fewer morphological defects. Indeed, this pre-condensed metal-hydroxyl network should also prevent crystallization of monomer salts during solvent evaporation, resulting in homogeneous film morphology. Additionally, heterometallic nanoclusters inhibit phase segregation during film formation, which results in a uniform distribution of metal cations.

Two classes of nitrate-stabilized metal-hydroxo nanoclusters commonly utilized as thin-film precursors have the general formula $[M_{13}(OH)_{24}(H_2O)_{24}](NO_3)_{15}$ (i.e., "M_{13}" where M can be Al^{3+} or Ga^{3+})[62,70,81–86] or $[Ln_6(O)(OH)_8(H_2O)_{12}(NO_3)_6](NO_3)_2$ (i.e., "Ln_6", where Ln = Y^{3+}, Gd^{3+}, Ho^{3+}, or Er^{3+}).[87] The resulting structure of "M_{13}" nanoclusters has a planar (i.e. "flat") arrangement of octahedrally-coordinated metal sites and "free" (i.e. unbound) nitrate counterions (Figure 2.7a). A variation of this "M_{13}" cluster type includes substitution of the six exterior metal sites to form heterometallic structures, of which "Ga_7In_6" and "Al_7In_6" have been prepared to date.[62,82]

Olation reactions that form nanocluster products of these types can be driven by reactions that increase solution pH, for example proton (Eq. 2.5) and nitrate (Eq. 2.6) reduction.

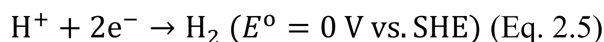

$$\mathrm{H^+ + 2e^- \rightarrow H_2}\ (E^{\circ} = 0\ \mathrm{V\ vs. SHE})\ \text{(Eq. 2.5)}$$

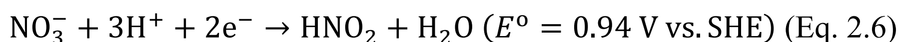

$$\mathrm{NO_3^- + 3H^+ + 2e^- \rightarrow HNO_2 + H_2O}\ (E^{\circ} = 0.94\ \mathrm{V\ vs. SHE})\ \text{(Eq. 2.6)}$$

Increased solution pH promotes cation hydrolysis (Eq. 2.1) and provides the reactive M-OH species for olation (Eq. 2.2). Eq. 2.6 is one of several possible nitrate-reduction reactions that increase pH, which all have similar reduction potentials (E° = 0.8 -1 V vs. SHE).[84] These reactions can be initiated with a variety of reductants, including organic molecules (i.e. nitrosobenzene),[81,83] zero-valent metals (Zn or Al), [82,85–88] or electrons via bulk electrolysis.[70,89,90] Metal-hydroxo nanoclusters can also be prepared from a "top-down" approach via digestion of metal hydroxide or oxide species in nitric acid. In this way, nanoclusters of a desired stoichiometry with specific M^{z+}:NO_3^- ratios can be targeted. Such "dissolution" methods have thus far been applied to the preparation of flat-

"Al_{13}" ($[Al_{13}(OH)_{24}(H_2O)_{24}](NO_3)_{15}$) and tin(II) hydroxide nitrate ($Sn(II)(OH)_x(NO_3)_y$) nanoclusters.[68,69]

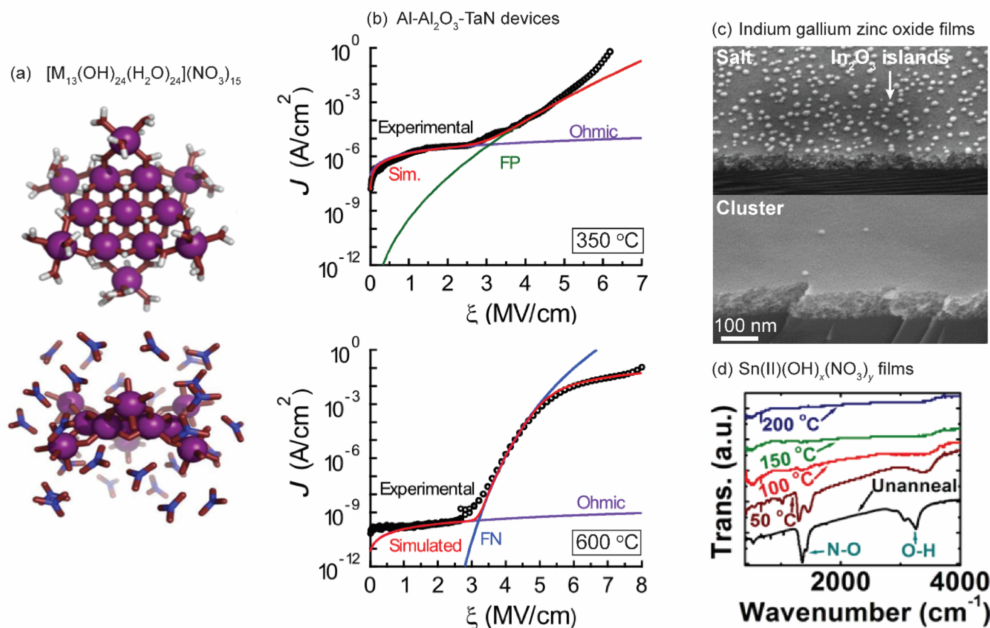

Figure 2.7. Metal-Hydroxo Nanoclusters as Thin-Film Precursors. (a) X-ray crystal structure of a $[M_{13}(OH)_{24}(H_2O)_{24}](NO_3)_{15}$ (M = Al^{3+} or Ga^{3+}) with (bottom) and without (top) non-coordinating nitrate counterions. (b) Current (J) – electric field (ξ) curve fitting of conduction mechanisms for Al_2O_3-based devices from "Al_{13}" precursors annealed at 350 (top) and 600 °C (bottom). The 350-°C-annealed film exhibits Frenkel Poole (FP) conduction, whereas the film annealed at 600 °C displays Fowler Nordheim (FN) tunneling. FN tunneling is indicative of a high-quality insulator. Reprinted from Ref. 88. Copyright 2018 American Chemical Society. (c) SEM images of indium gallium zinc oxide (IGZO) films prepared from nitrate salt solutions (top) and electrochemically-treated cluster solutions (bottom). Islands present on the surface of films from the salt precursor are phase-segregated In_2O_3. Electrochemically-treated solutions are believed to inhibit phase segregation as a result of the pre-condensed hydroxo network of "Ga_7In_6.". Images adapted from Ref. 90. Copyright 2015 American Chemical Society. (d) FT-IR spectra of films from the $Sn(II)(OH)_x(NO_3)_y$ nanocluster precursor. Vibrational modes for nitrate and hydroxyl groups (labeled) are nearly undetectable after annealing at 100 °C in air. Reprinted with permission from Ref. 68. Copyright 2013 American Chemical Society.

There are numerous examples of thin films from "M_{13}" (including its heterometallic variants) and "Ln_6" precursors that have excellent morphology and properties.[17,62,69,82,87–91] Such films are dense and exhibit essentially atomically-smooth surfaces,[17] which are properties critical for preparing high-performance electronic devices. Here we highlight select studies that demonstrate progress toward addressing common limitations of solution processing by using nanocluster precursors to prepare high-quality films.

As mentioned previously, impurities from solvents and counterions can inhibit condensation and densification processes in solution-deposited metal oxide thin films. Precursors from the "Al_{13}" nanocluster, which contain fewer nitrates per Al^{3+} (15:13) than the simple $Al(NO_3)_3$ salt (3:1) and a pre-condensed metal-hydroxyl network, have been used to produce dense, high-quality metal-oxide thin films with excellent insulating properties, as demonstrated in metal-insulator-metal (MIM) diodes. The insulating properties of Al_2O_3 thin films can be directly correlated with the chemical composition as a function of annealing temperature. At low annealing temperatures (350 °C), conduction is dominated by Frenkel-Poole emission at electric fields (ξ) above 3 MV cm^{-1}, which is a trap-mediated conduction mode (Figure 2.7b, top). The source of these trap states is suggested to be water, nitrate, and hydroxyl impurities remaining in the film, which are detected by temperature-programmed-desorption mass spectrometry (TPD-MS) and x-ray photoelectron spectroscopy (XPS). As the film annealing temperature is increased to 600 °C, chemical impurities are increasingly removed. The film further densifies, and, as a result, Frenkel-Poole emission is replaced by Fowler-Nordheim tunneling (Figure 2.7b, bottom). Fowler-Nordheim conduction requires low-defect density and had only been observed for devices from vapor-deposited thin films prior to this work. This study shows

that solution-deposited thin-film properties are sensitive to precursor chemistry and processing conditions. Additionally, having pre-condensed nanoclusters minimizes the amount of nitrate counterions that must be eliminated, aiding condensation and minimizing residual defects in the final films. The high-quality charge-transport characteristics obtained in solution-deposited thin films suggests there is opportunity to further design precursors to expand the application base of solution-processed films to those requiring low-defect-density materials (i.e. flash memory and solar cells).

Nanocluster precursors have also been used to combat phase segregation in multi-metal thin-film systems. Solutions of electrolyzed $In(NO_3)_3$, $Ga(NO_3)_3$, and $Zn(NO_3)_2$, which contain "Ga_7In_6" and $Zn(NO_3)_2$, can be used to prepare films with a homogeneous distribution of all metal atoms in indium gallium zinc oxide (IGZO) films.[90] In contrast, when the component salts are used, In_2O_3 islands decorate the film surface (Figure 2.7c). Phase segregation appears to be inhibited by the pre-condensed metal-hydroxo network of "Ga_7In_6." Nitrate reduction via electrolysis can also substantially reduce the nitrate concentration in solution, which leads to decreased mass loss during annealing and improved densification of the thin films, as evidenced by a 20% total mass change for films from nanocluster precursors vs. a 50% change for films from the component-salt precursors after a 300 °C anneal. Mass loss was monitored by thin-film thermal analysis using a quartz-crystal microbalance (QCM; described in *Characterization of the metal oxide thin-film reaction pathway*). Decreased mass loss correlates with denser films, as observed by x-ray reflectivity (XRR). Increased film homogeneity and densification translate to improved TFT device performance. Average channel mobilities increase from 5 to 9 $cm^2\ V^{-1}\ s^{-1}$ when electrolyzed solutions are used (400 °C annealing temperature).

Similar device performance improvements have been reported for IGO-based TFTs prepared from Ga_7In_6 precursors over films from Ga- and $In(NO_3)_3$ salts.[89]

An alternative strategy to initiate more-complete nitrate removal and condensation involves designing nanoclusters with reducing agents as a functional component of the final metal oxide film. We have synthesized precursors for SnO_2 and F-doped SnO_2 (F:SnO_2) that leverage redox reactions between Sn atoms and nitrate in a nanocluster with the general formula Sn(II)$(OH)_x(NO_3)_y$.[68] For F-doped films, SnF_2 is added to solution.

According to the Sn Pourbaix diagram, Sn^{2+} is stable over narrow pH (~ 0-1.6) and potential (~ 0 - 0.25 V) regions within the water stability window[60] and can oxidize readily to SnO_2 in water (Eq. 2.7). Standard reduction potentials indicate nitrates are capable of facilitating this oxidation process (Eq. 2.8 & 2.9). The following is one proposed reaction pathway for SnO_2 formation from the nanocluster precursor (Eq. 2.9).

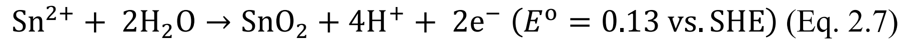

$$\mathrm{Sn^{2+} + 2H_2O \rightarrow SnO_2 + 4H^+ + 2e^-}\ (E^{\circ} = 0.13\ \text{vs. SHE})\ \text{(Eq. 2.7)}$$

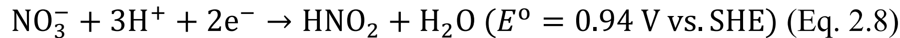

$$\mathrm{NO_3^- + 3H^+ + 2e^- \rightarrow HNO_2 + H_2O}\ (E^{\circ} = 0.94\ \text{V vs. SHE})\ \text{(Eq. 2.8)}$$

$$\mathrm{Sn^{2+} + NO_3^- + H_2O \rightarrow SnO_2 + HNO_2 + H^+}\ (E^{\circ}_{\mathrm{rxn}} = 0.81\ \text{V})\ \text{(Eq. 2.9)}$$

We observed by transmission Fourier transform infrared spectroscopy (FT-IR) that ~ 90% of nitrates are removed after annealing a film from the Sn(II)$(OH)_x(NO_3)_y$ nanocluster precursor at just 100 °C (Figure 2.7d). We hypothesize the redox reaction shown in Eq. 2.9 facilitates nitrate removal at low temperature. The resulting films are smooth, dense, and amorphous up to a 150 °C annealing temperature; at higher temperatures (e.g. 300 °C) crystalline, nanoporous SnO_2 forms. Porosity is likely caused

by rapid, low-temperature metal-oxide network formation, solid-state diffusional processes to densify the film are not sufficiently fast at these temperatures. Regardless, the resulting $F:SnO_2$ films are conductive ($\rho < 10^{-2}\ \Omega \cdot m$ at 250 °C annealing temperature) with high optical transparency in the visible spectrum (> 85%). Demonstrated compatibility with polyimide substrates suggest their usefulness as transparent conducting oxide materials for flexible devices.

Mitigating Metal-Nitrato (M-NO$_3$) Complex Formation in Solution

At solution concentrations relevant to thin-film precursor solutions (0.1 - 3 M in M^{z+}), many metal salts are capable of forming metal-anion complexes (abbreviated here as M-X). The presence of such complexes has been correlated with degraded electronic performance in resulting metal-oxide thin films. Work by Rim et al. on a variety of In_2O_3 precursors suggests the presence of fully-solvated $[In(H_2O)_6]^{3+}$ ions (i.e. in which there are no M-X complexes present) are critical for the preparation of high-quality In_2O_3 thin films at low annealing temperatures (~200 °C).[92] A comparison of the Raman spectra of $In(C_2H_3O_2)_3$, $InCl_3$, InF_3, and $In(NO_3)_3$ aqueous precursor solutions shows evidence of M-X complexes in all cases except $In(NO_3)_3$, in which only "free" (i.e. unbound) nitrate is detected ($\nu(NO_3^-) = 1050\ cm^{-1}$) (Figure 2.8a). A comparison of the stability constants for In-X complexes of these salts explains this observation, as the log K_1 value ($[M(H_2O)_6]^{3+} + X^- \overset{K_1}{\leftrightarrow} [M(H_2O)_5X]^{2+} + H_2O$) for $In(NO_3)_3$ complexes is lowest of all the salts investigated, indicating In-NO_3 complexes are weakest (log K_1 = 0.18, 2.32, 3.50, and 3.75 for $In(NO_3)_3$, $InCl_3$, InF_3, and $In(C_2H_3O_2)_3$, respectively).[92,93] A lack of M-X complexes in $In(NO_3)_3$ solutions is said to facilitate hydrolysis, requiring a lower

energy input for metal oxide formation, as there are no M-X bonds that must be broken. There is a loose correlation between log K_1 and metal oxide (M-O) character (determined by XPS). Films from $In(NO_3)_3$ and $InCl_3$ contain > 20% more metal-oxygen bonds than those from InF_3 and $In(C_2H_3O_2)_3$ (Figure 2.8b). TFT device performance of resulting In_2O_3 films from $In(NO_3)_3$ exceeds that of films from the other precursors. Saturated channel mobilities (μ_{sat}) and on-off current ratios are up to two-orders-of-magnitude higher than for the next-best devices from the InF_3 precursor ($In(NO_3)_3$: μ_{sat}= 24 cm^2 V^{-1} s^{-1}, $I_{on/off}$ = 10^8; InF_3: μ_{sat}= 1.2 cm^2 V^{-1} s^{-1}, $I_{on/off}$ = 10^6) (Figure 2.8b). The low μ_{sat} from $InCl_3$-based films is hypothesized to be to a result of Cl impurities due to incomplete decomposition at this 250 °C annealing temperature, despite high M-O content.

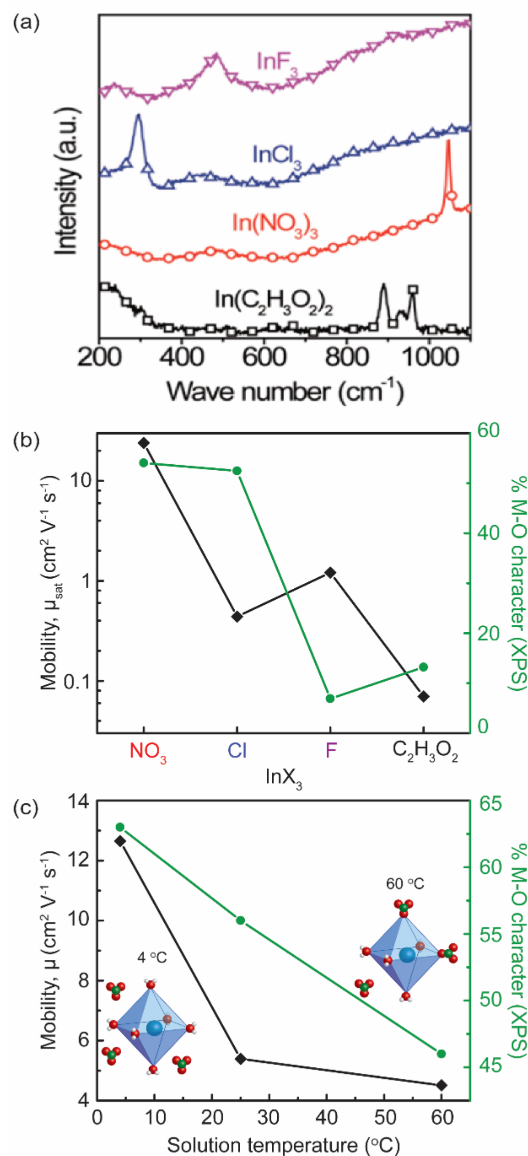

Figure 2.8. Metal–Nitrato ($M-NO_3$) Complex Formation in Thin-Film Solution Precursors. (a) Raman spectra of aqueous indium salt (InX_3) precursor solutions. The observed vibrational modes are assigned to M-X complexes, with the exception of the peak at 1050 cm^{-1} in $In(NO_3)_3$ spectra, which is assigned to "free" nitrate. Reproduced with permission from Ref. [92]. Copyright 2015 American Chemical Society. (b) TFT μ_{sat} and M-O content in In_2O_3 films from various indium precursors (data adapted from Ref. [92]). The high μ_{sat} for the In_2O_3 film from $In(NO_3)_3$ is a result of high metal-oxide content due to lack of $M-NO_3$ complex in the precursor solution, as well as few counterion impurities in the final metal oxide. All films for these TFTs were annealed at 250 °C. (c) Relationship between precursor solution temperature, TFT channel mobility (μ) and M-O content in indium zinc oxide thin films (data adapted from Ref. [94]). As precursor solution temperature is decreased, M-O content and μ increase, which is suggested to be a result of fewer $M-NO_3$ complexes present as the solution is cooled. The TFT data shown are for devices that use SiO_2 as the dielectric layer.

The presence of M-NO_3 complexes in thin-film precursor solutions has been correlated with degraded metal-oxide properties, despite the fact such complexes are thermodynamically weak compared to other M-*X* complexes. One reported strategy for mitigating M-NO_3 complex formation involves changing the precursor solution temperature. Lee and co-workers observe a decrease in the ratio of "free" to complexed nitrates in the Raman spectra of mixed $In(NO_3)_3/Zn(NO_3)_2$ solutions as the solution temperature is increased from 4 to 60 °C (Figure 2.8c).[94] The underlying assumption is that "free" nitrate will more readily decompose from the films, resulting in a greater degree of metal-oxide condensation in the thin film. The authors hypothesize that the high dielectric constant of water at lower temperatures ($\varepsilon_{H_2O} \approx 85$ at 4 °C, compared to ~70 at 60 °C) supports greater separation of charge, thereby favoring "free" nitrate over M-NO_3 complexes. However, given the majority solvent in this study is 2-methoxyethanol, which has a lower ε than water and a weak temperature dependence ($\varepsilon \approx 19$ at 4 °C and ~14 at 60 °C), the effect of ε is uncertain.[95] Chemical analysis by XPS of the O 1s spectra show the film from the 4 °C solution has 20% greater metal-oxygen character than the film from the 60 °C solution (Figure 2.8c). These chemical differences are apparently responsible for higher TFT mobilities (μ) for films from the 4 °C solution (Figure 2.8c). A similar study, in which aqueous $In(NO_3)_3$ precursor solutions are used, also shows chemical differences (by XPS) between films prepared from "chilled" and room-temperature $In(NO_3)_3$ solutions.[95] However, the differences in TFT performance between films from these two solutions are not appreciable (μ_{sat} = 0.94 cm^2 V^{-1} s^{-1} for the film from a "chilled" solution and 0.66 cm^2 V^{-1} s^{-1} for room temperature). High-temperature solution aging (70 °C for 72 h) has also been suggested to increase the "free"

nitrate concentration and improve metal-oxide condensation, leading to high-μ In_2O_3 TFTs (~24 cm^2 $V^{-1}s^{-1}$).[96]

The effect of precursor-solution temperature on thin-film formation chemistry is clearly complex. Mitigating $M\text{-}NO_3$ complexation and increasing "free" nitrate concentration appears to facilitate more-complete metal oxide condensation in the final thin film. However, the seemingly contradictory reports of improved device performance observed for films prepared from solutions that have undergone both low and high temperature treatments suggest that the dielectric of the solvent medium may not be responsible for this effect. It is clear that temperature influences $M\text{-}NO_3$ equilibria, which exhibits a correlation with thin-film composition and device performance. Further study is needed to elucidate how temperature-dependent equilibria influence thin-film formation processes.

Bridge

Chapter II detailed the fundamentals of metal-nitrate decomposition chemistry, as well as the complex equilibria that exist in aqueous metal-nitrate solutions. Alteration of solution conditions such as pH, concentration, and temperature has marked effects on resulting thin-film properties. Chapter III builds upon this discussion to characterize the thin-film portion of the reaction pathway (from gel to metal oxide) by reviewing the chemistries induced by different thin-film treatment methods utilized in this field of study.

CHAPTER III

SOLUTION-PROCESSED METAL-OXIDE THIN FILMS FOR ELECTRONIC AND ENERGY APPLICATIONS: UNIQUE CHEMISTRIES OF METAL NITRATE PRECURSORS

Authorship Statement

This chapter contains material previously published in *Journal of Materials Chemistry A* **2019**, *7*, 24124-24149. This work was coauthored by Elizabeth A. Cochran, Keenan N. Woods, Catherine J. Page, Darren W. Johnson, and Shannon W. Boettcher. This manuscript was written by E.A.C. with contributions and editorial assistance from all authors.

The Chemical Evolution of Metal Nitrate Gels: The Initial Stages of Metal Oxide Thin-Film Formation

From Solution to Thin Films: Fundamental Considerations for the Preparation of Metal Oxide Coatings

The previous chapter highlights important considerations for solution-precursor preparation. The following chapter will elaborate on the use of these metal-nitrate solution precursors and the reaction pathways from solution to solid-state thin films. Common thin-film solution deposition methods include spin-, spray-, and dip-coating, with many variations on each process. The physics governing material deposition from each of these methods is detailed elsewhere.[1–4] In order to deposit a uniform thin film, the substrate must first be wetted with solution (Figure 3.1, step I). In order to achieve

uniform wetting, the surface must be free of organic contaminants. For aqueous solutions, the surfaces must also be sufficiently hydrophilic to achieve proper wetting and reduce the interfacial energy between the solution and substrate.[4] Eliminating organic contaminants and generating polar hydrophilic surfaces can be achieved through a variety of dry and wet chemical processes. Common surface treatments include O_2 plasma, piranha (H_2O_2/H_2SO_4), and RCA-1 (H_2O_2/NH_4OH) cleaning methods. When choosing a surface treatment method, possible damage to the substrate through chemical degradation and/or physical roughening should be considered, which can negatively affect film and device properties. Once a favorable interaction between the solution and substrate is achieved, gel formation is initiated by solvent evaporation to begin the drying process (Figure 3.1, step II). This is accomplished via rapid substrate rotation in spin-coating and heating of the substrate during spray-coating, for example. At the end of the coating process, a concentrated metal-nitrate gel film is adhered to the substrate. In order to convert the gel into a metal-oxide thin film, remaining solvent must be evaporated (continuation of step II), nitrates removed/decomposed via HNO_3 and NO_x gas formation (Figure 3.1, step III), and metal-hydroxide groups condensed to form the metal oxide (M-O-M) network (Figure 3.1, step IV). These remaining steps require energy input, often in the form of thermal annealing.

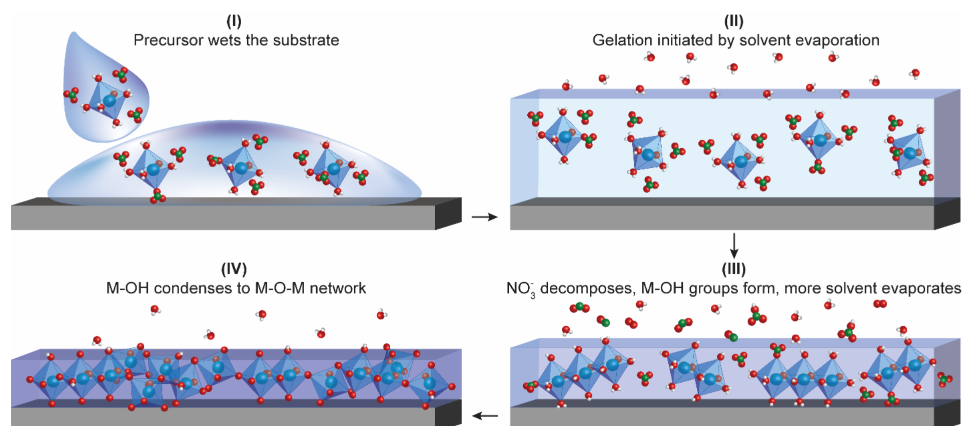

Figure 3.1 Stages of Thin-Film Formation from Solution Precursors. (I) The substrate is wetted with an aqueous metal nitrate solution. Adequate wetting is achieved via substrate surface preparation treatments to remove organic contaminants and introduce polar functional groups to impart hydrophilicity. (II) The thin-film precursor gel is formed by rapid evaporation of excess solvent (H_2O, in this example). The resulting metal-nitrate gel must then be decomposed to form a metal oxide. (III) With addition of energy (commonly thermal annealing), additional solvent is evaporated and nitrates decompose to HNO_3, NO_x, etc. Condensation is initiated, forming $M(OH)_x$ species. (IV) Once nitrates and solvent are removed, $M(OH)_x$ further condense to form the final metal oxide. See Figure 2.1a for representative chemical reactions for nitrate decomposition and hydroxyl condensation.

Controlling the reaction rates (and mechanisms) taking place in steps II-IV is crucial for controlling film morphology and structure (density, porosity, grain size, etc.), which ultimately influence device performance. If condensation of the rigid metal oxide network occurs rapidly, evaporation and decomposition byproducts will disrupt the network.[1,5] For example, as discussed previously, films from $Sn(II)(OH)_x(NO_3)_y$ nanocluster precursors experience rapid decomposition, resulting in nanoporosity.[6] Film morphology is also sensitive to annealing ramp rate. We observe for lanthanum zirconium oxide (LZO) films from nitrate salts that, as the temperature ramp rate is decreased from 125 to 0.25 °C min^{-1}, the films contain fewer voids and are denser. As the ramp rate slows, nitrate decomposition and hydroxide condensation are temporally separated.[7] This is a general consideration in the preparation of thin films from solution

precursors. The film-formation steps II-IV often overlap substantially. While difficult to control, the temporal overlap can be decreased in many cases by controlling the thermal processing parameters (i.e. ramp/hold profiles), which provides opportunity to optimize metal-oxide film properties.

In order to exercise greater control over film formation, which will influence the resulting film structure and properties, it is important to understand the decomposition behavior of nitrates in thin-film gels. We discuss here insights gained from studying thin-film reaction pathways as a function of temperature, as thermal energy is central to most processing methods currently used.

Characterization of the Metal Oxide Thin-Film Reaction Pathway

Metal nitrates are generally thermally unstable and decompose at modest annealing temperatures (Figure 2.2). As the annealing temperature is increased, solvent, nitrates, and impurities are increasingly removed and metal-oxide content increases. Film evolution as a function of temperature can be evaluated using a variety of characterization techniques. Here we highlight chemical insights gained from the thermal decomposition behavior of metal-nitrate gel films to elucidate the thin-film reaction pathway.

When studying thin-film reaction pathways, it is important to know at what temperatures decomposition processes occur. While TGA of bulk precursors can provide a good estimate of the metal-oxide formation temperature, thin films have been shown to decompose at lower annealing temperatures than their bulk counterparts.[8] Higher surface-area-to-volume ratios of nanoscale thin films compared to bulk powders leads to efficient mass and thermal transport through the thin film, which results in faster decomposition

kinetics.[8,9] Therefore, studying thin-film thermal analysis directly is important for understanding decomposition behavior. Traditional TGA has been successfully adapted to studies on films 300-500 nm thick; however, greater sensitivity is required to probe small mass changes in films below 100 nm thick, which are relevant thicknesses for many electronic applications. Quartz-crystal microbalance (QCM) analysis, which has $ng \cdot cm^{-2}$ sensitivity and has been extensively applied to studies of vapor-phase film deposition[10] as well as dissolution of electrode films during electrochemistry,[11] is a good candidate for studying small mass changes during annealing of solution-processed thin films. The effect of temperature on the crystal resonator must be accounted for in the application of QCM mass monitoring. The temperature range accessible is limited by a phase transition at 573 °C, above which the quartz crystal loses its piezoelectric properties;[10] practically, we find this temperature limit is ~ 300 °C, due to thermal shock that can result in cracking. Additionally, quartz resonators have a temperature-dependent frequency response. Therefore, to decouple effects from temperature and mass loss, we have performed these experiments ex situ (i.e. "step-wise" annealing the QCM with a deposited film at a fixed temperature, then returning to room temperature to measure the frequency following each annealing step). In principle, such limitations could be addressed to perform in situ thermal analysis on thin films using a resonator material with a small temperature coefficient, such as gallium orthophosphate ($GaPO_4$), and reliable temperature response calibration.[10] We have successfully applied ex situ QCM thermal analysis to study thin-film mass loss below 300 °C.[6,12,13] An example of QCM mass loss data can be seen for films from $Sn(II)(OH)_x(NO_3)_y$ nanocluster precursors in Figure 3.2a.[6] Mass loss for films is complete by 225 °C, whereas a 400 °C annealing temperature is needed to convert commonly-used bulk precursors to SnO_2.[14]

Because film properties are sensitive to chemical composition, studying thin-film chemical evolution is important for preparing thin films with desired properties. While thermal analysis by QCM is useful to understand when decomposition reactions occur, resolution limits resulting from ex situ measurements (i.e. step-wise annealing) makes assessing decomposition mechanisms difficult. Chemical characterization techniques are needed to obtain a complete picture of film formation reactions. The vibrational modes of nitrate, water, hydroxide, and metal-oxide bonds make FT-IR spectroscopy a convenient tool for monitoring the chemical composition as a function of annealing temperature. Representative FT-IR data that demonstrate the chemical evolution of a mixed $La(NO_3)_3/ZrO(NO_3)_2$ precursor for the preparation of lanthanum zirconium oxide (LZO) is shown in Figure 3.1b. Nitrate can be identified by a split N-O stretching mode, with bands centered at ~ 1300-1400 and 1600-1700 cm^{-1}. The splitting originates from a reduction of symmetry (D_{3h} to C_{2v}) due to covalent character between nitrate and the metal and/or different binding modes (monodentate, bidentate, or bridging).[15]

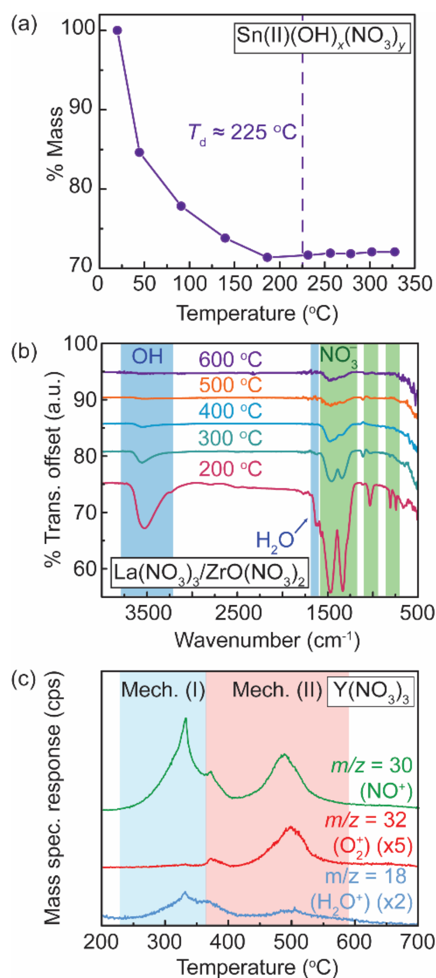

Figure 3.2 Characterization Techniques Used to Study the Metal-Oxide Thin-Film Reaction Pathway by Thermal Annealing. (a) Quartz-crystal-microbalance (QCM) thermal-analysis data is used to determine thin-film decomposition temperatures (T_d). The above example shows the T_d of a thin film from the $Sn(II)(OH)_x(NO_3)_y$ nanocluster precursor was estimated to be ~ 225 °C (data from Ref. 6). (b) Chemical composition of thin films as a function of annealing temperature can be monitored by Fourier transform infrared (FT-IR) spectroscopy, due to the intense nitrate IR active modes. Representative data of an FT-IR annealing study is shown for films from a $La(NO_3)_3/ZrO(NO_3)_2$ (1 La : 1 Zr) precursor for lanthanum zirconium oxide (LZO) films. These data are adapted from Ref. 28. (c) Thin-film decomposition products can be studied using temperature-programmed-desorption mass spectrometry (TPD-MS). Two distinct nitrate-decomposition mechanisms can be inferred from the data shown for $Y(NO_3)_3$ thin films. Mechanism I (highlighted in blue) is associated with “loosely-bound” nitrate, including the HNO_3/H_2O azeotrope as a decomposition product, as evidenced by concomitant detection of NO^+ and H_2O^+ fragments. Mechanism II (highlighted in red) is associated with nitrate in more thermally stable environments and is identified by simultaneous detection of NO^+ and O_2^+ fragments. These data are adapted from Ref. 13.

Weaker vibrational modes, associated with M-NO_3 complexes, appear at ~ 1000 and 800 cm^{-1}.[16] Water is identified by the OH stretch (~3500 cm^{-1}) and the H-O-H bending mode[17] (~1650 cm^{-1}); intensities of these modes decrease dramatically at low annealing temperatures (~ 200-300 °C). Once most of the nitrate and free water are gone, the OH stretch can be attributed primarily to metal hydroxides and the appearance of a weak, broad, metal-oxide stretch is observed near 700-800 cm^{-1}.

In addition to studying the evolution of thin-film chemical composition, decomposition byproducts can provide useful mechanistic insight into film formation. Temperature-programmed-desorption mass spectrometry (TPD-MS), a tool that has been used extensively in materials science to study interactions between absorbed gases and solid surfaces, has recently been applied to thin-film formation studies on solution-deposited films.[18–22] While TPD studies of metal-nitrate-based films are limited,[7,13,23] there is a wealth of literature on decomposition mechanisms of adsorbed nitrate on metal-oxide surfaces. While metal oxides with surface-adsorbed nitrates and metal nitrate thin-film gels are not analogous materials, there are similarities (described below) between the nitrate decomposition pathways observed by TPD-MS for both systems.

Two distinct nitrate decomposition events have been identified in the TPD literature from studies of nitrates on metal-oxide surfaces. The first (mechanism I) is a lower-temperature event that can be identified by the evolution of NO^+ (m/z = 30) as the primary fragment, with minor contributions from N_2^+ (28), N_2O^+ (44), and NO_2^+ (46).[24] The products that evolve by mechanism I are hypothesized to originate from "loosely-bound" nitrate. Corroborative FT-IR studies suggest bidentate (chelating and/or bridging) metal-nitrate complexes contribute to this decomposition mechanism.[24,25] At higher temperatures (mechanism II), NO^+ and O_2^+ (m/z = 32) evolution are concomitant and are

associated with decomposition of nitrates that are more thermally stable, such as monodentate or ionic nitrates.[24–26]

For films prepared from metal-nitrate precursors, we similarly identify two distinct nitrate decomposition and desorption events by TPD-MS. A detailed discussion of metal-nitrate decomposition chemistry can be found in the chapter II. Because we are unable to definitively assign IR-active nitrate modes for nitrates in thin films to specific binding motifs (Figure 3.2b), we do not assign these fragments as originating from specific nitrate environments. In addition to the fragments described by mechanism I, we observe H_2O^+ (m/z =18) accompanying this first nitrate decomposition event, which may suggest the H_2O/HNO_3 azeotrope contributes to the film decomposition pathway (Figure 2.1a, Eq. i).[13] For mechanism II, we believe these fragments are associated with the thermal decomposition of "tightly-bound" nitrate (Figure 2.1a, Eq. ii), likely M-NO_3 complexes. TPD-MS fragments produced from a film made from a $Y(NO_3)_3$ precursor are representative of fragmentation patterns typically observed from nitrate decomposition byproducts that evolve from thin-film samples (Figure 3.2c).

Once nitrate is effectively eliminated from the film, XPS is useful to continue studying film evolution. The degree of metal-oxide condensation can be evaluated as a function of annealing temperature by analyzing the O 1s regional spectrum. Three oxygen environments are commonly fit for metal-oxide thin-films: metal oxide (528-531 eV, denoted O_I), "oxygen vacancies" (531-532 eV, O_{II}), and metal hydroxide (531-534 eV, O_{III}) (Figure 3.3a).[27–32] Sometimes referred to as "oxygen-deficient states," the O_{II} region encompasses under-coordinated metal atoms due to sub-stoichiometric compositions, as well as weakly-bound impurities from adsorbed gases, residual nitrate, adventitious carbon, etc.[29–31] For $In(NO_3)_3$ precursors, the O_I peak area increases with

annealing temperature; there exists a linear correlation between the O_I peak area and In_2O_3 TFT mobility (Figure 3.3b).[27,28,32] Increased μ is attributed to improved condensation at higher annealing temperatures, as well as "clean" nitrate decomposition (i.e. few impurities remaining in the film), which facilitates densification.[28]

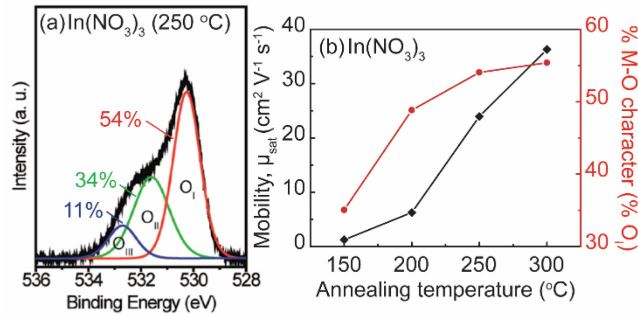

Figure 3.3. Evaluating the Quality of Metal Oxides from Metal-Nitrate Precursors. (a) O 1s XPS spectrum from an In_2O_3 film indicating oxygen environments typically observed in metal-oxide thin films. The O_I, O_{II}, and O_{III} environments, as denoted in the figure, are assigned to indium oxide (In-O), oxygen vacancies (i.e. nitrate (N-O), carbon (C-O), under-coordinated oxygen species, etc.), and indium hydroxide (In-OH), respectively. (b) Metal-oxide character and In_2O_3 TFT saturated channel mobility (μ_{sat}) increase with annealing temperature for films from $In(NO_3)_3$. Higher μ_{sat} at higher annealing temperatures is a result of increased M-O content and fewer nitrate impurities remaining in the film. The TFT data shown are for devices that use SiO_2 as the dielectric layer. Data reproduced and adapted with permission from Ref. [28]. Copyright 2015 American Chemical Society.

Alternatives to Conventional Thermal Processing: a Survey of Low-Temperature Processing Methods Utilizing Unique Metal Nitrate Chemistries

Because of their relatively low decomposition temperatures, metal nitrate precursors have been extensively used in the development of low-temperature solution-processing methods. Various chemical strategies have been introduced to produce high-quality metal-oxide thin films using a reduced thermal budget. The primary objective of so-called "low-temperature processing" methods is to improve compatibility of solution-

processed films with low-melting point, inexpensive polymeric substrates. Here, we highlight progress made toward low-temperature processing by utilizing the unique reactivity of nitrate with alternative energy sources and annealing atmospheres.

Combustion Processing

The combustion processing method, first introduced by Kim et. al,[33] endeavors to use the internally-produced exothermic heat from a combustion reaction between nitrate and an organic fuel. This approach is intended to lower thin-film processing temperatures relative to metal nitrate thermal decomposition reaction, which is an endothermic process. Figure 3.4a depicts a reaction coordinate diagram and representative chemical equations for the combustion and thermal decomposition pathways. Since the combustion process is highly exothermic, this change to the reaction enthalpy (ΔH) leads to a comparatively more spontaneous ΔG compared to the ΔG of the thermal decomposition reaction. Mild annealing conditions (~ 200-300 °C) are purported to ignite a combustion front that propagates through the thin-film volume. High local temperatures produced by this reaction (reported to be upward of 1000 °C for bulk systems, depending on the oxidizer-fuel mixture used[34]) are hypothesized to decompose nitrate and condense the metal-oxide network. Combustion processing is, in principle, compatible with low-melting-point polymeric substrates because the high surface-area-to-volume ratio of the film rapidly dissipates heat to the atmosphere.[33] Since the first report of thin-film combustion processing, which focused primarily on $In(NO_3)_3$-based precursors using acetylacetone and urea fuels,[33] the method has been applied to many other metal nitrate and fuel systems.[35–46]

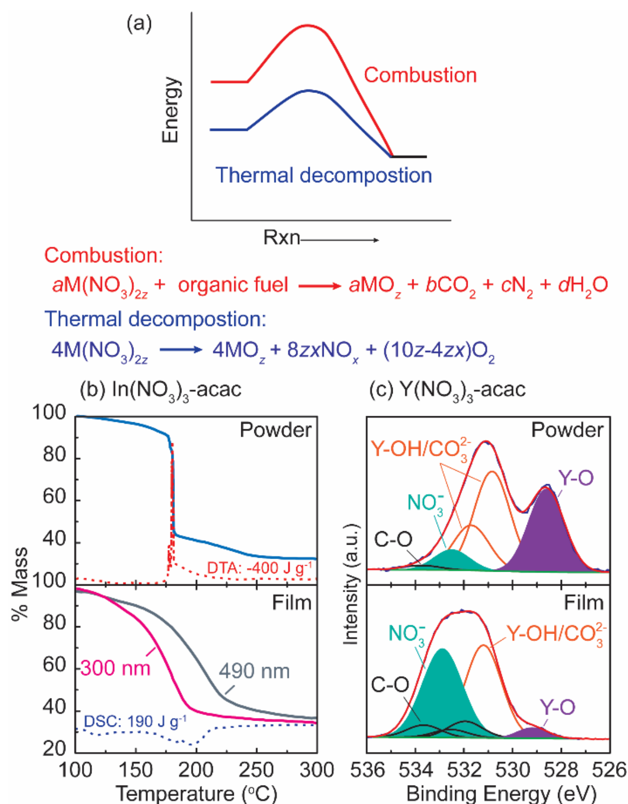

Figure 3.4. Reactivity of Combustion Precursors. (a) Reaction coordinate diagram depicting combustion and thermal decomposition pathways with their associated chemical reactions. Combustion is considered a low-temperature thin-film processing method because low applied temperatures (compared to thermal decomposition) lead to ignition of an exothermic combustion front. It is suggested the heat produced by combustion decomposes nitrates and condenses the metal-oxide network. (b) TGA comparison for a bulk powder (top) and thin film (bottom) prepared from the combustible mixture $In(NO_3)_3$ -acac. An exotherm (i.e. combustion) is detected for the bulk powder, whereas an endotherm (i.e. thermal decomposition) is detected for the thin film. Data adapted from Ref. [9]. (c) O 1s XP spectra for a powder and film prepared from a $Y(NO_3)_3$-acac mixture by annealing near the combustion ignition temperature. Composition analysis suggests combustion occurs in the powder (i.e. high Y-O, low NO_3^- content) but not in the thin film (i.e. low Y-O, high NO_3^-) when samples are annealed above the combustion ignition temperature (215 °C). Data adapted from Ref. 13.

The combustion method has been utilized to prepare a variety of metal-oxide films for TFTs[40–46] and photovoltaic applications.[35,36,39] In order to benchmark the performance of combustion-processed films relative to other common solution-deposition approaches, we compare here TFT-derived electron mobilities of In_2O_3 films (Figure 3.5). Combustion-synthesized films demonstrate respectable μ improvements compared to sol-gel films (i.e. 2-methoxyethanol solvent without combustion additives), especially when spray-deposited.[46] However, In_2O_3 films from aqueous precursors exhibit up to an order of magnitude higher μ than combustion and sol-gel films annealed at comparable temperatures. This is likely a result of increased densification and fewer carbon impurities in the films made from aqueous $In(NO_3)_3$ precursors.[47]

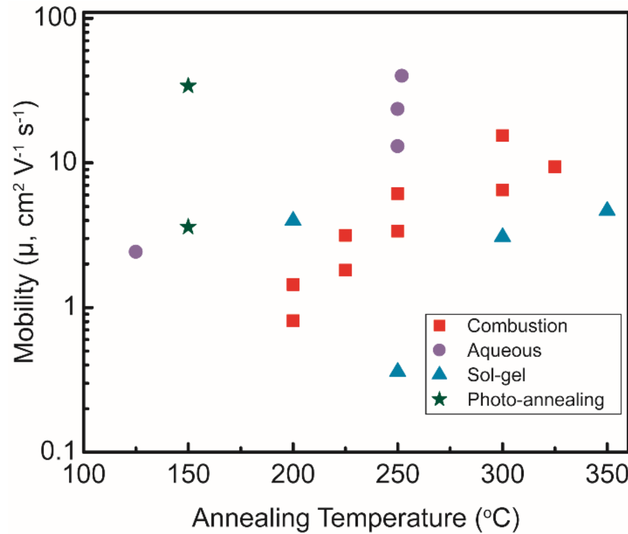

Figure 3.5. Comparison of In_2O_3 Films Prepared by Various Low-Temperature Processing Methods. Channel mobilities (μ) for In_2O_3 TFTs are used to compare the properties of thin films prepared using various low-temperature processing strategies. All data presented here are for TFTs with SiO_2 dielectric layers, for ease of comparison. The associated references for the data categories plotted above are as follows: combustion,[33,46] aqueous,[28,48–50] sol-gel,[51,52] and photo-annealing.[53,54]

For selective-contact applications in solar cells, combustion-processed thin films have demonstrated improved performance over other commonly-used methods/precursors. When paired with an organic absorber, combustion-synthesized NiO films perform similarly to widely-used organic hole-transport layers (HTLs), with power conversion efficiencies (PCE) of 1.6 and 1.7%, respectively, and outperforms NiO from a nickel acetate precursor (0.16%).[39] In another study, PCEs for combustion (17.7%) and sol-gel (15.5%) Cu-doped NiO films exhibit similar performance as selective contacts to perovskite active layers at drastically-reduced processing temperatures (150 and 500 °C, respectively).[36] Additionally, combustion-derived IGO and IGZO films have electronic structures that are tunable with composition, which demonstrates a design strategy for engineering charge-carrier selective contacts that can be tailored to match valence and conduction band energies of various absorber materials.[35] It should be noted, however, that direct comparisons in the literature of thin films from combustion precursors (metal nitrates with fuels) and metal nitrates without fuels are lacking; therefore, it is impossible to attribute improved solar-cell performance to combustion processing directly.

The number of examples of metal oxides prepared by the combustion method demonstrates these precursors are useful for making solution-processed films/devices of reasonable quality. However, several studies have called into question the fundamental chemistry of combustion reactions in thin films.[9,13,55–57] The $In(NO_3)_3$-acetylacetone (or "acac") mixture, first studied by Kim,[33] was further investigated using TGA in both the bulk and thin-film form.[9] Combustion is identified by an abrupt mass loss event, accompanied by an exotherm in the differential thermal analysis (DTA) signal, which is evident for the bulk system (Figure 3.4b, top). In contrast, gradual mass loss and an endotherm, associated with thermal decomposition, are detected for a thin film prepared

from the same precursor, suggesting combustion does not occur (Figure 3.4b, bottom). To investigate this observed difference in bulk and thin-film reactivity, we studied the chemical composition and thermal behavior of several model combustion-precursor systems. When we applied the thin-film QCM technique to $In(NO_3)_3$- and $Y(NO_3)_3$-acac precursors, we similarly observed gradual mass loss with annealing temperature, which is an indicator of thermal decomposition rather than combustion.[13] Additionally, XPS analysis of powders and films prepared from $Y(NO_3)_3$-acac show significant chemical differences when annealed near the combustion ignition temperature (T_{ig} ~ 200 °C). While the powder contains high Y-O content, the thin film contains comparatively low Y-O and retains significant $Y(NO_3)_3$ precursor character (Figure 3.4c). Incorporation of fuel into the precursor solutions does not improve precursor conversion to the corresponding metal oxide at lower processing temperatures for thin films, as it does in the bulk, which suggests combustion does not occur in thin films.

Computational modeling to simulate the decomposition kinetics and heat conduction in thin films corroborates experimental data that suggests thin-film combustion does not occur.[9,55–57] When modeled in the geometry of a bulk powder in a crucible, combustible mixtures exhibit an inhomogeneous reaction rate throughout the sample volume, consistent with combustion front propagation.[9] When the same precursor is modeled in the geometry of a thin film, a combustion front is not observed. Numerical modeling of reaction kinetics suggests that, in order to overcome the activation energy for combustion in a 1 μm-thick film, the substrate temperature and ramp rate must be at least 1200 K and 10^7 K min^{-1}, respectively.[57] These values are determined using expressions that exhibit strong dependence on the height-to-radius ratio of the sample (the sample volume is approximated as that of a cylinder) and the critical mass, which is dependent

on the thermal conductivity of the sample/substrate. Therefore, even when the same combustion precursors are used in the preparation of bulk and thin-film metal oxides, differences in thermal transport result in different reaction pathways.

In light of the experimental and computational results discussed here, thin-film combustion of metal nitrates at low temperatures is unlikely. Rather, the various improvements in device performance obtained when the combustion thin-film synthesis is used may be attributed to other factors, namely, the high volatility of metal nitrate decomposition products. Most studies compare films prepared from combustion precursors to those from metal chlorides and/or acetates,[33,36,39] which decompose at higher temperatures and leave non-volatile impurities in the metal-oxide thin films.[27,28] Additionally, some studies have observed fuels can improve film morphology, which can also improve device performance. NiO films from a $Ni(NO_3)_2$-urea precursor are smoother than those from a $Ni(C_2H_3O_2)_4$ precursor (R_{rms} roughness of 1.1 and 12.3 nm, respectively, by atomic force microscopy).[39] In our previous studies on combustion thin-film processing, films from the $In(NO_3)_3$-acac precursor show enhanced crystallinity by x-ray diffraction (XRD) compared to films from $In(NO_3)_3$, indicating fuel incorporation can influence the nanoscale structure of films.[13] Indeed, there may be ways in which film properties benefit from the use of "combustion" precursors, even if combustion does not occur.

Ultraviolet (UV) Photo-Annealing

A unique aspect of metal-nitrate chemistry is the susceptibility of nitrates to decomposition when irradiated with deep-ultraviolet (UV) light (λ = 185-254 nm). This chemistry has been applied to thin-film formation and is known as "photo-annealing" (Figure 3.6a).[53] The mechanism of nitrate removal from thin films was confirmed to be

nitrate photolysis (Eq. 3.1), through UV-visible and NMR studies on UV-irradiated $Al(NO_3)_3$ solutions.[58] The oxygen radical produced in Eq. 3.1 further reacts with water to form hydroxyl species (Eq. 3.2), which then condense to form the metal oxide.

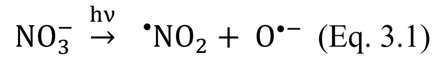

$$NO_3^- \xrightarrow{h\nu} {}^{\bullet}NO_2 + O^{\bullet -} \quad \text{(Eq. 3.1)}$$

$$O^{\bullet -} + H_2O \leftrightharpoons {}^{\bullet}OH + OH^- \quad \text{(Eq. 3.2)}$$

This reaction mechanism is consistent with previous literature on photolysis of nitrate in aqueous solution.[59,60] In thin films, the radicals produced by nitrate photolysis are hypothesized to facilitate decomposition of organic solvents and M-OH formation. While photo-annealing effectively eliminates nitrates from thin films at room temperature, moderate annealing treatments (~150-200 °C), using radiant heat from UV lamp operation or post-UV exposure, aid condensation to the final metal-oxide phase.[53,61] FT-IR spectroscopy confirms nitrates are removed from $Al(NO_3)_3$, as evidenced by disappearance of N-O vibrational modes (1340 and 1440 cm^{-1}) after 5 min of UV exposure (Figure 3.6b). In contrast, films from $Al(NO_3)_3$ thermally annealed at 150 °C for up to 120 min still exhibit intense N-O stretching modes, indicating photolysis enhances nitrate decomposition over moderate thermal annealing conditions.

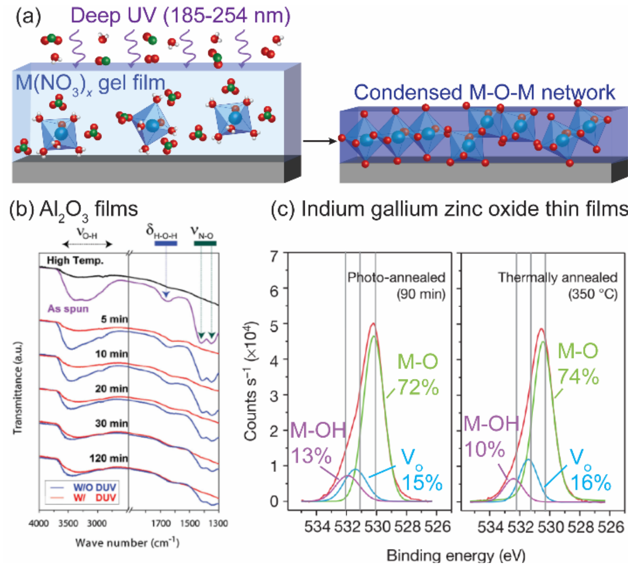

Figure 3.6. Photo-Annealing of Metal-Nitrate Gel Films. (a) Schematic of the photo-annealing reaction. UV light decomposes nitrates to various volatile NO_x products via photolysis. Photon energy from the UV source, as well as heat from operation of the UV lamp (~ 150 °C), facilitate condensation of $M(OH)_x$ to metal oxide. (b) FT-IR spectra of $Al(NO_3)_3$ films photo- and thermally-annealed (at 150 °C) as a function of irradiation/annealing time. IR active modes for nitrate are no longer visible after 5 min of photo-annealing (red), whereas nitrates are still present in thermally-annealed films (blue) after a 2 h annealing time. Reproduced with permission from Ref. 58. Copyright 2015 John Wiley & Sons. (c) Fitted O 1s XP spectra comparing the oxygen chemical environments present in photo- and thermally-annealed (350 °C) indium-gallium-zinc-oxide (IGZO) films. Photo-annealed films are chemically similar to films thermally-annealed at high temperature, which suggests photo-annealing is an effective low-temperature processing method for preparing IGZO with high metal oxide content. Reprinted with permission from Ref. 53. Copyright 2012 Nature Publishing Group.

Kim et al. demonstrated the effect of photo-annealing on IGZO films prepared from nitrate salts.[53] In this study, photo-annealed films were shown to have comparable metal-oxide content (determined by XPS) to films thermally annealed at 350 °C (Figure 3.6c). Similar optical band gaps ($E_g \approx 3.2$ eV) and higher average channel mobilities ($\mu \sim 9$ cm^2 V^{-1} s^{-1} compared to ~ 6 cm^2 V^{-1} s^{-1}) further confirm relatively high-performance metal oxides can be prepared at low temperature via this method. Mobilities of >30 cm^2 V^{-1} s^{-1} for photo-annealed In_2O_3 and IZO channel layers have since been reported.[54] Such improvements to device performance are attributed to O_3 production during photolysis,

which is suggested to mediate oxygen-vacancy formation in the resulting thin films, thereby reducing trap states.[62,63] The channel mobilities for photo-annealed films are comparable to (or even greater than) those achieved for aqueous, sol-gel, and combustion In_2O_3 films annealed at temperatures of 200 °C or higher, indicating photo-annealing is an effective low-temperature processing method for the preparation of high-quality electronic thin films (Figure 3.5).

Since these initial studies, photo-annealing has been used to prepare a variety of semiconductor and dielectric thin films for electronics,[58,64–66] as well as catalyst films for the oxygen-evolution reaction.[67] Aside from low metal-oxide formation temperatures, photo-annealing treatments have been correlated with increased film densification.[64,68] Denser films result in higher areal capacitance for dielectrics and higher carrier mobilities for semiconductors in TFTs. Additionally, photo-annealed films are observed to have low interfacial roughness due to improved wetting of subsequent layers, leading to a reduction of interfacial trap states.[58] Interestingly, films from flat-"Al_{13}" nanocluster precursors photo-annealed at 60 °C exhibit high breakdown fields (> 6 MV cm^{-1}) and respectable dielectric constants (κ = 8.37) in contrast to similarly-treated films from $Al(NO_3)_3$ precursor, which produce non-functional MIM devices at this annealing temperature.[69] Jo et al. suggest the pre-condensed M-O-M network and low counterion content in films from the "Al_{13}" precursor enable greater densification of the Al_2O_3 film (2.58 and 1.86 g cm^{-3} for "Al_{13}" cluster and $Al(NO_3)_3$ prepared films, respectively), which leads to improved insulating properties.

While there are numerous studies that utilize the photo-annealing method to prepare high-quality thin films, it is worth noting that nearly all systems studied to date are "low-T_d" metal nitrate salts. Thermal decomposition behavior has a strong

dependence on the metal cation identity, as discussed in chapter II. An interesting area of future work would involve studying the UV-susceptibility of “high-T_d” salts to determine if photolysis behavior exhibits a metal dependence similar to that observed for thermal decomposition.

Controlled-Atmosphere Annealing: the Role of Water Vapor in Film Formation

In addition to using different energy sources to initiate nitrate decomposition and metal-oxide formation, reactions of film components with atmospheric gases have also shown promise for lowering processing temperatures. Approaches include annealing under O_3, high pressure, and vacuum, which were discussed in depth in a recent review;[70] however, these annealing atmospheres are primarily used once the metal oxide has already formed, rather than to influence film formation chemistry. Here, we focus on the relatively underexplored water-vapor annealing process, which has been demonstrated to facilitate low-temperature film formation from a variety of solution precursors. For metal-alkoxide precursors, water facilitates removal of organic residues and improves metal-oxide conversion, resulting in high channel mobilities for In_2O_3-based TFTs (~ 30 $cm^2\ V^{-1}\ s^{-1}$).[71,72] A similar effect was reported for ZnO films from a $Zn(NH_3)_4^{2+}$ precursor.[73] A steady supply of water vapor is hypothesized to enhance the rate of hydrolysis of coordinating ligands by ensuring water does not become a not a limiting reagent as hydrolysis progresses. One study investigates the effect of water vapor on film formation from sol-gel (i.e. 2-methoxyethanol) metal-nitrate precursors; however, the authors do not comment on the reactions of nitrates with atmospheric water.[72]

We reported the effects of a water-vapor annealing atmosphere on films from all-inorganic aqueous precursors, which we refer to as the “steam-annealing” process.[7]

Advantages of steam annealing, compared to ambient "dry" annealing (~45% relative humidity at room temperature), are threefold: (1) enhanced nitrate removal at low annealing temperatures (< 200 °C), (2) improved resistance to water reabsorption, and (3) increased densification. The most striking reduction of nitrate content is observed in lanthanum zirconium oxide (LZO) films annealed at temperatures as low as 200 ºC.[7] We hypothesize nitrate removal is facilitated by maintaining the metal cation hydration sphere, thereby inhibiting the formation of $M-NO_3$ complexes, which require higher temperatures to decompose than "free" nitrates. Excess water also favors the removal of nitrate through the HNO_3/H_2O azeotrope (with a boiling point of 120 °C), offering an alternative pathway to thermal decomposition for "loosely-bound" nitrates. This hypothesis is supported by TPD-MS data, which shows a distinct difference in the annealing temperatures at which NO^+ decomposition fragments are observed, especially at temperatures below 400 °C (Figure 3.7a). Steam-annealed films are also resistant to post-processing water reabsorption, another indication of enhanced nitrate removal, as nitrates are hygroscopic. FT-IR spectra of steam- and dry-annealed films, collected immediately following annealing and again after 1 h in ambient, show significant water absorption for the dry-annealed film compared to the steam-annealed film (Figure 3.7b). A comparison of the N-O stretching region intensities in the FT-IR spectra further indicates that steam-annealed films contain fewer nitrates.

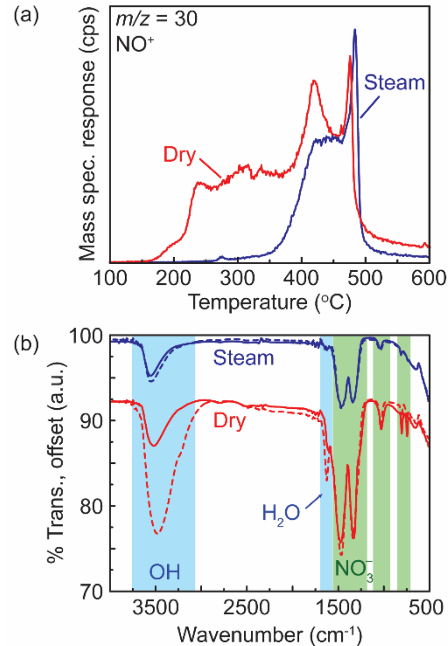

Figure 3.7 Chemical Analysis of Steam- and Dry-Annealed LZO Films. (a) Comparison of the NO^+ fragment (m/z = 30) desorption profile for dry- and steam-annealed LZO films (200 °C) shows a reduction in signal below 400 °C for the steam—annealed film compared to a dry-annealed film, indicating enhanced nitrate removal with steam annealing. (b) FT-IR spectra of LZO films annealed at 200 °C (solid lines), then left in ambient for 1 h (dotted lines). While dry-annealed films absorb water, as evidenced by the increased intensity of the OH stretching mode, steam-annealed films are moisture resistant. Data adapted from Ref. 7.

Enhanced nitrate removal via steam annealing enables improved densification. Cross-sectional scanning-electron-microscope (SEM) images confirm steam-annealed films are 15% thinner than dry-annealed films (Figure 3.8). Differences in film chemistry at or near the surface may influence densification processes. We hypothesize, for steam-annealed films, that water helps maintain surface hydroxyl groups, which allow for facile diffusion of HNO_3 and other decomposition byproducts out of the film (Figure 3.8a). In contrast, the surfaces of dry-annealed films are likely dehydrated, which may result in a dense surface layer that inhibits diffusion of nitrate decomposition byproducts to the film surface, resulting in thicker, lower-density films (Figure 3.8b).[74,75]

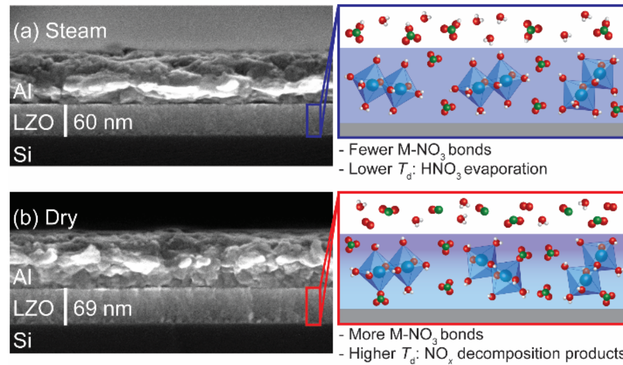

Figure 3.8 Improved Densification of Steam-Annealed Films. SEM images of (a) steam- and (b) dry-annealed films. The schematics show the different decomposition products that are hypothesized to form under each atmosphere (i.e. HNO_3 from steam-annealing and NO_x gases from dry-annealing), as well as the formation of a dense surface layer (indicated by the dark blue region at the film surface) in dry-annealed films, which we hypothesize inhibits densification.

The benefits of steam annealing on film composition and morphology led to higher dielectric constants (κ) for LZO films in metal-insulator-semiconductor (MIS) devices. The κ for MIS devices prepared from 500 °C dry-annealed films is comparable to that of 350 °C steam-annealed films (κ = 15 at 1 kHz). Notably, MIS devices prepared from 200 °C dry-annealed films are nonfunctional dielectrics, while steam-annealed films fabricated at the same temperature exhibit modest dielectric constants (κ = 11 at 1 kHz). In contrast to our reports of improved device performance for steam-annealed dielectrics, a previous study reported a degradation in the dielectric response of Al_2O_3 with increased relative humidity (RH) of the annealing environment ($Al(NO_3)_3$ precursor).[76] Devices prepared from films annealed in a 0% RH environment experience lower leakage currents and higher breakdown voltages than those annealed in a 60% RH atmosphere. A similar effect was observed for In_2O_3 channel mobility as the RH of the annealing atmosphere was increased. The authors suggest high humidity inhibits condensation by favoring metal hydroxyl species in the metal hydroxide/oxide equilibria. However, the films characterized in this study were of noticeably poor morphology. Optical microscope

images show increasing defects on the film surface as RH is increased, likely due to water droplets disturbing the film surface. High surface roughness is known to negatively impact TFT performance, and a roughness as small as a few nanometers has been shown to decrease field-effect mobility up to an order of magnitude.[77–79] For this reason it is critical to completely aerosolize and evaporate water for steam-annealing studies, as is done in our work, in order to avoid degrading film morphology in a water-vapor atmosphere.

Bridge

Chapter III reviewed different metal-nitrate decomposition chemistries induced by common thin-film treatment methods. These methods influence thin-film properties by changing the thin-film reaction pathway. Chapter IV builds upon the discussion of combustion chemistry and elucidates the role fuels play in thin-film formation chemistry.

CHAPTER IV.

ROLE OF COMBUSTION CHEMISTRY IN LOW-TEMPERATURE DEPOSITION OF METAL OXIDE THIN FILMS FROM SOLUTION

Authorship Statement

This chapter was previously published as a full article in *Chemistry of Materials*, **2017**, *29*, 9480-9488 and was coauthored by Elizabeth A. Cochran, Deok-Hie Park, Matthew G. Kast, Lisa J. Enman, Cory K. Perkins, Ryan H. Mansergh, Douglas A. Keszler, Darren W. Johnson, and Shannon W. Boettcher. The manuscript was written by E.A.C. with contributions from D.-H.P., M.G.K., L.J.E., C.K.P., and R.H.M. Editorial assistance was provided by D.A.K., D.W.J., and S.W.B. Experiments were performed by E.A.C., D.-H.P., and L.J.E. All authors participated in data analysis.

Introduction

Metal-oxide thin films are broadly employed in modern (opto)electronic devices,[1–7] with applications ranging from nano-scale transistors to large-area flat-panel displays and photovoltaics. Demand for inexpensive, environmentally benign, and large-area deposition technologies has led to a surge in solution-processed thin-film research as an alternative to vacuum-based deposition. Solution processing offers the possibility of high-throughput deposition, e.g., by roll-to-roll,[8,9] spray,[10] spin,[10,11] or slot-die[11] coating, under atmospheric conditions.

Many researchers have focused on reducing the thermal budget for metal oxide formation, i.e., to 100-300 °C, so that high-quality thin films can be deposited on low-melting point, polymeric substrates for flexible electronics applications.[12,13] We

previously reported on the design of aqueous precursor inks for ZnO[14] and F-doped SnO_2[15] thin films that form oxides at low annealing temperatures (≤ 150 °C). Park et. al. used deep UV irradiation for photochemical nitrate decomposition in as-spun sol-gel films to form In_2O_3 and indium gallium zinc oxide (IGZO) with electrical characteristics comparable to films thermally annealed at 350 °C.[16] Other low-temperature annealing techniques have also shown promise, e.g., humid atmosphere,[5] ozone,[17] and microwave treatments.[18] In most cases, solution-processed films still exhibit poor electronic properties compared to vacuum-deposited films, but the gap is closing.[19,20] To overcome barriers to improved performance, we seek to understand the chemical mechanisms of thin-film formation from solution precursors, specifically those induced by low-temperature processing treatments.

Beyond the above approaches, studies of "combustion processing" have shown the formation of metal-oxide films at low temperatures.[21–23] Such reactions for the synthesis of bulk oxide powders have been well studied.[22] Relying on a highly exothermic reaction between a metal-salt oxidant (e.g., a metal nitrate) and an organic-fuel reductant (e.g., acetylacetone, urea, etc.), high local temperatures, produced via the ignition and self-propagation of a combustion front, are responsible for metal oxide formation.[22,24] Combustion syntheses are typically self-contained systems of oxidizer and fuel that do not require an oxidative atmosphere to ignite. The extension of combustion processing to thin-film synthesis was first studied with combinations of $In(NO_3)_3$, $Zn(NO_3)_2$, and $SnCl_2$ (+ NH_4NO_3) and organic fuels (acetylacetone and urea).[23] Combustion in the bulk was confirmed by thermogravimetric analysis (TGA).[23] The technique has since been applied to the synthesis of many metal-oxide films.[25–31]

While many studies[32–46] describe combustion strategies to reduce the processing temperatures of solution-processed films, the fundamental chemical aspects of the process are poorly understood. Thermal analysis is typically performed on bulk precursors in which thermal and mass transport may be substantially different than in nanoscale thin films. Some studies have utilized conventional TGA techniques to probe the thin film reaction pathway and concluded that signatures of combustion cannot not be detected in thin films.[47–49] However, direct observation of combustion by thermal analysis techniques traditionally used for bulk materials is difficult in thin-film samples because of the need to measure small thermal changes. Additionally, such studies provide minimal information about the underlying thin-film formation reactions. Discrepancies related to the role of fuel additives in solution-processed thin-film chemistry warrant further study to elucidate potential differences between bulk and thin-film processes.

Here, we examine the thermal decomposition behavior, chemical composition, and chemical structure of bulk powders and thin films prepared from several combustion precursors. We choose acetylacetone and two nitrate salts, $In(NO_3)_3$ and $Y(NO_3)_3$, as model fuel and oxidizer systems, respectively, due to their prevalence as auto-combustion precursor components for semiconductor and dielectric thin films.[21,23,25,33–40,45] The efficacy of urea, another commonly-used fuel in thin-film combustion synthesis,[23,32,40,41] was also investigated (Figures A.22-A.26). Due to concerns about the high volatility and low decomposition temperature of acetylacetone and urea, respectively, we also examine glycine, a fuel with comparatively low volatility, with $Mg(NO_3)_2$ as the oxidizer source. This precursor could be used to prepare MgO films for protective coatings,[50] as well as components of dielectric[51] and semiconductor[52] layers in thin film transistors.

In addition to their relevance in device applications, we are specifically interested in the chosen model precursor systems due to their differing oxidizer and fuel chemistries. While the prevalence of the $In(NO_3)_3$-acetylacetone mixture as a combustion precursor for In_2O_3 films warrants a detailed investigation in the present study,[21,25,35,37,38] the low decomposition temperature of $In(NO_3)_3$ alone ($T_d \approx 250$ °C) makes identification of possible combustion events with fuel occurring at ~200 °C challenging. In contrast, high temperatures ($T_d \approx 500$ °C) are needed to fully convert pure $Y(NO_3)_3$ to Y_2O_3, making this an ideal model system for decoupling thermal decomposition and combustion events. We know the $Mg(NO_3)_2$-glycine precursor to undergo a highly exothermic combustion reaction in the bulk[53] and, while no studies of film preparation from this precursor have been performed to date, glycine has been utilized extensively in bulk solution combustion synthesis of many metal oxides,[22] as well as for the preparation of NiO thin films.[54]

We seek the chemical signatures of ignition and combustion in films by probing chemical transformations of the films themselves, rather than relying on bulk characterization. From measurements made directly on thin film samples, we discover reaction processes that appear not to include combustion – even when combustion reactions are readily observed in the corresponding bulk samples for the model systems we study here. These results therefore call into question the underlying assumptions of the thin film combustion process.

Experimental

Precursor Solution Preparation

Precursors for films made from $In(NO_3)_3 \cdot 5.3H_2O$ (Sigma-Aldrich, 99.9%) and $Y(NO_3)_3 \cdot 6H_2O$ salts (Johnson Matthey, Inc., 99.9%) were prepared at 0.2 M metal concentration in 5 mL of 2-methoxyethanol (Sigma-Aldrich, 99.8%). All salts were used as received from the manufacturer. All fuel-containing precursors were prepared as previously described.[23] Acetylacetone ($C_5H_8O_2$; Sigma-Aldrich, ≥ 99 %) was added in a 1.5:1 NO_3^- to fuel molar ratio (0.2 mL acetylacetone). Approximately 120 µL NH_4OH (EMD Millipore, ACS reagent) was added to the acetylacetone solutions to raise the pH and facilitate $M(acac)_x$ (acac = $C_5H_7O_2^-$) formation. The solutions were aged for 12 h. The $Mg(NO_3)_2$ precursors were prepared by dissolving $Mg(NO_3)_2 \cdot 6H_2O$ (J.T. Baker, 98.7%) in 18.2 MΩ·cm H_2O at 1.2 M metal concentration. For the combustion precursor, glycine ($C_2H_5NO_2$; OmniPur) was added to the $Mg(NO_3)_2$ solution in a 1.8:1 NO_3^--to-glycine molar ratio.[53] (*Caution: This solution explodes violently when heated to its ignition temperature. Use proper precautions when handling and processing this solution.*)

Chemical and Structural Analyses of Bulk Precursors

Samples containing fuels were prepared by evaporating solvent on a Schlenk line under reduced pressure to ensure atomic level mixing of the precursor components. For the controls without fuels, the hydrated salts were used as received by the manufacturer. Thermal analysis studies were performed using thermogravimetric analysis (TGA) and stepwise heating in order to identify expected ignition temperatures for films. For TGA, 10-20 mg of the dried precursors were heated at a 10 °C min^{-1} ramp rate under air flow

(20 mL min^{-1}) in Al sample pans from room temperature to 600 °C (TA Instruments Q500). For stepwise heating, the dried precursors (~ 50 mg) were placed on a Si wafer and the samples were annealed in approximately 50 °C temperature steps from 50 °C to 290 °C (5 min anneal at each temperature) and masses were measured using an analytical balance. The combustion byproducts were physically contained on the Si wafer substrate by placing a glass beaker over the top of the samples.

For all other powder characterization, the dried gels or salts were annealed for 30 min at least 15 °C above the combustion ignition temperature (T_{ig}) that was identified using TGA (~ 215 °C for acac mixtures, 300 °C for the $Mg(NO_3)_2$-glycine mixture). X-ray photoelectron spectroscopy (XPS) was used to quantify and compare metal oxide and nitrate content in powders and films. Measurements were performed using a ThermoScientific ESCALAB 250 instrument with a monochromatic (150 W, 20 eV pass energy, 500 μm spot size) Al Kα X-ray source. An in-lens electron flood gun was used for charge neutralization. Spectra were analyzed and fit using ThermoScientific Avantage 5.94 software (see Appendix A for additional fitting details). The binding energies were calibrated using the C-H peak for adventitious carbon in the C 1s spectrum at ~ 284.8 eV. X-ray diffraction (XRD) data were collected on a Rigaku SmartLab diffractometer (Cu Kα source, λ_{avg}= 1.5418 Å, Ni foil Kβ filter) with a step size of 0.1° and an integration of 30 s at each step. The line detector (D/teX Ultra 250) was swept in a Bragg-Brentano geometry. Crystalline domain sizes for the oxide powders were calculated using Scherrer analysis.[55] Peak fitting was performed using Rigaku PDXL2 software[56] and corrections were made to account for instrumental broadening. Instrumental broadening at $2\theta = 30°$, determined using a bulk In_2O_3 powder (Alfa Aesar, 99.99% purity; 325 mesh), is 0.185°

(or 0.0032 rad) and, for a bulk Y_2O_3 powder (Alfa Aesar, 99.999% purity; 5 μm particle size) is 0.225° (or 0.0039 rad) at 2θ = 29°.

Thin Film Preparation

All films were prepared via spin coating. Si substrates (Silicon, Inc. for single-side-polished; WRS Materials for double-side-polished) were sonicated in an aqueous 5% Contrad 70 solution (Decon Laboratories) for 10 min, spin-rinsed clean with 18.2 MΩ·cm H_2O, and O_2/N_2 plasma-cleaned for 5 min prior to film deposition. The precursor solutions were deposited onto the substrate through a syringe fitted with a 0.2 μm filter and then the substrate was spun at 3000 rpm for 30 s. For composition and structure characterization, films were annealed for 30 min at least 15 °C above T_{ig}. At these annealing temperatures, the film thicknesses range from approximately 20 to 50 nm, depending on the metal nitrate system used (see XRR results in Figure A.28 and Table A.1). These film thicknesses are well within the range of thicknesses reported for films prepared from combustion precursors (10-400 nm).[23,25–46]

Chemical and Structural Analysis of Thin Films

Thermal analysis was performed using a quartz crystal microbalance (QCM) to monitor mass changes in thin-film samples. Films were deposited on Au-coated quartz crystals (Stanford Research Systems) and annealed at 50 °C for 5 min. Impedance analysis was performed using a potentiostat (BioLogic SP200) by applying a 10-mV amplitude driving voltage with a 0 V DC offset and sweeping over a short frequency range (6000 Hz to achieve good resolution) to measure the crystal resonant frequency. The resonant frequency was identified by the frequency at the maximum conductance in

a plot of the real conductance (G) versus frequency (f).[57] The Sauerbrey equation,[58] $\Delta f = -C_f \times \Delta m$, where Δf is the frequency change (Hz), C_f is the crystal sensitivity factor (58.3 μg^{-1} cm^2),[59] and Δm is the mass change per unit area (μg cm^{-2}), was used to calculate changes in film mass. Films were annealed in approximately 50 °C temperature steps for 5 min at each temperature (T_i = 50 °C, T_f = 290 °C) and impedance spectra were collected after each annealing step. All impedance spectra were recorded ex situ at room temperature as the QCM measurement is not compatible with high temperature due to a temperature-dependent frequency response. The upper annealing temperature for QCM mass loss studies was limited to 290 °C, as the crystals are prone to thermal shock that results in cracking when heated to temperatures greater than 300 °C.

Chemical and structural analyses on films were performed using XPS and XRD. Grazing incidence (GI) scans were collected using a scintillation point detector (the incident X-ray beam was at 0.5° relative to sample plane). Scherrer analysis was performed on samples with crystalline oxide character to provide an estimate of crystallite size, acknowledging the difficulty of applying Scherrer analysis in the GI geometry. Corrections for instrumental peak broadening were thus not applied to data obtained from thin films.

Temperature-programmed desorption mass spectrometry (TPD-MS) was used to detect the byproducts of film formation. These experiments, conducted under ultrahigh vacuum (UHV), were performed using a TPD Workstation (Hiden Analytical) with a quadrupole mass analyzer (3F PIC, Hiden Analytical). The base pressure was $< 5 \times 10^{-9}$ Torr. One coat of each solution was deposited (3000 rpm, 30 s) onto a 100 nm thermally grown SiO_2 substrate and loaded into the vacuum chamber. The thin-film samples (1×1 cm^2) were heated from 25 °C to 625 °C at a rate of 10 °C min^{-1}. Electron ionization (EI)

mass spectra were acquired with a 70-eV ionization energy and 20 μA emission current. Selected mass-to-charge (*m/z*) ratios for each sample were monitored in multiple ion detection (MID) mode with a dwell time of 500 ms and a settle time of 50 ms.

To evaluate the effect of fuel incorporation on film quality, thickness and morphology studies were conducted using atomic force microscopy (AFM), scanning electron microscopy (SEM), and X-ray reflectivity (XRR). These data can be found in Figures A.27 and A.28 and Table A.1, along with corresponding experimental details and imaging parameters.

Results and Discussion

Comparing Thermal Behavior of Bulk Powders and Thin Films: TG and QCM analyses

A representative, idealized chemical equation for combustion between acac and trivalent metal nitrates is shown in eq 4.1. The precursor prepared for this study is best described as a partial metal acetylacetonate complex with non-coordinating nitrate counterions.

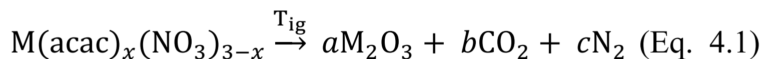

$$\mathrm{M(acac)}_x(\mathrm{NO_3})_{3-x} \xrightarrow{\mathrm{T_{ig}}} a\mathrm{M_2O_3} + b\mathrm{CO_2} + c\mathrm{N_2} \quad \text{(Eq. 4.1)}$$

We can identify combustion events using thermal analysis techniques by a sudden, (nearly) complete mass loss at a specific ignition temperature (T_{ig}), which signifies precursor conversion to the resulting metal oxide. Due to the intrinsically-small volume of nanoscale thin-film samples, it can be difficult to reliably measure film composition and properties by common bulk characterization methods. When direct comparisons between bulk and thin film materials are not feasible, we use the most-similar techniques available. For example, we monitor the thermal behavior of thin films via QCM, which has previously been used to characterize mass loss as a function of annealing temperature

on solution-processed metal oxide thin films,[15,60] in place of conventional TGA. Because the ramp rates of TGA and QCM are different, we also treat bulk powders using the same heating profile as the films to show combustion is not inhibited by stepwise heating and, therefore, combustion events should be similarly identifiable for bulk powders and thin films using this temperature profile (5 min anneal at each temperature step). For the bulk samples, we confirm which mass loss steps are associated with combustion through visual observation of combustion flames and/or explosions. We observe the $In(NO_3)_3$-acac and $Y(NO_3)_3$-acac bulk gels undergo combustion after the 200 and 250 °C annealing steps, respectively (Figure 4.1a-b). This is largely consistent with $T_{ig} \approx 200$ °C observed by constant ramp rate TGA (Figure 4.1a-b). For the bulk $Y(NO_3)_3$ without acac, mass loss occurs more gradually with increasing annealing temperature, consistent with no combustion events occurring. Interestingly, the $In(NO_3)_3$ powder itself shows rapid mass loss near 200 °C, indicating the thermal instability of this precursor in the absence of any fuel additive (Figure 4.1a). The $Al(NO_3)_3$ precursors also undergoes similar low-temperature thermal decomposition with and without fuel additives (Figure A.20).

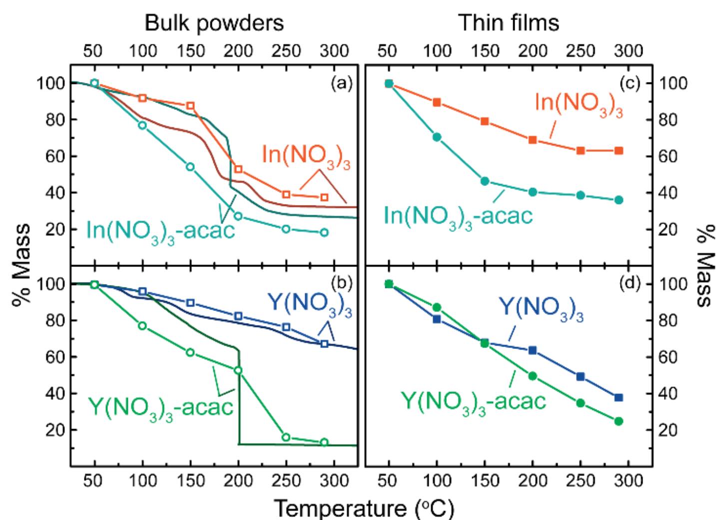

Figure 4.1. Thermal analysis on (a-b) bulk powders and (c-d) thin films from $In(NO_3)_3$ and $Y(NO_3)_3$ precursors. Bulk powders are shown in open markers, thin films in closed markers, and the darker solid lines are TGA curves (10 °C min^{-1} ramp rate). TGA curves for bulk powders covering the full temperature range investigated (up to 600 °C) can be found in Figure A.1. Each powder and film prepared from the same precursor appears in the same color. Combustion ignition temperatures for bulk powders of ~200 °C are in good agreement with ignition events observed when step-wise heating was used.

In contrast to the bulk combustible gels, QCM measurements show most of the films experience gradual mass loss as the annealing temperature is increased and continue to lose mass at $T > T_{ig}$, which is inconsistent with combustion (Figure 4.1c-d). For the film prepared from $In(NO_3)_3$-acac, rapid mass loss occurs from 50 to 150 °C (Figure 4.1c). However, we do not attribute this to combustion, as FT-IR measurements on films treated using the same thermal profile show IR active modes for acac disappear before the nitrate modes and the nitrate absorbance features decrease monotonically with annealing temperature (Figure A.2). Therefore, we hypothesize that acac and nitrate experience independent thermal decomposition in the films and likely do not combust. The possible mechanisms of film formation are discussed in more detail below (see "The Reaction Pathway of Thin Films: Monitoring Reaction Byproducts"). The fact that the powders clearly undergo combustion (i.e. experience abrupt mass loss due to a

combustion explosion) and films prepared from the same precursors gradually lose mass with increased annealing temperature suggests that the two systems experience different reaction pathways.

Chemical Composition and Structure of Bulk Powders and Thin Films

The success of a combustion reaction can be determined through the detection/quantification of metal oxide content (Eq. 4.1). Due to high local temperatures produced by combustion front ignition, the resulting product should exhibit enhanced oxide conversion compared to a metal nitrate salt thermally treated at the same temperature. Local temperatures at the combustion front in bulk samples can reach over 1000 °C[22] (depending on the oxidizer-fuel mixture used), which can provide sufficient energy to crystallize the oxide. Here, we compare the chemical composition and structure of powders and film samples prepared from metal nitrate and acac mixtures treated at $T > T_{ig}$.

We chose the $Y(NO_3)_3$ precursors as a model system for detailed XPS analysis of the films and powders. Since combustion of $Y(NO_3)_3$-acac and complete thermal decomposition of $Y(NO_3)_3$ occur at 200 and 500 °C, respectively, (Figure A.1) these two chemical events should result in different compositions that are distinguishable by XPS. To identify and quantify the oxygen environments, we fit the O 1s spectra for all films and powders prepared from $Y(NO_3)_3$ precursors. A comparison of the powder and film prepared from the same $Y(NO_3)_3$-acac precursor, annealed at the same temperature (~ 215 °C) above T_{ig}, show differences in their oxide content (Figure 4.2). While the film contains 0.1 metal oxide bonds per Y atom at the film surface (determined by comparing the integrated intensities of O 1s peak associated with Y-O to that of the Y 3d peak in the

XP spectra), the powder contains 0.8 metal oxide bonds per Y atom (Table 4.1). The films prepared with and without acac have similar metal oxide content of 0.1 and 0.2 oxide bonds per Y, respectively, whereas the powder from $Y(NO_3)_3$ does not have any measurable metal-oxide character. Additionally, both films prepared with and without acac contain approximately 1 nitrate per Y (determined by comparing the integrated intensities of the nitrate peak in the N 1s to that of Y 3d in the XP spectra), which is comparable to the 1.6 nitrates per Y present in the $Y(NO_3)_3$ powder without acac (Table 4.1).

The above results show that thermal treatment just above T_{ig} results in different products for films and powders when fuel is present. Low oxide and high nitrate content suggests combustion does not occur in the films from $Y(NO_3)_3$ precursors. Films prepared from the two $In(NO_3)_3$ precursors (with and without fuel) show equally efficient conversion to In_2O_3 and only trace nitrate content is detected in either case (Table 4.1). These data indicate that combustion is not necessary to decompose $In(NO_3)_3$ at low temperature, as $In(NO_3)_3$ alone readily decomposes by 200 °C (Figure A.1). All XP spectra for powders and films prepared from $Y(NO_3)_3$ and $In(NO_3)_3$ precursors can be found in Figures A.3-A.6 and A.7-A.8, respectively. The Mg XPS data is discussed below (see *Magnesium Nitrate and Glycine: A Low-Volatility Fuel as a Combustion Model System*).

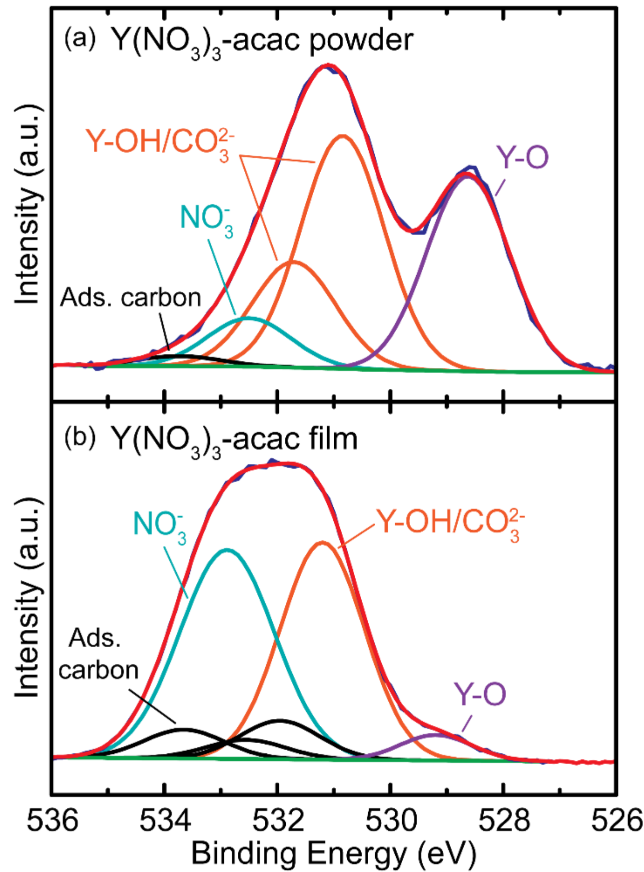

Figure 4.2. Fits of O 1s XP spectra for a (a) powder and (b) film prepared from the $Y(NO_3)_3$-acac precursor annealed above T_{ig} (~ 215 °C). Each plot contains raw data (dark blue), total fitted peak envelope (red), metal oxide peaks (purple), hydroxide and carbonate peaks (orange), nitrate peaks (teal), adsorbed carbon-oxygen species (black), and background (green).

Table 4.1. Complied XPS results for all powders and films prepared from combustion precursors and their corresponding control samples.

Precursor	Sample type	Oxide bonds per metal	Nitrates per metal
$Y(NO_3)_3$-acac	powder	0.8	0.1
	film	0.1	0.9
$Y(NO_3)_3$	powder	0	1.6
	film	0.2	1.0
$In(NO_3)_3$-acac	film	1.1	0
$In(NO_3)_3$	film	1.2	0
$Mg(NO_3)_2$-glycine	film	0.4	0.3
$Mg(NO_3)_2$	film	0.2	0.2

* Ratios are calculated using the percent of metal oxide, nitrates, and metal ions at the sample surface using integrated peak areas from the O 1s, N 1s, and metal spectra (Y 3d, In 3d, and Mg 1s), respectively. The In- and Y- containing films were annealed at 215 °C for 30 min, the Mg-containing films at 300 °C for 30 min.

The crystalline phases observed for the bulk and thin-film samples provides further insight into the effect of fuel additives on film structure. XRD patterns for all the bulk powders prepared with fuel contain oxide phases when heated above T_{ig} (Figure 4.3a-b). The powder prepared from the $In(NO_3)_3$-only precursor produces In_2O_3 with an average domain size of ~ 34 nm, with some remaining nitrate impurities, whereas the average particle size for the powder prepared from the $In(NO_3)_3$-acac precursor is ~ 84 nm (Figure 4.3a). The larger particle size observed for the bulk product from $In(NO_3)_3$-acac is consistent with a combustion reaction resulting in improved crystallinity compared to thermal decomposition. Grazing incidence diffraction patterns of the films

prepared from $In(NO_3)_3$ and $In(NO_3)_3$-acac precursors annealed at the same temperature show the cubic In_2O_3 phase, with grain sizes of < 1 nm and ~ 3.5 nm, respectively (Figure 4.3c). XPS measurements show acac does not lead to improved oxide conversion (Figure A.7 & A.8) and, therefore, it does not appear differences in particle size in the films are due to combustion. However, different ligands/counterions are known to experience different rates of hydrolysis/condensation,[61] which may affect crystallite size.

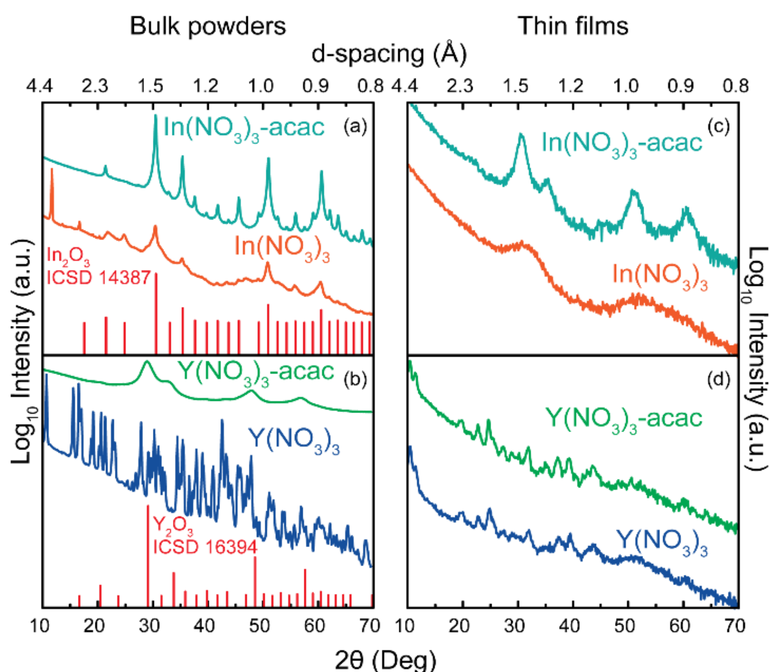

Figure 4.3. XRD patterns for (a-b) powders and (c-d) films prepared from $In(NO_3)_3$ and $Y(NO_3)_3$ precursors. All powder and films received the same heat treatment at $T > T_{ig}$ (~ 215 °C). While all bulk powders and films prepared from $In(NO_3)_3$ show diffraction from In_2O_3, only the powder from $Y(NO_3)_3$-acac shows diffraction from Y_2O_3. Films prepared from $Y(NO_3)_3$ precursors instead contain a layered (oxy)hydroxide phase.

For the $Y(NO_3)_3$ bulk precursors heated above T_{ig}, diffraction from the $Y(NO_3)_3$-only sample is consistent with a hydrated yttrium nitrate phase ($(Y(H_2O)_4)(NO_3)_3(H_2O)$; ICSD 31872), whereas Y_2O_3 (4.5 nm average grain size) is observed for the powder prepared from the $Y(NO_3)_3$-acac gel (Figure 4.3b) – consistent with combustion driving oxide formation at low applied temperatures in the bulk. For the thin-film samples, Figure 4.3d shows that only poorly-crystalline yttrium oxyhydroxide nitrate ($Y_6O(OH)_8(NO_3)_6(H_2O)_{12}(NO_3)_2(H_2O)_2$; ICSD 170885) is formed regardless of the presence or absence of acac. This result, in addition to XPS, suggests the heat needed to drive oxide formation at low applied temperatures is not produced in the model yttrium-containing thin films.

The Reaction Pathway of Thin Films: Monitoring Reaction Byproducts

Composition and structure analysis show that, in the case of the $Y(NO_3)_3$-acac precursor, bulk and film products are different. While these results indicate the final film products are not consistent with a combustion reaction, the thin-film reaction pathway is still unknown. In order to elucidate the chemical reactions taking place in films, we monitored the evolution of reaction byproducts as a function of annealing temperature using TPD-MS. As a comparable bulk technique, we identify fragments associated with thermal decomposition and combustion of the corresponding bulk materials by TGA-MS (Figure A.9). While TPD-MS experiments must be performed in ultra-high vacuum, combustion reactions should still occur, as they rely on an internal mixture of oxidizer and fuel without the presence of oxidative gases.

We, again, consider the $Y(NO_3)_3$ system in detail here. When combustion occurs in bulk powders, all nitrate and fuel components volatilize simultaneously over a

narrow temperature range of ~ 50 °C near T_{ig} (~ 200 °C), as identified by TGA-MS (Figure A.9b). For the $Y(NO_3)_3$ powder, which cannot undergo combustion, nitrate loss occurs over a large range from 350-600 °C (Figure A.9a). Similar differences in desorption temperatures would be expected for films when studied by TPD-MS if the same combustion and thermal decomposition reactions occur.

We use the NO^+ (m/z = 30) fragment to monitor nitrate removal from the film, which is known to be the primary fragment associated with nitrate decomposition produced by electron ionization (EI).[62,63] The majority of nitrates are removed from the $Y(NO_3)_3$-only film from 250-550 °C (Figure 4.4). For the $Y(NO_3)_3$-acac film, NO^+ is detected from ~ 75 to 550 °C (Figure 4.4). We speculate the presence of acac may alter the film reaction pathway at low temperature by aiding in the removal of some nitrate counterions as HNO_3, which could be accomplished through the donation of H^+ when $M(acac)_x$ complexes form (Figure A.10 and A.11 with additional discussion). The molecular fragment of the acac ligand (m/z = 99 for $C_5H_7O_2^+$) is detected from ~ 75-200 °C (Figure A.10d). Due to the apparent low-temperature removal of at least of portion of the acac in the film, as well as NO^+ detection above 500 °C for both films, we conclude that acac does not lower the temperature of nitrate removal from $Y(NO_3)_3$ films in a manner consistent with a combustion reaction. If combustion were occurring, acac removal would be coincident with nitrate removal and occur over a narrow temperature range, as was observed by TGA-MS for the bulk powders (Figure A.9). We suspect acac loss from the film at low temperature is facilitated by fast mass transport through the nanometer-thick films, whereas mass transport through bulk powders must be slower in comparison, as combustion is clearly observed in the bulk.

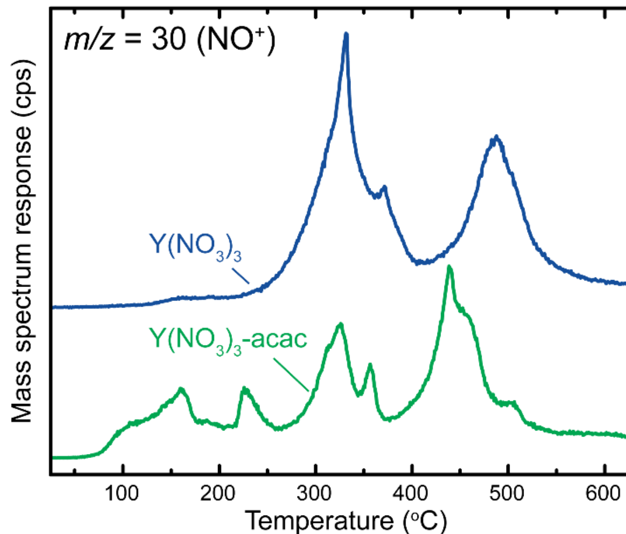

Figure 4.4. A comparison of the NO^+ fragment (m/z=30) detected by TPD-MS for films prepared from $Y(NO_3)_3$ precursors. While some differences are observed at low temperatures (~ 75-250 °C), the upper temperature of NO^+ removal (~ 550 °C) is largely unchanged in the presence of the acac fuel. For more fragment traces and detailed discussion, see Figure A.10.

Magnesium Nitrate and Glycine: A Low-Volatility Fuel as a Combustion Model System

The acac fuel is removed from the thin films at low temperature, as demonstrated in films prepared from $Y(NO_3)_3$-acac and evidenced by FT-IR (Figure A.2) and TPD-MS (Figure A.10). Therefore, it is a reasonable hypothesis that acac loss from the film below T_{ig} may contribute to the lack of observed combustion. Glycine, which has low volatility (melting/decomposition point = 233 °C,[64] compared to acac which has a boiling point of 140 °C), is another commonly-used fuel in bulk combustion syntheses,[22,65–67] and has been commonly combined with $Mg(NO_3)_2$ to produce MgO.[53,66] Thus, fuel losses prior to T_{ig} should be minimal, thereby preserving the solution composition in the film. The bulk system is explosive upon ignition and combustion occurs at $T_{ig} \approx 230$ °C as determined by bulk TGA (Figure A.12). Decomposition byproducts, composition, and structure data for the glycine system can be found in Figures A.13-A.19.

Fitting of the O 1s spectra for the two films shows the film prepared with glycine has a slightly higher metal oxide content, with 0.4 oxide bonds per Mg, compared to 0.2 for the film prepared from $Mg(NO_3)_2$ alone (Figure 4.5 and Table 4.1). However, both films, prepared with and without glycine, have comparable nitrate content, with 0.2 and 0.3 nitrates per Mg, respectively. Additionally, glycine is detected in the N 1s spectrum (Figure A.15), which, along with considerable nitrate content, suggests the small increase in oxide conversion observed for the $Mg(NO_3)_2$-glycine film is likely not a result of combustion. FT-IR spectra monitoring film composition as a function of annealing temperature corroborate the XPS results, showing glycine persists in the film even after a 400 °C anneal, whereas nitrates are no longer detectable (Figure A.16). TPD-MS results suggest that, even without combustion, glycine incorporation may lead to some changes the film reaction pathway (Figure A.18).

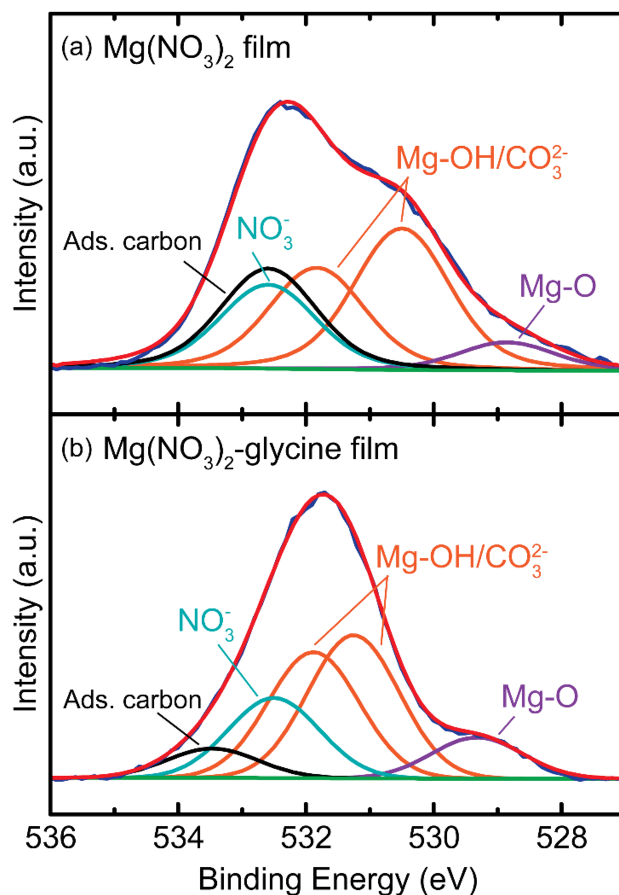

Figure 4.5. O 1s spectra for films prepared from (a) $Mg(NO_3)_2$ and (b) $Mg(NO_3)_2$-glycine precursors. The adsorbed carbon peak in (b) likely contains contributions from glycine. While the film prepared from $Mg(NO_3)_2$-glycine contains greater metal oxide content than the $Mg(NO_3)_2$ film, it also contains more nitrates, which suggests combustion has not occurred.

The Role of Fuels in Thin-Film Synthesis

While we observe combustion in the bulk metal nitrate-fuel systems studied, this oxide-forming reaction does not appear to translate to thin films for our oxidizer-fuel model systems. Our observations are consistent with thermal analysis comparisons of bulk and film samples in the literature,[47–49] but inconsistent with the conclusions of many other reports.[23,25–46] Films and devices fabricated from combustion precursors are often compared to those synthesized from sol-gel precursors prepared from metal chloride[68–70]

and acetate[70,71] salts. Chloride and acetate salts decompose at higher temperatures than metal nitrates[61,72] and thus are expected to have worse electrical characteristics when their corresponding films are prepared at low temperature. Control films we deposited from metal nitrate precursors alone show that improved low-temperature metal oxide formation is not achieved via the addition of fuel. By directly monitoring thin-film chemical decomposition and inferring their reaction mechanisms using FT-IR and TPD-MS, we find no evidence for combustion reactions in thin films prepared from $In(NO_3)_3$-acac, $Y(NO_3)_3$-acac, or $Mg(NO_3)_2$-glycine precursors.

Previous thin-film thermal analysis reported for the $In(NO_3)_3$-acac mixture shows no evidence of a combustion event by traditional TGA in films as thick as 400 nm.[47] The authors attribute the absence of combustion to the inability of the thin film to support and propagate a combustion front due to rapid heat exchange between the film and substrate, as well as the film and air, that is a result of their high surface area and small volume. This hypothesis is supported by analytical expressions that describe the heat propagation requirements to achieve thermal runaway (i.e. a combustion explosion) in bulk and thin-film geometries.[73] The solutions describe the conditions needed for thin-film combustion as requiring a substrate temperature of approximately 1200 K and a 10^7 K min^{-1} ramp rate in order to combust a 1 μm-thick film. Therefore, lack of thermal insulation, which is present in densely-packed, bulk material, is likely the primary reason combustion ignition is not readily achieved in thin films. Common metal salt precursors thermally decompose at much lower temperatures than that apparently needed for combustion to occur in thin films.

Through direct measurements of thin-film composition, structure, and reaction byproducts, we propose new descriptions of the film formation reaction pathways. We

observe larger nanocrystalline domain sizes by XRD in In_2O_3 films prepared with acac and hypothesize that fuels may aid in low-temperature counterion removal via HNO_3 formation, based on fragments observed by TPD-MS. Nonetheless, the incorporation of fuels in thin-film solution precursors does not appear to reduce metal oxide processing temperatures through combustion for the model systems investigated in this study.

Conclusions

Thermal and chemical analyses of thin-film precursors for In_2O_3, Y_2O_3, and MgO, both with and without fuel additives, have been performed to elucidate differences in the reaction pathways of powder and thin-film samples. XPS studies show that bulk powders prepared with fuels (heated at $T > T_{ig}$) contain metal oxide character, consistent with combustion, whereas thin films do not, with the exception of the $In(NO_3)_3$ film systems. This is explained by the fact that $In(NO_3)_3$ alone thermally decomposes at $T < T_{ig}$ and, therefore, fuel is not needed to obtain oxide films at low temperature. This study therefore illustrates that bulk and thin-film chemical processes are different and that combustion does not occur in the thin-film systems studied. Because thin-film chemistry is distinct and complex, greater effort should be directed to in situ elucidation of reaction pathways to improve understanding of film formation.

Bridge

Chapter IV elucidated the role of combustible fuels in metal-oxide thin-film formation. Fuel additives do not appear to result in combustion reactions in thin-film samples, whereas combustion is evident in bulk powders prepared from analogous precursors. The results of this study appear to suggest reactions that take place in bulk materials are not necessarily translatable to thin films due to differences in thermal and mass transport between the two materials classes. Therefore, combustion cannot be responsible for low-temperature metal oxide formation. Chapter V builds upon the investigation of steam annealing, first discussed in Chapter III, as an effective low-temperature thin-film processing method. The goal of this work is to provide improved mechanistic insights into the role of water vapor in film formation chemistry, specifically focused on explaining the apparent metal-dependent behavior.

CHAPTER V

CHEMISTRY OF COUTERION REMOVAL, CONDENSATION, AND DENSIFICATION PROCESSES AT LOW TEMPERATURE VIA STEAM-ANNEALING TO FORM METAL-OXIDE THIN FILMS FROM AQUEOUS PRECURSORS

Authorship Statement

The following chapter contains coauthored material written with contributions from Elizabeth A. Cochran, Peter N.P. Huynh, Keenan N. Woods, Catherine J. Page, Darren W. Johnson, and Shannon W. Boettcher. The manuscript was written by E.A.C. and experiments were performed by E.A.C. with assistance from P.N.P.H. Data analysis was performed by E.A.C., K.N.W., C.J.P, D.W.J., and S.W.B. Editorial assistance was provided by S.W.B.

Introduction

Metal-oxide thin films serve numerous functions in electronic and energy technologies, with applications including dielectrics,[1–3] semiconductors,[4–6] transparent-conducting oxides,[7,8] catalysts,[9–11] and protection layers.[12,13] Solution processing offers a potentially less-expensive, highly-scalable alternative deposition method to vacuum-based technologies (atomic-layer deposition, physical-vapor deposition, etc.).[14] However, the thermal budget necessary to form metal-oxide thin films from solution precursors, which requires high temperatures (> 300 °C) to evaporate solvent, decompose ligands/counterions, and condense metal-hydroxyl (M-OH) groups to form the metal-oxide product, remains a hindrance to high-volume manufacturing of solution-processed

materials. Many methods have been developed to reduce thin-film processing temperatures, which are referred to collectively as “low-temperature processing” methods. The objective of such research is to improve compatibility of solution thin-film deposition with polymeric substrates (e.g. with melting points of ~100-200 °C) to enable high-volume, roll-to-roll processing.[15,16] Reported low-temperature processing approaches, including aqueous precursor routes, ultraviolet (UV) photo-annealing, combustion processing, microwave annealing, and water-vapor annealing, have been discussed in recent reviews.[17–20]

The introduction of excess water vapor to thin-film annealing atmospheres facilitates low-temperature thin-film formation from a variety of precursors. For sol-gel (i.e. metal-alkoxide) thin-film synthesis, water serves as a reagent to hydrolyze and remove organic ligands, leaving M-OH groups, which condense to form the metal-oxide network. Elevated humidity ensures water does not become a limiting reagent as hydrolysis progresses.[4,21] Water vapor similarly facilitates low-temperature film formation from all-inorganic precursors, such as metal-ammonium (e.g. $Zn(NH_3)_4^{2+}$), metal-nitrate ($M(NO_3)_x$), and metal-chloride (MCl_x) species.[22,23] In our previous work studying the effects of water-vapor annealing (i.e. “steam annealing”) on thin-film formation from $M(NO_3)_x$ and MCl_x precursors, we hypothesized water serves two primary roles to facilitate counterion removal at low processing temperatures (~140-200 °C).[23] First, excess water prevents metal-anion complex formation (where X is Cl^- or NO_3^-):

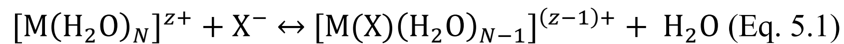

$$[M(H_2O)_N]^{z+} + X^- \leftrightarrow [M(X)(H_2O)_{N-1}]^{(z-1)+} + H_2O \text{ (Eq. 5.1)}$$

Metal-anion complexes require higher temperatures to decompose compared to metal-aquo complexes, due to the energy input required to break M-X bonds prior to

decomposition.[24] Because steam annealing facilitates aquo-cation ($[M(H_2O)_N]^{z+}$) formation, anions can decompose at lower temperatures. Water also promotes the formation of highly-volatile water-acid azeotropes of HCl and HNO_3, which boil at 110 and 120 °C, respectively, via the equilibrium:

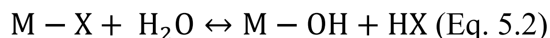

$$M - X + H_2O \leftrightarrow M - OH + HX \text{ (Eq. 5.2)}$$

Water-acid azeotrope formation provides a "low-energy" pathway for NO_3^- and Cl^- removal. Thermal decomposition to NO_x and Cl_2 gases, in contrast, can require temperatures in excess of 400 °C, depending on the metal-cation identity.[25–27]

We demonstrated steam annealing effectively removes NO_3^- at low annealing temperatures (~140-200 °C) from lanthanum-zirconium oxide (LZO), aluminum-yttrium oxide (AYO), and zinc oxide (ZnO) thin films (as well as Cl^- from a mixed $La(NO_3)_3/ZrOCl_2$ precursor, referred to as the LZO (NO_3^-/Cl^-) precursor).[23] These metal salts exhibit a broad range of decomposition, hydrolysis, and condensation rates, which suggests steam annealing is widely applicable to many $M(NO_3)_x$ precursors (and, presumably, MCl_x precursors). However, because these mixed-metal systems are prepared from mixtures of metal-salt precursors with disparate chemistries, we expect the magnitude of steam annealing effects on counterion removal to vary with precursor identity. For example, the decomposition temperatures of the hydrated $Al(NO_3)_3$ salt is more than 200 °C lower than that of $Y(NO_3)_3$.[20] Additionally, $Al(NO_3)_3$ and $Y(NO_3)_3$ are known to experience different decomposition mechanisms,[28,29] as well as different M-NO_3 interactions in the solid-state and in aqueous solution.[30,31] Such chemical factors may influence susceptibility of counterion removal in a steam atmosphere.

Low-temperature counterion removal via steam annealing can also positively influence thin-film morphology. We previously observed large voids in LZO (NO_3^-/Cl^-)

films annealed under dry, ambient conditions (i.e. relative humidity ~ 45% at room temperature). When steam-annealed, films from this same precursor were dense and void-free. Steam annealing may influence the metal-hydroxide/metal-oxide equilibrium by shifting the equilibrium toward M-OH:

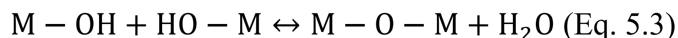

$$\mathrm{M-OH+HO-M \leftrightarrow M-O-M+H_2O} \text{ (Eq. 5.3)}$$

By maintaining greater M-OH character, the rate of metal-oxide condensation relative to the rate of counterion diffusion to the film-air interface is slowed. Void formation is suppressed during steam annealing because counterions and/or their decomposition products can diffuse to the film surface without disrupting a rigid metal-oxide network. The combined effect of steam annealing on the equilibria for reactions in Eq. 5.2 and Eq. 5.3 appears to prevent void formation. In the present study, we examine the morphology of films from several NO_3^-/Cl^- precursors to determine if void formation is similarly prevented in a steam atmosphere for other metal-oxide precursor systems.

In this study, we report the effect of steam annealing on low-temperature counterion removal from Al, In, Y, and Zr single-metal $M(NO_3)_x$ and MCl_x precursors. We observe removal of NO_3^- and Cl^- exhibits a dependence on the metal-cation identity. The magnitude of counterion removal is influenced by the effect of water vapor on the equilibrium involved in preventing M-X complex formation (Eq. 5.1), thereby making more "free" (i.e. unbound) counterions available to form HNO_3 or HCl (Eq. 5.2). Steam annealing can effectively remove counterions in thin films from precursors that are known to form stable M-X complexes. We also elucidate chemical factors that influence void formation/suppression by studying the effects of dry- and steam-annealing on the resulting morphologies of metal-oxide films from NO_3^-/Cl^- precursors. We find that void formation in dry-annealed films is not universal. Instead, voids form when precursors that

experience disparate metal-oxide condensation rates are mixed. The results discussed in the present study provide additional insight into the mechanism of thin-film formation induced by steam annealing. We identify additional benefits and limitations of this low-temperature processing method and provide recommendations for utilizing steam annealing to maximize metal-oxide thin-film quality.

Experimental Section

Precursor Solution Preparation

Precursors were prepared by dissolving metal-nitrate or metal-chloride salts in 18.2 MΩ·cm H_2O. The following salts were used: $Al(NO_3)_3 \cdot 9H_2O$ (Sigma Aldrich, 99%), $AlCl_3 \cdot 9H_2O$ (Sigma Aldrich, 99%), $In(NO_3)_3 \cdot xH_2O$ (Sigma Aldrich, 99.9%), $InCl_3 \cdot 4H_2O$ (Sigma Aldrich, 99.9%), $La(NO_3)_3 \cdot 6H_2O$ (Alfa Aesar, 99.9%), $Y(NO_3)_3 \cdot 6H_2O$ (Sigma Aldrich, 98%), $YCl_3 \cdot 6H_2O$ (Sigma Aldrich, 99.9%), $ZrO(NO_3)_2 \cdot xH_2O$ (Sigma Aldrich, 99%), and $ZrOCl_2 \cdot 8H_2O$ (Alfa Aesar, 99.9%). Mixed precursors (i.e. NO_3^-/Cl^-) were prepared by mixing single-source precursors of the same concentration in the ratios specified. All films were deposited from either 1, 1.5, or 2 M aqueous metal-salt solutions.

Thin-Film Preparation

Films were deposited on Si substrates (2 × 2 cm^2). Prior to deposition, the Si was sonicated in a 5% Contrad 70 solution (Decon Laboratories) for 10 min, then spin-rinsed with 18.2 MΩ·cm H_2O. Clean, dry substrates were O_2/N_2 plasma cleaned for 5 min in order to activate the Si surface and achieve proper wetting with the precursor solution. Precursor solutions were deposited onto the substrate through 0.2 μm PTFE filter and

spun at 3000 rpm for 30 s to form the thin-film gel. The resulting thin-film gel was soft-baked for 5 min on a hot plate set to 125 °C. Dry-annealed samples remained on the hot plate while steam-annealed samples were transferred to a custom heating stage that was placed inside a tube furnace fitted with a humidifier (schematic can be found in supplemental information for Ref. 23). The temperature of the tube furnace was set to 125 °C to prevent condensation of water on thin-film samples. Both the hotplate and custom heating stage were ramped to the final specified temperature using PID controllers. A 12.5 °C min^{-1} ramp rate was used, unless otherwise specified. All films were annealed for 1 h at their final specified annealing temperature.

Thin-Film Characterization

Chemical analysis was performed using Fourier-transform infrared (FT-IR) spectroscopy and x-ray photoelectron spectroscopy (XPS). FT-IR spectra were collected in transmission mode using a Thermo Fisher Nicolet 6700 spectrometer on thin-film samples prepared using 2 M precursor solutions. Background corrections were made using a Si wafer with the same thermal history as the thin-film samples (i.e. dry or steam environment, same annealing ramp/hold profile). Double-side polished, infrared-transparent Si (> 3000 Ω·cm) was used. Regional XP spectra were collected using a ThermoScientific ESCALAB 250 equipped with an Al Kα source (150 W, 20 eV pass energy, 500 μm spot size). Charge neutralization was achieved using an in-lens electron flood gun. Spectra were analyzed and fit using ThermoScientific Avantage 5.94 software. Binding energies were calibrated using the C-H peak for adventitious carbon (~ 284.8 eV). Additional information about fitting procedures can be found in Appendix B. Films analyzed by XPS were prepared from 1 M precursor solutions. Time-of-flight secondary-

ion mass spectrometry (TOF-SIMS) was used to create depth profiles of dry- and steam-annealed films to evaluate counterion distribution in films from 1 M precursor solutions. A 400 × 400 μm crater was sputtered using a Cs^+ ion beam. A Bi^{3+} ion beam was used as the analysis source to collect negative-ion mass spectra from a 85 × 85 μm analysis area in the middle of the crater. Film thicknesses, determined using variable-angle ellipsometry (Cauchy model), were used to estimate the sputter rate/sampling depth.

Film thicknesses and densities were determined using X-ray reflectivity (XRR). These data were collected using a Bruker D8 Discover diffractometer with a Cu Kα X-ray source (λ_{avg}=1.5418 Å). The data were modeled using Bede REFS software. Films prepared from 1.5 M precursor solutions were used for XRR analysis.

Film morphology was characterized using scanning electron microscopy (SEM) on films prepared from 1.5 M precursor solutions. Cross-sectional SEM images were captured using a FEI Helios 600i DualBeam using a 5-kV accelerating voltage and 86 pA beam current. Films were coated with thermally-evaporated Al metal to prevent sample charging during image acquisition.

Results and Discussion

Susceptibility of Single-Metal Precursors to Counterion Removal by Steam Annealing

Chemical compositions of thin films from $M(NO_3)_x$ precursors (annealed at 140 °C) were analyzed qualitatively using FT-IR (Figure 5.1). Comparison of the primary NO_3^- vibrational bands (split N-O stretching mode centered at 1300-1400 and 1600-1700 cm^{-1}) indicates NO_3^- content in $Al(NO_3)_3$ films is unaffected by steam annealing at 140 °C, as the intensity of these bands is not altered by the annealing environment (Figure 5.1a). For the three remaining precursors, $In(NO_3)_3$, $Y(NO_3)_3$, and $ZrO(NO_3)_2$, the

intensity of the NO_3^- mode decreases when the films are steam-annealed (Figure 5.1b-d). We similarly observe changes in the FT-IR spectrum for $Sc(NO_3)_3$ thin films steam-annealed at 140 °C, indicating enhanced NO_3^- removal (Figure B.1). Films from $Ga(NO_3)_3$ precursors, like $Al(NO_3)_3$, are largely unaffected by steam annealing (Figure B.1).

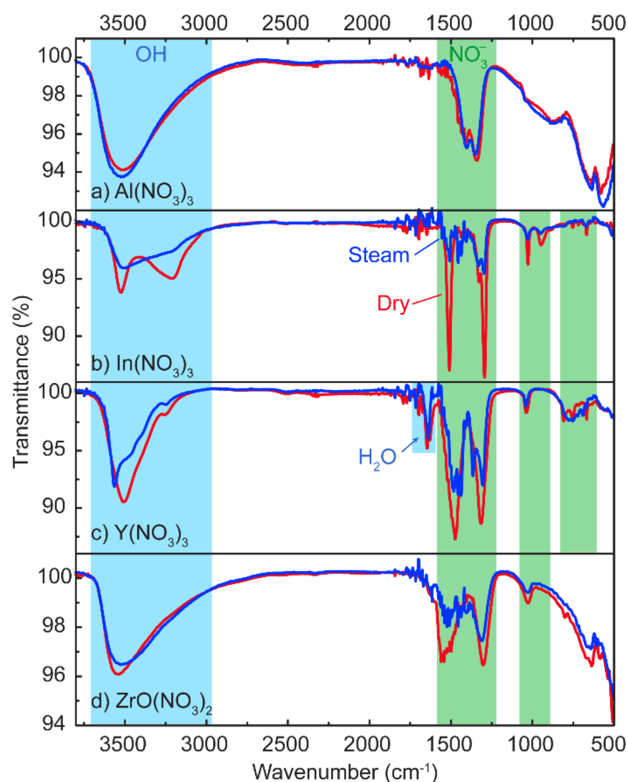

Figure 5.1. FT-IR Spectra for $M(NO_3)_x$ Precursors. All films were annealed at 140 °C under dry (red) or steam (blue) conditions. For all precursors, except $Al(NO_3)_3$, steam annealing facilitates NO_3^- removal, as evidenced by a reduction in the intensity of the NO_3^- vibrational modes relative to the dry-annealed films (highlighted in green).

While FT-IR is an excellent tool for analyzing the chemical composition of $M(NO_3)_x$ films, the presence of IR-active modes for water vapor that overlap with NO_3^- bands (identified by spectral "noise" from ~1300-1900 cm^{-1}) makes NO_3^- quantification by FT-IR unreliable. Additionally, FT-IR cannot be used to analyze chemical composition of thin films from MCl_x precursors due to a lack of IR-active vibrational

modes. Instead, we use XPS to analyze and compare NO_3^- and Cl^- content in dry- and steam-annealed films from $M(NO_3)_x$ and MCl_x precursors. NO_3^- and Cl^- content was determined by integrating N 1s and Cl 2s peak areas from XP spectra and was normalized to the integrated peak areas of each metal (Al 2p, In 3d, Y 3d, or Zr 3d) to calculate the X:M ratios, where X is N or Cl. All peak integrations are weighted using sensitivity factors specific to each element. Atomic percentages from all XP spectra for each $M(NO_3)_x$ and MCl_x film are in Tables B.1 and B.2. Both Ga and Sc have photoelectron lines that interfere with N 1s quantification. Because of this, we have excluded $Sc(NO_3)_3$ and $Ga(NO_3)_3$ from this XPS study.

Films from $Al(NO_3)_3$ and $AlCl_3$ precursors do not exhibit a measureable difference in X:M ratios when the annealing ambient is changed from a dry to steam atmosphere (Figure 5.2). This corroborates observations made about the chemical composition of dry- and steam-annealed $Al(NO_3)_3$ films from FT-IR analysis (Figure 5.1a). Both $M(NO_3)_x$ and MCl_x precursors for In_2O_3 and ZrO_2 films experience the largest reduction in counterion content (~ 50-65%) with steam annealing (Figure 5.2). Films from $ZrO(NO_3)_2$ and $ZrOCl_2$ precursors contain low counterion content even under dry-annealing conditions (N:M and Cl:M ratios of 0.3 and 0.2, respectively), due to their low decomposition temperatures as observed by thermogravimetric analysis (TGA, Figure B.2). While the magnitude of the steam-annealing effect is similar for In_2O_3 and ZrO_2 precursors, the reduction of counterion content in steam-annealed films from $In(NO_3)_3$ and $InCl_3$ is most striking. For films from $Y(NO_3)_3$ and YCl_3 precursors, a modest enhancement of counterion removal with steam annealing is observed (~ 25 and 40%, respectively, Figure 5.2).

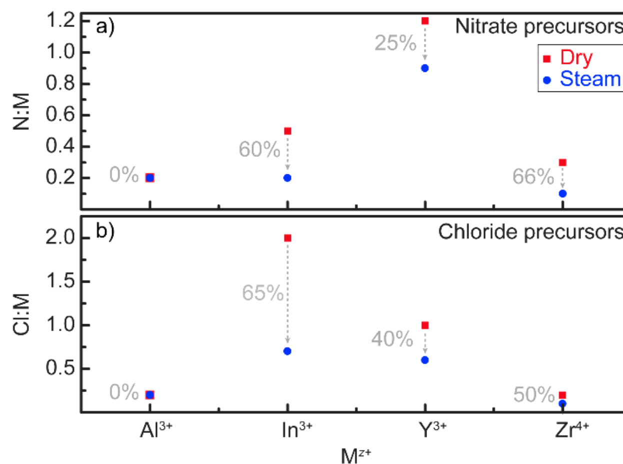

Figure 5.2. XPS Quantification of Counterion Content in Films Annealed Under Dry and Steam Conditions at 140 °C. Ratios of atomic percentages calculated using the integrated peak areas for the N 1s (or Cl 2s) to the metal cation (Al 2p, In 3d, Y 3d, or Zr 3d) from surface spectra are shown. The percentages (grey font) indicate the reduction in counterion content from dry- to steam-annealing conditions.

We attempt to explain the observed precursor-dependence of steam annealing on counterion removal by considering the metal-dependent behavior of such salts, as it relates to their decomposition pathways and M-X complex stabilities. We hypothesized in our previous study that steam annealing enhances counterion removal by: (1) maintaining the cation hydration sphere, thereby, preventing M-X complex formation (Eq. 5.1) and facilitating the formation of the HNO_3- or HCl-H_2O azeotrope (Eq. 5.2), which evaporate at low temperatures (120 and 110 °C, respectively). The aluminum aquo cation, $[Al(H_2O)_6]^{3+}$, is thermodynamically stable, with a large, negative free energy of hydration (ΔG_{hyd} = -4525 kJ mol^{-1}).[32] Because of the exceptional stability of $[Al(H_2O)_6]^{3+}$, neither NO_3^- nor Cl^- form Al-X complexes in the solid-state[33,34] or aqueous solution.[30] Additionally, the respective HNO_3- and HCl-H_2O azeotropes are known to contribute substantially to the decomposition products of hydrated $Al(NO_3)_3$ and $AlCl_3$ salts under dry atmospheric conditions.[28,35] The chemical equilibrium described by Eq. 5.1 favors $[Al(H_2O)_6]^{3+}$ for $Al(NO_3)_3$ and $AlCl_3$ precursors, due to the large, negative ΔG_{hyd} of

$[Al(H_2O)_6]^{3+}$. We hypothesize steam annealing does not noticeably enhance counterion removal from $Al(NO_3)_3$ and $AlCl_3$ thin films because water vapor does not result in large shifts to the equilibria relevant to their decomposition pathways (Eq. 5.1 & 5.2). The gallium aquo cation, $[Ga(H_2O)_6]^{3+}$, exhibits similar thermodynamic stability to its aluminum counterpart (ΔG_{hyd} = -4515 kJ mol^{-1}).[32] However, small quantities of Ga-NO_3 complex have been observed in concentrated aqueous solutions (~ 5% $[Ga(NO_3)(H_2O)_5]^{2+}$ relative to $[Ga(H_2O)_6]^{3+}$ in ~ 2 M solutions).[36] These chemical similarities between $Al(NO_3)_3$ and $Ga(NO_3)_3$ may explain why counterion content in $Ga(NO_3)_3$ films also appear largely unaffected by steam annealing (Figure B.1).

For the metal-salt systems that experience enhanced counterion removal with steam annealing (In, Y, and Zr), the aquo cations are less stable than those of Al^{3+} and Ga^{3+} (ΔG_{hyd}= -3980 for In^{3+} and -3450 kJ mol^{-1} for Y^{3+}, respectively).[32] Because of this, NO_3^- or Cl^- can exchange for H_2O to form M-X complexes (Eq. 5.1). While the ΔG_{hyd} of Zr^{4+} is not known, as the aquo cation has never been observed in aqueous solution, Zr-X complexes are known.[37,38]

Indeed, many $M(NO_3)_x$ salts form weak M-NO_3 complexes in aqueous solutions.[30,31,36,39] Thermodynamic stability constants for M-X complex formation in aqueous solution provide a metric by which we can compare relative M-X stabilities. We acknowledge solution behavior may not be directly translatable to thin-film gels; however, previous relationships have been established between M-X complex stabilities in aqueous thin-film precursor solutions and low-temperature film formation.[24,40–42] Namely, precursors that form M-X complexes require higher temperatures to decompose than precursors that contain $[M(H_2O)_N]^{z+}$ due to the energy input required to break M-X bonds so that counterion decomposition can occur. We compare here stability constants

(K_1) at room temperature (25 °C), as we are unable to account for the influence of temperature on K_1 for all systems due to a lack of available formation enthalpy (ΔH) and entropy (ΔS) data.[43]

For the $M(NO_3)_x$ precursors studied here, the log K_1 values that describe the equilibrium for M-X complex formation (Eq. 5.1) are as follows: 0.18 (In^{3+}), 0.1 (Y^{3+}), and 0.3 (Zr^{4+}). We make the assumption that the log K_1 value for Y^{3+} is equal to that of La^{3+}, due to the similarity of yttrium to lanthanides, as no value for Y^{3+} is reported.[43] The stability of M-NO_3 complexes ($Zr^{4+} > In^{3+} > Y^{3+}$) is loosely correlated with the amount of NO_3^- removed with steam annealing ($Zr^{4+} \approx In^{3+} > Y^{3+}$). It appears water vapor acts upon the equilibrium in Eq. 5.1 to prevent formation of more-stable M-NO_3 complexes. For the MCl_x precursors, the log K_1 values for M-Cl complex formation are: 2.32 (In^{3+}), -0.1 (Y^{3+}), and 0.3 (Zr^{4+}).[43] There is, again, a correlation between Cl^- removal ($In^{3+} > Zr^{4+} > Y^{3+}$) and M-Cl complex stability ($In^{3+} > Zr^{4+} > Y^{3+}$). The $InCl_3$ precursor has the largest log K_1 value by an order of magnitude and experiences the largest change in Cl^- content with steam annealing (Figure 5.2).

It is apparent that steam-annealing effects are not isolated to metal salts that form weak M-X complexes. Films from $InCl_3$ experience the largest reduction in Cl^- content with steam annealing (65% from dry to steam conditions, Figure 5.2), yet In-Cl has the largest log K_1 value of all the precursor systems studied here. Additionally, In-Cl complex formation is endothermic ($\Delta H \approx + 5.02$ kJ mol^{-1}).[43] At 140 °C, log K_1 is estimated to be 3.74, indicating a shift in Eq. 5.1 farther toward products and increased stability of the In-Cl complex at elevated temperatures. Steam annealing appears to effectively prevent the formation of relatively-strong In-Cl complexes in order to facilitate low-temperature counterion removal.

A consideration of the equilibrium expression for M-X complex formation and the rate of metal-oxide condensation elucidates why precursors that form more-stable M-X complexes experience more counterion removal with steam annealing. The equilibrium expression for Eq 5.1 is as follows, where $[\mathrm{M(H_2O)}_N]^{z+}$ is abbreviated as "M-H_2O" and $[\mathrm{M(X)(H_2O)}_{N-1}]^{(z-1)+}$ as "M-X":

$$K_1 = \frac{[\mathrm{M{-}X}][\mathrm{H_2O}]}{[\mathrm{M{-}H_2O}][\mathrm{X}]} \text{ (Eq 5.4)}$$

We make the assumption that the rate of metal-oxide condensation is governed by the concentration [M-H_2O] by the following rate expression:

$$\text{rate} = k[\mathrm{M} - \mathrm{H_2O}] \text{ (Eq. 5.5)}$$

Using Eq. 5.4 and 5.5, we can establish a dependence of metal-oxide condensation rate on K_1 and [H_2O] (i.e. the amount of water in the steam atmosphere):

$$\frac{\text{rate}}{k} = [\mathrm{M} - H_2\mathrm{O}] = \frac{[\mathrm{H_2O}][\mathrm{M_{tot}}]}{[\mathrm{H_2O}]+K_1[\mathrm{X}]} \text{ (Eq. 5.6)}$$

where [M_{tot}]=[M-H_2O]+[M-X]. When K_1 is large, a large increase in [H_2O] will result in a large shift of the equilibrium to favor the aquo cation over the M-X complex. When K_1 is small, if [H_2O] is already large, changing [H_2O] will result in small equilibrium shifts, as the aquo complex is already favored over the M-X complex. Indeed, M-X complexes with large K_1 values will experience enhanced counterion removal with steam annealing because water has a greater effect on the equilibrium in Eq. 5.1.

Temperature Dependence of Counterion Removal with Steam Annealing

Enhanced counterion removal with steam annealing is not isolated to temperatures near the azeotrope boiling points. For the two thin-film systems that exhibit the greatest

reduction in counterion content at 140 °C, $In(NO_3)_3$ and $InCl_3$, we examine the temperature dependence of steam annealing. For annealing temperatures ranging from 140 to 250 °C, we observe that steam annealing continues to reduce both NO_3^- and Cl^- content as the annealing temperature is increased (Figure 5.3). Once a 200 °C annealing temperature is reached, steam annealing has a minimal effect on NO_3^- removal from $In(NO_3)_3$ films (N:In is reduced from 0.07 to 0.05) (Figure 5.3a). Trace NO_3^- quantities are still present in $In(NO_3)_3$ films dry-annealed at 250 °C (0.03 N:In ratio, or 1% total surface composition), whereas steam-annealed films contain no detectable nitrogen in XP surface spectra (Table B.3). The bulk $In(NO_3)_3$ salt decomposes at low temperature in air (~ 250 °C; Figure B.2). The benefits of steam annealing for low-temperature NO_3^- removal, therefore, primarily apply to annealing temperatures < 200 °C. The largest reduction in chloride content is, similarly, observed below 200 °C for $InCl_3$ films (Figure 5.3b). At a 250 °C annealing temperature, the effects of steam annealing are still significant, as the Cl:In ratio is reduced from 0.2 to 0.06 from dry- to steam-annealing conditions. Atomic percentages of all elements of interest for the films analyzed in Figure 5.3 can be found in Tables B.3 and B.4.

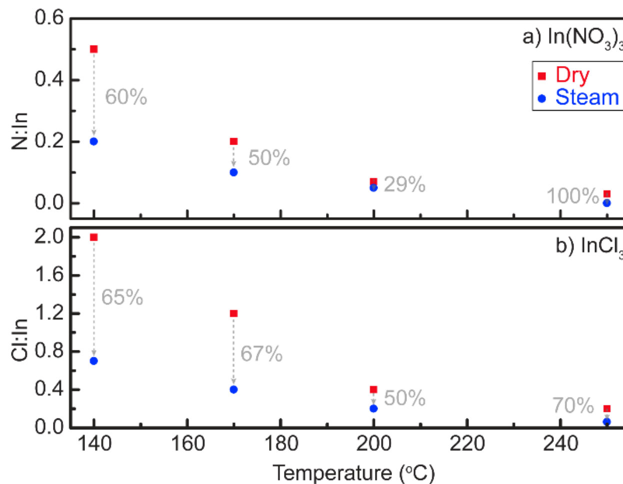

Figure 5.3. Temperature Dependence of NO_3^- and Cl^- Removal from Films Prepared Using In_2O_3 Precursors. Ratios of atomic percentages of NO_3^- and Cl^- content to In were calculated using the following integrated peak areas from XPS surface spectra: N 1s, Cl 2s, and In 3d. Percent reduction in counterion content at each annealing temperature is show in grey font. The data points at 140 °C are reprinted here from Figure 5.2 in order to show changes in counterion content with annealing temperature.

Fitted O 1s spectra for $In(NO_3)_3$ films that were dry- and steam-annealed at 250 °C show differences in the chemical environments of oxygen (Figure 5.4a-b). The steam-annealed film contains less indium oxide character (In-O) and more indium hydroxide (In-OH) character than the dry-annealed film, as indicated by the In-O:In and In-OH:In ratios shown in Figure 5.4. This result agrees with our previously-stated hypothesis that water vapor shifts the M-OH/M-O-M equilibria toward M-OH species (Eq. 5.3). In contrast, for $InCl_3$ films, the steam-annealed film contains slightly more In-O and less In-OH character than the dry-annealed film (Figure 5.4c-d). Interestingly, at lower annealing temperatures (170 °C), we observe more In-O character in the dry-annealed $InCl_3$ film, as evidenced by a prominent shoulder in the O 1s regional spectrum at ~ 530.5 eV (Figure B.3). For $In(NO_3)_3$ films annealed at 170 °C, the O 1s spectra for dry- and steam-annealed films have the same spectral shape and likely contain oxygen in similar

chemical environments (Figure B.3). It appears, at annealing temperatures ≤ 170 °C, steam annealing inhibits metal-oxide condensation in the $InCl_3$ film by shifting the equilibrium in Eq. 5.3 to the left (i.e. toward M-OH). We hypothesized, in our previous study, this equilibrium shift allows for increased Cl^- diffusion to the thin-film surface.[23] Further condensation in the 250 °C dry-annealed film may be inhibited by higher Cl^- content, as evidenced by larger In-OH:In (Figure 5.4) and Cl:In (Figure 5.2) ratios for dry- compared to steam-annealed films.

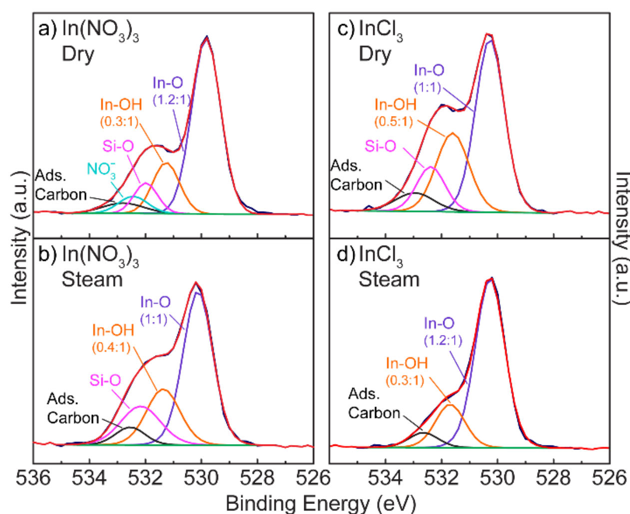

Figure 5.4. Fitted O 1s Spectra for Dry- and Steam-Annealed Films (250 °C) from $In(NO_3)_3$ and $InCl_3$ Precursors. Ratios show in parentheses indicate the number of indium oxide (In-O) or indium hydroxide (In-OH) bonds per In calculated from the integrated peak areas of In-O or In-OH from the fitted O 1s and In 3d spectra.

Counterion Distribution in Dry- and Steam-Annealed Films

Depth-profiling experiments reveal different distributions of counterions in dry- and steam-annealed films. Films from $Sc(NO_3)_3$ annealed at 140 °C were chosen for this study, in place of $In(NO_3)_3$ films, because films from this precursor are "full-coverage" of the Si substrate, as evidenced by the steep increase in Si signal by TOF-SIMS at the film-

substrate interface (Figure 5.5). For films from the $In(NO_3)_3$ precursor, Si is detected in the XPS surface spectra (Table B.3). This indicates the films are not continuous, which would result in poor axial resolution in the depth profile. For a dry-annealed $Sc(NO_3)_3$ film, we observe an even distribution of NO_3^- from the film surface to the Si substrate interface (Figure 5.5a). For a steam-annealed $Sc(NO_3)_3$ film, NO_3^- content declines rapidly within the top ~15 nm of the film. Through the remaining thickness of the film, trace NO_3^- content is detected (Figure 5.5b).

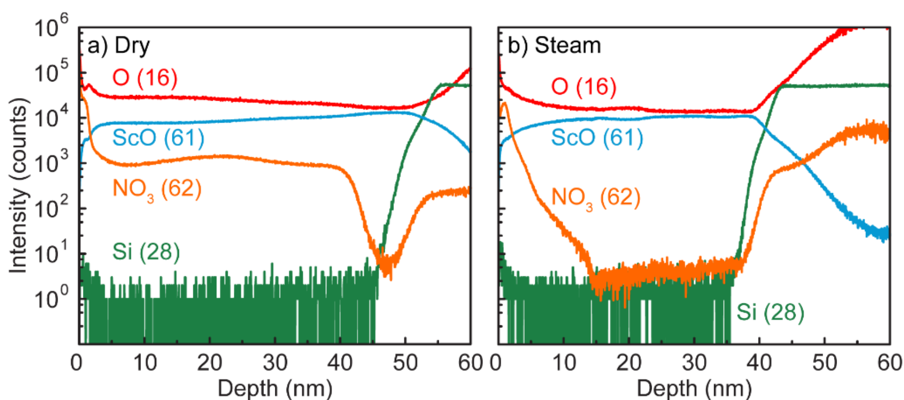

Figure 5.5. TOF-SIMS Evaluation of NO_3^- Distribution in $Sc(NO_3)_3$ Films Annealed at 140 °C. The depth profile for a dry-annealed film reveals a homogenous distribution of NO_3^- throughout the thickness of the film (a), whereas NO_3^- is disproportionately located within the top 15 nm of the steam-annealed film (b). The numbers in parentheses specify the mass-to-charge (m/*z*) ratio of the negative fragment used to track each element in the film. Film thicknesses are 46 and 37 nm for dry- and steam-annealed films, respectively. The rise in signal from the m/*z* = 62 fragment within the Si substrate is a result of interference with the $^{30}SiO_2$ fragment. We attribute increased signal from m/*z* = 16 within the Si substrate to matrix effects and is not indicative of local oxygen concentration.

The differences in NO_3^- distribution between the two films indicates steam annealing impacts the chemical composition of the entire film, rather than merely removing NO_3^- from the surface region. Clearly, NO_3^- is able to more easily diffuse to the surface in a steam-annealed film than a dry-annealed film, presumably due to suppressed metal-oxide condensation (Eq. 5.3). The steep NO_3^- concentration gradient in

the steam-annealed film suggests film chemistry near the surface provides a more favorable/stable environment for NO_3^-. It is possible the presence of water vapor in the annealing atmosphere increases the tendency of NO_3^- to reside at the film-air interface prior to forming the HNO_3-H_2O azeotrope and evaporating from the film. It is known that anions in aqueous solution have a propensity to reside at the air-water interface, instead of within the solution bulk.[44–46] It is hypothesized an anion's "preference" for the interface is related to its polarizability. Asymmetric solvation at the surface results in a net dipole for the anion, which provides a stabilizing force that can balance or overcome the energy penalty of incomplete solvation.[44] It is possible we observe a similar phenomenon of NO_3^- localization at the air-film interface in steam-annealed films. Further studies of anion distribution in films from metal-salt precursors with anions of different polarizabilities could be useful to relate interactions between anions and atmospheric water to thin-film formation reactions.

The Effect of Steam Annealing on MCl_x Film Morphology

The MCl_x precursors are prone to crystallization of the salt on the substrate surface in the early stages of annealing, once excess solvent has evaporated (see Figure 5.6e). This results in a rough surface morphology (i.e. non-specular film surfaces). When films from $InCl_3$ and YCl_3 precursors are steam annealed, their surfaces become smooth and specular (Figure 5.6d and 5.6g). We hypothesize that water vapor rehydrates the MCl_x salt, allowing ions to rearrange and smooth the film surface in order to completely wet the hydrophilic SiO_x substrate. Films from the $AlCl_3$ precursor, however, retain their rough surface morphology, even after steam annealing (Figure 5.6a-b). This is likely a result of substantial decomposition to Al_2O_3 by 140 °C, which prevents the film from

effectively rehydrating. This effect is akin to solvent-vapor annealing, which has been used to control surface morphology and grain size of both organic polymer[47] and perovskite[48] thin films. Steam-annealing could similarly be an effective way to "repair" thin-film morphology, especially rough surfaces, which is known to degrade electronic properties in thin-film devices.[6,49,50]

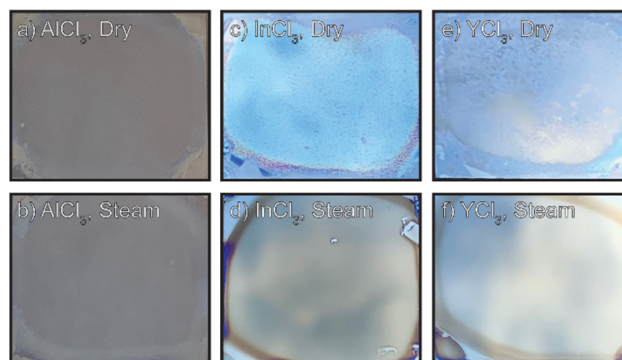

Figure 5.6. Photographs of (a-b) $AlCl_3$, (c-d) $InCl_3$, and (e-f) YCl_3 Films (Dry- and Steam- annealed at 140 °C) After < 5 min Exposure to Ambient. All films have a hazy appearance (see: $AlCl_3$ films) once placed on the hotplate. Steam annealing "repairs" the surface of $InCl_3$ and YCl_3 films, resulting in smooth, specular surfaces. Dry-annealed $InCl_3$ and YCl_3 film absorb atmospheric water shortly after being removed from the hotplate, resulting in a blue appearance, which is indicative of increased thickness.

Additionally, the films from $InCl_3$ and YCl_3 exhibit enhanced stability to water reabsorption when left in ambient, with no visible change to film thickness (Figure 5.6d and 5g). We previously observed similar moisture resistance for steam-annealed LZO (NO_3^-/Cl^-) films.[23] In contrast, dry-annealed films readily adsorb water, as evidenced by increased film thickness and de-wetting as films sit in ambient for only a few minutes (Figure 5.6c and 5.6e). We attribute improved ambient stability of steam-annealed MCl_x films to reduced chloride content (Figure 5.2). For films from $AlCl_3$, these films contain low chloride content (~ 4 % of total surface composition, Table B.4) regardless of dry or

steam annealing treatments; as a result, these films appear to be stable in ambient but exhibit rough surface morphologies.

Understanding the Chemical Factors that Influence Void Formation

We previously observed, for LZO (NO_3^-/Cl^-) films, that steam annealing improves film morphology (relative to dry-annealed films) by inhibiting void formation.[23] We hypothesize steam annealing suppresses the metal-oxide condensation rate (Eq. 5.3) relative to the rate of counterion diffusion to the film-air interface. This equilibrium shift allows volatile species to leave the film without disrupting a rigid metal-oxide network. We attribute void formation in dry-annealed films to Cl^- (or its decomposition products) that has become trapped in the film by the rigid metal-oxide network (i.e. residual Cl^-, but not NO_3^-, is observed by XPS in dry-annealed films with voids). We do not observe voids in films from all-$M(NO_3)_x$ precursors.

To determine if the benefits to film morphology we observed for the LZO (NO_3^-/Cl^-) system apply more generally to other thin-film precursors, we studied the effects of steam annealing on film morphology of several mixed NO_3^-/Cl^- precursors. Of the mixed single-metal precursors studied, only dry-annealed In_2O_3 films contain voids (Figure 5.7c). The appearance of voids in In_2O_3 films can be explained by comparing the decomposition behavior of $In(NO_3)_3$ and $InCl_3$. TGA shows decomposition of $In(NO_3)_3$ to In_2O_3 is complete by ~ 250 °C, as evidenced by the lack of further mass loss at higher temperatures (Figure B.2). For $InCl_3$, decomposition is not complete until temperatures > 450 °C (Figure B.2). The Cl^- ions likely become trapped in the film, as a result of low-temperature In_2O_3 formation from $In(NO_3)_3$ decomposition, and Cl^- disrupts the condensed metal-oxide network when it decomposes and leaves the film. When steam

annealed, In_2O_3 (NO_3^-/Cl^-) films are void-free (Figure 5.7d). We attribute void suppression in the In_2O_3 (NO_3^-/Cl^-) precursor system to suppressed metal-oxide condensation (Eq. 5.3), as we previously suggested is the case for the LZO (NO_3^-/Cl^-) system. Additionally, the appearance of Kiessig fringes in the XRR pattern indicates the steam-annealed In_2O_3 film is smoother and denser than the dry-annealed film (Figure B.4). Films from the Y_2O_3 (NO_3^-/Cl^-) precursor, in contrast, do not contain voids (Figure 5.7e-f) because YCl_3 decomposes at a lower temperature than $Y(NO_3)_3$ (no further mass loss after ~ 450 °C and 550 °C, respectively; Figure B.2). For this precursor system, it appears diffusion of NO_3^- and Cl^- (and/or their decomposition products) must sufficiently outcompete the rate of Y_2O_3 condensation to suppress void formation, even under dry conditions. Steam annealing also improves Y_2O_3 film morphology, as evidenced by the appearance of Kiessig fringes at higher 2θ (Figure B.4). Curiously, modeling of the XRR pattern indicates steam-annealed Y_2O_3 (NO_3^-/Cl^-) films are thicker and less-dense than dry-annealed films, which may suggest steam-annealing inhibits condensation of Y_2O_3, even at a 500 °C annealing temperature.

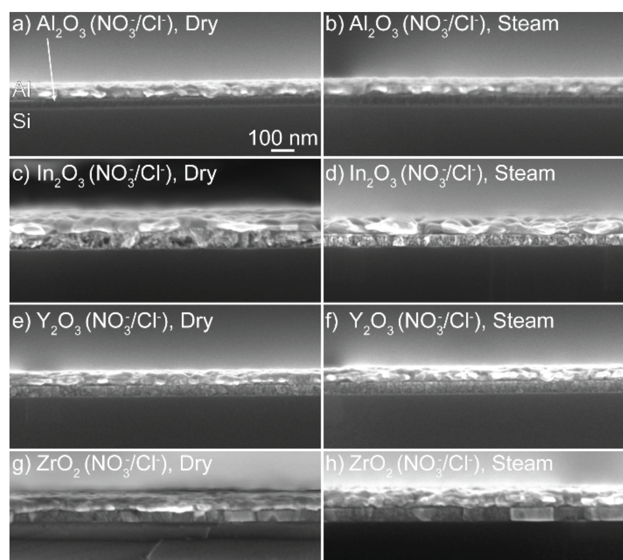

Figure 5.7. SEM Images of Mixed NO_3^-/Cl^- Films from Single-Metal Precursors. All films were prepared from 1 NO_3^-: 1 Cl^- mixtures, with the exception of Al_2O_3 films, which were prepared using a 3 NO_3^-: 1 Cl^- ratio. Precursor ratios were limited by the highest MCl_x content that resulted in specular thin films suitable for XRR analysis. The films were annealed at 500 °C for 1 h under dry or steam conditions (ramped from 125 °C at 25 °C min^{-1}).

The Al_2O_3 and ZrO_2 thin films from NO_3^-/Cl^- mixtures produce films that are similarly void-free and dense, regardless of the annealing atmosphere (Figure 5.7a-b and 5.7g-h). The $Al(NO_3)_3$ and $AlCl_3$ precursors, as well as $ZrO(NO_3)_2$ and $ZrOCl_2$, experience similar decomposition profiles and decompose at low temperatures (majority of mass loss occurs by < 200 °C, Figure B.2). For these $M(NO_3)_x$ and MCl_x precursors, the relative rates of metal-oxide condensation and counterion diffusion through the film appear to be well matched. Steam annealing does not enhance counterion removal from either Al_2O_3 precursor; therefore, dry- and steam-annealed films from the mixed NO_3^-/Cl^- precursor results in films with similar thickness, density, and roughness, as determined by XRR (Figure B.4). The ZrO_2 (NO_3^-/Cl^-) films whether dry- or steam-annealed, also produce similar XRR patterns, indicating steam annealing does not improve ZrO_2 film morphology (Figure B.4). While both NO_3^- and Cl^- content are

reduced by steam annealing in single-source ZrO_2 precursors, dry-annealed films already contain low counterion content by a 140 °C annealing temperature (Figure 5.1). This appears to suggest that benefits of steam annealing we previously observed for LZO (NO_3^-/Cl^-) films can be largely attributed to the effect of water vapor on the $La(NO_3)_3$ decomposition pathway, rather than on $ZrO(NO_3)_2$ or $ZrOCl_2$ decomposition.

In order to determine if void suppression in steam-annealed LZO (NO_3^-/Cl^-) thin films is a result of changes to $La(NO_3)_3$ decomposition chemistry, we prepared $M_yZr_{1-y}O_x$ mixtures of $ZrOCl_2$ with several $M(NO_3)_x$ salts (where M= Al, La, or Y). Both $Al(NO_3)_3$ and $ZrOCl_2$ experience large mass loss steps by 150 °C (~ 65 and 50% mass loss, respectively) and, therefore, are expected to produce homogeneous, void-free films under dry conditions. We hypothesize the disparate decomposition temperatures of $La(NO_3)_3$ and $ZrOCl_2$ (separated by > 200 °C) are responsible for void formation in LZO films, as a result of different metal-oxide condensation rates. The $Y(NO_3)_3$ decomposition temperature is intermediate to $Al(NO_3)_3$ and $La(NO_3)_3$ (50% mass loss occurs at ~ 375 °C) but, still, much higher than $ZrOCl_2$ (see Figure B.2 for TGA curves for the above-mentioned salts). As a result, films from $Y_yZr_{1-y}O_x$ precursors were, similarly, expected to contain voids. Each mixture was prepared at both low (~ 10 %) and high (50 %) $M(NO_3)_x$ concentration to evaluate the effect of composition on void formation.

For the $M_{0.1}Zr_{0.9}O_x$ compositions, all films have uniform morphologies and do not contain voids (Figure 5.8a, c, and e). Of the $M_{0.5}Zr_{0.5}O_x$ mixtures, $La_{0.5}Zr_{0.5}O_x$ is the only film with voids (Figure 5.8d). Since voids appear at higher La concentrations, we can attribute void formation to changes in the film decomposition pathway induced by $La(NO_3)_3$. While it was expected the $Al_yZr_{1-y}O_x$ films would be void-free, based on the similar decomposition chemistries of the component salts, it is somewhat surprising that

there are no voids in the $Y_yZr_{1-y}O_x$ films. This suggests $Y(NO_3)_3$ has a slower condensation rate than $La(NO_3)_3$, despite having a lower decomposition temperature, allowing for diffusion of counterions and/or their decomposition products to the thin-film surface without disrupting film morphology under dry conditions (Figure B.2). Therefore, it appears relative decomposition temperatures alone are not a reliable indicator of void formation, as is the case for the single-metal (NO_3^-/Cl^-) precursors (Figure 5.7).

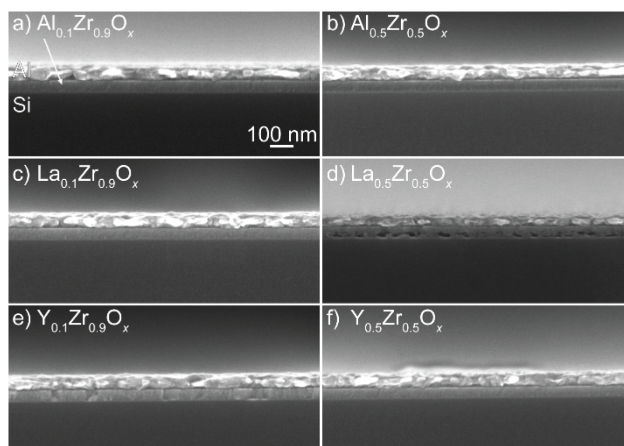

Figure 5.8. SEM Images of $M_yZr_{1-y}O_x$ Films. All films were annealed at 500 °C for 1 h prior to imaging (ramped from 125 °C at 25 °C min^{-1}) under dry conditions. Voids were only observed in $La_{0.5}Zr_{0.5}O_x$ films, indicating changes to thin-film decomposition chemistry/condensation rate with $La(NO_3)_3$ incorporation are responsible for degraded film morphology. Steam annealing LZO (NO_3^-/Cl^-) films prevents the formation of such voids.[23]

The Role of Different Annealing Treatments in Void Formation

We previously proposed that excess water vapor acts upon the metal M-OH/M-O-M equilibrium to favor the formation of M-OH at low annealing temperatures (Eq. 5.3). It may then be possible take advantage of this equilibrium shift to repair voids that have formed during a dry anneal using a subsequent steam-annealing treatment. To determine if voids can be repaired, we dry-annealed LZO (NO_3^-/Cl^-) films at low temperature (200

°C), then transferred the films to a steam environment to continue ramping to a 500 °C final annealing temperature. Voids are still visible in films that were treated with this annealing profile (Figure 5.9a-b). This result indicates that, once the metal-oxide network has formed, excess water vapor cannot revert sufficiently to M-OH and sufficiently increase diffusion to enable rearrangement of the metal-oxide network over nm-length scales. When the temperature ramp rate during the steam annealing step is slowed from 25 °C min^{-1} (Figure 5.9a) to 5 °C min^{-1} (Figure 5.9b), further densification is observed by XRR (5.39 compared to 5.65 g cm^{-3}, Figure B.5), but voids are still present. Improved densification can, therefore, largely be attributed to enhanced counterion diffusion/removal relative to the metal-oxide condensation rate, rather than the elimination of large voids.

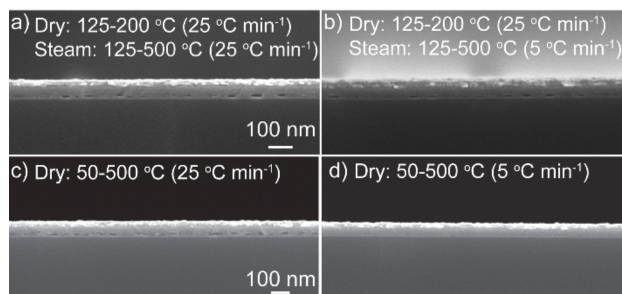

Figure 5.9. SEM Images of LZO (NO_3^-/Cl^-) Films Thermally Treated Using Various Annealing Profiles. Films that are first dry-annealed at 200 °C, then transferred to a steam environment (ramped to 500 °C), contain voids (a and b). This indicates that steam annealing is not capable of "healing" voids once they have formed. Films annealed at a 50 °C soft-bake temperature contain voids when a 25 °C min^{-1} ramp rate is used; when the ramp rate is slowed to 5 °C min^{-1}, void formation is suppressed.

We previously reported on the importance of temperature ramp rate for achieving dense films with uniform morphology.[23] In our previous study, when the annealing ramp rate was decreased from 125 to 0.25 °C min^{-1} in dry conditions, we observed the void size

decrease and the pore-free region near the surface of LZO (NO_3^-/Cl^-) films become thicker.[23] We hypothesized that slower ramp rates allow for temporal separation of counterion diffusion/decomposition and metal-oxide condensation, which results in a similar, positive effect on film morphology to steam annealing. For the previous study, we used a soft-bake temperature of 125 °C. At this temperature, water and the HCl and HNO_3-azeotrope will begin to boil and leave the film. Therefore, it is possible that void formation has been initiated before the ramp profile has begun. Here, we decrease the soft-bake temperature to 50 °C. At this temperature, counterion decomposition should be minimal and most of the film mass loss can be attributed to water evaporation, which is evidenced by little to no mass loss from the bulk salts by TGA (Figure B.2). As a result, we expect lowering the soft-bake temperature to 50 °C will prevent void formation. For LZO (NO_3^-/Cl^-) films dry-annealed using a 25 °C min^{-1} ramp rate (from 50-500 °C), voids are still present (Figure 5.9c). When the ramp rate is slowed to 5 °C min^{-1}, voids are nearly eliminated (Figure 5.9d). While a low soft-bake temperature combined with a slow ramp rate effectively eliminates voids, the resulting films are less dense than steam-annealed films soft-baked at 125 °C (5.38 compared to 5.68 g cm^{-3} by XRR, Figure B.5). When films are steam-annealed for the entire annealing duration, a slow ramp rate (5 vs. 25 °C min^{-1}) provides minimal benefits to thin-film density (5.68 vs. 5.59 g cm^{-3}, respectively). This indicates metal-oxide condensation and counterion diffusion processes under steam-annealing conditions, even at faster ramp rates, are sufficiently temporally separated to maximize film density. Interestingly, these films from the LZO (NO_3^-/Cl^-) precursor are denser than films from all-nitrate precursors (dry-annealed) we reported on in a previous study (~ 5 g cm^{-3} at 500 °C annealing temperature), which further

demonstrates the benefits of steam annealing for achieving high-density, high-quality metal-oxide thin films.[3]

Utilizing Steam Annealing to Maximize Metal-Oxide Thin-Film Quality: A Practical Guide

The results of the present study elucidate additional benefits, as well as limitations, of the steam-annealing method for low-temperature metal-oxide thin-film formation. The purpose of the discussion below is to frame our findings from the perspective of when steam annealing is "most practical" for maximizing the quality of metal-oxide thin films from solution precursors.

The susceptibility of $M(NO_3)_x$ and MCl_x precursors to counterion removal with steam annealing is precursor dependent. We hypothesize this effect is modulated by the extent to which water vapor acts upon the equilibria relevant to precursor decomposition, by inhibiting M-X complex formation and modulating acid-water azeotrope formation. The "gains" in processing temperatures will vary based on the precursor used. Counterion removal at low temperatures (140 ºC) with steam is appreciable for all the precursors studied here, with the exception of $Al(NO_3)_3$ and $AlCl_3$ (Figure 5.2). For a restricted thermal budget (especially below 200 ºC), steam annealing will effectively lower counterion content in a variety of precursors and improve ambient stability to water re-absorption, which should result in films of higher electronic quality than dry-annealed films. We previously observed this directly for LZO (NO_3^-/Cl^-) films steam annealed at low temperature. A 200 ºC steam anneal resulted in thin films with a respectably-high dielectric constant (11.5 at 1 kHz), whereas 200 ºC dry-annealed films produced non-

functional dielectrics.[23] We expect the benefits to electronic properties for low-temperature steam-annealed films apply more broadly to other thin-film precursors.

It is, fundamentally, interesting that steam annealing has such a marked effect on the decomposition pathway of $InCl_3$ films, especially at low temperature. Practically, however, $In(NO_3)_3$ is the superior precursor if low-temperature In_2O_3 formation is desired, due to a low decomposition temperature (~250 °C) in dry ambient conditions (Figure B.2). It is worth noting that steam-annealed In_2O_3 films from $InCl_3$ appear to have highly-uniform morphology, whereas $In(NO_3)_3$ are "patchy" (i.e. Si is detected in surface XPS spectra for $In(NO_3)_3$ and dry-annealed $InCl_3$ films, Figure 5.4). If film continuity is critical for a particular application, steam-annealed films from $InCl_3$ may be preferred. The greatest benefits of steam-annealing as a low-temperature processing method, however, are for MCl_x precursors that decomposes at lower temperatures than $M(NO_3)_x$, such is the case for the YCl_3 precursor (Figure B.2). Because steam annealing can repair the surface morphology of films from MCl_x precursors, there is opportunity to prepare high-quality metal oxide thin films from aqueous MCl_x precursors that was previously impossible under dry conditions.

On the topic of film morphology, we observe void formation in dry-annealed films when two precursors with disparate counterion decomposition and metal-oxide condensation rates are mixed. Interestingly, precursors with disparate decomposition temperatures do not always produce voids, as it appears condensation rates are not always directly correlated with decomposition temperatures. For example, in the case of films from the mixed NO_3^-/Cl^- precursors for Y_2O_3 and $Y_yZr_{1-y}O_x$, we do not observe voids in dry-annealed films, despite the disparate decomposition temperatures of the two-salt components. While $La(NO_3)_3$ has a higher decomposition temperature than $Y(NO_3)_3$, we

observe voids in $La_{0.5}Zr_{0.5}O_x$ films, which suggests $La(NO_3)_3$ enhances the film condensation rate relative to $Y(NO_3)_3$. In contrast to films from MCl_x precursors, we do not observe void formation in dry-annealed films from all-$M(NO_3)_x$ precursors. Degraded film morphology can be mitigated entirely, even under dry conditions, by avoiding MCl_x precursors. Additionally, suppressing void formation in films from NO_3^-/Cl^- precursors under dry conditions requires longer annealing times (i.e. low soft-bake temperatures and slow ramp rates). Still, such films are considerably less dense than steam-annealed films. Densification of steam-annealed films is also largely insensitive to ramp rate because decomposition and condensation processes are already sufficiently separated in time. Therefore, steam annealing serves a practical purpose of producing denser films from mixed precursors with disparate decomposition chemistries using shorter duration annealing treatments than under dry conditions.

Conclusions

Further investigation into the chemistry of steam annealing as a low-temperature metal-oxide thin-film formation method indicates the effect of water-vapor on counterion removal from $M(NO_3)_x$ and MCl_x precursors is dependent on the metal cation, as well as anion, identity. We hypothesize susceptibility of counterion removal to steam annealing is related to the ability of water vapor to mitigate M-X complex formation. Water vapor appears to effectively inhibit the formation of strong M-X complexes, such as In-Cl, to allow for low-temperature counterion removal. However, it appears water vapor does not act upon the equilibria to remove observable quantities of couterion from all precursor systems, as we do not see evidence of enhanced counterion removal in films from $Al(NO_3)_3$ and $AlCl_3$ precursors. Additionally, steam annealing continues to remove

counterions from $In(NO_3)_3$ and $InCl_3$ films at higher annealing temperatures (up to at least 250 °C), and can "repair" rough surfaces of MCl_x films to produce specular thin films.

Morphology studies on films from NO_3^-/Cl^- precursors provide additional chemical insight into annealing conditions that result in void formation in dry-annealed films. We observe voids in films when two precursors with disparate decomposition and condensation rates are mixed. Voids can be effectively eliminated for many mixed-metal precursors using steam annealing. We have also determined there is an important interplay between the soft-bake temperature and the annealing ramp rate in dry conditions. While void-free films can be achieved in dry-annealed films using a low soft-bake temperature (50 °C) and slow ramp rate (5 °C min^{-1}), these films are noticeably less dense than steam-annealed films.

The insights gained regarding the chemistry of steam annealing suggests the effects of atmosphere on thin-film formation chemistry is complex. One result from this study we find particularly interesting is the effect of steam annealing on anion distribution in thin films. Further study of thin films from metal-salt precursors that contain anions with different polarizabilities could establish interesting parallels to the chemistry of anions at air-water interfaces. Because film-formation chemistry is highly dependent on annealing atmosphere, improved understanding of reactions between atmospheric molecules and thin-film gel components is critical for elucidating the thin-film reaction pathway. We have detailed here several benefits (and limitations) of the low-temperature steam annealing method that are useful for understanding ways in which this method can inform process development for metal-oxide thin films from aqueous precursors to maximize and optimize thin-film quality.

Bridge

Chapter V investigates and explains the metal-dependent behavior of steam annealing on thin-film formation chemistry and morphology. Such differences can be explained by the impact of water vapor on the established reaction equilibria involving metal-nitrate and metal-chloride interactions, as well as metal hydroxide condensation to metal oxide. This dissertation concludes with Chapter VI by putting insights gained from studying the entire thin-film reaction pathway of metal nitrates into the context of process development for industrial manufacturing of solution-processed metal-oxide thin films.

CHAPTER VI

CONCLUSION AND OUTLOOK

Authorship Statement

This chapter contains material previously published in *Journal of Materials Chemistry A* **2019**, *7*, 24124-24149. This work was coauthored by Elizabeth A. Cochran, Keenan N. Woods, Catherine J. Page, Darren W. Johnson, and Shannon W. Boettcher. This manuscript was written by E.A.C. with contributions and editorial assistance from all authors.

Outlook: Toward Implementation of Solution-Processed Metal-Oxide Thin Films in Manufacturing

This dissertation has discussed ways in which the unique aspects of metal-nitrate chemistry have been used to facilitate the development of high-quality, solution-processed metal-oxide thin films. Detailed knowledge of the chemical interactions and reactions that influence metal-oxide film formation is important for the future integration of solution deposition into industrial manufacturing. David Mitzi, in his book, *Solution Processing of Inorganic Materials*,[1] discusses six primary drivers that must be addressed in order to make high-volume production of solution-processed inorganic materials commercially viable. Here we discuss how each of the following drivers can be addressed by utilizing and controlling metal-nitrate chemistry:

Low Cost per Unit Area and Large Area-Deposition (Drivers 1 & 2)

In many ways, metal-nitrate precursors are ideal candidates for large-scale production of solution-processed coatings. Metal-nitrate salts are generally inexpensive; however, scalable synthetic methods for metal-nitrate-based precursors have the potential to further decrease raw materials cost. We demonstrated a dissolution approach for the preparation of flat-"Al_{13}" nanocluster precursors from HNO_3 digestion of the abundant, inexpensive $Al(OH)_3$ gibbsite mineral (~ \$0.04 mol^{-1}, compared to ~ \$0.3 mol^{-1} for $Al(NO_3)_3 \cdot 9H_2O$ at 2019 bulk international commodity prices) and demonstrated its usefulness as a Al_2O_3 film precursor.[2] One could imagine extension of this approach to other mineral, hydroxide, or oxide systems to reduce cost and generate large quantities of metal-nitrate precursors.

Another aspect of metal-nitrate chemistry with potential to further address cost is their UV susceptibility, which makes these precursors "self-patterning."[3,4] Because photo-annealing is a metal-oxide-forming reaction, exposure through a shadow mask results in selected-area metal-oxide condensation to pattern the functional material. Therefore, there is potential to utilize such reactions to eliminate photolithography steps.

Solution processing is compatible with a variety of high-volume, ambient processing deposition techniques. The ability to deposit metal oxides via spray-coating, ink-jet, slot-die, etc. makes solution deposition an attractive option for low-cost, large-area deposition technologies, such as roll-to-roll processing.

Ability to Deposit on Diverse Substrates (Driver 3)

The development of low-temperature processing methods, including those discussed in this review, have potential to improve compatibility of solution-deposited thin films with temperature-sensitive substrates. In particular, low-T_d nitrate salts (i.e. In, Ga, Zn, and Al nitrates) have already demonstrated some level of compatibility with low-melting-point polymeric substrates.[5–8] There are comparatively few examples of effective low-temperature processing methods for their high-T_d counterparts (i.e. Y and La).[9,10] There remains substantial opportunity to design processes to lower decomposition temperatures for such materials, including further investigations of UV photo-annealing and steam annealing. A particularly under-explored area of thin-film processing chemistry is that of alternative annealing atmospheres. Metal-nitrate decomposition exhibits a strong dependence on the surrounding ambient. Introduction of different gases to control decomposition kinetics and reaction pathways could provide additional control over thin-film decomposition temperatures and resulting film properties, as we have demonstrated for steam annealing. Control over metal-nitrate decomposition chemistry is crucial for expanding the application base of solution-processed metal oxides to flexible devices.

"Adequate" Electronic Performance (Driver 4)

Recently, great strides have been made to improve the electronic performance of solution-deposited films, with some semiconductors and dielectrics approaching the electronic quality equivalent to vacuum-deposited films.[11–14] The electronic properties of the films are sensitive to impurities (i.e. residual counterions and hydroxides), density, morphology and degree of crystallinity and crystallite size. Improvements to electronic

properties rely heavily on designing processes that leverage control over metal-nitrate chemistry, both in solution and during film formation. As is clear from the wide range of chemical processes that influence the thin-film reaction pathway, controlling these processes is not simple. Complete impurity removal is imperative for maximizing metal-oxide condensation and density. The most-effective strategies demonstrated in the literature thus far include the use of nanocluster precursors and steam annealing, which both result in fewer counterions in the resulting film and enhanced film densification. Control over film morphology/crystallinity would additionally improve electronic performance. In cases where amorphous materials are preferred (for example in the dielectric layers of TFTs), crystallization can often be suppressed by controlling multi-metal composition and annealing conditions.

High Yield, Low Variability (Driver 5)

Devices from solution-processed thin films are often afflicted by low yield and high variability. While these are primarily process-engineering challenges to be addressed during production ramp, consideration of precursor chemistry has been utilized to address such issues on a laboratory scale. Many of the studies highlighted in this review demonstrate how the chemical nature of precursors influences thin-film electronic performance (i.e. olation products, solution temperature, purity, etc.). An understanding of how concentration, temperature, and pH influence solution chemistry could decrease lot-to-lot variation and inform how precursor conditions affect film properties. Additionally, as was demonstrated for electrochemically-treated IGZO precursors, purposeful and controlled changes to solution chemistry can improve film homogeneity by preventing phase segregation, which is a source of variability.[12] While some "M_{13}"-

type nanoclusters are thermodynamic products,[15] there are likely many metal-hydroxo nanoclusters throughout the periodic table that are kinetic products,[16,17] which may present additional scale-up and storage challenges that would need to be addressed in order to maintain batch-to-batch consistency.

Long-Term Stability and Durability (Driver 6)

Long-term stability of metal-oxide films produced from metal-nitrate precursor solutions is strongly dependent on successful elimination of hygroscopic nitrate counterions. Additionally, some metal oxides are prone to water absorption (i.e. La_2O_3),[18] which can be exacerbated by residual nitrate content in thin films. This is another area in which chemistry can be used to improve processing conditions to enhance stability. We have shown steam-annealing metal-nitrate-based thin films improves moisture resistance. We attribute the ambient stability of steam-annealed films to differences in their chemical and physical properties compared to dry-annealed films, namely fewer residual nitrates and higher density.[19] Another strategy to improve thin-film stability toward water involves incorporating moisture-resistant components into the film using capping layers or preparing ternary metal-oxide compositions. Thin capping layers of HfO_2[20,21] and ZrO_2[22] on hygroscopic metal-oxide thin films have also proven to be successful strategies for inhibiting water uptake. Our research groups have developed aqueous routes for the preparation of lanthanum zirconium and lanthanum aluminum oxides (LZO, $LaAlO_3$) from metal-nitrate precursors, which exhibit reduced hygroscopicity compared to La_2O_3.[23,24] Apart from water absorption, ternary metal-oxide compositions can improve stability toward other impurities. LZO thin films are more resistant to atmospheric

carbonate absorption compared to La_2O_3,[19,24] whereas $LaAlO_3$ contains fewer hydrogen impurities than Al_2O_3,[25] which results in improved dielectric properties.

Metal-oxide thin-film stability and durability are influenced by precursor choice, processing conditions, and intrinsic metal-oxide properties, all of which must be considered when developing solution-deposition methods.

Conclusions

This dissertation has highlighted ways in which understanding metal-nitrate chemistry has contributed to the advancement of solution deposition as a method for preparing high-quality metal-oxide thin films. An examination of bulk metal-nitrate chemistry demonstrates the sensitivity of decomposition behavior to the metal identity and the annealing atmosphere, which has implications for selecting processing conditions that optimize metal-oxide formation in thin films. Solution-speciation chemistry exhibits a complex dependence on concentration, pH, and temperature and can influence film properties, including density, homogeneity, and chemical composition. Some unique aspects of metal-nitrate reactivity, such as UV photolysis and reactions with water vapor (i.e. steam annealing), are utilized to enhance nitrate removal and metal-oxide conversion during thin-film formation. Continued improvement of our understanding of metal-nitrate chemistry will further aid process optimization to facilitate high-volume manufacturing of high-quality metal oxide thin films for (opto)electronic applications.

APPENDIX A

CHAPTER IV SUPPLEMENTARY INFORMATION

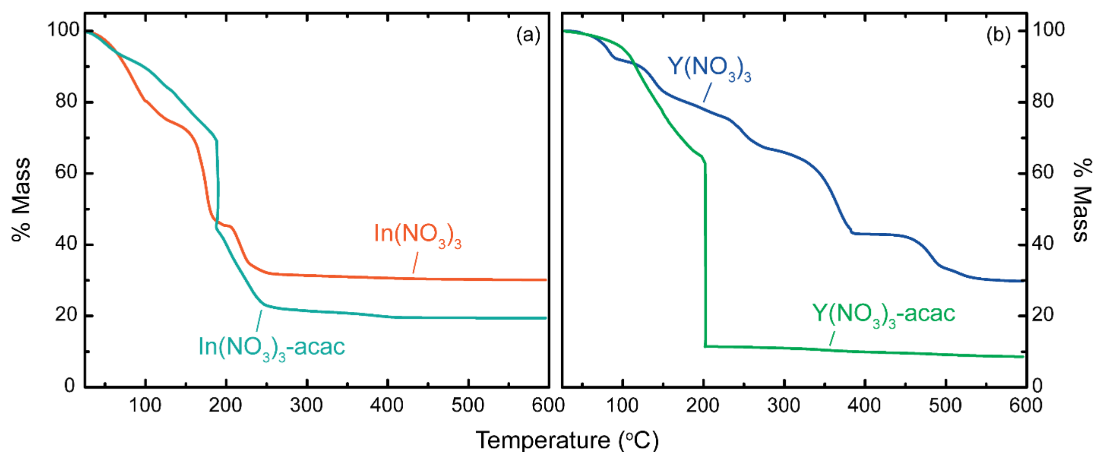

Figure A.1. TGA curves for $In(NO_3)_3$ and $Y(NO_3)_3$ combustible mixtures and their corresponding controls. The $In(NO_3)_3$-acac trace shows a slight tail after the combustion event at 200 °C, which we attribute to the "cool zone" effect,[1] that results in thermal decomposition of remaining starting material. The $Y(NO_3)_3$-acac mixture is explosive leading to mass loss from the sample pan. Therefore, the final mass reading is not representative of complete conversion to Y_2O_3.

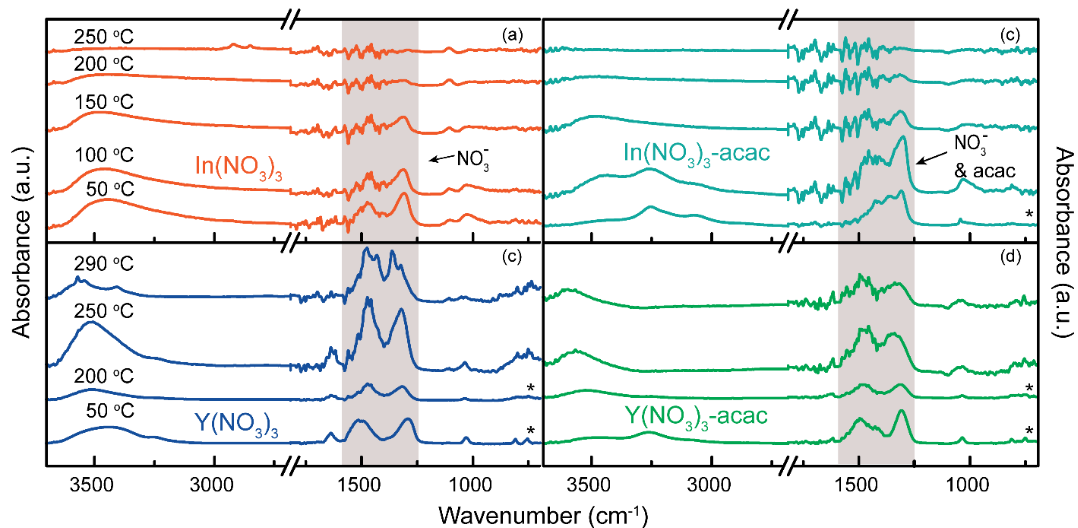

Figure A.2. Transmission FT-IR analysis of films spun from acac precursors and their corresponding controls without fuels. Unless indicated with *, a multiplicative factor of 5 was applied to the absorbance in order to make low-intensity modes more visible. The most intense modes associated with the fuels and nitrates (highlighted in gray) were monitored to determine the temperatures of fuel and nitrate removal. For acac, these modes correspond to C=O, C-H, and C-C (1300-1600 cm^{-1} all overlapping[2]) for $M(acac)_x$ complexes. A monotonic decrease in absorbance with annealing temperature for acac and nitrate active modes is observed in all cases. These data support the conclusion that acac and nitrates decompose by independent thermal decomposition.

XPS Fitting Procedure

The O 1s spectra of several film and powder samples were fit in order to quantify metal oxide and nitrate content to evaluate the efficacy of the combustion reactions. First, the C 1s spectra were fit in order to charge shift the spectra and identify/quantify contributions of carbon-oxygen species (from adventitious carbon and combustion byproducts) to the O 1s spectra. The C 1s spectra were fit with the following five peaks centered at: 284.8 (C-H, peak A), A + 1.5 (C-O, peak B), A + 3.0 (O=C, peak C), A + 4.0 (O=C-O, peak D), and A + 4.5 eV (CO_3^{2-}, peak E). The positions of these peaks were allowed to vary by ± 0.2 eV. The FWHM and Lorentz/Gaussian (L/G) ratio of all peaks in the C 1s spectra were constrained to be the same values, fit by the software. For the O 1s spectra, the ester oxygen peak was initially set to 533.7 (O=C-**O**, peak F) and the ether and ketone peaks were constrained to F-0.9 (± 0.2) (C-O) and F-1.5 (± 0.2) (**O**=C-O & **O**=C) relative to the ester peak.[3] In most cases, better fits were obtained by fitting all adsorbed carbon as one peak. For the powder samples, the positions of these peaks were allowed to vary by as much as ± 0.7 eV, as differential charging led to greater uncertainty in these binding energies. Additional peaks for NO_3^-, OH, and M-O were also included and initially centered at 533 (± 0.5), 530.5 (no constraints), and 528-529 eV (no constraints; dependent on oxide "shoulder" position), respectively. For some samples, the hydroxide and carbonate species were fit as one peak, since their binding energies are known to overlap (531-532 eV for OH, 530.5-531.5 eV for CO_3^{2-}).[4] The full-width at half maximum (FWHM) was set to 1.5 eV and constrained to ± 0.5 eV (in cases where the C-H peak in the C 1s spectrum was closer to 2 eV, ± 1 eV was used). The FWHM and Lorentz/Gaussian (L/G) ratio of all peaks in the O 1s spectra were constrained to be the same values, fit by the software. The total integrated areas of the ester, ether and

ketone/carbonate peaks were constrained to reflect the expected relative quantities based on the C 1s fit.

The positions of the hydroxide and oxide peaks in the O 1s spectra for the films and powders prepared from $Y(NO_3)_3$,[5,6] $In(NO_3)_3$,[7] and $Mg(NO_3)_2$[4,8] precursors are in agreement with literature reports (Figure 4.2, 4.5, & AA3-AA8). Quantitative comparisons of metal oxide and nitrate content for each sample are shown in Table 4.1.

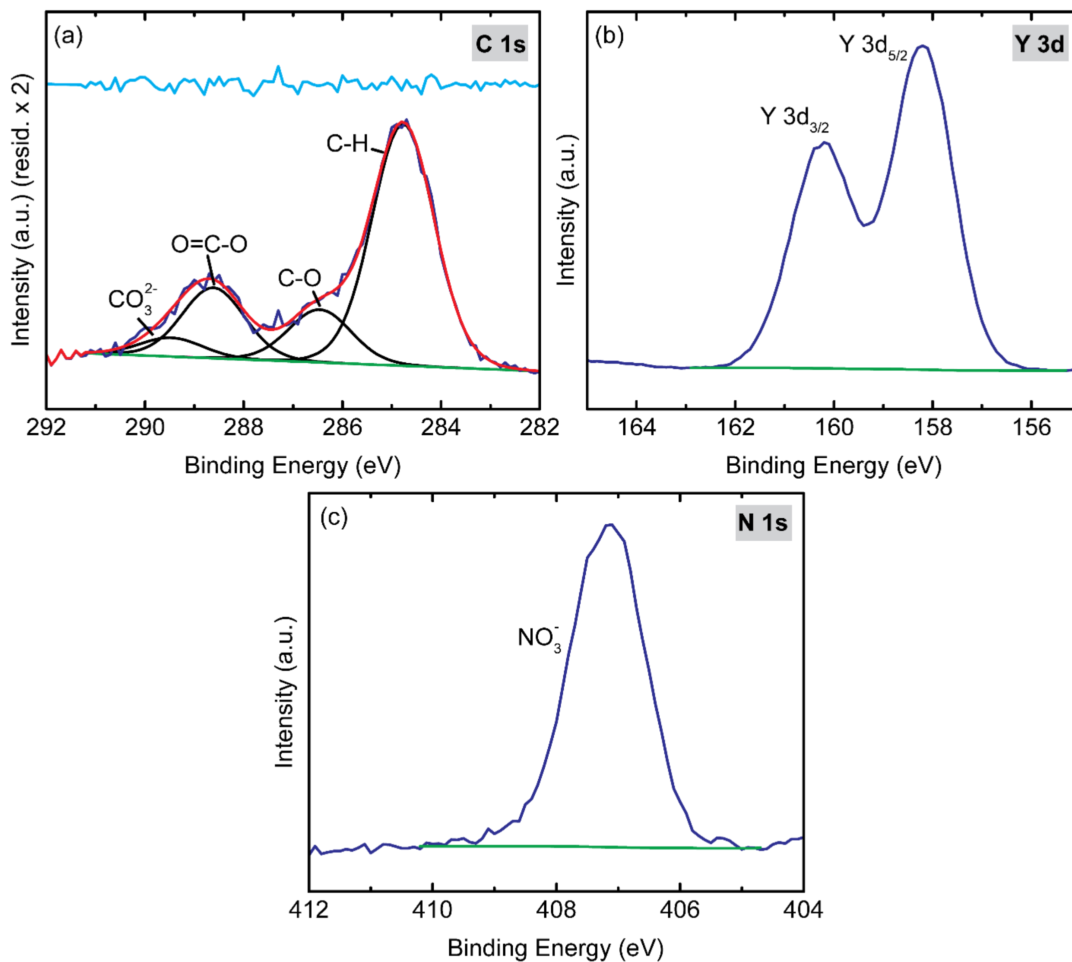

Figure A.3. XP spectra of a $Y(NO_3)_3$-acac film for (a) C 1s (fitted), (b) Y 3d, and (c) N 1s. The fitted O 1s spectrum can be found in Figure 4.2. Each plot contains the raw data (dark blue) and background (green). For the fitted C 1s spectrum, the total fitted peak envelope (red) and individual adventitious carbon peaks (black), and the fit residuals (light blue) are also shown.

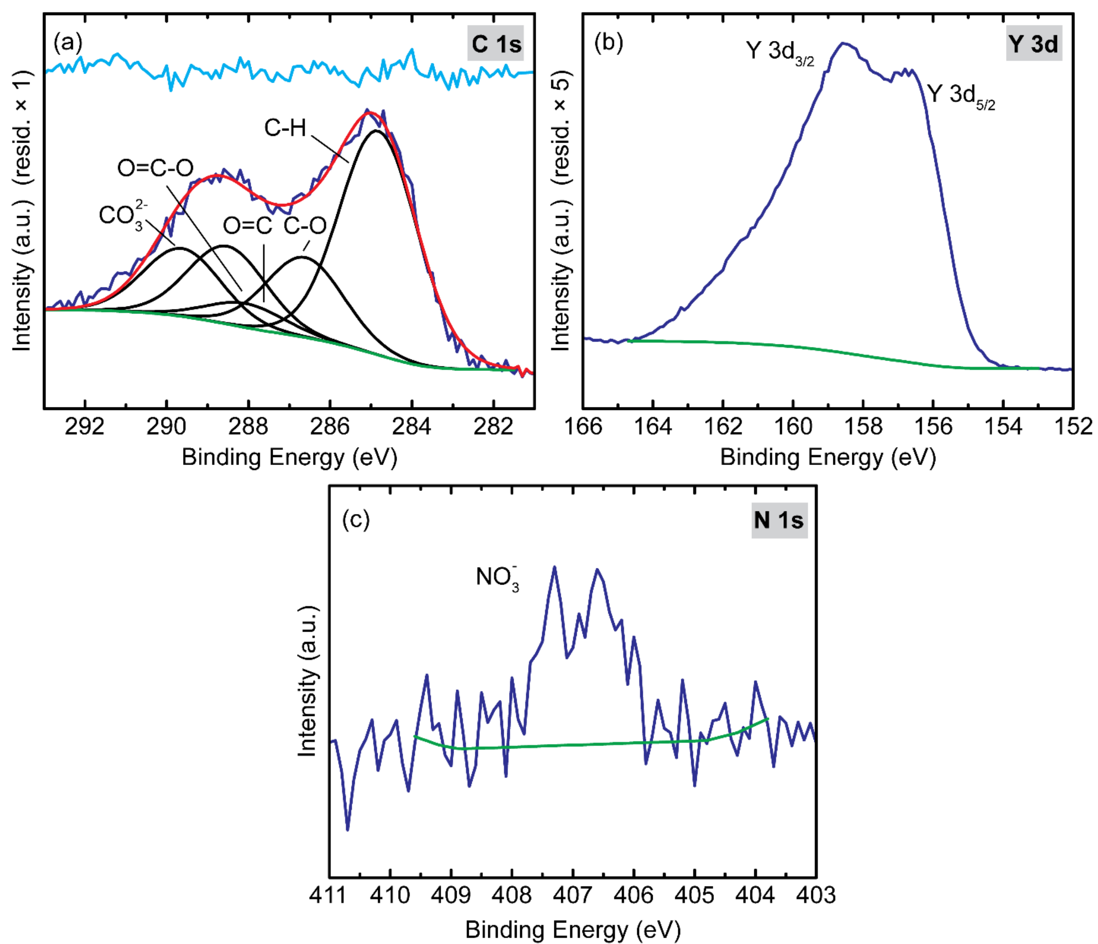

Figure A.4. XP spectra of the $Y(NO_3)_3$-acac powder that has undergone combustion. The fitted O 1s spectrum can be found in Figure 4.2.

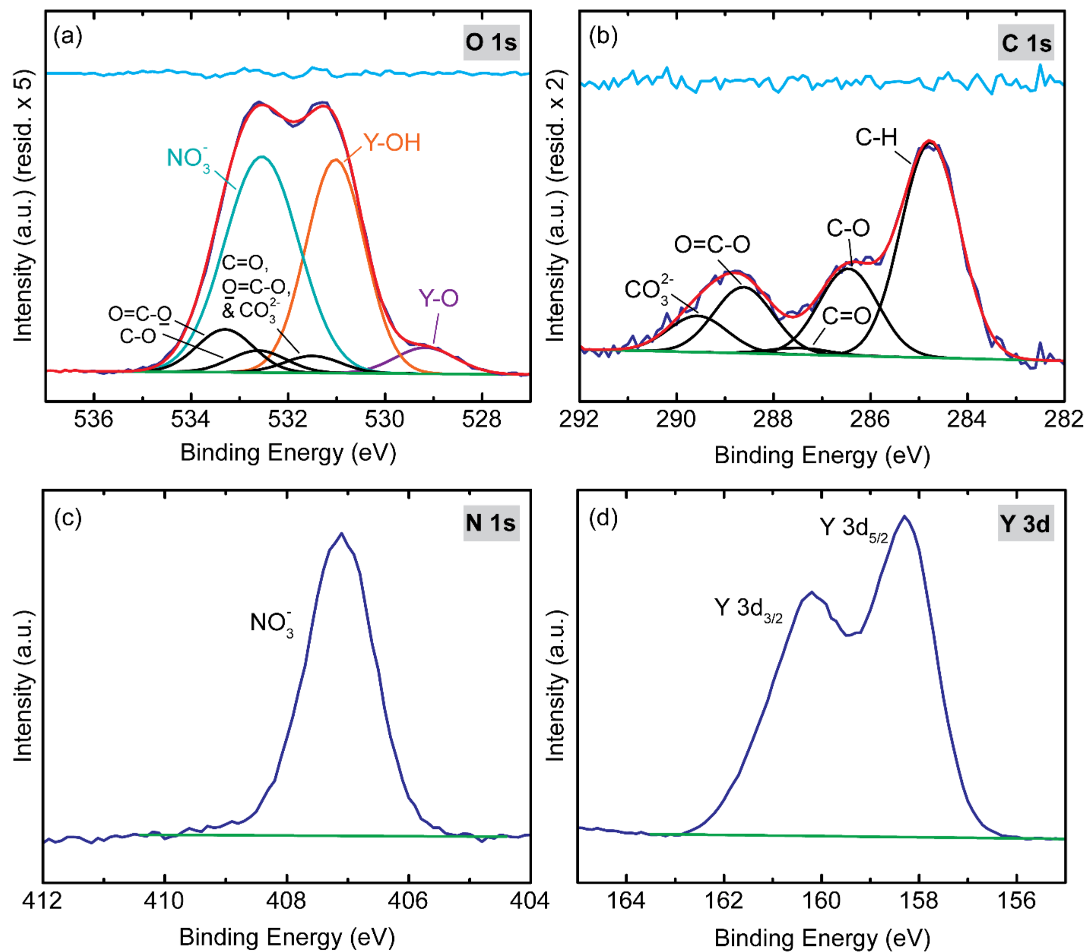

Figure A.5. XP spectra for a $Y(NO_3)_3$ film (no fuel). The O 1s spectrum (a) is fit to compare Y-O content to the $Y(NO_3)_3$-acac film (see Table 4.1 for compiled results). Additional spectra shown are (b) C 1s, (c) N 1s, and (d) Y 3d.

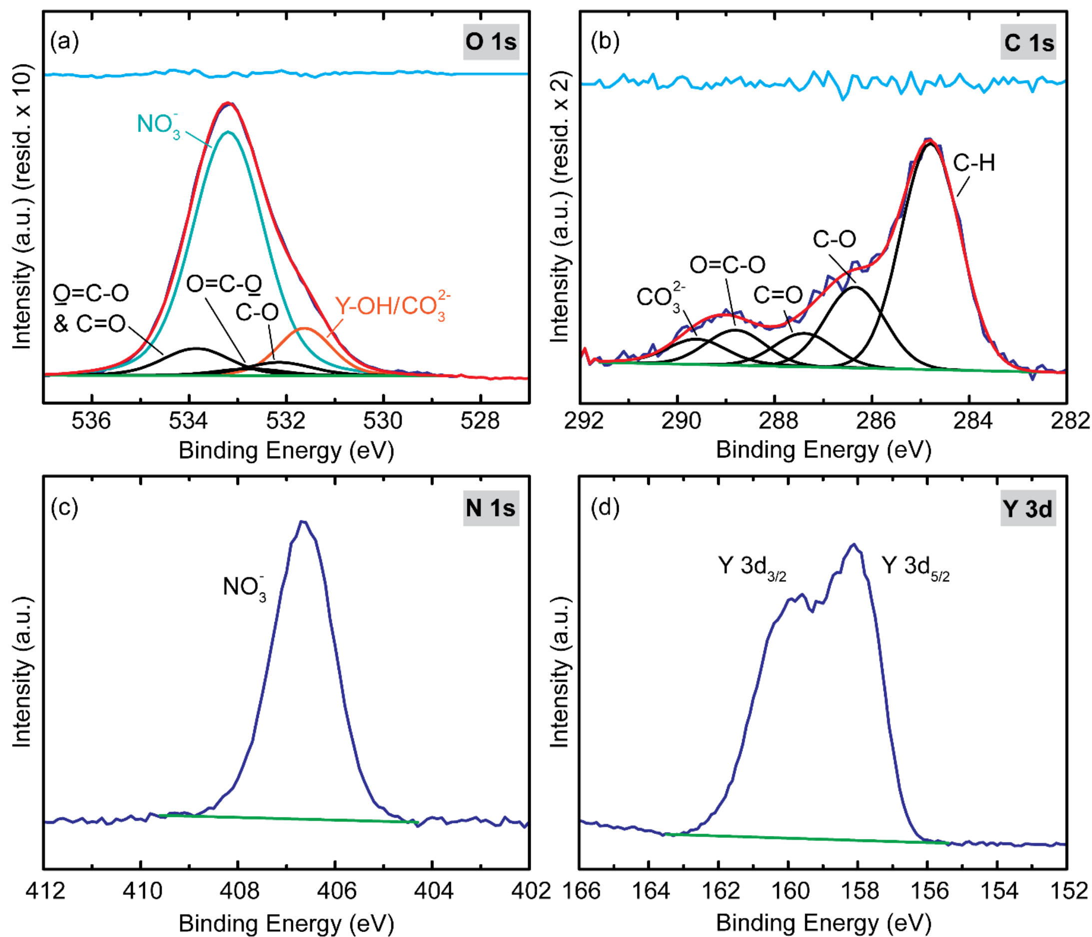

Figure A.6. XPS for $Y(NO_3)_3$ powder annealed at the same temperature as the combustion mixtures. A peak associated with metal-oxygen content was not fit for this powder (a). Note nitrate content (c) is similar to that of films prepared from $Y(NO_3)_3$ and $Y(NO_3)_3$-acac precursors (Table 4.1). Additional spectra shown are (b) C 1s and (d) Y 3d.

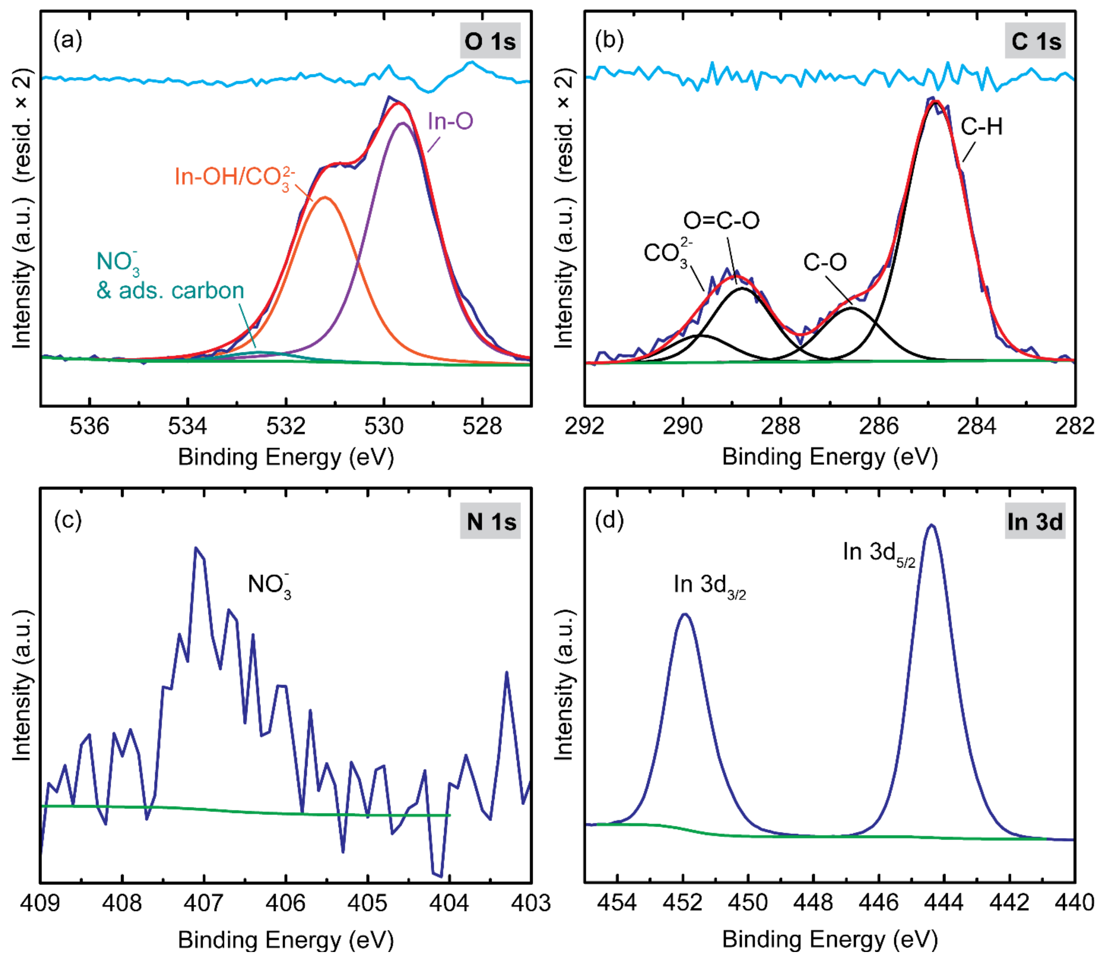

Figure A.7. XP spectra for a film prepared from $In(NO_3)_3$ (no fuel). Adsorbed, adventitious carbon and nitrate are fit as one peak (teal) in the O 1s spectrum (a). Other spectra shown are: (b) C 1s, (c) N 1s, and (d) In 3d.

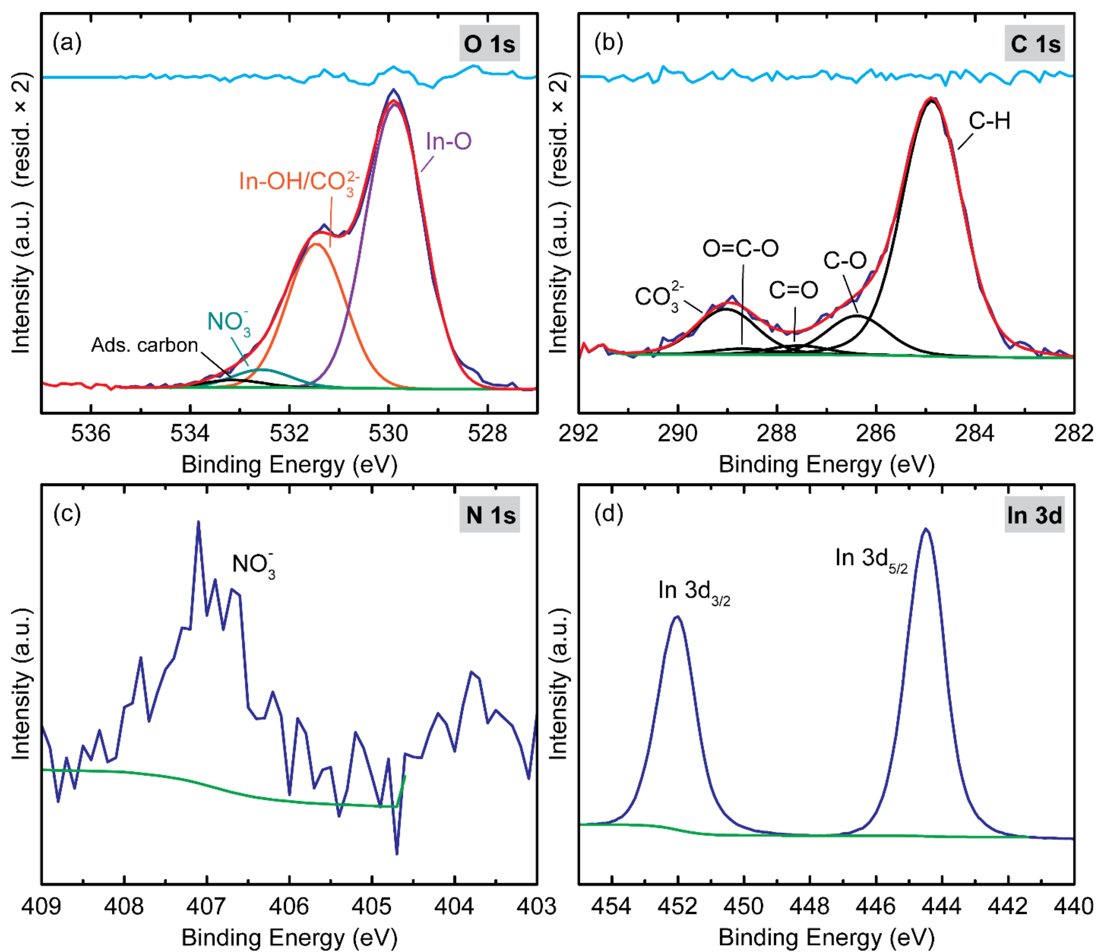

Figure A.8. XP spectra for an $In(NO_3)_3$-acac film. Note the film prepared from the $In(NO_3)_3$ (no fuel) precursor contains similar metal-oxygen (a) and nitrate (c) content (Table 4.1). Spectra for (b) C 1s and (d) In 3d are also shown.

TGA-MS Experimental Details

Thermogravimetric analysis mass spectrometry (TGA-MS) was performed using a TA Instruments Q600 equipped with a Hiden Analytical HPR-20 quadrupole mass analyzer. Samples (20 to 30 mg) were heated at a rate of 10 °C min^{-1} under N_2 (flow rate: 100 mL min^{-1}) in alumina sample pans. Electron ionization (EI) mass spectra were acquired with a 70-eV ionization energy and 100 μA emission current. Selected mass-to-charge (*m/z*) ratios for each sample were monitored in multiple ion detection (MID) mode with a dwell time of 500 ms and a settle time of 50 ms.

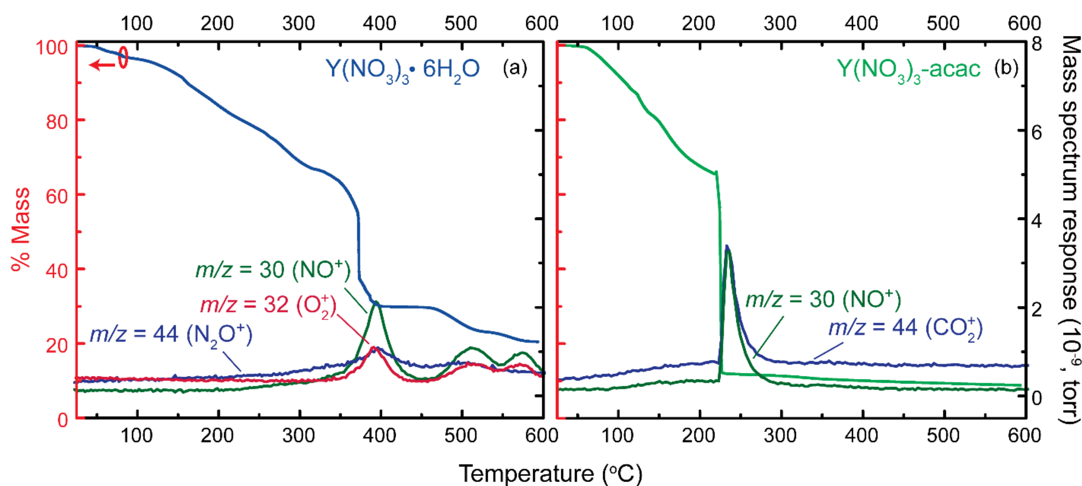

Figure A.9. TGA-MS results for $Y(NO_3)_3$ powders/gels with and without acac. Other fragments associated with acac and solvent were detected but are omitted for clarity. While nitrate loss is observed over a 250 °C temperature range for the $Y(NO_3)_3$ salt, as determined by detection of the NO^+ fragment, this occurs over a 50 °C range when acac is present. These results clearly illustrate combustion leads to nitrate removal at lower temperatures. We use these data to inform our interpretation of TPD-MS data on the corresponding film systems.

Supplemental Discussion of TPD-MS Data on the $Y(NO_3)_3$ Film Systems

Nitrate decomposition has two distinct mechanisms identifiable by TPD-MS.[9–13] Low temperature decomposition involves the formation of various NO_x gases, with the primary fragment being NO^+ (*m/z* = 30), accompanied by N_2^+ (*m/z* = 28) and N_2O^+ (*m/z* = 44).[9] The second higher temperature mechanism involves the detection of NO^+ and O_2^+ (*m/z* = 32).[9–13] For the film prepared from $Y(NO_3)_3$, these two mechanisms are observed from ~ 200-400 °C and 400-600 °C, respectively (Figure A.10a-b).

The $Y(NO_3)_3$-acac film shows these same two nitrate removal mechanisms, with the high-temperature mechanism (NO^+ and O_2^+ fragmentation) clearly visible from ~ 400-550 °C (Figure A.10c). While the nitrate removal temperature is lowered by ~ 50 °C when acac is present, we do not attribute this to combustion. We observe that acac incorporation likely does alter film formation chemistry in the low-temperature region (75-250 °C). However, we speculate most of the fragments shown contain contributions of multiple species and, therefore, the chemistry occurring is complex.

The mass fragment for the acac molecular ion (*m/z* = 99 for $C_5H_7O_2^+$) is detected from ~ 75-200 °C (Figure A.10d). We suspect the acac ligand becomes displaced (by H_2O, NO_3^-, or OH groups) as the pH of the film changes with increased annealing temperature. In addition to the *m/z* = 99 fragment, we observe a feature in the *m/z* = 28 trace over this same temperature range, which we assign to CO^+. The similar shape of the two mass traces in this low-temperature range suggests these fragments are produced from the same desorbed species. We hypothesize that CO^+ is associated with acac desorption rather than decomposition or combustion, as *m/z* = 28 can also be a minor fragment from electron ionization of acetylacetone.[14] From 230 °C to almost 400 °C, we see NO^+ (*m/z* = 30), N_2^+ (28), and N_2O^+ (44) appearing in similar ratios in the $Y(NO_3)_3$

film without fuel (Figure A.10c-d). The onset of nitrate decomposition occurs ~ 100 °C lower than in the film without fuel (Figure A.10a-b). We hypothesize this is a result of HNO_3 formation, which is facilitated by is H^+ donation when Y(acac)$_x$ is formed. It appears that H_2O desorption is associated with nitrate removal at these temperatures, based on the similar features in the fragment traces for H_2O^+ and NO^+ (Figure A.11b). This may be indicative of HNO_3/H_2O azeotrope formation at low temperatures.

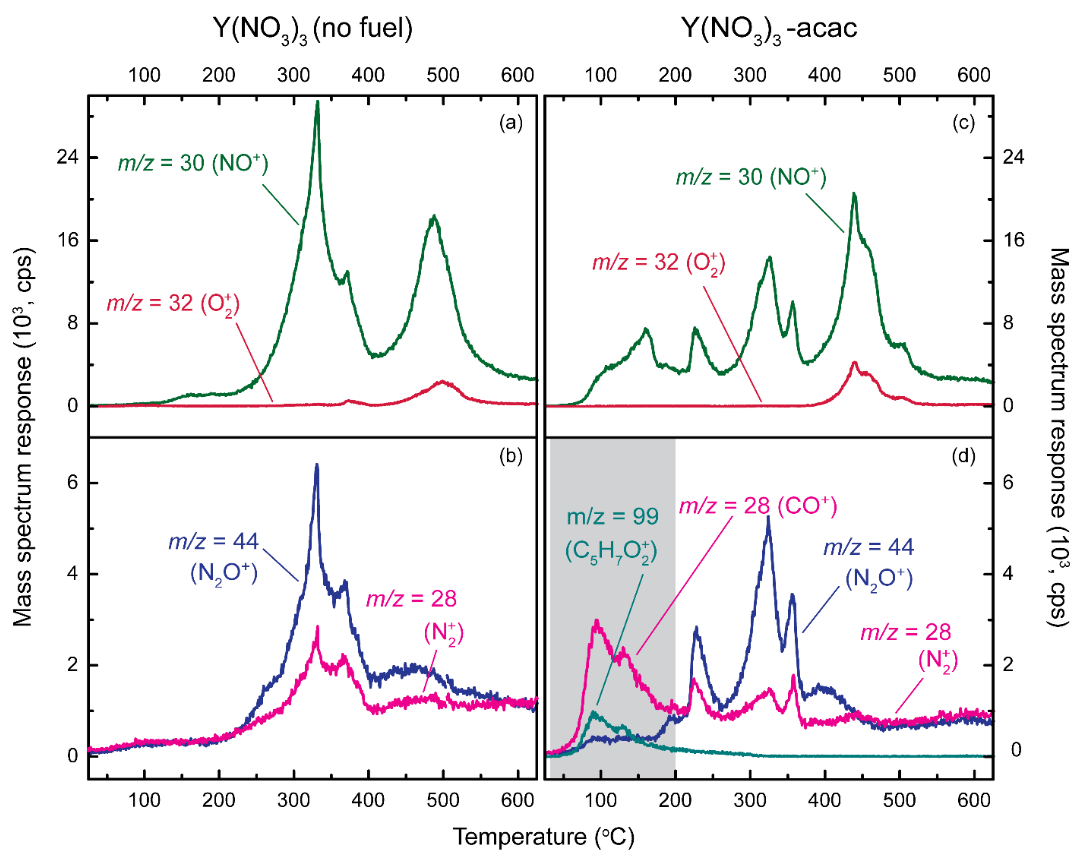

Figure A.10. TPD-MS results for (a-b) $Y(NO_3)_3$ and (c-d) $Y(NO_3)_3$-acac films. Note that free acac fragments appear to desorb from the film early in the annealing process and below the combustion ignition temperature (T_{ig} = 200 °C measured for bulk samples by TGA). Differences in mass fragments associated with nitrate (e.g., NO^+, N_2^+, and N_2O^+) are observed at low temperature when acac is present.

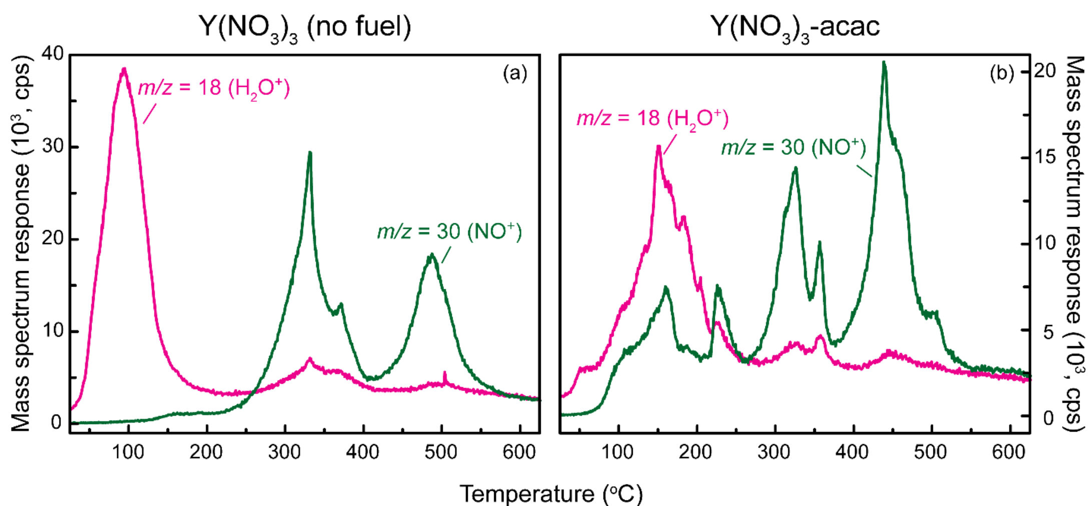

Figure A.11. H_2O^+ and NO^+ fragments observed by TPD for films spun from the (a) $Y(NO_3)_3$ and (b) $Y(NO_3)_3$-acac precursors. From 25-200 °C, desorption of the NO^+ fragment is accompanied by water, which may be indicative of HNO_3/H_2O azeotrope formation. NO^+ detected above this temperature is associated with thermal NO_3^- decomposition (Figure A.10).

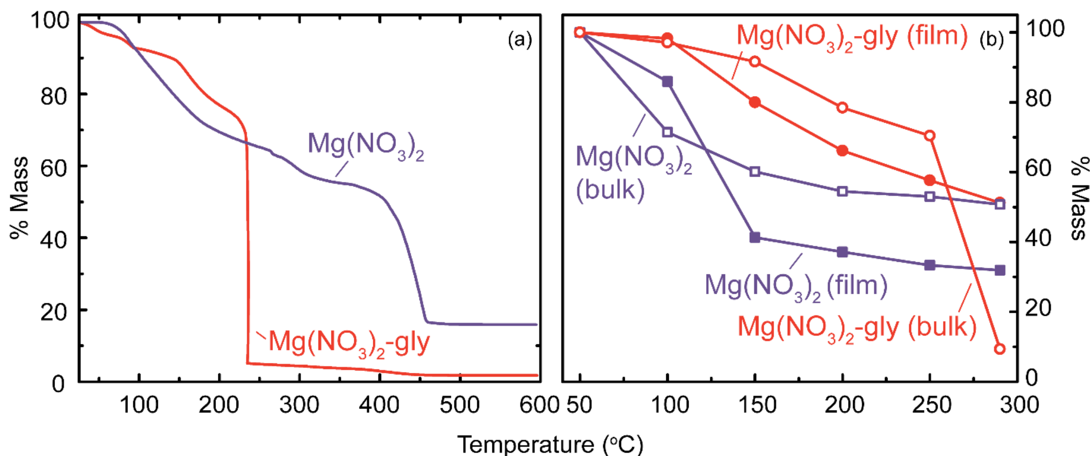

Figure A.12. Thermal characterization of (a) bulk $Mg(NO_3)_2$ (-glycine) precursors by TGA and (b) bulk gels and thin films (QCM) by step-wise heating. In (b), the same color and marker style are used for powders and films prepared from the same precursor, with open and filled markers representing powder and film samples, respectively. The percent mass reading of 2 % in (a) for the $Mg(NO_3)_2$-glycine mixture is a result of an explosive combustion reaction that nearly empties the sample pan. For stepwise heating of this same powder, we attempted to contain the majority of the combustion byproduct in a glass beaker placed over the sample. The combustion T_{ig} is identified as 230 °C for the bulk $Mg(NO_3)_2$-glycine mixture, approximately 200 °C lower than the decomposition temperature of $Mg(NO_3)_2$. When stepwise heating is used, a 290 °C anneal is needed in order for $Mg(NO_3)_2$-glycine to undergo combustion. Additionally, an Al TGA pan was needed in order ingite a combustion front in the $Mg(NO_3)_2$-glycine sample (all other bulk samples where annealed on a Si wafer piece). We speculate the higher thermal conductivity of Al compared to Si speeds up ignition.

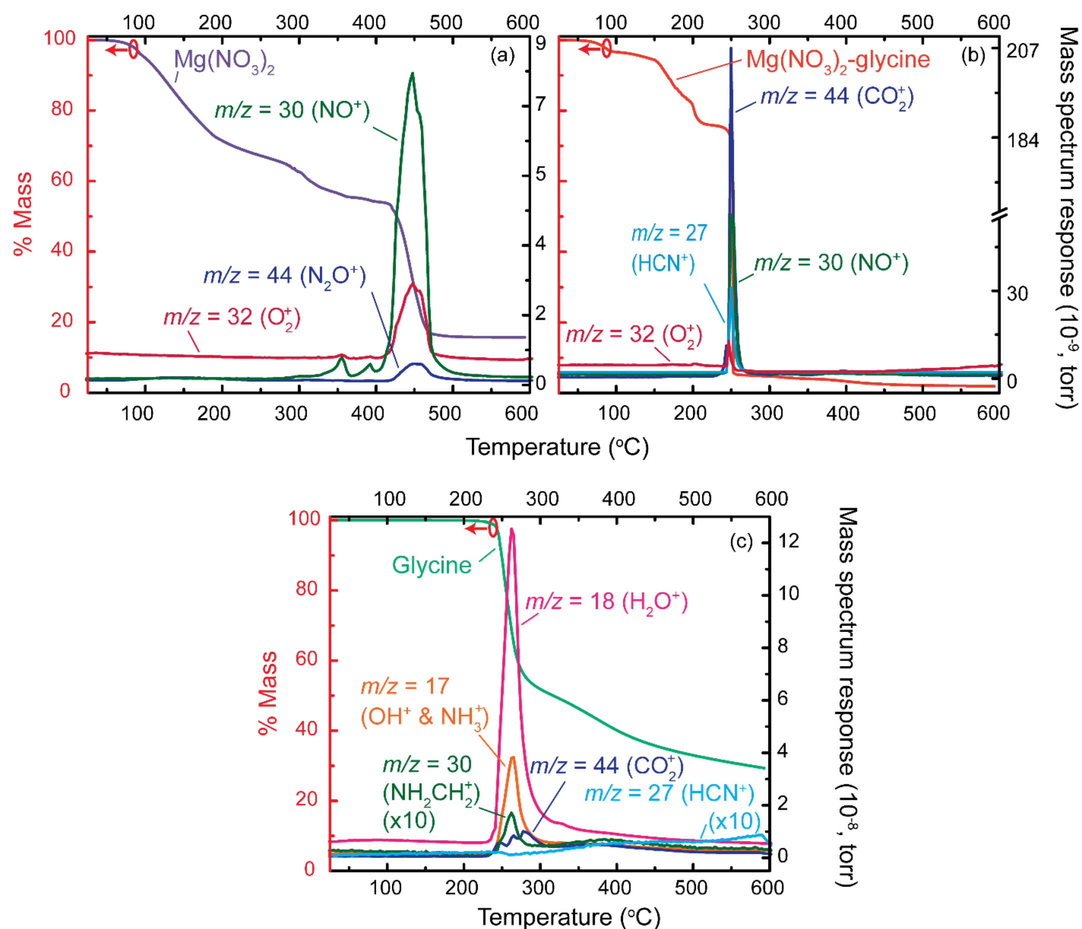

Figure A.13. TGA-MS results for bulk gels/powders of (a) $Mg(NO_3)_2$, (b) $Mg(NO_3)_2$-glycine, and (c) glycine. We observe the decomposition and fragmentation of NO_3^- into NO^+, O_2^+, and N_2O^+ from 350 to 500 °C for $Mg(NO_3)_2$ (a). When glycine is added (b), these same fragments and a combustion explosion are detected over a 20 °C temperature range centered at 250 °C, indicating a change in the metal oxide formation mechanism when the fuel is used. The glycine spectrum (c) shows that $NH_2CH_2^+$ is a minor contributor to the *m/z* = 30 fragment but likely contributes to the mass trace for this fragment we observe by TPD-MS in the $Mg(NO_3)_2$-glycine film.

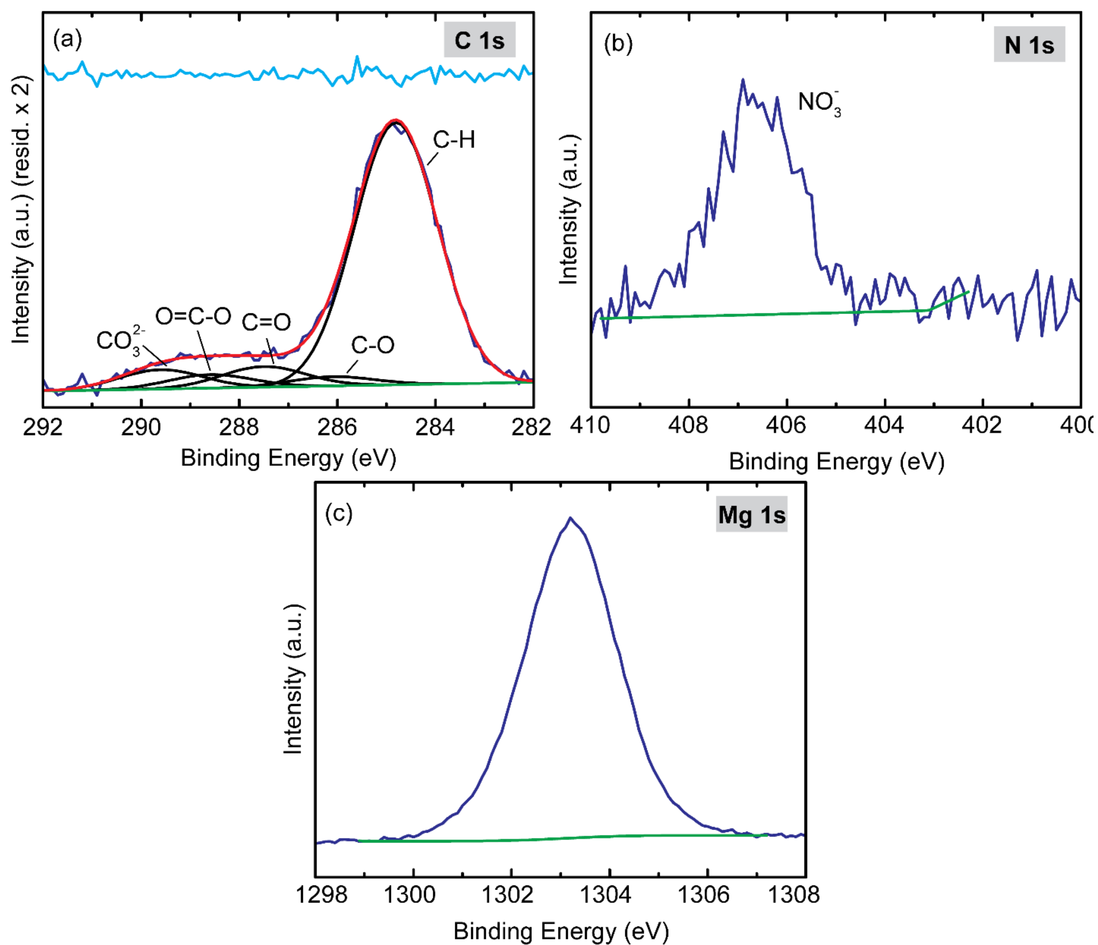

Figure A.14. Remaining XP spectra for a $Mg(NO_3)_2$ film (no fuel). The O 1s spectrum can be found in Figure 4.5a. Spectra shown are: (a) C 1s, (b) N 1s, and (C) Mg 1s.

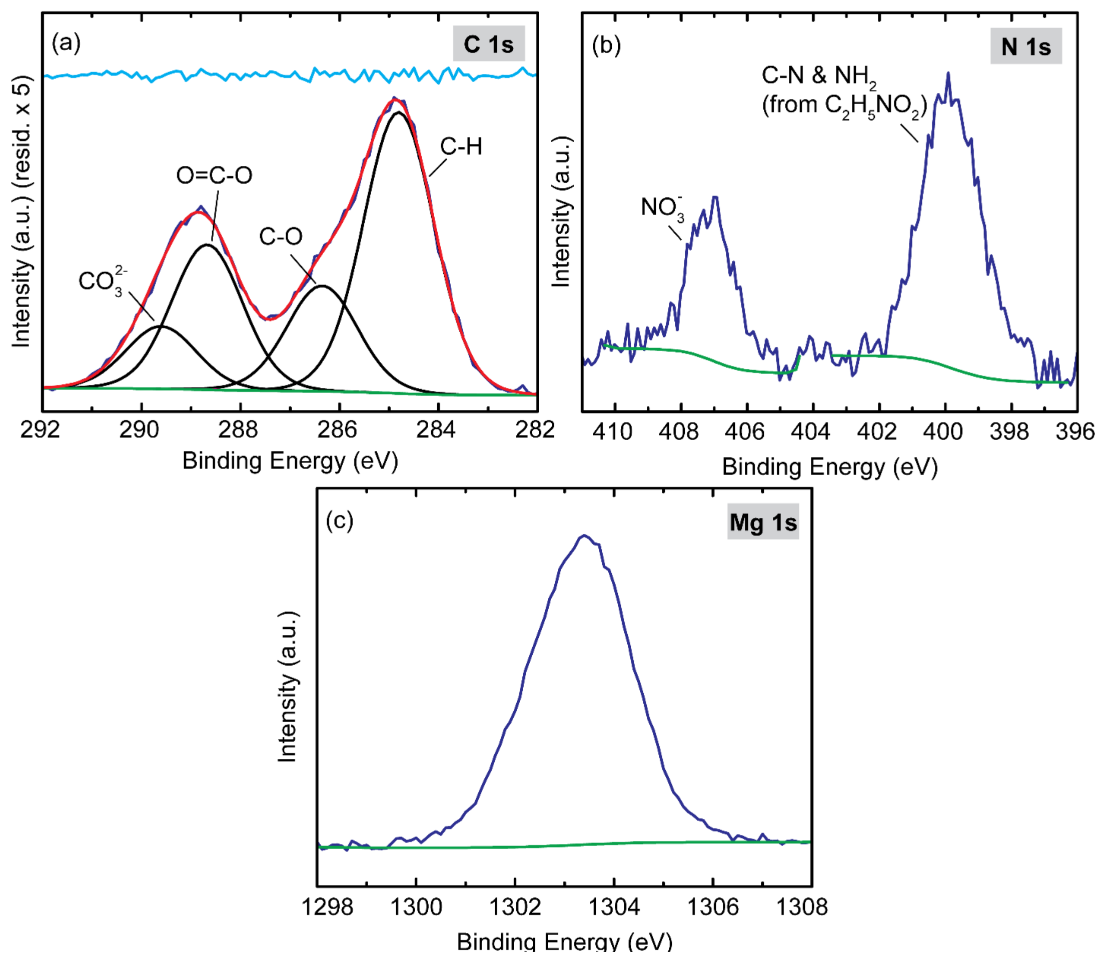

Figure A.15. Remaining XP spectra for a film prepared from the $Mg(NO_3)_2$-glycine precursor. The O 1s spectrum can be found in Figure 4.5b. The N 1s spectrum (b) shows glycine is still present, as evidenced by the peak at 399.7[15] eV. Adsorbed carbon in the O 1s and C ls spectra likely also contain contributions from glycine. The C 1s (a) and Mg 1s spectra (c) are also shown.

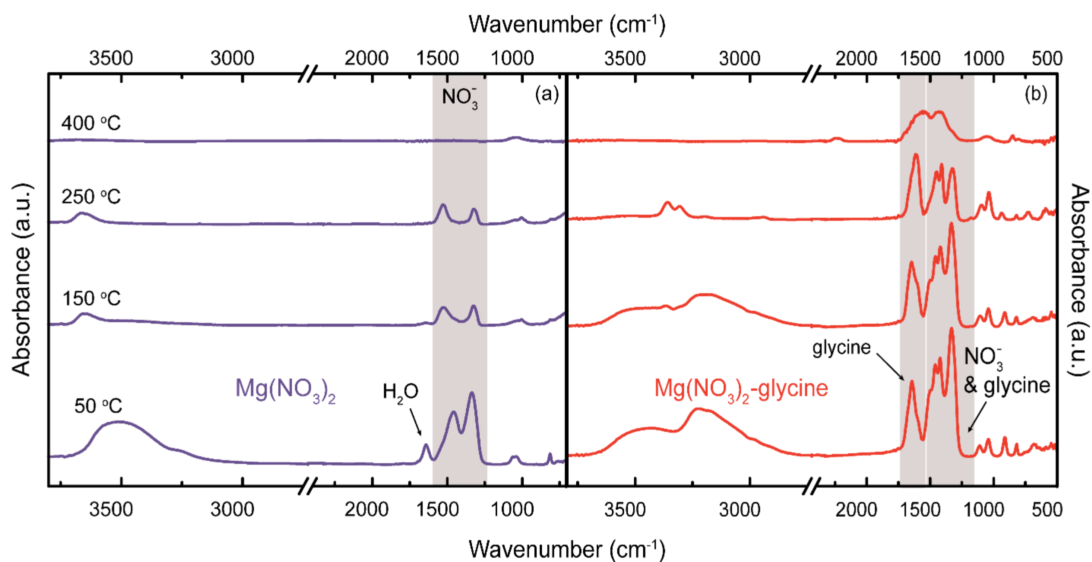

Figure A.16. FT-IR characterization of (a) $Mg(NO_3)_2$ and (b) $Mg(NO_3)_2$-glycine films. Note that glycine modes are detectable in the film at least 150 °C beyond where nitrates are no longer detected, indicating that the fuel is likely less volatile than the nitrate counterions. These films were annealed in 50 °C temperature steps from 50 to 400 °C (5 min at each step).

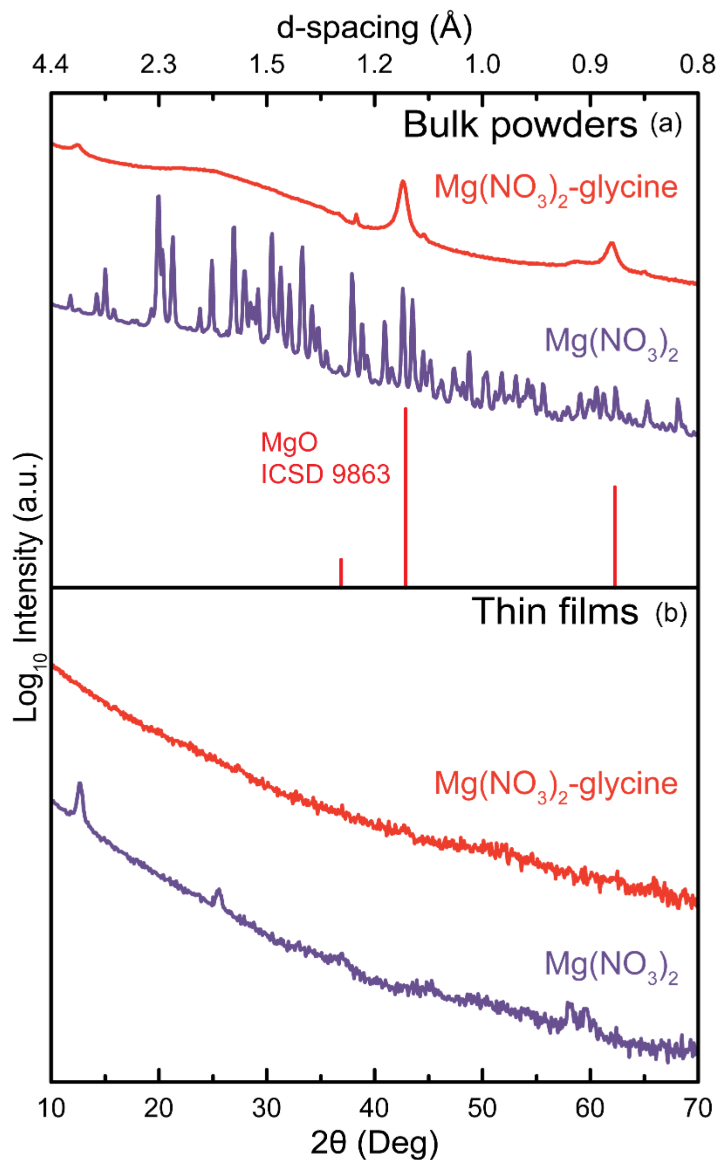

Figure A.17. XRD patterns for $Mg(NO_3)_2$-containing (a) bulk precursors and (b) films annealed at 300 °C for 30 min. The bulk $Mg(NO_3)_2$-glycine mixture forms MgO upon combustion. A low-angle peak at ~12° suggests a layered (oxy)hydroxide structure is present (not indexed). The bulk $Mg(NO_3)_2 \cdot 6H_2O$ salt does not decompose when thermally treated ($Mg(H_2O)_6(NO_3)_2$; ICSD 23220). A film prepared from the $Mg(NO_3)_2$-glycine precursor is X-ray amorphous, whereas the film prepared from the $Mg(NO_3)_2$ precursor shows diffraction indicative of the same layered structure observed in the bulk $Mg(NO_3)_2$-glycine combustion byproduct. (We note that the combustion byproduct of the bulk $Mg(NO_3)_2$-glycine mixture was most explosive when reacted in small quantities, i.e. ~ 100 mg in thermally-conductive Al pans.)

Supplemental Discussion of TPD Results for the $Mg(NO_3)_2$ Film Systems

Like for the $Y(NO_3)_3$ system, we observe two distinct modes of nitrate removal in the film prepared without glycine. The NO^+ fragment is detected in the 300-600 °C range from a $Mg(NO_3)_2$ film, accompanied by N_2^+ and N_2O^+ from ~ 300-400 °C and O_2^+ from 450-600 °C (some N_2^+ and N_2O^+ is still observed at these higher temperatures) (Figure A.18a-b). While there is likely some contribution from glycine to *m/z* = 30 ($NH_2CH_2^+$), TGA-MS on the glycine powder confirms it is a minor decomposition product (Figure A.13). NO^+ is detected at lower temperatures, from 150-300 °C, when glycine is present (Figure A.18c). However, fragments associated with glycine decomposition[16–18] (*m/z* = 27 (HCN^+), 28 (CO^+) and 44 (CO_2^+)) are still detected up to 600 °C (Figure A.18d), well above the temperatures of NO^+ detection. We do not attribute this apparent shift in nitrate decomposition/desorption to combustion, as nitrate and glycine decomposition byproducts desorb independently. Simultaneous desorption of all volatile film components is expected upon ignition if a combustion reaction were to occur.

Again, contributions of multiple fragments with the same *m/z* make deducing the film formation chemistry complex. Control experiments performed with $MgCl_2$ in place of $Mg(NO_3)_2$, i.e., with no oxidizer present, show a similar shift in the temperature of chloride removal (*m/z* (Cl^+) = 35), from 400-500 °C for $MgCl_2$ alone, to 200-300 °C when glycine is present (Figure A.19). Additionally, HCl^+ (*m/z* = 36) is detected at these lower temperatures, suggesting that glycine may facilitate acid formation, which can readily evaporate. We suggest glycine has a similar effect in the $Mg(NO_3)_2$ system.

It is well known that Mg^{2+} and NO_3^- do not form ion pairs in solution (provided Mg^{2+} maintains at least six waters of hydration)[19,20] and, instead, they associate via outer-

sphere interactions. Glycine is a coordinating ligand capable of complexing with many metal ions including Mg^{2+}.[21] The zwitterionic character of glycine ($^{+}H_3NCH_2CO_2^{-}$) in the precursor solution (pH = 5) enables its carboxylic acid group to effectively complex alkaline earth cations like Mg^{2+}.[22] We hypothesize that as the film reaches advanced stages of dehydration (< 6 mol H_2O per mol Mg^{2+}), glycine ligands prevent ion pair interactions between Mg^{2+} and NO_3^-, which changes the chemical pathway for nitrate loss. We note the O_2^+ fragment (m/z = 32), which is indicative of NO_3^- thermal decomposition (to NO^+ and O_2^+, discussed previously),[9–13] appears over a lower temperature range, from 50-400 °C (Figure A.19c) compared to 500-600 °C (Figure A.19a) when fuel is not used. These results indicate NO_3^- thermal decomposition occurs at lower temperatures when glycine is present. We propose NO_3^- can also leave the film as HNO_3, with possible proton donors being H_2O and the terminal NH_3^+ on the glycine ligand. While evidence suggests glycine incorporation in the precursor solution lowers the nitrate removal temperature, it appears to occur through low-temperature thermal decomposition and possibly HNO_3 formation, not via combustion. However, due to the fact that nitrates are still detected in a comparable film by XPS, we suspect the absolute temperature of nitrate removal is different than what we observe by TPD-MS. Nevertheless, TPD-MS corroborates XPS results that suggest the film does not undergo combustion.

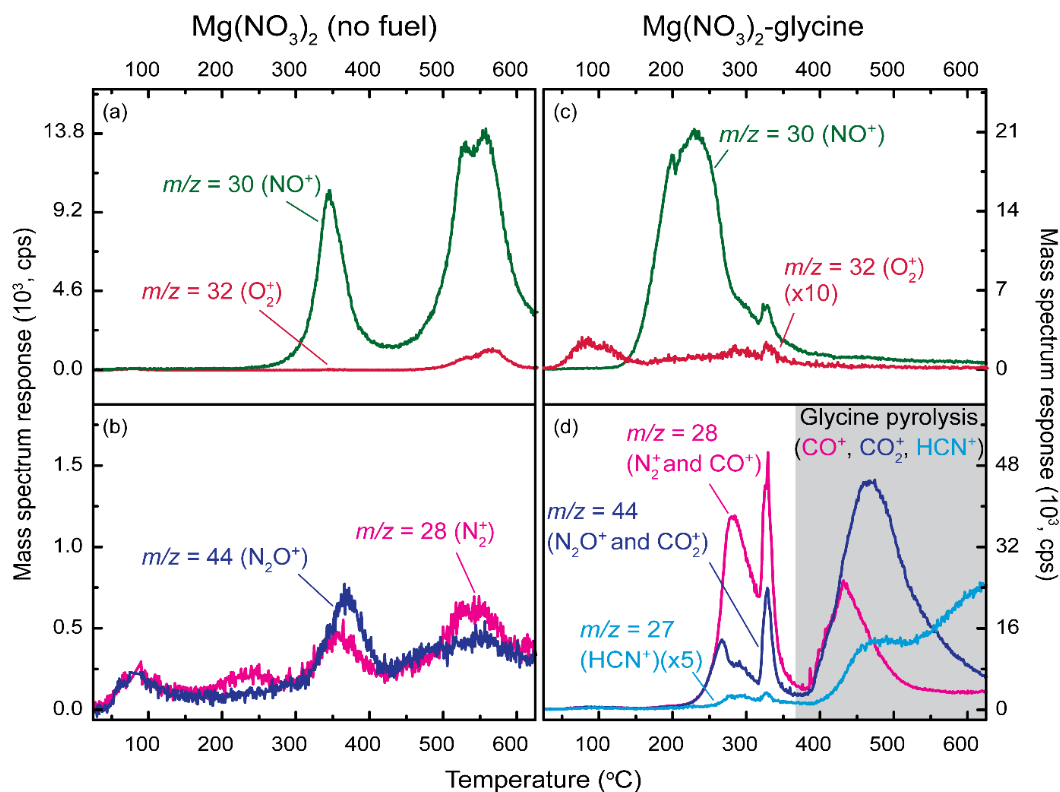

Figure A.18. TPD-MS results for (a-b) $Mg(NO_3)_2$ and (c-d) $Mg(NO_3)_2$-glycine films. These results show a reduced nitrate removal temperature when glycine is present, identified by the shift in NO^+ desorption temperatures (a and c). Features in the *m/z* = 28 and 44 traces (d) from 200-350 °C are attributed to overlapping events of NO_3^- and glycine thermal decomposition. From 350-600 °C, glycine pyrolysis byproducts contribute to these fragment traces (d). The observation of substantial glycine thermal decomposition at high temperature is not consistent with low temperature combustion of the glycine/nitrate mixture in the thin films.

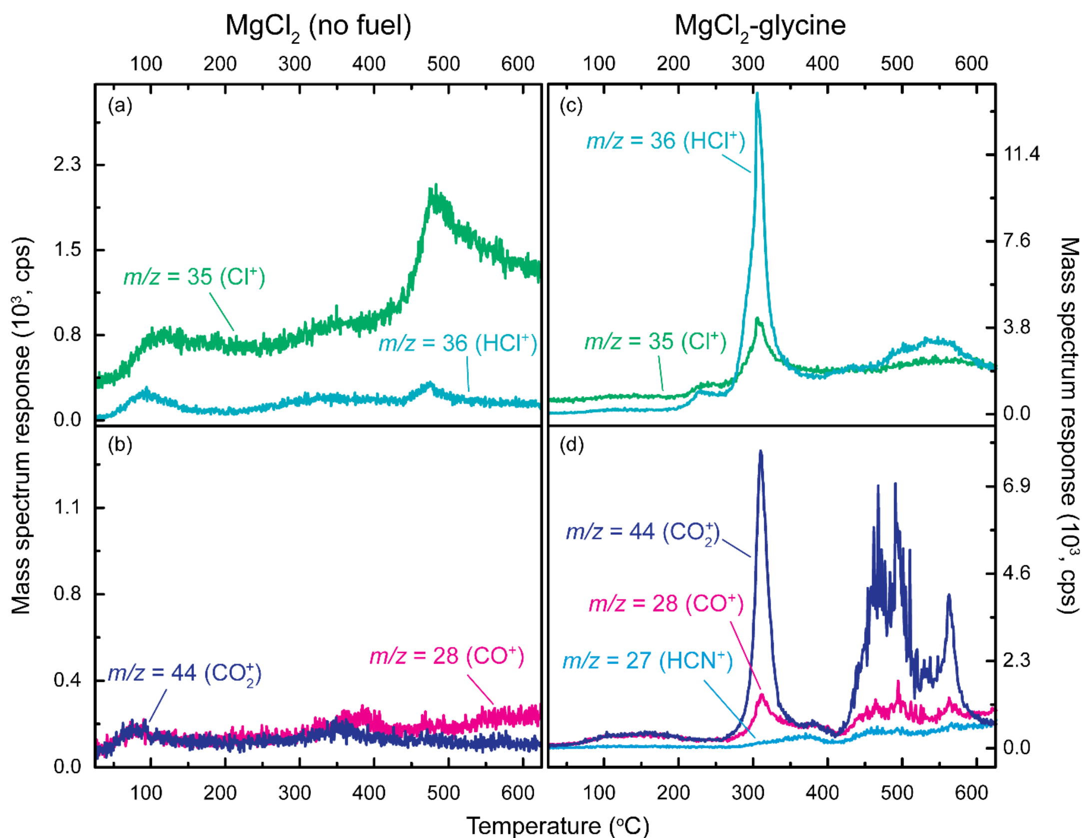

Figure A.19. TPD-MS results for films made from $MgCl_2$ precursors show glycine affects the temperature range of Cl^- removal ($m/z = 35$). The observation of HCl^+ fragments ($m/z = 36$) supports our hypothesis that the temperature of NO_3^- removal is altered due to glycine deprotonation and acid formation (HNO_3, in that case).

Additional Oxidizer and Fuel Systems

We investigated a variety of $M(NO_3)_x$ oxidizer systems with a wide range of thermal decomposition temperatures. The $Al(NO_3)_3$(-acac) precursor was prepared in a similar fashion ($Al(NO_3)_3 \cdot 9H_2O$; Strem chemicals, 98+% purity), using the same 1.5:1 NO_3^- to fuel molar ratio, as in the $In(NO_3)_3$-acac and $Y(NO_3)_3$-acac precursors. Bulk $Al(NO_3)_3 \cdot 9H_2O$ has a very low decomposition temperature and loses most of its mass by 200 ^oC (Figure A.20a). The $Al(NO_3)_3$ and acac mixture losses most of its mass just above 100 ^oC. However, mass loss is not complete at this temperature and mass loss continues up to 350 ^oC (Figure A.20a), which we attribute to the "cool zone" effect[1] (described previously). For the films, QCM measurements show that both films lose most of their mass by 200 ^oC (Figure A.20b). XRD patterns show all films and powders, with the exception of heat-treated $Al(NO_3)_3$ (which appears to remain a complex nitrate phase), are X-ray amorphous (Figure A.21). Due to the lack of evidence for combustion in our other film systems, we attribute the low-temperature amorphous Al_2O_3 formation to a low decomposition temperature of $Al(NO_3)_3$ in thin-film form.

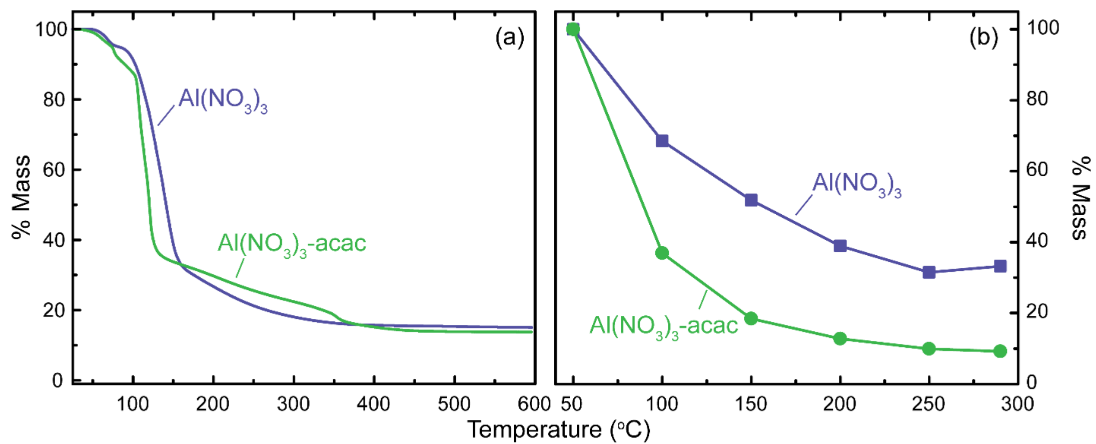

Figure A.20. Thermal analysis of $Al(NO_3)_3$(-acac) by (a) bulk TGA and (b) QCM for powders and films, respectively.

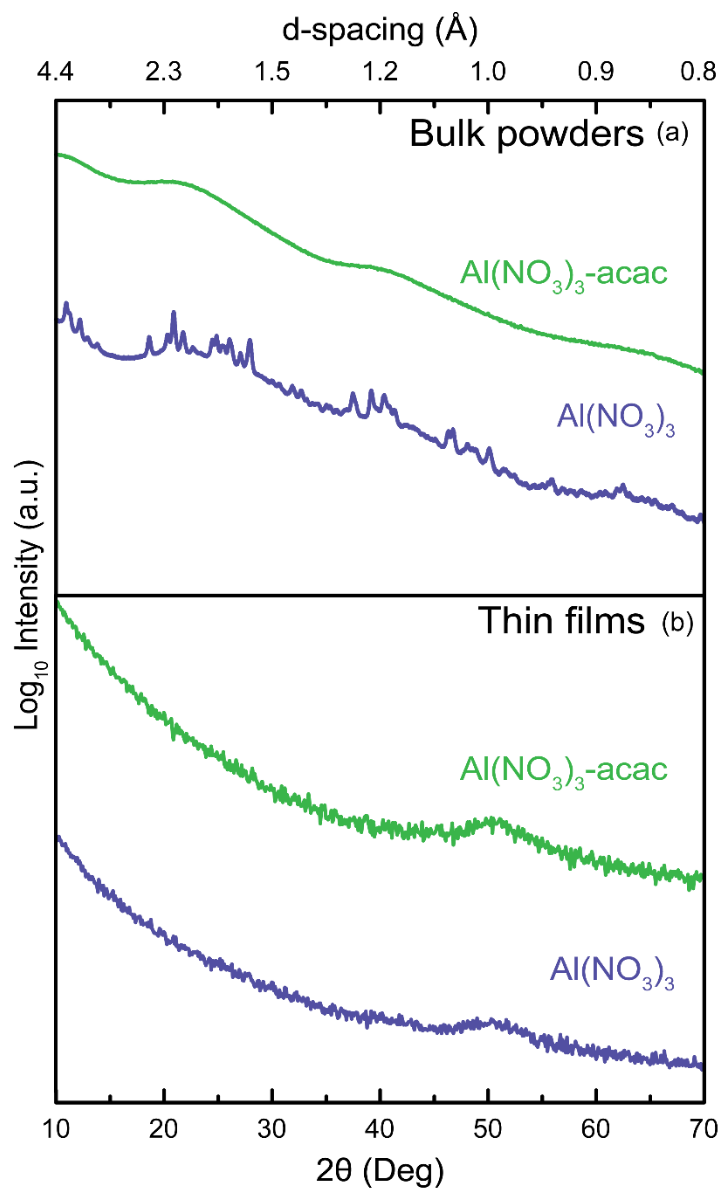

Figure A.21. XRD patterns for $Al(NO_3)_3$ and $Al(NO_3)_3$-acac (a) powders and (b) films. All powders and films were annealed at ~ 215 °C for 30 min. Three-layer films were used for the GIXRD scans (scan parameters used were optimized for films 30 nm thick; single-layer films were only 10-15 nm).

Urea, another commonly-used fuel in combustion thin-film synthesis, was also investigated. The fuel (100 mg; Alfa Aesar, 99.3+ %) was added to the 0.2 M $M(NO_3)_3$ 2-methoxyethanol solutions (where M= Al, In, and Y) and the precursor was aged for 72 h, per a previously-described procedure.[23]

Figure A.22a shows that urea, while a frequently-used fuel in solution combustion synthesis of bulk Al_2O_3,[24] In_2O_3,[25] and Y_2O_3,[26] it is less effective than acac under the conditions used in the TGA (i.e. slow heating rates, air flow). These combustion reactions using urea all reportedly require annealing temperatures ≥ 500 °C;[24–26] therefore, it is unsurprising that we do not observe low-temperature combustion in these systems. These high temperatures may be needed in order to prevent fuel decomposition prior to ignition, as we observe by TGA that urea rapidly decomposes beginning at 150 °C under air (Figure A.22c). Urea provides a slight decrease in the final mass loss event for the $Al(NO_3)_3$ and $Y(NO_3)_3$ systems from 300 to 250 °C and 500 to 450 °C, respectively, compared to the hydrated nitrate salts (Figure A.1, A.20, & A.22). While T_{ig} is not identifiable for the $Y(NO_3)_3$ with urea system from the TGA trace, steep mass loss events at 150 and 200 °C in the $Al(NO_3)_3$ system appear to signify combustion (Figure A.22a). All films lose a majority of their starting mass by the 200 °C annealing step (Figure A.22b).

We monitored film evolution with annealing temperature by FT-IR to correlate the mass loss observed by QCM with specific chemical species. By tracking the IR active modes of urea and nitrate, we see that urea, $Al(NO_3)_3$, and $In(NO_3)_3$ decompose at similar temperatures and, therefore, it is difficult to discern the reactions taking place in these two films (Figure A.23a-b). However, for the $Y(NO_3)_3$ film, we see the urea modes

disappear before the nitrate modes (Figure A.23c), which suggests combustion does not occur in these films.

By considering the chemical reactions occurring before and during the combustion process, we can understand why acac appears to be a better low-temperature fuel than urea for bulk powders. It is well known that the first step in hydrated metal nitrate decomposition is nitric acid (HNO_3) liberation, which is accomplished through protonation of nitrate ions as the salt dehydrates.[27–29] Many mechanistic explanations for combustion between nitrate and fuels have been proposed, and several conclude the strong oxidizer HNO_3 must form for combustion to occur.[30–33] This pre-combustion HNO_3 formation must occur at temperatures below the fuel decomposition temperature. Mechanistic studies of $Y(NO_3)_3$•$6H_2O$ thermal decomposition suggest a product with a Y^{3+} to NO_3^- molar ratio of 2:5 forms near 200 °C, consistent with HNO_3 evolution.[28] Provided enough heat has accumulated for ignition, combustion occurs when HNO_3 contacts the acac ligands. While no mechanistic studies of $In(NO_3)_3$ decomposition have been reported, the salt likely also liberates HNO_3 near 200 °C. Conversely, $Al(NO_3)_3$ releases HNO_3 as the H_2O-HNO_3 azeotrope beginning at 120 °C.[27] This higher volatility of HNO_3 in the $Al(NO_3)_3$ salt compared with $Y(NO_3)_3$ and $In(NO_3)_3$ leads to oxidizer depletion, as well as heat dissipation as HNO_3 evaporates, which may explain why combustion ignition is not readily observed at slow ramp rates used in TGA (10 °C min^{-1}) for $Al(NO_3)_3$-fuel mixtures. Thermal analysis of urea powder alone shows the fuel begins to decompose rapidly at ~ 150 °C in air (Figure A.22c), which is before the onset of HNO_3 formation in the $Y(NO_3)_3$ and $In(NO_3)_3$ systems, and thus perhaps prevents ignition of the combustion reaction.

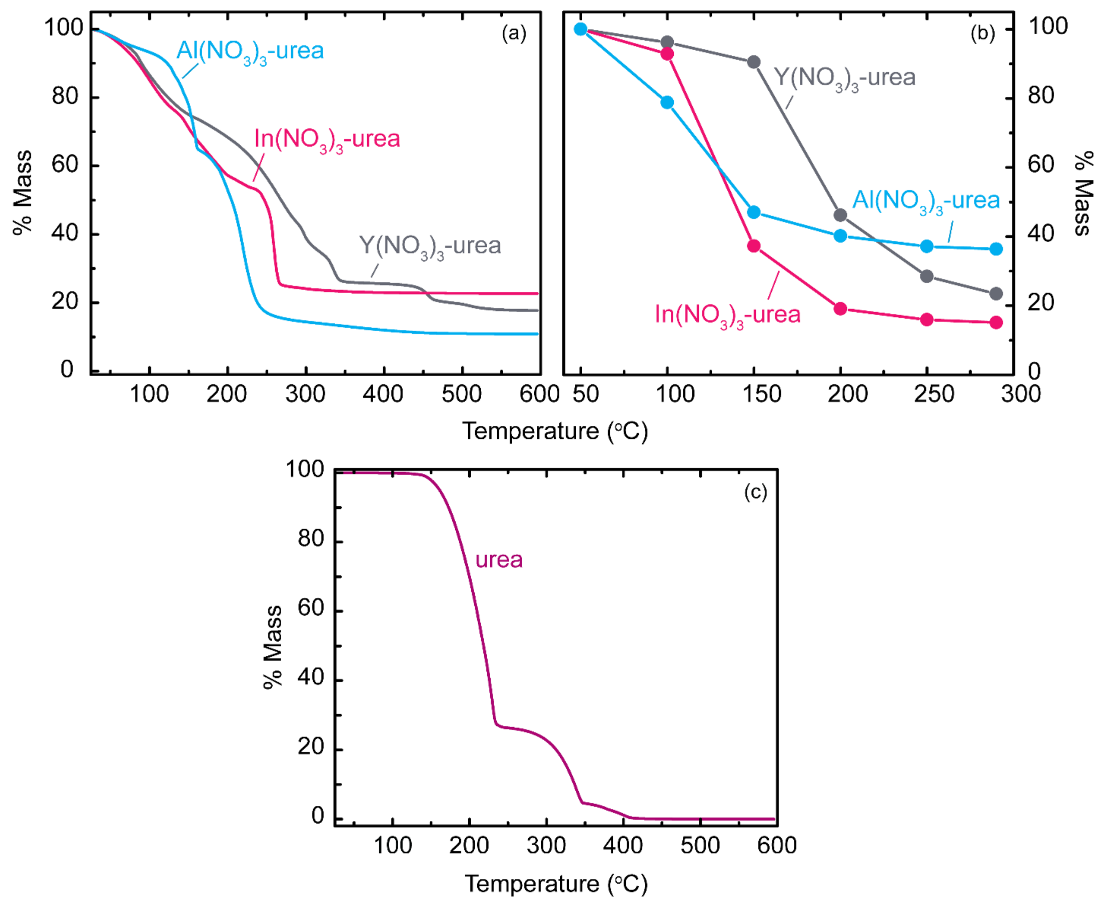

Figure A.22. Thermal analysis of (a) urea-containing gels by bulk TGA, (b) thin films prepared from urea precursors by QCM, and (c) urea powder by bulk TGA.

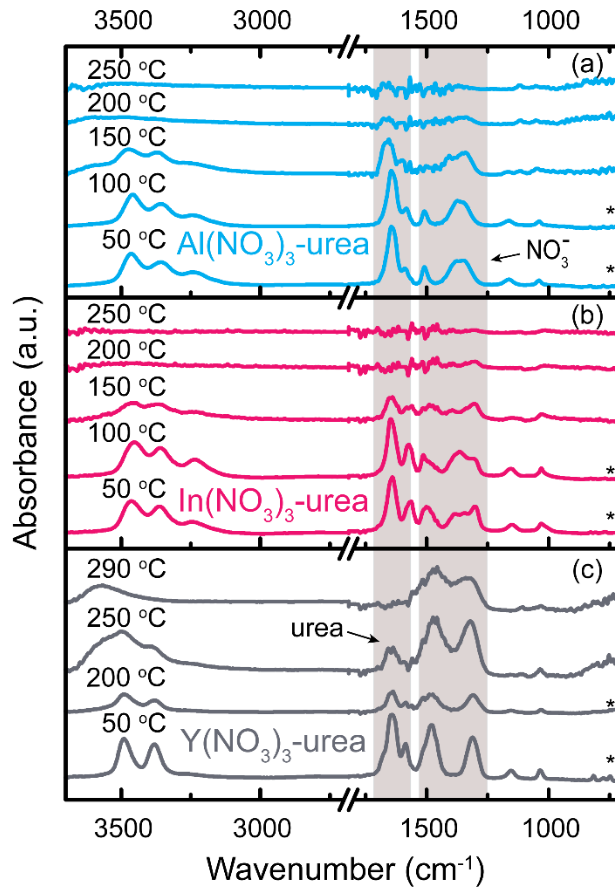

Figure A.23. Transmission FT-IR analysis of films spun from urea precursors. Unless indicated with *, a multiplicative factor of 5 was applied to the absorbance in order to make low-intensity modes more visible. The most intense modes associated with the fuels and nitrates (highlighted in gray) were monitored to determine the temperatures of fuel and nitrate removal. These modes correspond to C=O, N-H (both ~ 1500-1650 cm^{-1}) and C-N (1480-1490 cm^{-1}, overlapping with NO_3^-) for urea. Additional peaks for urea can be seen at 3350 and 3460 cm^{-1}, assigned to N-H modes.

Since the $Al(NO_3)_3$-urea is the only oxidizer-urea mixture for which a clear T_{ig} can be identified (~ 300 °C), we use XRD to confirm combustion occurs. Figure A.24 shows the bulk $Al(NO_3)_3$-urea powder contains crystalline phases when annealed at 300 °C.[34] The product is likely a complex mixture of several different (oxy)hydroxide structures, as the boehmite and diaspore structures do not account for all the diffraction peaks observed. The film prepared from this precursor is X-ray amorphous, further suggesting that combustion does not occur in thin films.

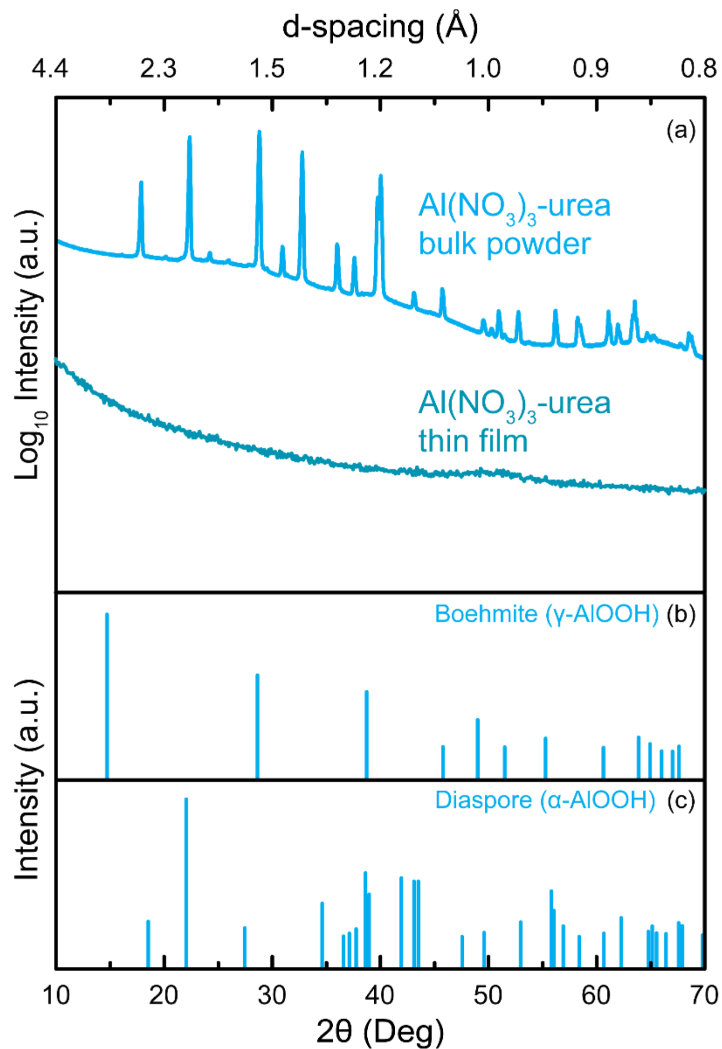

Figure A.24. XRD of the powder and film prepared from the $Al(NO_3)_3$-urea precursor (a). Panels (b) and (c) show potential reference patterns for the bulk powder product. While these patterns are non-ideal matches, we suspect this product contains a complex mixture of other AlOOH or $Al(OH)_3$ phases that we are unable to identify.

While combustion is not readily observed for the $Y(NO_3)_3$-urea mixture by TGA under air flow, TGA-MS shows a combustion event occurs at ~ 300 °C (Figure A.25). We attribute this difference to different decomposition kinetics of urea under the N_2 carrier gas used in these experiments. TPD-MS results for a $Y(NO_3)_3$-urea film shows, like in the $Y(NO_3)_3$-acac film (Figure A.10), the fuel leaves the film in the undecomposed form, as evidenced by the broad peak in the m/z = 28, 44, and 60 detected from 100-250 °C (Figure A.26). Substantial nitrate desorption/decomposition begins at 325 °C and the onset can be identified by the sharp peak at this temperature in the NO^+, N_2^+ and N_2O^+ fragments (m/z = 30, 28, and 44, respectively). Remaining nitrate is removed from the film via decomposition into NO^+ and O_2^+ up to 550 °C. These data suggest urea and nitrate undergo separate decomposition pathways and do not participate in a combustion reaction.

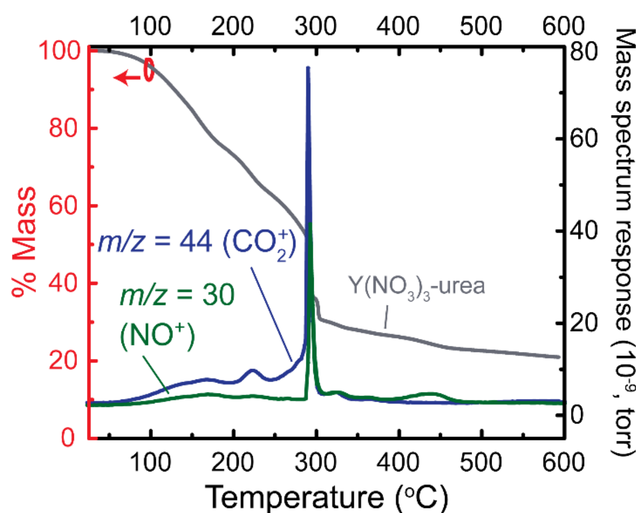

Figure A.25. TGA-MS results for the $Y(NO_3)_3$-urea bulk powder. Other fragments associated with fuel and residual solvent were observed but are omitted for clarity. Combustion with urea under N_2 is evident at 300 °C but is incomplete, as small amounts of the NO^+ fragment are still detected from 400-500 °C

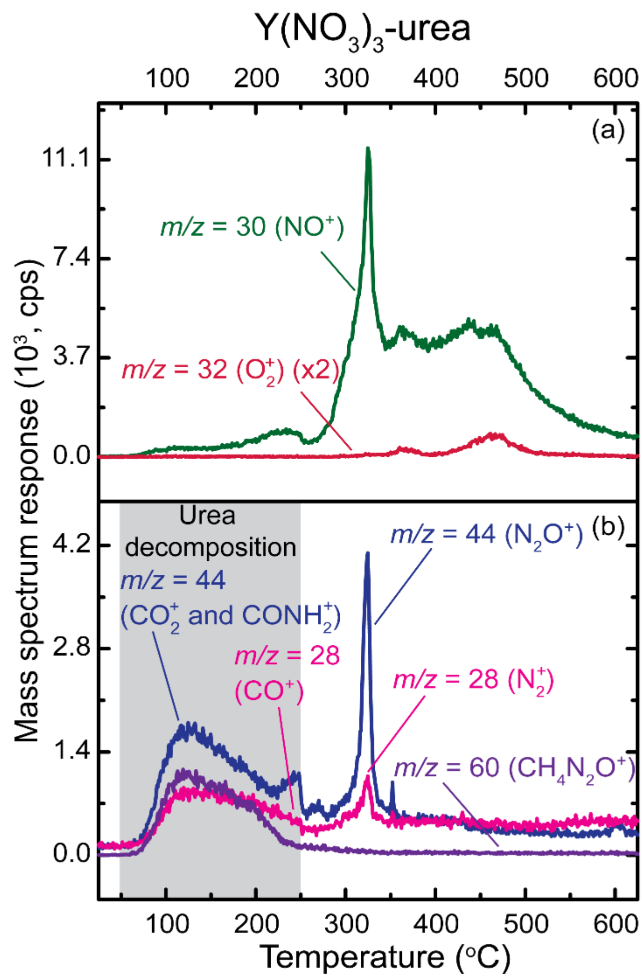

Figure A.26. TPD-MS of a $Y(NO_3)_3$-urea film. Fragments associated with urea decomposition desorb from the film from ~ 75-250 °C, whereas the majority of the nitrate fragments are detected from 300-600 °C. Like in the acac system, fuel is lost at low temperatures and remaining nitrates in the film thermally decompose.

Investigating the Effect of Fuels on Film Morphology

AFM and cross-sectional SEM were used to assess the extent to which the film surface and interior structure are affected by the use of fuel additives for a select set of precursors. Films made from the $Al(NO_3)_3$-acac precursor contain large voids (Figure A.27b & A.27e), which we associate with several film formation reactions happening simultaneously (solvent evaporation, acac and nitrate removal, hydroxyl condensation, etc.) as Al_2O_3 forms. The $Al(NO_3)_3$-urea precursor results in dendritic crystallites in the surface of the film (Figure A.27f). For films prepared from $In(NO_3)_3$ and $Y(NO_3)_3$ precursors, there are minimal differences between film and surface morphologies with and without fuels (Figure A.27g-l & A.27m-r). Measurements of surface roughness modeled from X-ray reflectivity patterns, which probes a larger film area than AFM and SEM, show substantial roughening of all films when fuels are introduced, with the exception of the $Y(NO_3)_3$-urea film (Figure A.28, Table A.1).

Films with high surface roughness can negatively affect device performance, through poor electrical contact between layers and the introduction of charge trap states. This effect has been demonstrated in both inorganic[35] and organic[36] TFTs with substantially reduced mobilities, as well as poor current versus voltage characteristics in metal-insulator-metal tunnel diodes, even when surface roughness is less than 20% of the film thickness.[37] Additionally, zinc tin oxide thin-film transistors prepared with urea exhibit lower mobilities and variable electrical characteristics due to incomplete combustion.[38] We demonstrate here that high quality, low roughness films (in some cases, sub-0.1 nm) can be made from metal nitrate solutions without fuel additives.

Microscopy Imaging Experimental Details

AFM images were collected in tapping mode using a Bruker Dimension Icon. Images were taken using 512 nm lines per image and a 2 Hz scan rate over a 1 μm square window. Physical roughness values were calculated after first performing a first-order flatten and third-order plane fit on the images using Nanoscope Analysis 1.5 software (Bruker). SEM imaging was performed on three-layer films on a FEI Helios 600i DualBeam using a 5-kV accelerating voltage and 86 pA beam current. Each layer was annealed for 30 min at a temperature at least 15 °C above T_{ig}, except films from $Y(NO_3)_3$, which were annealed at 400 °C, as films annealed at lower temperatures were prone to excessive electron beam damage. Samples for SEM were coated in Al metal prior to imaging to reduce electrical charging artifacts under the beam.

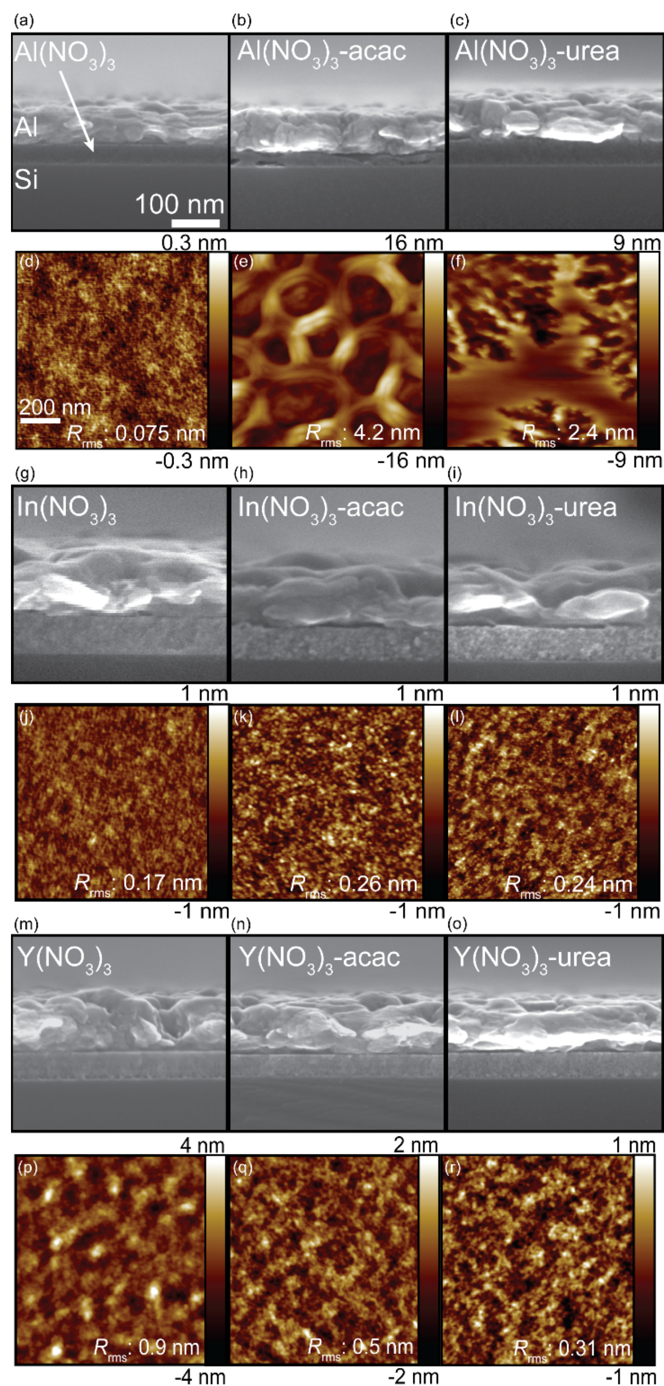

Figure A.27. Morphological characterization of films synthesized from precursors with and without fuel additives. Cross-sectional SEM micrographs showing bulk film morphology of three-layer films prepared from $Al(NO_3)_3$ (a-c), $In(NO_3)_3$ (g-i), and $Y(NO_3)_3$ (m-o) precursors. The top layer in the SEM images is Al metal, deposited to reduce electrical charging under the imaging conditions and the bottom is the Si substrate. AFM images collected in tapping mode show surface morphology of films from $Al(NO_3)_3$ (d-f), $In(NO_3)_3$ (j-l), and $Y(NO_3)_3$ (p-r) precursors.

X-Ray Reflectivity Experimental Details

Film thickness, electron density, and surface roughness information was determined through X-ray reflectivity (XRR) measurements and were collected using a Bruker D8 Discover diffractometer with a Cu Kα radiation source (λ_{avg}= 1.5418 Å), a Ni foil Kβ filter, and a 0.1 mm slit to filter stray X-rays. Data were modeled using the Bede REFS software package. All models include an SiO_2 layer, which was fit and ranged from 2-5 nm thick, and the roughness of the Si substrate was fit while thickness and density were fixed at infinity and 100%, respectively. Multiple layers were used to fit the metal oxide layer of interest, as gradients in thickness and film density in spun-coat films are known.[39] All fitting outputs are summarized in Table A.1.

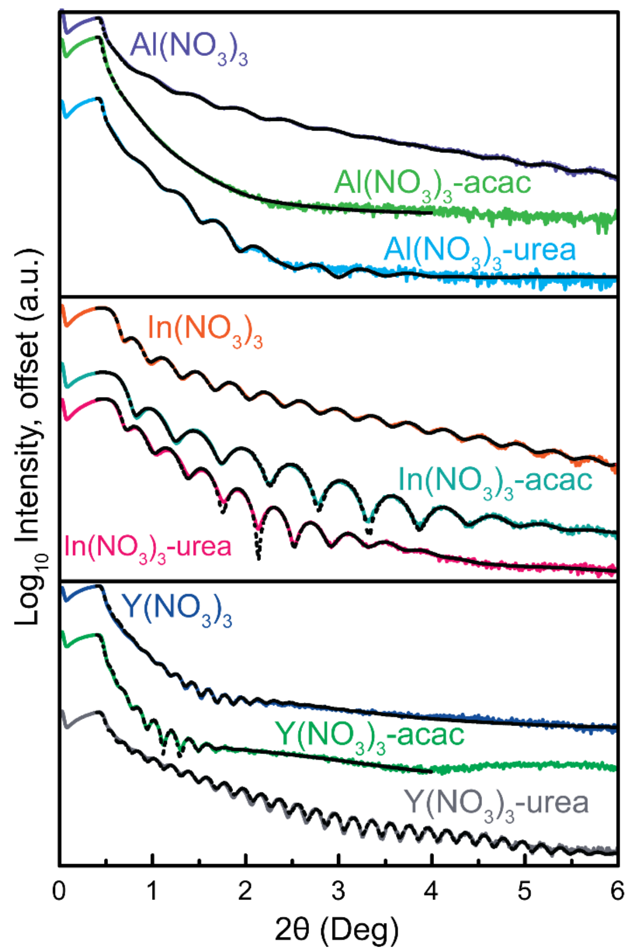

Figure A.28. XRR patterns for combustion precursor films with models shown in dotted black lines.

Table A.1. Summary of XRR modeling outputs.

Precursor	Thickness of layers (nm)	Total thickness (nm)	Average film density ($g\ cm^{-3}$)	Roughness of surface layer (nm)	Goodness of fit
$Al(NO_3)_3$	1.0	16.2	2.9	0.2	0.02
	15.2				
$Al(NO_3)_3$-acac	16.9	20.9	0.58	4.7	0.05
	4.0				
$Al(NO_3)_3$-urea	3.0	18.1	2.3	1.3	0.06
	15.1				
$In(NO_3)_3$	1.4	22.6	4.6	0.2	0.03
	21.2				
$In(NO_3)_3$-acac	1.5	16.3	5.8	0.7	0.04
	14.8				
$In(NO_3)_3$-urea	3.6	21.7	5.1	1.1	0.06
	18.1				
$Y(NO_3)_3$	2.1	50.9	2.2	1.4	0.06
	3.0				
	45.8				
$Y(NO_3)_3$-acac	5.4	43.6	2.5	2.5	0.05
	36.5				
	1.7				
$Y(NO_3)_3$-urea	3.0	43.8	3.0	0.5	0.07
	40.8				

APPENDIX B

CHAPTER V SUPPLEMENTARY INFORMATION

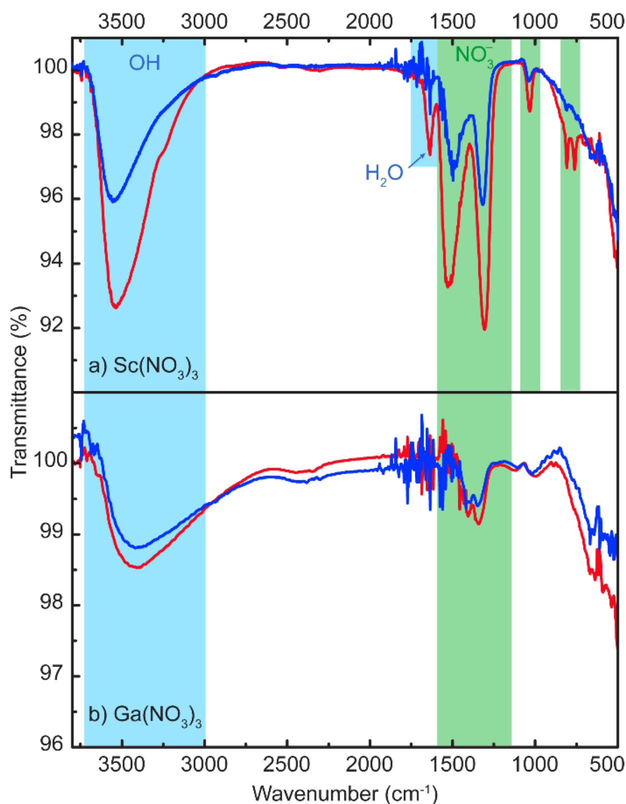

Figure B.1. FT-IR spectra for dry- (red) and steam-annealed (blue) films from $Sc(NO_3)_3$ and $Ga(NO_3)_3$ precursors (140 °C).

XPS Fitting Procedure

Carbon 1s spectra were fit with 5 peaks: 284.8 (C-H, peak A), A + 1.5 (C-O, peak B), A + 3.0 (O=C, peak C), A + 4.0 (O=C-O, peak D), and A + 4.5 eV (CO32-, peak E). The peaks positions were constrained to ± 0.2 eV from the specified position. The FWHM and Lorentzian/Gaussian ratios for all carbon peaks where constrained to the same values, which were fit by the software. All spectra were charge-shifted to match the position of the C-H peak to 284.8 eV. The following peak positions/constraints were used

to fit the O 1s spectra for films from In_2O_3 precursors: In-O (528-530 eV), In-OH 530.8-532 eV), N-O from NO_3^- (532.5-533.5 eV), and adventitious carbon-oxygen species (523.5-534 eV). For films that had detectible Si signal in the surface spectra, a Si-O peak (532.5-533.2 eV) was added. All peaks where allowed a ± 0.2 eV tolerance. The peak areas for N-O, carbon-oxygen, and Si-O where constrained to reflect the amount of each species quantified using the fitted N 1s, C 1s, and Si 2p peaks. The FWHM and Lorentzian/Gaussian ratios for peaks in the O 1s spectra were, in most cases, constrained to the same values. These constraints were allowed to relax, if needed, in order to improve the overall fit.

Table B.1. XPS atomic percentages from surface spectra of $M(NO_3)_x$ films dry- and steam-annealed at 140 °C.

Precursor	C species	At. % Dry	At. % Steam	Other	At. % Dry	At. % Steam
$Al(NO_3)_3$	C-H	7.5	7.7	O	59	59.6
	C-O	1.2	1.6	N	4.6	4.2
	C=O	0.7	0.4	Al	26.2	25.7
	O=C-O	0	0.8			
	CO_3	0.8	0			
$In(NO_3)_3$	C-H	10.9	10.2	O	59.4	60.8
	C-O	2.3	2.8	N	7.7	3.4
	C=O	0.2	0.5	In	17	20.2
	O=C-O	2.6	1.3			
	CO_3	0	0.9			
$Y(NO_3)_3$	C-H	9.4	8.9	O	58.4	62.6
	C-O	2.1	3.6	N	15.3	10.8
	C=O	0.4	0.5	Y	12.8	11.7
	O=C-O	1.6	1			
	CO_3	0	0.9			
$ZrO(NO_3)_2$	C-H	10.5	9.8	O	63.9	63.9
	C-O	1.5	2.9	N	4.9	2.4
	C=O	0	0	Zr	16.7	18.4
	O=C-O	2.5	2.5			
	CO_3	0	0			

Table B.2. XPS atomic percentages from surface spectra of MCl_x films dry- and steam-annealed at 140 °C.

Precursor	C species	At. % Dry	At. % Steam	Other	At. % Dry	At. % Steam
$AlCl_3$	C-H	5.6	6.7	O	33.5	31.5
	C-O	1.8	1.4	Cl	7.6	7.4
	C=O	0	0	Al	49.2	50.7
	O=C-O	0.9	1.4			
	CO_3	1.4	1			
$InCl_3$	C-H	17.5	9.9	O	21.0	48.9
	C-O	2.2	3.5	Cl	36.5	14.4
	C=O	1.2	0	In	18.2	20.9
	O=C-O	1.7	2.4			
	CO_3	1.7	0			
YCl_3	C-H	11.3	10.2	O	41.5	51.1
	C-O	2.2	2	Cl	20.6	12.3
	C=O	0.5	0.4	Y	20.9	20.5
	O=C-O	2.5	2.6			
	CO_3	0.6	0.9			
$ZrOCl_2$	C-H	12.6	9.1	O	59.8	64.5
	C-O	1.5	1.6	Cl	3.8	2.3
	C=O	0.1	0	Zr	20	20.9
	O=C-O	2.3	1.7			
	CO_3	0	0			

Table B.3. XPS atomic percentages from surface spectra for $In(NO_3)_3$ films dry- and steam-annealed at various temperatures.

Annealing Temperature (°C)	C species	At. % Dry	At. % Steam	Other	At. % Dry	At. % Steam
170	C-H	14.7	12.2	O	57.2	60.9
	C-O	1.2	0.9	N	3.6	2.3
	C=O	0	0.1	In	21.0	21.7
	O=C-O + CO_3	2.4	1.9			
200	C-H	6.7	6.1	O	57.1	58.7
	C-O	0.9	0.8	N	1.9	1.2
	C=O	0	0	In	25.6	24.9
	O=C-O	2.0	1.5	Si	5.7	6.8
	CO_3	0.1	0			
250	C-H	3.4	3.5	In-O	36.7	30.9
	C-O	0.4	0.7	In-OH	9.8	12.7
	C=O	0	0	N-O	3.1	0
	O=C-O	1.3	0.3	C-O + C=O + O=C-O + CO_3	3.6	3.6
	CO_3	0	0.6	Si-O	5.2	10.4
				N	1.0	0
				In	29.4	28.8
				Si	2.8	5.5

Table B.4. XPS atomic percentages from surface spectra for $InCl_3$ films dry- and steam-annealed at various temperatures.

Annealing Temperature (°C)	C species	At. % Dry	At. % Steam	Other	At. % Dry	At. % Steam
170	C-H	15.6	10.12	O	37.2	53.6
	C-O	1.6	2.56	Cl	22.6	9.0
	C=O	1.3	0	In	19.5	22.9
	O=C-O $+CO_3$	2.3	1.82			
	CO_3	0	0.98			
200	C-H	7.4	7.59	O	48.9	55.6
	C-O	1.8	2.07	Cl	10.1	6.1
	C=O	0.1	0.13	In	25.2	26.9
	O=C-O	0.7	0.76	Si	4.7	0
	CO_3	1.1	0.82			
250	C-H	3.8	4	In-O	27.2	42.7
	C-O	1	0.73	In-OH	14.0	10.9
	C=O	0.2	0	C-O + C=O + O=C-O + CO_3	3.9	3.8
	O=C-O + CO_3	1.4	1.1	Si-O	6.9	0
				Cl	6.4	2.1
				In	27.8	34.7
				Si	4.0	0

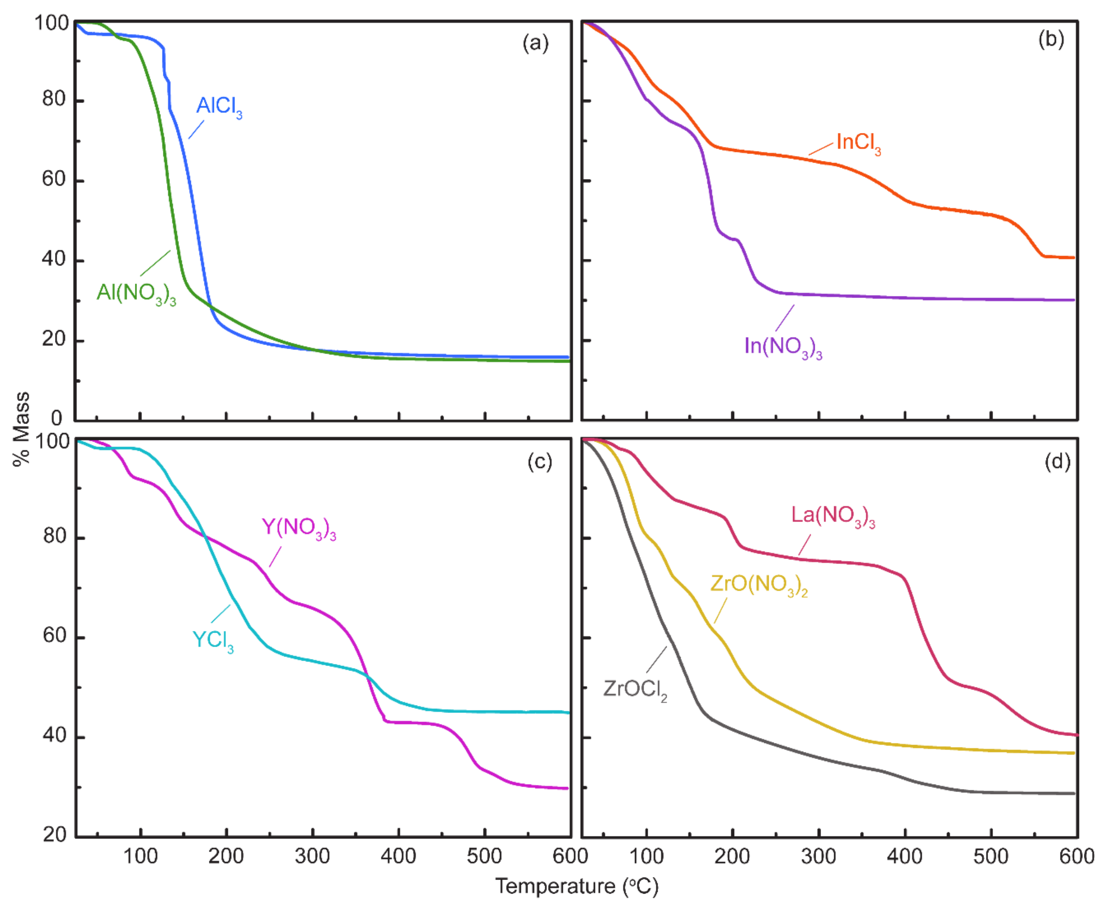

Figure B.2. Thermogravimetric analysis (TGA) curves for hydrated $M(NO_3)_x$ and MCl_x salts used as thin-film precursors in this study. Samples were ramped at 10 ºC per min^{-1}in air.

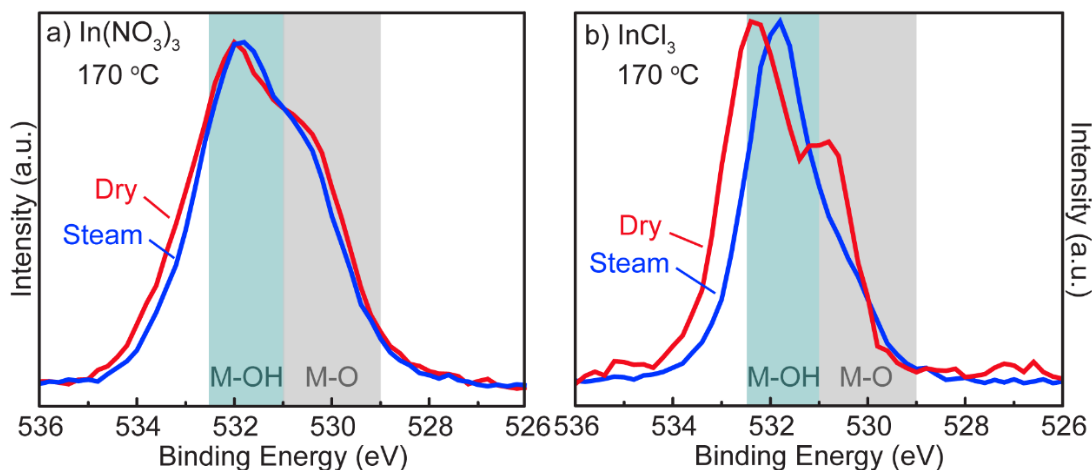

Figure B.3. O 1s spectra overlays for $In(NO_3)_3$ and $InCl_3$ films dry- and steam annealed at 170 °C.

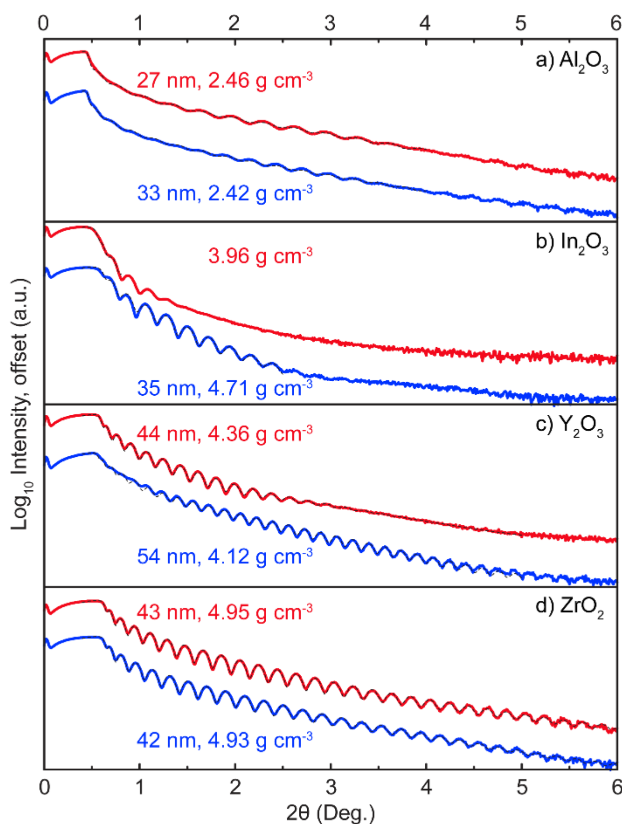

Figure B.4. XRR patterns for mixed NO_3^-/Cl^- single-metal precursor films that were dry- (red) or steam-annealed (blue). Densities reported here are weighted averages from two- or three-layer models. For the dry-annealed In_2O_3 film, the density reported here is the average film density, as the fit was restricted to the critical angle. A thickness is not reported for this film, due to a lack of extended Keissig fringes.

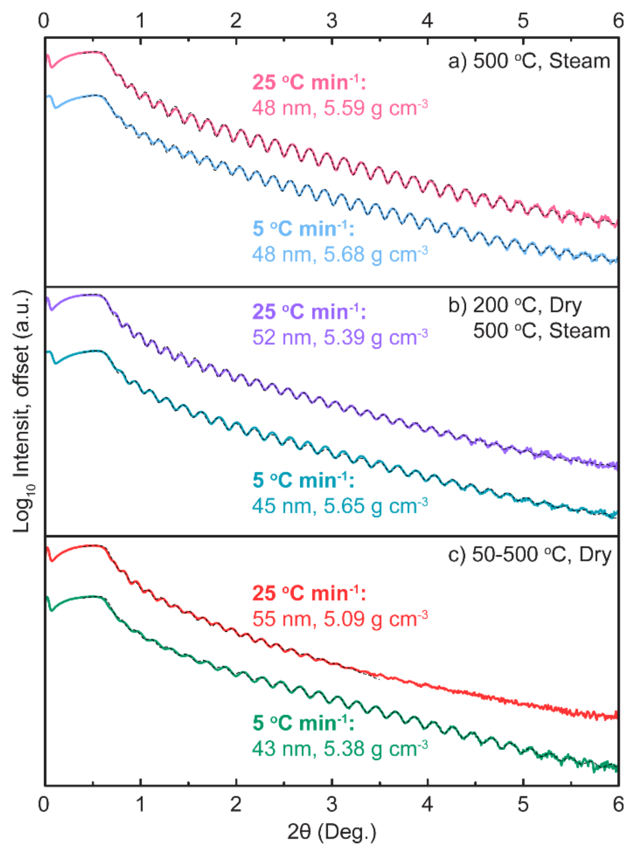

Figure B.5. XRR patterns for LZO films treated using different annealing conditions/temperature ramp profiles. Densities reported here are weighted averages from two- or three-layer models.

REFERENCES CITED

Chapter I

(1) J. S. Park, W. J. Maeng, H. S. Kim and J. S. Park, *Thin Solid Films*, 2012, **520**, 1679–1693.

(2) A. Liu, H. Zhu, H. Sun, Y. Xu and Y. Noh, *Adv. Mater.*, 2018, **30**, Article No. 1706364.

(3) E. Fortunato, P. Barquinha and R. Martins, *Adv. Mater.*, 2012, **24**, 2945–2986.

(4) S. C. Dixon, D. O. Scanlon, C. J. Carmalt and I. P. Parkin, *J. Mater. Chem. C*, 2016, **4**, 6946–6961.

(5) A. N. Banerjee and K. K. Chattopadhyay, *Prog. Cryst. Growth Charact. Mater.*, 2005, **50**, 52–105.

(6) M. Lorenz, M. S. Ramachandra Rao, T. Venkatesan, E. Fortunato, P. Barquinha, R. Branquinho, D. Salgueiro, R. Martins, E. Carlos, A. Liu, F. K. Shan, M. Grundmann, H. Boschker, J. Mukherjee, M. Priyadarshini, N. DasGupta, D. J. Rogers, F. H. Teherani, E. V Sandana, P. Bove, K. Rietwyk, A. Zaban, A. Veziridis, A. Weidenkaff, M. Muralidhar, M. Murakami, S. Abel, J. Fompeyrine, J. Zuniga-Perez, R. Ramesh, N. A. Spaldin, S. Ostanin, V. Borisov, I. Mertig, V. Lazenka, G. Srinivasan, W. Prellier, M. Uchida, M. Kawasaki, R. Pentcheva, P. Gegenwart, F. Miletto Granozio, J. Fontcuberta and N. Pryds, *J. Phys. D. Appl. Phys.*, 2016, **49**, Article No. 433001.

(7) X. Yu, T. J. Marks and A. Facchetti, *Nat. Mater.*, 2016, **15**, 383–396.

(8) X. Yang, Q. Bi, H. Ali, K. Davis, W. V. Schoenfeld and K. Weber, *Adv. Mater.*, 2016, **28**, 5891–5897.

(9) X. Yin, C. Battaglia, Y. Lin, K. Chen, M. Hettick, M. Zheng, C. Y. Chen, D. Kiriya and A. Javey, *ACS Photonics*, 2014, **1**, 1245–1250.

(10) E. J. Juarez-Perez, M. Wußler, F. Fabregat-Santiago, K. Lakus-Wollny, E. Mankel, T. Mayer, W. Jaegermann and I. Mora-Sero, *J. Phys. Chem. Lett.*, 2014, **5**, 680–685.

(11) P. P. Boix, J. Ajuria, I. Etxebarria, R. Pacios, G. Garcia-Belmonte and J. Bisquert, *J. Phys. Chem. Lett.*, 2011, **2**, 407–411.

(12) M. S. White, D. C. Olson, S. E. Shaheen, N. Kopidakis and D. S. Ginley, *Appl. Phys. Lett.*, 2006, **89**, 143517.

(13) C. Battaglia, X. Yin, M. Zheng, I. D. Sharp, T. Chen, S. McDonnell, A. Azcatl, C. Carraro, B. Ma, R. Maboudian, R. M. Wallace and A. Javey, *Nano Lett.*, 2014, **14**, 967–971.

(14) A. K. K. Kyaw, X. W. Sun, C. Y. Jiang, G. Q. Lo, D. W. Zhao and D. L. Kwong, *Appl. Phys. Lett.*, 2008, **93**, 2006–2009.

(15) K. X. Steirer, J. P. Chesin, N. E. Widjonarko, J. J. Berry, A. Miedaner, D. S. Ginley and D. C. Olson, *Org. Electron.*, 2010, **11**, 1414–1418.

(16) X. Xu, Z. Liu, Z. Zuo, M. Zhang, Z. Zhao, Y. Shen, H. Zhou, Q. Chen, Y. Yang and M. Wang, *Nano Lett.*, 2015, **15**, 2402–2408.

(17) Y. Wang, E. L. Runnerstrom and D. J. Milliron, *Annu. Rev. Chem. Biomol. Eng.*, 2016, **7**, 283–304.

(18) C. G. Granqvist, *Thin Solid Films*, 2014, **564**, 1–38.

(19) Z. Fan, C. C. Chao, F. Hossein-Babaei and F. B. Prinz, *J. Mater. Chem.*, 2011, **21**, 10903–10906.

(20) X. Chen, N. J. Wu, L. Smith and A. Ignatiev, *Appl. Phys. Lett.*, 2004, **84**, 2700–2702.

(21) A. S. Asundi, J. A. Raiford and S. F. Bent, *ACS Energy Lett.*, 2019, **4**, 908–925.

(22) M. G. Kast, L. J. Enman, N. J. Gurnon, A. Nadarajah and S. W. Boettcher, *ACS Appl. Mater. Interfaces*, 2014, **6**, 22830–22837.

(23) R. D. L. Smith, M. S. Prevot, R. D. Fagan, Z. Zhang, P. A. Sedach, M. K. J. Siu, S. Trudel and C. P. Berlinguette, *Science*, 2013, **340**, 60–63.

(24) L. Trotochaud, J. K. Ranney, K. N. Williams and S. W. Boettcher, *J. Am. Chem. Soc.*, 2012, **134**, 17253–17261.

(25) T. P. St. Clair and D. W. Goodman, *Top. Catal.*, 2000, **13**, 5–19.

(26) H. J. Freund and G. Pacchioni, *Chem. Soc. Rev.*, 2008, **37**, 2224–2242.

(27) D. B. Mitzi, Ed., *Solution Processing of Inorganic Materials*, John Wiley & Sons Inc., Hoboken, 1st edn., 2009.

(28) K. M. Kim, C. W. Kim, J. S. Heo, H. Na, J. E. Lee, C. B. Park, J. U. Bae, C. D. Kim, M. Jun, Y. K. Hwang, S. T. Meyers, A. Grenville and D. A. Keszler, *Appl. Phys. Lett.*, 2011, **99**, 242109.

(29) W. Xu, H. Li, J. Bin Xu and L. Wang, *ACS Appl. Mater. Interfaces*, 2018, **10**, 25878–25901.

(30) C. J. Brinker and G. W. Scherer, *Sol-Gel Science: The Physics and Chemistry of Sol-Gel Processing*, Academic Press, Inc., Boston, 1st edn., 1990.

(31) R. W. Schwartz, T. Schneller and R. Waser, *Comptes Rendus Chim.*, 2004, **7**, 433–461.

(32) A. Nadarajah, M. Z. B. Wu, K. Archila, M. G. Kast, A. M. Smith, T. H. Chiang, D. A. Keszler, J. F. Wager and S. W. Boettcher, *Chem. Mater.*, 2015, **27**, 5587–5596.

(33) K.-H. Lim, J. Lee, J.-E. Huh, J. Park, J.-H. Lee, S.-E. Lee and Y. S. Kim, *J. Mater. Chem. C*, 2017, **5**, 7768–7776.

(34) S. Jeong, J. Y. Lee, S. S. Lee, Y. Choi and B. H. Ryu, *J. Phys. Chem. C*, 2011, **115**, 11773–11780.

(35) W. J. Scheideler, R. Kumar, A. R. Zeumault and V. Subramanian, *Adv. Funct. Mater.*, 2017, **27**, Article No. 1606062.

(36) Y. S. Rim, H. Chen, T.-B. Song, S.-H. Bae and Y. Yang, *Chem. Mater.*, 2015, **27**, 5808–5812.

(37) G. Liu, A. Liu, H. Zhu, B. Shin, E. Fortunato, R. Martins, Y. Wang and F. Shan, *Adv. Funct. Mater.*, 2015, **25**, 2564–2572.

(38) A. Liu, G. X. Liu, H. H. Zhu, F. Xu, E. Fortunato, R. Martins and F. K. Shan, *ACS Appl. Mater. Interfaces*, 2014, **6**, 17364–17369.

(39) P. N. Plassmeyer, K. Archila, J. F. Wager and C. J. Page, *ACS Appl. Mater. Interfaces*, 2015, **7**, 1678–1684.

(40) K. N. Woods, T. H. Chiang, P. N. Plassmeyer, M. G. Kast, A. C. Lygo, A. K. Grealish, S. W. Boettcher and C. J. Page, *ACS Appl. Mater. Interfaces*, 2017, **9**, 10897–10903.

(41) C. K. Perkins, M. Jenkins, T.-H. Chiang, R. H. Mansergh, V. Gouliouk, N. Kenane, J. Wager, J. F. Conley and D. A. Keszler, *ACS Appl. Mater. Interfaces*, 2018, **10**, 36082–36087.

(42) K. N. Woods, E. C. Waddington, C. A. Crump, E. A. Bryan, T. S. Gleckler, M. R. Nellist, B. A. Duell, D. P. Nguyen, S. W. Boettcher and C. J. Page, *RSC Adv.*, 2017, **7**, 39147–39152.

(43) A. Liu, G. Liu, H. Zhu, H. Song, B. Shin, E. Fortunato, R. Martins and F. Shan, *Adv. Funct. Mater.*, 2015, **25**, 7180–7188.

(44) A. Liu, G. Liu, H. Zhu, B. Shin, E. Fortunato, R. Martins and F. Shan, *RSC Adv.*, 2015, **5**, 86606–86613.

(45) C. Zhu, A. Liu, G. Liu, G. Jiang, Y. Meng, E. Fortunato, R. Martins and F. Shan, *J. Mater. Chem. C*, 2016, **4**, 10715–10721.

(46) R. M. Pasquarelli, D. S. Ginley and R. O. Hayre, *Chem. Soc. Rev.*, 2011, **40**, 5406–5441.

(47) A. Nadarajah, M. E. Carnes, M. G. Kast, D. W. Johnson and S. W. Boettcher, *Chem. Mater.*, 2013, **25**, 4080–4087.

(48) P. Richter, P. N. Plassmeyer, J. Harzdorf, T. Rüffer, H. Lang, J. Kalbacova, N. Jöhrmann, S. Schulze, M. Hietschold, S. S. P. K. Arekapudi, M. Albrecht, D. R. T. Zahn, C. J. Page and G. Salvan, *Chem. Mater.*, 2016, **28**, 4917–4927.

(49) D. R. Clayton, D. Lepage, P. N. Plassmeyer, C. J. Page and M. C. Lonergan, *RSC Adv.*, 2017, **7**, 7046–7051.

(50) N. Zhou, M.-G. Kim, S. Loser, J. Smith, H. Yoshida, X. Guo, C. Song, H. Jin, Z. Chen, S. M. Yoon, A. J. Freeman, R. P. H. Chang, A. Facchetti and T. J. Marks, *Proc. Natl. Acad. Sci.*, 2015, **112**, 7897–7902.

(51) J. W. Jung, C. C. Chueh and A. K. Y. Jen, *Adv. Mater.*, 2015, **27**, 7874–7880.

(52) M.-G. Kim, M. G. Kanatzidis, A. Facchetti and T. J. Marks, *Nat. Mater.*, 2011, **10**, 382–388.

(53) Y.-H. Kim, J.-S. Heo, T.-H. Kim, S. Park, M.-H. Yoon, J. Kim, M. S. Oh, G.-R. Yi, Y.-Y. Noh and S. K. Park, *Nature*, 2012, **489**, 128–132.

(54) K. N. Woods, P. N. Plassmeyer, D. H. Park, L. J. Enman, A. K. Grealish, B. L. Kirk, S. W. Boettcher, D. A. Keszler and C. J. Page, *Chem. Mater.*, 2017, **29**, 8531–8538.

(55) Y. S. Rim, S. H. Bae, H. Chen, N. De Marco and Y. Yang, *Adv. Mater.*, 2016, **28**, 4415–4440.

(56) I. Bretos, R. Jiménez, J. Ricote and M. L. Calzada, *Chem. Soc. Rev.*, 2018, **47**, 291–308.

Chapter II

(1) S. Yuvaraj, F. Y. Lin, T. H. Chang and C. T. Yeh, *J. Phys. Chem. B*, 2003, **107**, 1044–1047.

(2) M. Wolters, H. Daly, A. Goguet, F. C. Meunier, C. Hardacre, J. H. Bitter, P. E. De Jongh and K. P. De Jong, *J. Phys. Chem. C*, 2010, **114**, 7839–7845.

(3) Y. Li and B. W. L. Jang, *Ind. Eng. Chem. Res.*, 2010, **49**, 8433–8438.

(4) M. R. Quddus, M. M. Hossain and H. I. De Lasa, *Catal. Today*, 2013, **210**, 124–134.

(5) P. Melnikov, V. A. Nascimento, I. V. Arkhangelsky, L. Z. Zanoni Consolo and L. C. S. De Oliveira, *J. Therm. Anal. Calorim.*, 2013, **111**, 543–548.

(6) P. Melnikov, V. A. Nascimento and L. Z. Z. Consolo, *J Therm Anal Calorim*, 2012, **107**, 1117–1121.

(7) P. Melnikov, V. A. Nascimento, L. Z. Z. Consolo and A. F. Silva, *J. Therm. Anal. Calorim.*, 2013, **111**, 115–119.

(8) P. Melnikov, V. A. Nascimento, I. V Arkhangelsky, L. C. S. de Oliveira, A. F. Silva and L. Z. Z. Consolo, *J Therm Anal Calorim*, 2014, **119**, 1073–1079.

(9) A. J. Kozak, *J. Therm. Anal. Calorim.*, 1999, **58**, 647–651.

(10) W. W. Wendlandt and J. L. Bear, *J. Inorg. Nucl. Chem.*, 1960, **12**, 276–280.

(11) P. K. Gallagher and D. W. Johnson Jr., *J. Electrochem. Soc.*, 1971, **118**, 1530–1534.

(12) A. Małecki and B. Małecka, *Thermochim. Acta*, 2006, **446**, 113–116.

(13) J. Zhuang, Q. J. Sun, Y. Zhou, S. T. Han, L. Zhou, Y. Yan, H. Peng, S. Venkatesh, W. Wu, R. K. Y. Li and V. A. L. Roy, *ACS Appl. Mater. Interfaces*, 2016, **8**, 31128–31135.

(14) B. Yang, G. He, L. Zhu, C. Zhang, Y. Zhang, Y. Xia, F. Alam and Z. Sun, *ACS Appl. Electron. Mater.*, 2019, **1**, 625–636.

(15) K. N. Woods, T. H. Chiang, P. N. Plassmeyer, M. G. Kast, A. C. Lygo, A. K. Grealish, S. W. Boettcher and C. J. Page, *ACS Appl. Mater. Interfaces*, 2017, **9**, 10897–10903.

(16) P. N. Plassmeyer, K. Archila, J. F. Wager and C. J. Page, *ACS Appl. Mater. Interfaces*, 2015, **7**, 1678–1684.

(17) M. G. Kast, E. A. Cochran, L. J. Enman, G. Mitchson, J. Ditto, C. Siefe, P. N. Plassmeyer, A. L. Greenaway, D. C. Johnson, C. J. Page and S. W. Boettcher, *J. Am. Chem. Soc.*, 2016, **138**, 16800–16808.

(18) E. A. Cochran, D.-H. Park, M. G. Kast, L. J. Enman, C. K. Perkins, R. H. Mansergh, D. A. Keszler, D. W. Johnson and S. W. Boettcher, *Chem. Mater.*, 2017, **29**, 9480–9488.

(19) R. D. Shannon, *Acta Crystallogr. Sect. A*, 1976, **32**, 751–767.

(20) J. Schefer and M. Grube, *Mater. Res. Bull.*, 1995, **30**, 1235–1241.

(21) D. Lazar, B. Ribár and B. Prelesnik, *Acta Crystallogr. Sect. C Cryst. Struct. Commun.*, 1991, **47**, 2282–2285.

(22) A. D. Hendsbee, C. C. Pye and J. D. Masuda, *Acta Crystallogr. Sect. E Struct. Reports*, 2009, **65**, i65.

(23) M. A. Malyarik, S. P. Petrosyants, A. B. Ilyukhin and Y. A. Buslaev, *Zhurnal Neorg. Khimii*, 1993, **38**, 1975–1980.

(24) T. J. Boyle, J. M. Sears, M. L. Neville, T. M. Alam and V. G. Young, *Inorg. Chem.*, 2015, **54**, 11831–11841.

(25) D. Lazar, B. Ribár, V. Divjaković and C. Mészáros, *Acta Crystallogr. Sect. C Cryst. Struct. Commun.*, 1991, **47**, 1060–1062.

(26) D. Popov, R. Herak, N. Radulovic and B. Ribar, *Zeitschrift für Krist.*, 1975, **142**, 347–355.

(27) N. J. Hair and J. K. Beattie, *Inorg. Chem.*, 1977, **16**, 245–250.

(28) P. V. Prelesnik, F. Gabela, B. Ribar and I. Krstanovic, *Acta Crystallogr. Sect. C Cryst. Struct. Commun.*, 1973, **2**, 581–583.

(29) F. Bigoli, A. Braibanti, A. Tiripicchio and M. T. Camellini, *Acta Crystallogr. Sect. B Struct. Crystallogr. Cryst. Chem.*, 1971, **27**, 1427–1434.

(30) B. Morosin, *Acta Crystallogr. Sect. B Struct. Crystallogr. Cryst. Chem.*, 1970, **26**, 1203–1208.

(31) V. B. Ribar and W. Nowacki, *Zeitschrift für Krist.*, 1970, **131**, 175–185.

(32) B. Ribar, N. Milinski, Z. Budovalcev and I. Krstanovic, *Acta Crystallogr. Sect. C Cryst. Struct. Commun.*, 1980, **9**, 203–206.

(33) P. Bénard, M. Louër and D. Louër, *J. Solid State Chem.*, 1991, **94**, 27–35.

(34) A. Gobichon, M. Loue, D. Loue and J. P. Auffre, *J. Solid State Chem.*, 1996, **126**, 127–134.

(35) N. Milinski, P. Radivojevic, B. Ribar and S. Djuric, *Acta Crystallogr. Sect. C Cryst. Struct. Commun.*, 1982, **11**, 1241–1244.

(36) D. J. Rogers, N. J. Taylor and G. E. Toogood, *Acta Crystallogr. Sect. C Cryst. Struct. Commun.*, 1983, **39**, 939–941.

(37) R. Kawashima, M. Sasaki, S. Satoh, H. Isoda, Y. Kino and Y. Shiozak, *J. Phys. Soc. Japan*, 2000, **69**, 3297–3303.

(38) S. Stockhause and G. Meyer, *Zeitschrift für Krist.*, 1997, **212**, 315.

(39) G. Shengli, M. Huairang and Y. Zupei, *Xibei Daxue Xuebao, Ziran Kexueban*, 1990, **20**, 53–58.

(40) C. Rincke, H. Schmidt and W. Voigt, *Zeitschrift fur Anorg. und Allg. Chemie*, 2017, **643**, 437–442.

(41) A.-E. Gobichon, J.-P. Auffrékdic and D. Louër, *Solid State Ionics*, 1997, **93**, 51–64.

(42) W. Wang, I.-Y. Chang, L. Zakharov, P. H.-Y. Cheong and D. A. Keszler, *Inorg. Chem.*, 2013, **52**, 1807–1811.

(43) J. R. A. Sietsma, J. D. Meeldijk, J. P. Den Breejen, M. Versluijs-Helder, A. J. Van Dillen, P. E. De Jongh and K. P. De Jong, *Angew. Chemie - Int. Ed.*, 2007, **46**, 4547–4549.

(44) B. Małecka, A. Łącz, E. Drozdz and A. Małecki, *J. Therm. Anal. Calorim.*, 2015, **119**, 1053–1061.

(45) Y. S. Rim, S. H. Bae, H. Chen, N. De Marco and Y. Yang, *Adv. Mater.*, 2016, **28**, 4415–4440.

(46) K. N. Woods, P. N. Plassmeyer, D. H. Park, L. J. Enman, A. K. Grealish, B. L. Kirk, S. W. Boettcher, D. A. Keszler and C. J. Page, *Chem. Mater.*, 2017, **29**, 8531–8538.

(47) K. N. Woods, D. M. Hamann and C. J. Page, *Solid State Sci.*, 2018, **75**, 34–38.

(48) K. N. Woods, E. C. Waddington, C. A. Crump, E. A. Bryan, T. S. Gleckler, M. R. Nellist, B. A. Duell, D. P. Nguyen, S. W. Boettcher and C. J. Page, *RSC Adv.*, 2017, **7**, 39147–39152.

(49) J. Livage, *Catal. Today*, 1998, **41**, 3–19.

(50) W. W. Rudolph, D. Fischer, M. R. Tomney and C. C. Pye, *Phys. Chem. Chem. Phys.*, 2004, **6**, 5145–5155.

(51) W. W. Rudolph and G. Irmer, *Dalt. Trans.*, 2015, **44**, 18492–18505.

(52) W. W. Rudolph and G. Irmer, *Dalt. Trans.*, 2015, **44**, 295–305.

(53) C. J. Brinker and G. W. Scherer, *Sol-Gel Science: The Physics and Chemistry of Sol-Gel Processing*, Academic Press, Inc., Boston, 1st edn., 1990.

(54) G. Wulfsberg, *Inorganic Chemistry*, University Science Books, Sausalito, 1st edn., 2000.

(55) M. Henry, J. P. Jolivet and J. Livage, in *Chemistry, Spectroscopy and Applications of Sol-Gel Glasses. Structure and Bonding, vol. 77*, eds. R. Reisfeld and C. K. JJørgensen, Springer, Berlin, 1992, pp. 153–206.

(56) R. E. Mesmer and C. F. Baes, *MRS Proc.*, 1990, **281**, 935–962.

(57) D. T. Richens, *The Aqueous Chemistry of Aqua Ions*, John Wiley & Sons, Ltd, Chichester, England, 1st edn., 1997.

(58) C. F. Baes and R. E. Mesmer, *The Hydrolysis of Cations*, John Wiley & Sons Inc., New york, 1976.

(59) M. Pourbaix, *Atlas of Electrochemical Equilibria in Aqueous Solutions*, Pergamon Press, Oxford, 1st edn., 1966.

(60) G. K. Schweitzer and L. L. Pesterfield, *The Aqueous Chemistry of the Elements*, Oxford University Press, Oxford, 2013, vol. 48.

(61) M. N. Jackson, M. K. Kamunde-Devonish, B. A. Hammann, L. A. Wills, L. B. Fullmer, S. E. Hayes, P. H. Y. Cheong, W. H. Casey, M. Nyman and D. W. Johnson, *Dalt. Trans.*, 2015, **44**, 16982–17006.

(62) M. K. Kamunde-Devonish, M. N. Jackson, Z. L. Mensinger, L. N. Zakharov and D. W. Johnson, *Inorg. Chem.*, 2014, **53**, 7101–7105.

(63) C. K. Perkins, E. S. Eitrheim, B. L. Fulton, L. B. Fullmer, C. A. Colla, D. H. Park, A. F. Oliveri, J. E. Hutchison, M. Nyman, W. H. Casey, T. Z. Forbes, D. W. Johnson and D. A. Keszler, *Angew. Chemie - Int. Ed.*, 2017, **56**, 10161–10164.

(64) L. Allouche, C. Gerardin, T. Loiseau, G. Ferey and F. Taulelle, *Angew. Chemie - Int. Ed.*, 2000, **39**, 511–514.

(65) G. Biedermann and D. Ferri, *Acta Chem. Scand. A*, 1982, **36**, 611–622.

(66) L. A. Wills, X. Qu, I. Y. Chang, T. J. L. Mustard, D. A. Keszler, K. A. Persson and P. H. Y. Cheong, *Nat. Commun.*, 2017, **8**, 1–7.

(67) J. Livage, M. Henry and C. Sanchez, *Prog. Solid State Chem.*, 1988, **18**, 259–341.

(68) A. Nadarajah, M. E. Carnes, M. G. Kast, D. W. Johnson and S. W. Boettcher, *Chem. Mater.*, 2013, **25**, 4080–4087.

(69) B. L. Fulton, C. K. Perkins, R. H. Mansergh, M. A. Jenkins, V. Gouliouk, M. N. Jackson, J. C. Ramos, N. M. Rogovoy, M. T. Gutierrez-Higgins, S. W. Boettcher, J. F. Conley, D. A. Keszler, J. E. Hutchison and D. W. Johnson, *Chem. Mater.*, 2017, **29**, 7760–7765.

(70) W. Wang, W. Liu, I.-Y. Chang, L. A. Wills, L. N. Zakharov, S. W. Boettcher, P. H.-Y. Cheong, C. Fang and D. A. Keszler, *Proc. Natl. Acad. Sci. U. S. A.*, 2013, **110**, 18397–401.

(71) W. W. Rudolph, R. Mason and C. C. Pye, *Phys. Chem. Chem. Phys.*, 2000, **2**, 5030–5040.

(72) W. W. Rudolph and C. C. Pye, *Phys. Chem. Chem. Phys.*, 2002, **4**, 4319–4327.

(73) Y. Marcus, *J. Chem. Soc. Faraday Trans.*, 1991, **87**, 2295–2999.

(74) F. P. Rotzinger, *J. Am. Chem. Soc.*, 1997, **119**, 5230–5238.

(75) S. Kobayashi, S. Nagayama and T. Busujima, *J. Am. Chem. Soc.*, 1998, **120**, 8287–8288.

(76) L. Helm and A. E. Merbach, *Dalt. Trans.*, 2002, 633–641.

(77) A. E. Danks, S. R. Hall and Z. Schnepp, *Mater. Horizons*, 2016, **3**, 91–112.

(78) Z. Wang, U. Helmersson and P. O. Käll, *Thin Solid Films*, 2002, **405**, 50–54.

(79) Q. Fan, B. McQuillin, A. K. Ray, M. L. Turner and A. B. Seddon, *J. Phys. D. Appl. Phys.*, 2000, **33**, 2683–2686.

(80) J.-B. Seo, Y. H. Cho, W. H. Lee, J.-H. Lee, Y. S. Kim and K. Char, *Japan Soc. Appl. Phys.*, 2019, **12**, Article No. 071004.

(81) E. Rather, J. T. Gatlin, P. G. Nixon, T. Tsukamoto, V. Kravtsov and D. W. Johnson, *J. Am. Chem. Soc.*, 2005, **127**, 3242–3243.

(82) Z. L. Mensinger, J. T. Gatlin, S. T. Meyers, L. N. Zakharov, D. A. Keszler and D. W. Johnson, *Angew. Chemie - Int. Ed.*, 2008, **47**, 9484–9486.

(83) J. T. Gatlin, Z. L. Mensinger, L. N. Zakharov, D. Macinnes and D. W. Johnson, *Inorg. Chem.*, 2008, **47**, 1267–1269.

(84) A. J. Bard, R. Parsons and J. Jordan, *Standard Potentials in Aqueous Solution*, International Union of Pure and Applied Chemistry, 1st edn., 1985.

(85) W. Wang, K. M. Wentz, S. E. Hayes, D. W. Johnson and D. A. Keszler, *Inorg. Chem.*, 2011, **50**, 4683–4685.

(86) M. N. Jackson, L. A. Wills, I. Y. Chang, M. E. Carnes, L. F. Scatena, P. H. Y. Cheong and D. W. Johnson, *Inorg. Chem.*, 2013, **52**, 6187–6192.

(87) D. A. Marsh, S. Goberna-Ferrón, M. K. Baumeister, L. N. Zakharov, M. Nyman and D. W. Johnson, *Dalt. Trans.*, 2017, **46**, 947–955.

(88) C. K. Perkins, M. Jenkins, T.-H. Chiang, R. H. Mansergh, V. Gouliouk, N. Kenane, J. Wager, J. F. Conley and D. A. Keszler, *ACS Appl. Mater. Interfaces*, 2018, **10**, 36082–36087.

(89) M. E. Carnes, C. C. Knutson, A. Nadarajah, M. N. Jackson, A. F. Oliveri, K. M. Norelli, B. M. Crockett, S. R. Bauers, H. A. Moreno-Luna, B. N. Taber, D. J. Pacheco, J. Z. Olson, K. R. Brevick, C. E. Sheehan, D. W. Johnson and S. W. Boettcher, *J. Mater. Chem. C*, 2014, **2**, 8492–8496.

(90) A. Nadarajah, M. Z. B. Wu, K. Archila, M. G. Kast, A. M. Smith, T. H. Chiang, D. A. Keszler, J. F. Wager and S. W. Boettcher, *Chem. Mater.*, 2015, **27**, 5587–5596.

(91) C. K. Perkins, R. H. Mansergh, J. C. Ramos, C. E. Nanayakkara, D.-H. Park, S. Goberna-Ferrón, L. B. Fullmer, J. T. Arens, M. T. Gutierrez-Higgens, Y. R. Jones, J. I. Lopez, T. M. Rowe, D. M. Whitehurst, M. Nyman, Y. J. Chabal and D. A. Keszler, *Opt. Mater. Express*, 2017, **7**, 273–280.

(92) Y. S. Rim, H. Chen, T.-B. Song, S.-H. Bae and Y. Yang, *Chem. Mater.*, 2015, **27**, 5808–5812.

(93) R. M. Smith and A. E. Martell, *Critical Stability Constants*, Springer, New York, 1976, vol. 4.

(94) K. H. Lee, J. H. Park, Y. B. Yoo, W. S. Jang, J. Y. Oh, S. S. Chae, K. J. Moon, J. M. Myoung and H. K. Baik, *ACS Appl. Mater. Interfaces*, 2013, **5**, 2585–92.

(95) C.-M. Kang, J. H. Ryu, H. Kim, Y.-W. O. K.-H. Baek and L.-M. Do, *J. Nanosci. Nanotechnol.*, 2016, **16**, 8473–8477.

(96) J. Park, T. Gergely, Y. S. Rim and S. Pyo, *ACS Appl. Electron. Mater.*, 2019, **1**, 505–512.

Chapter III

(1) R. W. Schwartz, T. Schneller and R. Waser, *Comptes Rendus Chim.*, 2004, **7**, 433–461.

(2) A. Liu, H. Zhu, H. Sun, Y. Xu and Y. Y. Noh, *Adv. Mater.*, 2018, **30**, 1–39.

(3) R. M. Pasquarelli, D. S. Ginley and R. O. Hayre, *Chem. Soc. Rev.*, 2011, **40**, 5406–5441.

(4) P. Martin, *Handbook of Deposition Technologies for Films and Coatings: Science, Applications and Technologies*, Elsevier, Inc., Oxford, 3rd edn., 2005.

(5) I. Bretos, R. Jiménez, J. Ricote and M. L. Calzada, *Chem. Soc. Rev.*, 2018, **47**, 291–308.

(6) A. Nadarajah, M. E. Carnes, M. G. Kast, D. W. Johnson and S. W. Boettcher, *Chem. Mater.*, 2013, **25**, 4080–4087.

(7) K. N. Woods, P. N. Plassmeyer, D. H. Park, L. J. Enman, A. K. Grealish, B. L. Kirk, S. W. Boettcher, D. A. Keszler and C. J. Page, *Chem. Mater.*, 2017, **29**, 8531–8538.

(8) P. Roura, J. Farjas, S. Ricart, M. Aklalouch, R. Guzman, J. Arbiol, T. Puig, A. Calleja, O. Peña-Rodríguez, M. Garriga and X. Obradors, *Thin Solid Films*, 2012, **520**, 1949–1953.

(9) D. Sanchez-Rodriguez, J. Farjas, P. Roura, S. Ricart, N. Mestres, X. Obradors and T. Puig, *J. Phys. Chem. C*, 2013, **117**, 20133–20138.

(10) J. W. Elam and M. J. Pellin, *Anal. Chem.*, 2005, **77**, 3531–3535.

(11) D. A. Buttry and M. D. Ward, *Chem. Rev.*, 1992, **92**, 1355–1379.

(12) A. Nadarajah, M. Z. B. Wu, K. Archila, M. G. Kast, A. M. Smith, T. H. Chiang, D. A. Keszler, J. F. Wager and S. W. Boettcher, *Chem. Mater.*, 2015, **27**, 5587–5596.

(13) E. A. Cochran, D.-H. Park, M. G. Kast, L. J. Enman, C. K. Perkins, R. H. Mansergh, D. A. Keszler, D. W. Johnson and S. W. Boettcher, *Chem. Mater.*, 2017, **29**, 9480–9488.

(14) P. G. L. Baker, R. D. Sanderson and A. M. Crouch, *Thin Solid Films*, 2007, **515**, 6691–6697.

(15 F. Vratny, *Appl. Spectrosc.*, 1959, **13**, 59–70.

(16) R. A. Nyquist, C. L. Putzig, M. A. Leugers and R. O. Kagel, *The Handbook of Infrared and Raman Spectra of Inorganic Compounds and Organic Salts*, Academic Press, Inc., San Diego, CA, 1997.

(17) H. A. Al-abadleh and V. H. Grassian, *Langmuir*, 2003, **19**, 341–347.

(18) T. Takahashi and T. Nishide, *Jorunal Ceram. Soc. Japan*, 2004, **238**, 234–238.

(19) H. Shimizu, S. Konagai, M. Ikeda and T. Nishide, *Jpn. J. Appl. Phys.*, 2009, **48**, 1011011–1011016.

(20) H. Shimizu, D. Nemoto, M. Ikeda and T. Nishide, *Jpn. J. Appl. Phys.*, 2010, **49**, 1–8.

(21) R. H. Mansergh, L. B. Fullmer, D. H. Park, M. Nyman and D. A. Keszler, *Chem. Mater.*, 2016, **28**, 1553–1558.

(22) R. T. Frederick, J. M. Amador, S. Goberna-Ferrón, M. Nyman, D. A. Keszler and G. S. Herman, *J. Phys. Chem. C*, 2018, **122**, 16100–16112.

(23) J. Cui, M. G. Kast, B. A. Hammann, Y. Afriyie, K. N. Woods, P. N. Plassmeyer, C. K. Perkins, Z. L. Ma, D. A. Keszler, C. J. Page, S. W. Boettcher and S. E. Hayes, *Chem. Mater.*, 2018, **30**, 7456–7463.

(24) Y. Chi and S. S. C. Chuang, *J. Phys. Chem. B*, 2000, **104**, 4673–4683.

(25) X. Zhang, H. He, H. Gao and Y. Yu, *Spectrochim. Acta - Part A Mol. Biomol. Spectrosc.*, 2008, **71**, 1446–1451.

(26) F. Prinetto, G. Ghiotti, I. Nova, L. Lietti, E. Tronconi and P. Forzatti, *J. Phys. Chem. B*, 2001, **105**, 12732–12745.

(27) S. Jeong, J. Y. Lee, S. S. Lee, Y. Choi and B. H. Ryu, *J. Phys. Chem. C*, 2011, **115**, 11773–11780.

(28) Y. S. Rim, H. Chen, T.-B. Song, S.-H. Bae and Y. Yang, *Chem. Mater.*, 2015, **27**, 5808–5812.

(29) S. Jeong, J. Y. Lee, S. S. Lee, Y. H. Seo, S. Y. Kim, J. U. Park, B. H. Ryu, W. Yang, J. Moon and Y. Choi, *J. Mater. Chem. C*, 2013, **1**, 4236–4243.

(30) X. Yu, L. Zeng, N. Zhou, P. Guo, F. Shi, D. B. Buchholz, Q. Ma, J. Yu, V. P. Dravid, R. P. H. Chang, M. Bedzyk, T. J. Marks and A. Facchetti, *Adv. Mater.*, 2015, **27**, 2390–2399.

(31) Y. K. Kim, C. H. Ahn, M. G. Yun, S. W. Cho, W. J. Kang and H. K. Cho, *Sci. Rep.*, 2016, **6**, 1–9.

(32) H. Wang, T. Sun, W. Xu, F. Xie, L. Ye, Y. Xiao, Y. Wang, J. Chen and J. Xu, *RSC Adv.*, 2014, **4**, 54729–54739.

(33) M.-G. Kim, M. G. Kanatzidis, A. Facchetti and T. J. Marks, *Nat. Mater.*, 2011, **10**, 382–388.

(34) A. Varma, A. Mukasyan, A. Rogachev and K. V Manukyan, *Chem. Rev.*, 2016, **116**, 14493–14586.

(35) N. Zhou, M.-G. Kim, S. Loser, J. Smith, H. Yoshida, X. Guo, C. Song, H. Jin, Z. Chen, S. M. Yoon, A. J. Freeman, R. P. H. Chang, A. Facchetti and T. J. Marks, *Proc. Natl. Acad. Sci.*, 2015, **112**, 7897–7902.

(36) J. W. Jung, C. C. Chueh and A. K. Y. Jen, *Adv. Mater.*, 2015, **27**, 7874–7880.

(37) B. Wang, L. Zeng, W. Huang, F. S. Melkonyan, W. C. Sheets, L. Chi, M. J. Bedzyk, T. J. Marks and A. F. Facchetti, *J. Am. Chem. Soc.*, 2016, **138**, 7067–7074.

(38) Y. Chen, B. Wang, W. Huang, X. Zhang, G. Wang, M. J. Leonardi, Y. Huang, Z. Lu, T. J. Marks and A. Facchetti, *Chem. Mater.*, 2018, **30**, 3323–3329.

(39) Y. Zhang and Z. Li, *Ceram. Int.*, 2015, **42**, 6360–6368.

(40) R. Branquinho, D. Salgueiro, L. Santos, P. Barquinha, L. Pereira, R. Martins and E. Fortunato, *ACS Appl. Mater. Interfaces*, 2014, **6**, 19592–19599.

(41) Y. H. Kang, S. Jeong, J. M. Ko, J.-Y. Lee, Y. Choi, C. Lee and S. Y. Cho, *J. Mater. Chem. C*, 2014, **2**, 4247–4256.

(42) Q. Jiang, L. Feng, C. Wu, R. Sun, X. Li, B. Lu, Z. Ye and J. Lu, *Appl. Phys. Lett.*, 2015, **106**, Article No. 053503.

(43) J. Smith, L. Zeng, R. Khanal, K. Stallings, A. Facchetti, J. E. Medvedeva, M. J. Bedzyk and T. J. Marks, *Adv. Electron. Mater.*, 2015, **1**, Article No. 1500146.

(44) J. W. Hennek, J. Smith, A. Yan, M. G. Kim, W. Zhao, V. P. Dravid, A. Facchetti and T. J. Marks, *J. Am. Chem. Soc.*, 2013, **135**, 10729–10741.

(45) J. W. Hennek, M. G. Kim, M. G. Kanatzidis, A. Facchetti and T. J. Marks, *J. Am. Chem. Soc.*, 2012, **134**, 9593–9596.

(46) X. Yu, J. Smith, N. Zhou, L. Zeng, P. Guo, Y. Xia, A. Alvarez, S. Aghion, H. Lin, J. Yu, R. P. H. Chang, M. J. Bedzyk, R. Ferragut, T. J. Marks and A. Facchetti, *Proc. Natl. Acad. Sci.*, 2015, **112**, 3217–3222.

(47) K.-H. Lim, J. Lee, J.-E. Huh, J. Park, J.-H. Lee, S.-E. Lee and Y. S. Kim, *J. Mater. Chem. C*, 2017, **5**, 7768–7776.

(48) Y. H. Hwang, J. S. Seo, J. M. Yun, H. J. Park, S. Yang, S. H. K. Park and B. S. Bae, *NPG Asia Mater.*, 2013, **5**, Article No. e45.

(49) I. Isakov, H. Faber, M. Grell, G. Wyatt-Moon, N. Pliatsikas, T. Kehagias, G. P. Dimitrakopulos, P. P. Patsalas, R. Li and T. D. Anthopoulos, *Adv. Funct. Mater.*, 2017, **27**, 1–9.

(50) J. Park, T. Gergely, Y. S. Rim and S. Pyo, *ACS Appl. Electron. Mater.*, 2019, **1**, 505–512.

(51) J. S. Lee, Y.-J. Kwack and W.-S. Choi, *ACS Appl. Mater. Interfaces*, 2013, **5**, 11578–11583.

(52) Y. Meng, G. Liu, A. Liu, H. Song, Y. Hou, B. Shin and F. Shan, *RSC Adv.*, 2015, **5**, 37807–37813.

(53) Y.-H. Kim, J.-S. Heo, T.-H. Kim, S. Park, M.-H. Yoon, J. Kim, M. S. Oh, G.-R. Yi, Y.-Y. Noh and S. K. Park, *Nature*, 2012, **489**, 128–132.

(54) R. A. John, A. C. Nguyen, S. Shukla, N. Tiwari, S. Chen, G. I. Ng and N. Mathews, *Chem. Mater.*, 2016, **28**, 8305–8313.

(55) D. Sanchez-Rodriguez, H. Eloussifi, J. Farjas, P. Roura and M. Dammak, *Thermochim. Acta*, 2014, **589**, 37–46.

(56) P. Roura, J. Farjas, H. Eloussi, L. Carreras, S. Ricart, T. Puig and X. Obradors, *Thermochim. Acta*, 2015, **601**, 1–8.

(57) D. Sánchez-Rodriguez, J. Farjas and P. Roura, *Combust. Flame*, 2017, **186**, 211–219.

(58) S. Park, K. H. Kim, J. W. Jo, S. Sung, K. T. Kim, W. J. Lee, J. Kim, H. J. Kim, G. R. Yi, Y. H. Kim, M. H. Yoon and S. K. Park, *Adv. Funct. Mater.*, 2015, **25**, 2807–2815.

(59) S. Goldstein and J. Rabani, *J. Am. Chem. Soc.*, 2007, **129**, 10597–10601.

(60) J. Mack and J. R. Bolton, *J. Photochem. Photobiol. A Chem.*, 1999, **128**, 1–13.

(61) T. B. Daunis, D. Barrera, G. Gutierrez-Heredia, O. Rodriguez-Lopez, J. Wang, W. E. Voit and J. W. P. Hsu, *J. Mater. Res.*, 2018, **33**, 2454–2462.

(62) B.-Y. Su, S.-Y. Chu, Y.-D. Juang and H.-C. Chen, *Appl. Phys. Lett.*, 2013, **102**, Article No. 192101.

(63) Y. J. Kim, J. K. Jeong, J. H. Park, B. J. Jeong, H. D. Lee and G. W. Lee, *Jpn. J. Appl. Phys.*, 2018, **57**, 4–8.

(64) J. Hwang, K. Lee, Y. Jeong, Y. U. Lee, C. Pearson, M. C. Petty and H. Kim, *Adv. Mater. Interfaces*, 2014, **1**, Article No. 1400206.

(65) C. Zhu, A. Liu, G. Liu, G. Jiang, Y. Meng, E. Fortunato, R. Martins and F. Shan, *J. Mater. Chem. C*, 2016, **4**, 10715–10721.

(66) G. Liu, A. Liu, H. Zhu, B. Shin, E. Fortunato, R. Martins, Y. Wang and F. Shan, *Adv. Funct. Mater.*, 2015, **25**, 2564–2572.

(67) J. He, D. M. Weekes, W. Cheng, K. E. Dettelbach, A. Huang, T. Li and C. P. Berlinguette, *J. Am. Chem. Soc.*, 2017, **139**, 18174–18177.

(68) J. Leppäniemi, K. Eiroma, H. Majumdar and A. Alastalo, *ACS Appl. Mater. Interfaces*, 2017, **9**, 8774–8782.

(69) J. Jo, Y. Kim, J. Park, J. S. Heo, S. Hwang, W. Lee, M. Yoon, M. Kim and S. K. Park, *ACS Appl. Mater. Interfaces*, 2017, **9**, 35114–35124.

(70) W. Xu, H. Li, J.-B. Xu and L. Wang, *ACS Appl. Mater. Interfaces*, 2018, **10**, 25878–25901.

(71) K. K. Banger, Y. Yamashita, K. Mori, R. L. Peterson, T. Leedham, J. Rickard and H. Sirringhaus, *Nat. Mater.*, 2011, **10**, 45–50.

(72) W. T. Park, I. Son, H. W. Park, K. B. Chung, Y. Xu, T. Lee and Y. Y. Noh, *ACS Appl. Mater. Interfaces*, 2015, **7**, 13289–13294.

(73) J. Chang, K. L. Chang, C. Chi, J. Zhang and J. Wu, *J. Mater. Chem. C*, 2014, **2**, 5397–5403.

(74) K. C. Fairley, D. R. Merrill, K. N. Woods, J. Ditto, C. Xu, R. P. Oleksak, T. Gustafsson, D. W. Johnson, E. L. Garfunkel, G. S. Herman, D. C. Johnson and C. J. Page, *ACS Appl. Mater. Interfaces*, 2016, **8**, 667–672.

(75) K. N. Woods, M. C. Thomas, G. Mitchson, J. Ditto, C. Xu, D. Kayal, K. C. Frisella, T. Gustafsson, E. Garfunkel, Y. J. Chabal, D. C. Johnson and C. J. Page, *ACS Appl. Mater. Interfaces*, 2017, **9**, 37476–37483.

(76) K. H. Lim, J. E. Huh, J. Lee, N. K. Cho, J. W. Park, B. Il Nam, E. Lee and Y. S. Kim, *ACS Appl. Mater. Interfaces*, 2017, **9**, 548–557.

(77) K. Okamura and H. Hahn, *Appl. Phys. Lett.*, 2010, **97**, Article No. 153114.

(78) S. Polster, M. P. M. Jank and L. Frey, *J. Appl. Phys.*, 2016, **119**, Article No. 024504.

(79) S. R. Thomas, P. Pattanasattayavong and T. D. Anthopoulos, *Chem. Soc. Rev.*, 2013, **42**, 6910–23.

Chapter IV

(1) *Solution Processing of Inorganic Materials*; Mitzi, D. B., Ed.; John Wiley & Sons Inc.: Hoboken, 2009.

(2) Boucle, J.; Ravirajan, P.; Nelson, J. Hybrid Polymer-Metal Oxide Thin Films for Photovoltaic Applications. *J. Mater. Chem.* **2007**, *17*, 3141–3153.

(3) Yan, K.; Long, M.; Zhang, T.; Wei, Z.; Chen, H.; Yang, S.; Xu, J. Hybrid Halide Perovskite Solar Cell Precursors: Colloidal Chemistry and Coordination Engineering behind Device Processing for High Efficiency. *J. Am. Chem. Soc.* **2015**, *137*, 4460–4468.

(4) Mitzi, D. B. Solution-Processed Inorganic Semiconductors. *J. Mater. Chem.* **2004**, *14*, 2355–2365.

(5) Banger, K. K.; Yamashita, Y.; Mori, K.; Peterson, R. L.; Leedham, T.; Rickard, J.; Sirringhaus, H. Low-Temperature, High-Performance Solution-Processed Metal Oxide Thin-Film Transistors Formed by a “Sol–Gel on Chip” Process. *Nat. Mater.* **2011**, *10*, 45–50.

(6) Thomas, S. R.; Pattanasattayavong, P.; Anthopoulos, T. D. Solution-Processable Metal Oxide Semiconductors for Thin-Film Transistor Applications. *Chem. Soc. Rev.* **2013**, *42*, 6910–6923.

(7) Kim, S. J.; Yoon, S.; Kim, H. J. Review of Solution-Processed Oxide Thin-Film Transistors. *Jpn. J. Appl. Phys.* **2014**, *2*, Article No. 02BA02.

(8) Bae, S.; Kim, H.; Lee, Y.; Xu, X.; Park, J.-S.; Zheng, Y.; Balakrishnan, J.; Lei, T.; Kim, H. R.; Song, Y. Il; Kim, Y.-J.; Kim, K. S.; Ozyilmaz, B.; Ahn, J.-H.; Hong, B. H.; Iijima, S. Roll-to-Roll Production of 30-Inch Graphene Films for Transparent Electrodes. *Nat. Nanotechnol.* **2010**, *5*, 574–578.

(9) Galagan, Y.; de Vries, I. G.; Langen, A. P.; Andriessen, R.; Verhees, W. J. H.; Veenstra, S. C.; Kroon, J. M. Technology Development for Roll-to-Roll Production of Organic Photovoltaics. *Chem. Eng. Process. Process Intensif.* **2011**, *50*, 454–461.

(10) Schwartz, R. W.; Schneller, T.; Waser, R. Chemical Solution Deposition of Electronic Oxide Films. *Comptes Rendus Chim.* **2004**, *7*, 433–461.

(11) Krebs, F. C. Fabrication and Processing of Polymer Solar Cells: A Review of Printing and Coating Techniques. *Sol. Energy Mater. Sol. Cells* **2009**, *93*, 394–412.

(12) Street, R. A. Thin-Film Transistors. *Adv. Mater.* **2009**, *21*, 2007–2022.

(13) Sun, Y.; Rogers, J. A. Inorganic Semiconductors for Flexible Electronics. *Adv. Mater.* **2007**, *19*, 1897–1916.

(14) Meyers, S. T.; Anderson, J. T.; Hung, C. M.; Thompson, J.; Wager, J. F.; Keszler, D. A. Aqueous Inorganic Inks for Low-Temperature Fabrication of ZnO TFTs. *J. Am. Chem. Soc.* **2008**, *130*, 17603–17609.

(15) Nadarajah, A.; Carnes, M. E.; Kast, M. G.; Johnson, D. W.; Boettcher, S. W. Aqueous Solution Processing of F-Doped SnO_2 Transparent Conducting Oxide Films Using a Reactive Tin(II) Hydroxide Nitrate Nanoscale Cluster. *Chem. Mater.* **2013**, *25*, 4080–4087.

(16) Kim, Y.-H.; Heo, J.-S.; Kim, T.-H.; Park, S.; Yoon, M.-H.; Kim, J.; Oh, M. S.; Yi, G.-R.; Noh, Y.-Y.; Park, S. K. Flexible Metal-Oxide Devices Made by Room-Temperature Photochemical Activation of Sol–gel Films. *Nature* **2012**, *489*, 128–132.

(17) Han, S. Y.; Herman, G. S.; Chang, C. H. Low-Temperature, High-Performance, Solution-Processed Indium Oxide Thin-Film Transistors. *J. Am. Chem. Soc.* **2011**, *133*, 5166–5169.

(18) Jun, T.; Song, K.; Jeong, Y.; Woo, K.; Kim, D.; Bae, C.; Moon, J. High-Performance Low-Temperature Solution-Processable ZnO Thin Film Transistors by Microwave-Assisted Annealing. *J. Mater. Chem.* **2011**, *21*, 1102–1108.

(19) Smith, S. W.; Wang, W.; Keszler, D. A.; Conley, J. F. Solution Based Prompt Inorganic Condensation and Atomic Layer Deposition of Al_2O_3 Films: A Side-by-Side Comparison. *J. Vac. Sci. Technol. A Vacuum, Surfaces, Film.* **2014**, *32*, 41501.

(20) Kim, K. M.; Kim, C. W.; Heo, J. S.; Na, H.; Lee, J. E.; Park, C. B.; Bae, J. U.; Kim, C. D.; Jun, M.; Hwang, Y. K.; Meyers, S. T.; Grenville, A.; Keszler, D. A. Competitive Device Performance of Low-Temperature and All-Solution-Processed Metal-Oxide Thin-Film Transistors. *Appl. Phys. Lett.* **2011**, *99*, Article No. 242109.

(21) Yu, X.; Marks, T. J.; Facchetti, A. Metal Oxides for Optoelectronic Applications. *Nat. Mater.* **2016**, *15*, 383–396.

(22) Varma, A.; Mukasyan, A.; Rogachev, A.; Manukyan, K. V. Solution Combustion Synthesis of Nanoscale Materials. *Chem. Rev.* **2016**, *116*, 14493–14586.

(23) Kim, M.-G.; Kanatzidis, M. G.; Facchetti, A.; Marks, T. J. Low-Temperature Fabrication of High-Performance Metal Oxide Thin-Film Electronics via Combustion Processing. *Nat. Mater.* **2011**, *10*, 382–388.

(24) Manukyan, K. V.; Cross, A.; Roslyakov, S.; Rouvimov, S.; Rogachev, A. S.; Wolf, E. E.; Mukasyan, A. S. Solution Combustion Synthesis of Nano-Crystalline Metallic Materials: Mechanistic Studies. *J. Phys. Chem. C* **2013**, *117*, 24417–24427.

(25) Hennek, J. W.; Kim, M. G.; Kanatzidis, M. G.; Facchetti, A.; Marks, T. J. Exploratory Combustion Synthesis: Amorphous Indium Yttrium Oxide for Thin-Film Transistors. *J. Am. Chem. Soc.* **2012**, *134*, 9593–9596.

(26) Kim, M. G.; Hennek, J. W.; Kim, H. S.; Kanatzidis, M. G.; Facchetti, A.; Marks, T. J. Delayed Ignition of Autocatalytic Combustion Precursors: Low-Temperature Nanomaterial Binder Approach to Electronically Functional Oxide Films. *J. Am. Chem. Soc.* **2012**, *134*, 11583–11593.

(27) Smith, J.; Zeng, L.; Khanal, R.; Stallings, K.; Facchetti, A.; Medvedeva, J. E.; Bedzyk, M. J.; Marks, T. J. Cation Size Effects on the Electronic and Structural Properties of Solution-Processed In-X-O Thin Films. *Adv. Electron. Mater.* **2015**, *1*, Article No. 1500146.

(28) Hennek, J. W.; Smith, J.; Yan, A.; Kim, M. G.; Zhao, W.; Dravid, V. P.; Facchetti, A.; Marks, T. J. Oxygen "Getter" Effects on Microstructure and Carrier Transport in Low Temperature Combustion-Processed a-InXZnO (X = Ga, Sc, Y, La) Transistors. *J. Am. Chem. Soc.* **2013**, *135*, 10729–10741.

(29) Everaerts, K.; Zeng, L.; Hennek, J. W.; Canacho, D. I.; Jariwala, D.; Bedzyk, M. J.; Hersam, M. C.; Marks, T. J. Printed Indium Gallium Zinc Oxide Transistors. Self-Assembled Nanodielectric Effects on Low-Temperature Combustion Growth and Carrier Mobility. *ACS Appl. Mater. Interfaces* **2013**, *5*, 11884–11893.

(30) Cui, B.; Zeng, L.; Keane, D.; Bedzyk, M. J.; Buchholz, D. B.; Chang, R. P. H.; Yu, X.; Smith, J.; Marks, T. J.; Xia, Y.; Facchetti, A. F.; Medvedeva, J. E.; Grayson, M. Thermal Conductivity Comparison of Indium Gallium Zinc Oxide Thin Films: Dependence on Temperature, Crystallinity, and Porosity. *J. Phys. Chem. C* **2016**, *120*, 7467–7475.

(31) Wang, B.; Zeng, L.; Huang, W.; Melkonyan, F. S.; Sheets, W. C.; Chi, L.; Bedzyk, M. J.; Marks, T. J.; Facchetti, A. F. Carbohydrate-Assisted Combustion Synthesis to Realize High-Performance Oxide Transistors. *J. Am. Chem. Soc.* **2016**, *138*, 7067–7074.

(32) Carlos, E.; Branquinho, R.; Kiazadeh, A.; Barquinha, P.; Martins, R.; Fortunato, E. UV-Mediated Photochemical Treatment for Low-Temperature Oxide-Based Thin-Film Transistors. *ACS Appl. Mater. Interfaces* **2016**, *8*, 31100–31108.

(33) Yu, X.; Zeng, L.; Zhou, N.; Guo, P.; Shi, F.; Buchholz, D. B.; Ma, Q.; Yu, J.; Dravid, V. P.; Chang, R. P. H.; Bedzyk, M.; Marks, T. J.; Facchetti, A. Ultra-flexible, "Invisible" Thin-Film Transistors Enabled by Amorphous Metal Oxide/Polymer Channel Layer Blends. *Adv. Mater.* **2015**, *27*, 2390–2399.

(34) Kang, Y. H.; Jeong, S.; Ko, J. M.; Lee, J.-Y.; Choi, Y.; Lee, C.; Cho, S. Y. Two-Component Solution Processing of Oxide Semiconductors for Thin-Film Transistors via Self-Combustion Reaction. *J. Mater. Chem. C* **2014**, *2*, 4247–4256.

(35) Wang, H.; Xu, W.; Zhou, S.; Xie, F.; Xiao, Y.; Ye, L.; Chen, J.; Xu, J. Oxygen Plasma Assisted High Performance Solution-Processed Al_2O_x Gate Insulator for Combustion-Processed $InGaZnO_x$ Thin Film Transistors. *J. Appl. Phys.* **2015**, *117*, Article No. 035703.

(36) Yao, C.; Xu, X.; Wang, J.; Shi, L.; Li, L. Low-Temperature, Solution-Processed Hole Selective Layers for Polymer Solar Cells. *ACS Appl. Mater. Interfaces* **2013**, *5*, 1100–1107.

(37) Jiang, Q.; Lu, J.; Cheng, J.; Li, X.; Sun, R.; Feng, L.; Dai, W.; Yan, W.; Ye, Z. Combustion-Process Derived Comparable Performances of Zn-(In:Sn)-O Thin-Film Transistors with a Complete Miscibility. *Appl. Phys. Lett.* **2014**, *105*, Article No. 132105.

(38) Tue, P. T.; Inoue, S.; Takamura, Y.; Shimoda, T. Combustion Synthesized Indium-Tin-Oxide (ITO) Thin Film for Source/Drain Electrodes in All Solution-Processed Oxide Thin-Film Transistors. *Appl. Phys. A* **2016**, *122*, Article No. 623.

(39) Jung, J. W.; Chueh, C. C.; Jen, A. K. Y. A Low-Temperature, Solution-Processable, Cu-Doped Nickel Oxide Hole-Transporting Layer via the Combustion Method for High-Performance Thin-Film Perovskite Solar Cells. *Adv. Mater.* **2015**, *27*, 7874–7880.

(40) Branquinho, R.; Salgueiro, D.; Santos, L.; Barquinha, P.; Pereira, L.; Martins, R.; Fortunato, E. Aqueous Combustion Synthesis of Aluminum Oxide Thin Films and Application as Gate Dielectric in GZTO Solution-Based TFTs. *ACS Appl. Mater. Interfaces* **2014**, *6*, 19592–19599.

(41) Zhang, Y.; Li, Z. Low-Temperature Fabrication of Sol-Gel NiO Film for Optoelectronic Devices Based on the "Fuel" of Urea. *Ceram. Int.* **2015**, *42*, 6360–6368.

(42) Lee, J. S.; Kwack, Y.-J.; Choi, W.-S. Inkjet-Printed In_2O_3 Thin-Film Transistor below 200 °C. *ACS Appl. Mater. Interfaces* **2013**, *5*, 11578–11583.

(43) Jiang, Q.; Feng, L.; Wu, C.; Sun, R.; Li, X.; Lu, B.; Ye, Z.; Lu, J. Amorphous ZnAlSnO Thin-Film Transistors by a Combustion Solution Process for Future Displays. *Appl. Phys. Lett.* **2015**, *106*, Article No. 053503.

(44) Kim, S. J.; Song, A. R.; Lee, S. S.; Nahm, S.; Choi, Y.; Chung, K.-B.; Jeong, S. Independent Chemical/Physical Role of Combustive Exothermic Heat in Solution-Processed Metal Oxide Semiconductors for Thin-Film Transistors. *J. Mater. Chem. C* **2014**, *3*, 1457–1462.

(45) Liu, A.; Zhu, H.; Guo, Z.; Meng, Y.; Liu, G.; Fortunato, E.; Martins, R.; Shan, F. Solution Combustion Synthesis: Low-Temperature Processing for P-Type Cu:NiO Thin Films for Transparent Electronics. *Adv. Mater.* **2017**, *29*, Article No. 1701599.

(46) Weng, J.; Chen, W.; Xia, W.; Zhang, J.; Jiang, Y.; Zhu, G. Low-Temperature Solution-Based Fabrication of High-K HfO_2 Dielectric Thin Films via Combustion Process. *J. Sol-Gel Sci. Technol.* **2017**, *81*, 662–668.

(47) Sanchez-Rodriguez, D.; Farjas, J.; Roura, P.; Ricart, S.; Mestres, N.; Obradors, X.; Puig, T. Thermal Analysis for Low Temperature Synthesis of Oxide Thin Films from Chemical Solutions. *J. Phys. Chem. C* **2013**, *117*, 20133–20138.

(48) Sanchez-Rodriguez, D.; Eloussifi, H.; Farjas, J.; Roura, P.; Dammak, M. Thermal Gradients in Thermal Analysis Experiments: Criterions to Prevent Inaccuracies When Determining Sample Temperature and Kinetic Parameters. *Thermochim. Acta* **2014**, *589*, 37–46.

(49) Roura, P.; Farjas, J.; Eloussi, H.; Carreras, L.; Ricart, S.; Puig, T.; Obradors, X. Thermal Analysis of Metal Organic Precursors for Functional Oxide Preparation : Thin Films Versus Powders. *Thermochim. Acta* **2015**, *601*, 1–8.

(50) Jung, H. S.; Lee, J. K.; Hong, K. S.; Youn, H. J. Ion-Induced Secondary Electron Emission Behavior of Sol-Gel-Derived MgO Thin Films Used for Protective Layers in Alternating Current Plasma Display Panels. *J. Appl. Phys.* **2002**, *92*, 2855–2860.

(51) Jiang, G.; Liu, A.; Liu, G.; Zhu, C.; Meng, Y.; Shin, B.; Fortunato, E.; Martins, R.; Shan, F. Solution-Processed High-K Magnesium Oxide Dielectrics for Low-Voltage Oxide Thin-Film Transistors. *Appl. Phys. Lett.* **2016**, *109*, Article No. 183508.

(52) Kim, G. H.; Jeong, W. H.; Du Ahn, B.; Shin, H. S.; Kim, H. J.; Kim, H. J.; Ryu, M. K.; Park, K. B.; Seon, J. B.; Lee, S. Y. Investigation of the Effects of Mg Incorporation into InZnO for High-Performance and High-Stability Solution-Processed Thin Film Transistors. *Appl. Phys. Lett.* **2010**, *96*, 94–97.

(53) Li, D. Phosphor Development: Synthesis, Characterization, and Chromatic Control. Ph.D. Dissertation, Oregon State University, Corvallis, OR, 1999.

(54) Bai, S.; Cao, M.; Jin, Y.; Dai, X.; Liang, X.; Ye, Z.; Li, M.; Cheng, J.; Xiao, X.; Wu, Z.; Xia, Z.; Sun, B.; Wang, E.; Mo, Y.; Gao, F.; Zhang, F. Low-Temperature Combustion-Synthesized Nickel Oxide Thin Films as Hole-Transport Interlayers for Solution-Processed Optoelectronic Devices. *Adv. Energy Mater.* **2014**, *4*, Article No. 1301460.

(55) Scherrer, P. Bestimmung Der Grösse Und Der Inneren Struktur von Kolloidteilchen Mittels Röntgenstrahlen. *Nachr. Ges. Wiss. Göttingen* **1918**, *2*, 98–100.

(56) Advanced Integrated X-Ray Powder Diffraction Suite- PDXL 2. *Rigaku J.* **2012**, *28*, 29–30.

(57) Buttry, D. A.; Ward, M. D. Measurement of Interfacial Processes at Electrode Surfaces with the Electrochemical Quartz Crystal Microbalance. *Chem. Rev.* **1992**, *92*, 1355–1379.

(58) Sauerbrey, G. Verwendung von Schwingquarzen Zur Wägung Dünner Schichten Und Zur Mikrowägung. *Zeitschrift für Phys.* **1959**, *155*, 206–222.

(59) Trotochaud, L.; Ranney, J. K.; Williams, K. N.; Boettcher, S. W. Solution-Cast Metal Oxide Thin Film Electrocatalysts for Oxygen Evolution. *J. Am. Chem. Soc.* **2012**, *134*, 17253–17261.

(60) Nadarajah, A.; Wu, M. Z. B.; Archila, K.; Kast, M. G.; Smith, A. M.; Chiang, T. H.; Keszler, D. A.; Wager, J. F.; Boettcher, S. W. Amorphous In–Ga–Zn Oxide Semiconducting Thin Films with High Mobility from Electrochemically Generated Aqueous Nanocluster Inks. *Chem. Mater.* **2015**, *27*, 5587–5596.

(61) Rim, Y. S.; Chen, H.; Song, T.-B.; Bae, S.-H.; Yang, Y. Hexaaqua Metal Complexes for Low-Temperature Formation of Fully Metal Oxide Thin-Film Transistors. *Chem. Mater.* **2015**, *27*, 5808–5812.

(62) Chi, Y.; Chuang, S. S. C. Infrared and TPD Studies of Nitrates Adsorbed on Tb_4O_7, La_2O_3, BaO, and MgO/γ-Al_2O_3. *J. Phys. Chem. B* **2000**, *104*, 4673–4683.

(63) Prinetto, F.; Ghiotti, G.; Nova, I.; Lietti, L.; Tronconi, E.; Forzatti, P. FT-IR and TPD Investigation of the NO_x Storage Properties of BaO/Al_2O_3 and Pt−BaO/Al_2O_3 Catalysts. *J. Phys. Chem. B* **2001**, *105*, 12732–12745.

(64) Dunn, M. S.; Brophy, T. W. Decomposition Points of the Amino Acids. *J. Biol. Chem.* **1932**, *99*, 221–229.

(65) Wu, L.; Yu, J. C.; Zhang, L.; Wang, X.; Li, S. Selective Self-Propagating Combustion Synthesis of Hexagonal and Orthorhombic Nanocrystalline Yttrium Iron Oxide. *J. Solid State Chem.* **2004**, *177*, 3666–3674.

(66) Ianoş, R.; Lazău, I.; Păcurariu, C.; Barvinschi, P. Solution Combustion Synthesis of $MgAl_2O_4$ Using Fuel Mixtures. *Mater. Res. Bull.* **2008**, *43*, 3408–3415.

(67) Bai, J.; Liu, J.; Li, C.; Li, G.; Du, Q. Mixture of Fuels Approach for Solution Combustion Synthesis of Nanoscale $MgAl_2O_4$ Powders. *Adv. Powder Technol.* **2011**, *22*, 72–76.

(68) Kim, H. S.; Byrne, P. D.; Facchetti, A.; Marks, T. J. High Performance Solution-Processed Indium Oxide Thin-Film Transistors. *J. Am. Chem. Soc.* **2008**, *130*, 12580–12581.

(69) Alam, M. J.; Cameron, D. C. Investigation of Annealing Effects on Sol-Gel Deposited Indium Tin Oxide Thin Films in Different Atmospheres. *Thin Solid Films* **2002**, *420–421*, 76–82.

(70) Seo, S.-J.; Choi, C. G.; Hwang, Y. H.; Bae, B.-S. High Performance Solution-Processed Amorphous Zinc Tin Oxide Thin Film Transistor. *J. Phys. D. Appl. Phys.* **2008**, *42*, Article No. 035106.

(71) Choi, C. G.; Seo, S.; Bae, B. Solution-Processed Indium-Zinc Oxide Transparent Thin-Film Transistors. *Electrochem. Solid-State Lett.* **2008**, *11*, H7–H9.

(72) Jeong, S.; Lee, J. Y.; Lee, S. S.; Choi, Y.; Ryu, B. H. Impact of Metal Salt Precursor on Low-Temperature Annealed Solution-Derived Ga-Doped In_2O_3 Semiconductor for Thin-Film Transistors. *J. Phys. Chem. C* **2011**, *115*, 11773–11780.

(73) Sánchez-Rodriguez, D.; Farjas, J.; Roura, P. The Critical Conditions for Thermal Explosion in a System Heated at a Constant Rate. *Combust. Flame* **2017**, *186*, 211–219.

Chapter V

(1) Liu, A.; Zhu, H.; Sun, H.; Xu, Y.; Noh, Y. Solution Processed Metal Oxide High-κ Dielectrics for Emerging Transistors and Circuits. *Adv. Mater.* **2018**, *30*, 1706364.

(2) Plassmeyer, P. N.; Archila, K.; Wager, J. F.; Page, C. J. Lanthanum Aluminum Oxide Thin-Film Dielectrics from Aqueous Solution. *ACS Appl. Mater. Interfaces* **2015**, *7*, 1678–1684.

(3) Woods, K. N.; Chiang, T. H.; Plassmeyer, P. N.; Kast, M. G.; Lygo, A. C.; Grealish, A. K.; Boettcher, S. W.; Page, C. J. High-κ Lanthanum Zirconium Oxide Thin Film Dielectrics from Aqueous Solution Precursors. *ACS Appl. Mater. Interfaces* **2017**, *9*, 10897–10903.

(4) Banger, K. K.; Yamashita, Y.; Mori, K.; Peterson, R. L.; Leedham, T.; Rickard, J.; Sirringhaus, H. Low-Temperature, High-Performance Solution-Processed Metal Oxide Thin-Film Transistors Formed by a 'Sol–Gel on Chip' Process. *Nat. Mater.* **2011**, *10*, 45–50.

(5) Mitzi, D. B. Solution-Processed Inorganic Semiconductors. *J. Mater. Chem.* **2004**, *14*, 2355–2365.

(6) Thomas, S. R.; Pattanasattayavong, P.; Anthopoulos, T. D. Solution-Processable Metal Oxide Semiconductors for Thin-Film Transistor Applications. *Chem. Soc. Rev.* **2013**, *42*, 6910–6923.

(7) Pasquarelli, R. M.; Ginley, D. S.; Hayre, R. O. Solution Processing of Transparent Conductors : From Flask to Film. *Chem. Soc. Rev.* **2011**, *40*, 5406–5441.

(8) Nadarajah, A.; Carnes, M. E.; Kast, M. G.; Johnson, D. W.; Boettcher, S. W. Aqueous Solution Processing of F-Doped SnO_2 Transparent Conducting Oxide Films Using a Reactive Tin(II) Hydroxide Nitrate Nanoscale Cluster. *Chem. Mater.* **2013**, *25*, 4080–4087.

(9) Smith, R. D. L.; Prevot, M. S.; Fagan, R. D.; Zhang, Z.; Sedach, P. A.; Siu, M. K. J.; Trudel, S.; Berlinguette, C. P. Photochemical Route for Accessing Amorphous Metal Oxide Materials for Water Oxidation Catalysis. *Science* **2013**, *340*, 60–63.

(10) He, J.; Weekes, D. M.; Cheng, W.; Dettelbach, K. E.; Huang, A.; Li, T.; Berlinguette, C. P. Photodecomposition of Metal Nitrate and Chloride Compounds Yields Amorphous Metal Oxide Films. *J. Am. Chem. Soc.* **2017**, *139*, 18174–18177.

(11) Trotochaud, L.; Ranney, J. K.; Williams, K. N.; Boettcher, S. W. Solution-Cast Metal Oxide Thin Film Electrocatalysts for Oxygen Evolution. *J. Am. Chem. Soc.* **2012**, *134*, 17253–17261.

(12) Kast, M. G.; Cochran, E. A.; Enman, L. J.; Mitchson, G.; Ditto, J.; Siefe, C.; Plassmeyer, P. N.; Greenaway, A. L.; Johnson, D. C.; Page, C. J.; Boettcher, S. W. Amorphous Mixed-Metal Oxide Thin Films from Aqueous Solution Precursors with Near-Atomic Smoothness. *J. Am. Chem. Soc.* **2016**, *138*, 16800–16808.

(13) Wang, D.; Bierwagen, G. P. Sol-Gel Coatings on Metals for Corrosion Protection. *Prog. Org. Coatings* **2009**, *64*, 327–338.

(14) *Solution Processing of Inorganic Materials*, 1st ed.; Mitzi, D. B., Ed.; John Wiley & Sons Inc.: Hoboken, 2009.

(15) Rim, Y. S.; Bae, S. H.; Chen, H.; De Marco, N.; Yang, Y. Recent Progress in Materials and Devices toward Printable and Flexible Sensors. *Adv. Mater.* **2016**, *28*, 4415–4440.

(16) Petti, L. Metal Oxide Semiconductor Thin-Film Transistors for Flexible Electronics. *Appl. Phys. Rev.* **2016**, *3*, Article No. 021303.

(17) Bretos, I.; Jiménez, R.; Ricote, J.; Calzada, M. L. Low-Temperature Crystallization of Solution-Derived Metal Oxide Thin Films Assisted by Chemical Processes. *Chem. Soc. Rev.* **2018**, *47*, 291-308.

(18) Xu, W.; Li, H.; Xu, J.-B.; Wang, L. Recent Advances of Solution-Processed Metal Oxide Thin-Film Transistors. *ACS Appl. Mater. Interfaces* **2018**, *10*, 25878–25901.

(19) Park, J. W.; Kang, B. H.; Kim, H. J. A Review of Low-Temperature Solution-Processed Metal Oxide Thin-Film Transistors for Flexible Electronics. *Adv. Funct. Mater.* **2019**, Article No. 1904632.

(20) Cochran, E. A.; Woods, K. N.; Johnson, D. W.; Page, C. J.; Boettcher, S. W. Unique Chemistries of Metal-Nitrate Precursors to Form Metal-Oxide Thin Films from Solution: Materials for Electronic and Energy Applications. *J. Mater. Chem. A* **2019**, *7*, 24124-24149.

(21) Park, W. T.; Son, I.; Park, H. W.; Chung, K. B.; Xu, Y.; Lee, T.; Noh, Y. Y. Facile Routes To Improve Performance of Solution-Processed Amorphous Metal Oxide Thin Film Transistors by Water Vapor Annealing. *ACS Appl. Mater. Interfaces* **2015**, *7*, 13289–13294.

(22) Chang, J.; Chang, K. L.; Chi, C.; Zhang, J.; Wu, J. Water Induced Zinc Oxide Thin Film Formation and Its Transistor Performance. *J. Mater. Chem. C* **2014**, *2*, 5397–5403.

(23) Woods, K. N.; Plassmeyer, P. N.; Park, D. H.; Enman, L. J.; Grealish, A. K.; Kirk, B. L.; Boettcher, S. W.; Keszler, D. A.; Page, C. J. Low-Temperature Steam Annealing of Metal Oxide Thin Films from Aqueous Precursors: Enhanced Counterion Removal, Resistance to Water Absorption, and Dielectric Constant. *Chem. Mater.* **2017**, *29*, 8531–8538.

(24) Rim, Y. S.; Chen, H.; Song, T.-B.; Bae, S.-H.; Yang, Y. Hexaaqua Metal Complexes for Low-Temperature Formation of Fully Metal Oxide Thin-Film Transistors. *Chem. Mater.* **2015**, *27*, 5808–5812.

(25) Yuvaraj, S.; Lin, F. Y.; Chang, T. H.; Yeh, C. T. Thermal Decomposition of Metal Nitrates in Air and Hydrogen Environments. *J. Phys. Chem. B* **2003**, *107*, 1044–1047.

(26) Wendlandt, W. W. The Thermal Decomposition of Yttrium, Scandium, and Some Rare-Earth Chloride Hydrates. *J. Inorg. Nucl. Chem.* **1957**, *5*, 118–122.

(27) Bhattacharya, A. K.; Hartridge, A.; Mallick, K. K.; Werrett, C. R.; Woodhead, J. L. Low-Temperature Decomposition of Hydrated Transition Metal Chlorides on Hydrous Gel Substrates. *J. Mater. Sci.* **1996**, *31*, 4479–4482.

(28) Melnikov, P.; Nascimento, V. A.; Arkhangelsky, I. V.; Zanoni Consolo, L. Z.; De Oliveira, L. C. S. Thermal Decomposition Mechanism of Aluminum Nitrate Octahydrate and Characterization of Intermediate Products by the Technique of Computerized Modeling. *J. Therm. Anal. Calorim.* **2013**, *111*, 543–548.

(29) Melnikov, P.; Nascimento, V. A.; Consolo, L. Z. Z.; Silva, A. F. Mechanism of Thermal Decomposition of Yttrium Nitrate Hexahydrate, $Y(NO_3)_3 \bullet 6H_2O$ and Modeling of Intermediate Oxynitrates. *J. Therm. Anal. Calorim.* **2013**, *111*, 115–119.

(30) Rudolph, W. W.; Mason, R.; Pye, C. C. Aluminium(III) Hydration in Aqueous Solution. A Raman Spectroscopic Investigation and an Ab Initio Molecular Orbital Study of Aluminium(III) Water Clusters. *Phys. Chem. Chem. Phys.* **2000**, *2*, 5030–5040.

(31) Rudolph, W. W.; Irmer, G. Hydration and Ion Pair Formation in Aqueous Y^{3+} – Salt Solutions. *Dalt. Trans.* **2015**, *44*, 18492–18505.

(32) Marcus, Y. Thermodynamics of Solvation of Ions. *J. Chem. Soc. Faraday Trans.* **1991**, *87*, 2295–2999.

(33) Lazar, D.; Ribár, B.; Prelesnik, B. Redetermination of the Structure of Hexaaquaaluminium(III) Nitrate Trihydrate. *Acta Crystallogr. Sect. C Cryst. Struct. Commun.* **1991**, *47*, 2282–2285.

(34) Buchanan, D. R.; Harris, P. M. A Neutron and X-Ray Diffraction Investigation of Aluminum Chloride Hexahydrate. *Acta Crystallogr. Sect. B Struct. Crystallogr. Cryst. Chem.* **1968**, *B24*, 953–960.

(35) Hartman, M.; Trnka, O.; Šolcová, O. Thermal Decomposition of Aluminum Chloride Hexahydrate. *Ind. Eng. Chem. Res.* **2005**, *44*, 6591–6598.

(36) Rudolph, W. W.; Pye, C. C. Gallium(III) Hydration in Aqueous Solution of Perchlorate, Nitrate and Sulfate. Raman and 71-Ga NMR Spectroscopic Studies and Ab Initio Molecular Orbital Calculations of Gallium(III) Water Clusters *Phys. Chem. Chem. Phys.* **2002**, *4*, 4319–4327.

(37) Richens, D. T. *The Aqueous Chemistry of Aqua Ions*, 1st ed.; John Wiley & Sons, Ltd: Chichester, England, 1997.

(38) Connick, R. E.; McVey, W. H. The Aqueous Chemistry of Zirconium. *J. Am. Chem. Soc.* **1949**, *71*, 3182–3191.

(39) Rudolph, W. W.; Fischer, D.; Tomney, M. R.; Pye, C. C. Indium(III) Hydration in Aqueous Solutions of Perchlorate, Nitrate and Sulfate. Raman and Infrared Spectroscopic Studies and Ab-Initio Molecular Orbital Calculations of Indium(III) Water Clusters. *Phys. Chem. Chem. Phys.* **2005**, *36*, 5145–5155.

(40) Lee, K. H.; Park, J. H.; Yoo, Y. B.; Jang, W. S.; Oh, J. Y.; Chae, S. S.; Moon, K. J.; Myoung, J. M.; Baik, H. K. Effects of Solution Temperature on Solution-Processed High- Performance Metal Oxide Thin-Film Transistors. **2013**, *5*, 2585-2592.

(41) Kang, C.-M.; Ryu, J. H.; Kim, H.; Baek, Y.-W. O. K.-H.; Do, L.-M. Improved Thin-Film Transistor Performance of Low-Temperature, Solution-Processed Indium Oxide by Controlling Solution Temperature. *J. Nanosci. Nanotechnol.* **2016**, *16*, 8473–8477.

(42) Park, J.; Gergely, T.; Rim, Y. S.; Pyo, S. Significant Performance Improvement of Solution-Processed Metal-Oxide Transistors by Ligand Dissociation Through Coupled Temperature-Time Treatment of Aqueous Precursors. *ACS Appl. Electron. Mater.* **2019**, *1*, 505–512.

(43) Smith, R. M.; Martell, A. E. *Critical Stability Constants*; Springer: New York, 1976; Vol. 4.

(44) Jungwirth, P.; Tobias, D. J. Ions at the Air / Water Interface. *J. Phys. Chem. B* **2002**, *106*, 6361–6373.

(45) Knipping, E. M.; Lakin, M. J.; Foster, K. L.; Jungwirth, P.; Tobias, D. J.; Gerber, R. B.; Dabdub, D.; Finlayson-Pitts, B. J. Experiments and Simulations of Ion-Enhanced Interfacial Chemistry on Aqueous NaCl Aerosols. *Science* **2000**, *288*, 301–306.

(46) Chen, X.; Yang, T.; Kataoka, S.; Cremer, P. S. Specific Ion Effects on Interfacial Water Structure near Macromolecules. *J. Am. Chem. Soc.* **2007**, *129*, 12272–12279.

(47) Sinturel, C.; Vayer, M.; Morris, M.; Hillmyer, M. A. Solvent Vapor Annealing of Block Polymer Thin Films. *Macromolecules* **2013**, *46*, 5399–5415.

(48) Liu, J.; Gao, C.; He, X.; Ye, Q.; Ouyang, L.; Zhuang, D.; Liao, C.; Mei, J.; Lau, W. Improved Crystallization of Perovskite Films by Optimized Solvent Annealing for High Efficiency Solar Cell. *ACS Appl. Mater. Interfaces* **2015**, *7*, 24008–24015.

(49) Okamura, K.; Hahn, H. Carrier Transport in Nanocrystalline Field-Effect Transistors: Impact of Interface Roughness and Geometrical Carrier Trap. *Appl. Phys. Lett.* **2010**, *97*, Article No. 153114.

(50) Polster, S.; Jank, M. P. M.; Frey, L. Correlation of Film Morphology and Defect Content with the Charge-Carrier Transport in Thin-Film Transistors Based on ZnO Nanoparticles. *J. Appl. Phys.* **2016**, *119*, Article No. 024504.

Chapter VI

(1) D. B. Mitzi, Ed., *Solution Processing of Inorganic Materials*, John Wiley & Sons Inc., Hoboken, 1st edn., 2009.

(2) B. L. Fulton, C. K. Perkins, R. H. Mansergh, M. A. Jenkins, V. Gouliouk, M. N. Jackson, J. C. Ramos, N. M. Rogovoy, M. T. Gutierrez-Higgins, S. W. Boettcher, J. F. Conley, D. A. Keszler, J. E. Hutchison and D. W. Johnson, *Chem. Mater.*, 2017, **29**, 7760–7765.

(3) Y. S. Rim, H. S. Lim and H. J. Kim, *ACS Appl. Mater. Interfaces*, 2013, **5**, 3565–3571.

(4) Y. S. Rim, H. Chen, Y. Liu, S. H. Bae, H. J. Kim and Y. Yang, *ACS Nano*, 2014, **8**, 9680–9686.

(5) M.-G. Kim, M. G. Kanatzidis, A. Facchetti and T. J. Marks, *Nat. Mater.*, 2011, **10**, 382–388.

(6) Y.-H. Kim, J.-S. Heo, T.-H. Kim, S. Park, M.-H. Yoon, J. Kim, M. S. Oh, G.-R. Yi, Y.-Y. Noh and S. K. Park, *Nature*, 2012, **489**, 128–132.

(7) J. Leppäniemi, K. Eiroma, H. Majumdar and A. Alastalo, *ACS Appl. Mater. Interfaces*, 2017, **9**, 8774–8782.

(8) E. Carlos, R. Branquinho, A. Kiazadeh, P. Barquinha, R. Martins and E. Fortunato, *ACS Appl. Mater. Interfaces*, 2016, **8**, 31100–31108.

(9) K. Song, W. Yang, Y. Jung, S. Jeong and J. Moon, *J. Mater. Chem.*, 2012, **22**, 21265–21271.

(10 S. Y. Je, B. G. Son, H. G. Kim, M. Y. Park, L. M. Do, R. Choi and J. K. Jeong, *ACS Appl. Mater. Interfaces*, 2014, **6**, 18693–18703.

(11) C. K. Perkins, M. Jenkins, T.-H. Chiang, R. H. Mansergh, V. Gouliouk, N. Kenane, J. Wager, J. F. Conley and D. A. Keszler, *ACS Appl. Mater. Interfaces*, 2018, **10**, 36082–36087.

(12) A. Nadarajah, M. Z. B. Wu, K. Archila, M. G. Kast, A. M. Smith, T. H. Chiang, D. A. Keszler, J. F. Wager and S. W. Boettcher, *Chem. Mater.*, 2015, **27**, 5587–5596.

(13) I. Isakov, H. Faber, M. Grell, G. Wyatt-Moon, N. Pliatsikas, T. Kehagias, G. P. Dimitrakopulos, P. P. Patsalas, R. Li and T. D. Anthopoulos, *Adv. Funct. Mater.*, 2017, **27**, 1–9.

(14) X. Yu, J. Smith, N. Zhou, L. Zeng, P. Guo, Y. Xia, A. Alvarez, S. Aghion, H. Lin, J. Yu, R. P. H. Chang, M. J. Bedzyk, R. Ferragut, T. J. Marks and A. Facchetti, *Proc. Natl. Acad. Sci.*, 2015, **112**, 3217–3222.

(15) L. A. Wills, X. Qu, I. Y. Chang, T. J. L. Mustard, D. A. Keszler, K. A. Persson and P. H. Y. Cheong, *Nat. Commun.*, 2017, **8**, 1–7.

(16) A. Nadarajah, M. E. Carnes, M. G. Kast, D. W. Johnson and S. W. Boettcher, *Chem. Mater.*, 2013, **25**, 4080–4087.

(17) D. A. Marsh, S. Goberna-Ferrón, M. K. Baumeister, L. N. Zakharov, M. Nyman and D. W. Johnson, *Dalt. Trans.*, 2017, **46**, 947–955.

(18) Y. Zhao, K. Kita and A. Toriumi, *Appl. Phys. Lett.*, 2010, **96**, 2001–2004.

(19) K. N. Woods, P. N. Plassmeyer, D. H. Park, L. J. Enman, A. K. Grealish, B. L. Kirk, S. W. Boettcher, D. A. Keszler and C. J. Page, *Chem. Mater.*, 2017, **29**, 8531–8538.

(20) J. T. Anderson, W. Wang, K. Jiang, T. Gustafsson, C. Xu, E. L. Gafunkel and D. A. Keszler, *ACS Sustain. Chem. Eng.*, 2015, **3**, 1081–1085.

(21) C. K. Perkins, R. H. Mansergh, D. H. Park, C. E. Nanayakkara, J. C. Ramos, S. R. Decker, Y. Huang, Y. J. Chabal and D. A. Keszler, *Solid State Sci.*, 2016, **61**, 106–110.

(22) T. B. Daunis, J. M. H. Tran and J. W. P. Hsu, *ACS Appl. Mater. Interfaces*, 2018, **10**, 39435–39440.

(23) P. N. Plassmeyer, K. Archila, J. F. Wager and C. J. Page, *ACS Appl. Mater. Interfaces*, 2015, **7**, 1678–1684.

(24) K. N. Woods, T. H. Chiang, P. N. Plassmeyer, M. G. Kast, A. C. Lygo, A. K. Grealish, S. W. Boettcher and C. J. Page, *ACS Appl. Mater. Interfaces*, 2017, **9**, 10897–10903.

(25) K. Banger, C. Warwick, J. Lang, K. Broch, J. E. Halpert, J. Socratous, A. Brown, T. Leedham and H. Sirringhaus, *Chem. Sci.*, 2016, **7**, 6337–6346.

Appendix A

(1) Sanchez-Rodriguez, D.; Farjas, J.; Roura, P.; Ricart, S.; Mestres, N.; Obradors, X.; Puig, T. Thermal Analysis for Low Temperature Synthesis of Oxide Thin Films from Chemical Solutions. *J. Phys. Chem. C* **2013**, *117*, 20133–20138.

(2) Alarcon-Flores, G.; Aguilar-Frutis, M.; Garcia-Hipolito, M.; Guzman-Mendoza, J.; Canseco, M. A.; Falcony, C. Optical and Structural Characteristics of Y_2O_3 Thin Films Synthesized from Yttrium Acetylacetonate. *J. Mater. Sci.* **2008**, *43*, 3582–3588.

(3) López, G. P.; Castner, D. G.; Ratner, B. D. XPS O 1s Binding Energies for Polymers Containing Hydroxyl, Ether, Ketone and Ester Groups. *Surf. Interface Anal.* **1991**, *17*, 267–272.

(4) Moulder, J. F.; Stickle, W. F.; Sobol, P. E.; Bomben, K. D. *Handbook of X-Ray Photoelectron Spectroscopy: A Reference Book of Standard Spectra for Identification and Interpretation of XPS Data*; Chastain, J., Ed.; Perkin-Elmer: Eden Prarie, MN, 1992.

(5) Gougousi, T.; Chen, Z. Deposition of Yttrium Oxide Thin Films in Supercritical Carbon Dioxide. *Thin Solid Films* **2008**, *516*, 6197–6204.

(6) Majumdar, D.; Chatterjee, D. X-Ray Photoelectron Spectroscopic Studies on Yttria, Zirconia, and Yttria-Stabilized Zirconia. *J. Appl. Phys.* **1991**, *70*, 988–992.

(7) Hollinger, G.; Skheyta-Kabbani, R.; Gendry, M. Oxides on GaAs and InAs Surfaces An X-Ray-Photoelectron-Spectroscopy Study of Reference Compounds. *Phys. Rev. B* **1994**, *49*, 11159–11167.

(8) Vasquez, R. P. MgO(100) by XPS. *Surf. Sci. Spectra* **1993**, *2*, 13–19.

(9) Chi, Y.; Chuang, S. S. C. Infrared and TPD Studies of Nitrates Adsorbed on Tb_4O_7, La_2O_3, BaO, and MgO/γ-Al_2O_3. *J. Phys. Chem. B* **2000**, *104*, 4673–4683.

(10) Prinetto, F.; Ghiotti, G.; Nova, I.; Lietti, L.; Tronconi, E.; Forzatti, P. FT-IR and TPD Investigation of the NO_x Storage Properties of BaO/Al_2O_3 and Pt−BaO/Al_2O_3 Catalysts. *J. Phys. Chem. B* **2001**, *105*, 12732–12745.

(11) Kameoka, S.; Ukisu, Y.; Miyadera, T. Selective Catalytic Reduction of NO_x with CH_3OH, C_2H_5OH and with C_3H_6 in the Presence of O_2 over Ag/Al_2O_3 Catalyst: Role of Surface Nitrate Species. *Phys. Chem. Chem. Phys.* **2000**, *2*, 367–372.

(12) Zhang, X.; He, H.; Gao, H.; Yu, Y. Experimental and Theoretical Studies of Surface Nitrate Species on Ag/Al_2O_3 Using DRIFTS and DFT. *Spectrochim. Acta - Part A Mol. Biomol. Spectrosc.* **2008**, *71*, 1446–1451.

(13) Szanyi, J.; Kwak, J. H.; Kim, D. H.; Burton, S. D.; Peden, C. H. F. NO_2 Adsorption on BaO/Al_2O_3: The Nature of Nitrate Species. *J. Phys. Chem. B* **2005**, *109*, 27–29.

(14) Stein, S. E. "Mass Spectra" in NIST Chemistry WebBook, NIST Standard Reference Database Number 69, Eds. P.J. Linstrom and W.G. Mallard National Institute of Standards and Technology, Gaithersburg MD, 20899, doi:10.18434/T4D303.

(15) Ahmed, M. H.; Byrne, J. A.; McLaughlin, J. A. D.; Elhissi, A.; Ahmed, W. Comparison between FTIR and XPS Characterization of Amino Acid Glycine Adsorption onto Diamond-like Carbon (DLC) and Silicon Doped DLC. *Appl. Surf. Sci.* **2013**, *273*, 507–514.

(16) Gao, F.; Li, Z.; Wang, Y.; Burkholder, L.; Tysoe, W. T. Chemistry of Glycine on Pd(111): Temperature-Programmed Desorption and X-Ray Photoelectron Spectroscopic Study. *J. Phys. Chem. C* **2007**, *111*, 9981–9991.

(17) Löfgren, P.; Krozer, A.; Lausmaa, J.; Kasemo, B. Glycine on Pt(111): A TDS and XPS Study. *Surf. Sci.* **1997**, *370*, 277–292.

(18) Tzvetkov, G.; Ramsey, M. G.; Netzer, F. P. Adsorption of Glycine on a NiAl(1 1 0) Alloy Surface. *Surf. Sci.* **2003**, *526*, 383–393.

(19) Chang, T. I. DE. Raman and Infrared Spectral Study of Magnesium Nitrate-Water Systems. *J. Phys. Chem.* **1973**, *77*, 52–57.

(20) Zhang, Y. H.; Choi, M. Y.; Chan, C. K. Relating Hygroscopic Properties of Magnesium Nitrate to the Formation of Contact Ion Pairs. *J. Phys. Chem. A* **2004**, *108*, 1712–1718.

(21) Kiss, T.; Sóvágó, I.; Gergely, A. Critical Survey of Stability Constants of Complexes of Glycine. *Pure Appl. Chem.* **1991**, *63*, 597–638.

(22) Chick, L. A.; Pederson, L. R.; Maupin, G. D.; Bates, J. L.; Thomas, L. E.; Exarhos, G. J. Glycine-Nitrate Combustion Synthesis of Oxide Ceramic Powders. *Mater. Lett.* **1990**, *10*, 6–12.

(23) Kim, M.-G.; Kanatzidis, M. G.; Facchetti, A.; Marks, T. J. Low-Temperature Fabrication of High-Performance Metal Oxide Thin-Film Electronics via Combustion Processing. *Nat. Mater.* **2011**, *10*, 382–388.

(24) Ianoş, R.; Lazău, I.; Păcurariu, C. The Influence of Combustion Synthesis Conditions on the α-Al_2O_3 Powder Preparation. *J. Mater. Sci.* **2009**, *44*, 1016–1023.

(25) Mapa, M.; Sivaranjani, K.; Bhange, D. S.; Saha, B.; Chakraborty, P.; Viswanath, A. K.; Gopinath, C. S. Structure, Electronic Structure, Optical, and Dehydrogenation Catalytic Study of $(Zn_{1-z}In_z)(O_{1-x}N_x)$ Solid Solution. *Chem. Mater.* **2010**, *22*, 565–578.

(26) Mangalaraja, R. V.; Mouzon, J.; Hedström, P.; Camurri, C. P.; Ananthakumar, S.; Odén, M. Microwave Assisted Combustion Synthesis of Nanocrystalline Yttria and Its Powder Characteristics. *Powder Technol.* **2009**, *191*, 309–314.

(27) Melnikov, P.; Nascimento, V. A.; Arkhangelsky, I. V.; Zanoni Consolo, L. Z.; De Oliveira, L. C. S. Thermal Decomposition Mechanism of Aluminum Nitrate Octahydrate and Characterization of Intermediate Products by the Technique of Computerized Modeling. *J. Therm. Anal. Calorim.* **2013**, *111*, 543–548.

(28) Melnikov, P.; Nascimento, V. A.; Consolo, L. Z. Z.; Silva, A. F. Mechanism of Thermal Decomposition of Yttrium Nitrate Hexahydrate, $Y(NO_3)_3 \cdot 6H_2O$ and Modeling of Intermediate Oxynitrates. *J. Therm. Anal. Calorim.* **2013**, *111*, 115–119.

(29) Kozak, A. J. The Thermal Decomposition of $Fe(NO_3)_3 \cdot 9H_2O$. *J. Therm. Anal. Calorim.* **1999**, *58*, 647–651.

(30) Erri, P.; Pranda, P.; Varma, A. Oxidizer−Fuel Interactions in Aqueous Combustion Synthesis. 1. Iron(III) Nitrate−Model Fuels. *Ind. Eng. Chem. Res.* **2004**, *43*, 3092–3096.

(31) Deshpande, K.; Mukasyan, A.; Varma, A. Direct Synthesis of Iron Oxide Nanopowders by the Combustion Approach : Reaction Mechanism and Properties. *Chem. Mater.* **2004**, *16*, 4896–4904.

(32) Kumar, A.; Wolf, E. E.; Mukasyan, A. S. Solution Combustion Synthesis of Metal Nanopowders: Nickel-Reaction Pathways. *AIChE* **2011**, *57*, 2207–2214.

(33) Oxley, J. C.; Smith, J. L.; Rogers, E.; Yu, M. Ammonium Nitrate: Thermal Stability and Explosivity Modifiers. *Thermochim. Acta* **2002**, *384*, 23–45.

(34) Wefers, K.; Misra, C. Oxides and Hydroxides of Aluminum. *Alcoa Tech. Pap.* **1987**, *19*, 1–100.

(35) Lee, J.-M.; Choi, B.-H.; Ji, M.-J.; Park, J.-H.; Kwon, J.-H.; Ju, B.-K. The Improved Performance of a Transparent ZnO Thin-Film Transistor with AlN/Al_2O_3 Double Gate Dielectrics. *Semicond. Sci. Technol.* **2009**, *24*, Article No. 055008.

(36) Jung, Y.; Kline, J. R.; Fischer, D. A.; Kline, R. J.; Heeney, M.; McCulloch, L.; DeLongchamp, D. M. The Effect of Interfacial Roughness on the Thin Film Morphology and Charge Transport of High-Performance Polythiophenes. *Adv. Funct. Mater.* **2008**, *18*, 742–750.

(37) Alimardani, N.; William Cowell, E.; Wager, J. F.; Conley, J. F.; Evans, D. R.; Chin, M.; Kilpatrick, S. J.; Dubey, M. Impact of Electrode Roughness on Metal-Insulator-Metal Tunnel Diodes with Atomic Layer Deposited Al_2O_3 Tunnel Barriers. *J. Vac. Sci. Technol. A Vacuum, Surfaces, Film.* **2012**, *30*, Article No. 01A113.

(38) Salgueiro, D.; Kiazadeh, A.; Branquinho, R.; Santos, L.; Barquinha, P.; Martins, R.; Fortunato, E. Solution Based Zinc Tin Oxide TFTs: The Dual Role of the Organic Solvent. *J. Phys. D. Appl. Phys.* **2017**, *50*, Article No. 065106.

(39) Fairley, K. C.; Merrill, D. R.; Woods, K. N.; Ditto, J.; Xu, C.; Oleksak, R. P.; Gustafsson, T.; Johnson, D. W.; Garfunkel, E. L.; Herman, G. S.; Johnson, D. C.; Page, C. J. Non-Uniform Composition Profiles in Inorganic Thin Films from Aqueous Solutions. *ACS Appl. Mater. Interfaces* **2016**, *8*, 667–672.